

7-11-2013

# HYPERSENSITIVE LINE-SCANNING MICROSCOPY FOR HIGH-SPEED MULTICOLOR QUANTUM DOT TRACKING

Michael David Malik

Follow this and additional works at: [https://digitalrepository.unm.edu/phyc\\_etds](https://digitalrepository.unm.edu/phyc_etds)

---

## Recommended Citation

Malik, Michael David. "HYPERSENSITIVE LINE-SCANNING MICROSCOPY FOR HIGH-SPEED MULTICOLOR QUANTUM DOT TRACKING." (2013). [https://digitalrepository.unm.edu/phyc\\_etds/39](https://digitalrepository.unm.edu/phyc_etds/39)

This Dissertation is brought to you for free and open access by the Electronic Theses and Dissertations at UNM Digital Repository. It has been accepted for inclusion in Physics & Astronomy ETDs by an authorized administrator of UNM Digital Repository. For more information, please contact [disc@unm.edu](mailto:disc@unm.edu).

Michael Malik

*Candidate*

---

Department of Physics and Astronomy

*Department*

---

This dissertation is approved, and it is acceptable in quality and form for publication:

*Approved by the Dissertation Committee:*

Keith A. Lidke, Chairperson

---

Diane S. Lidke

---

James L. Thomas

---

Sudhakar Prasad

---



**HYPERSPECTRAL LINE-SCANNING  
MICROSCOPY FOR HIGH-SPEED  
MULTICOLOR QUANTUM DOT TRACKING**

**BY**

**MICHAEL DAVID MALIK**

M.S., Physics, University of New Mexico, 2006

B.A., Physics, North Central College, 2002

**DISSERTATION**

Submitted in Partial Fulfillment of the  
Requirements for the Degree of

**Doctor of Philosophy**

**Physics**

The University of New Mexico

Albuquerque, New Mexico

May, 2013

©2013, Michael David Malik

# Dedication

*To my beautiful, loving, and supportive wife, Aimee.*

*And to my parents, Gerald and Carlyn Malik, who have helped make all of this possible, for their limitless encouragement and patience.*

# Acknowledgments

First, I would like to thank my research advisor, Keith Lidke, who has been a fantastic influence and has provided terrific instruction and advice. It has been an honor working in Keith's lab.

I would like to thank my co-advisor, Diane Lidke for her expert advice in the many aspects of cell biology and protein labeling.

I would like to thank Patrick Cutler for his extremely important contributions to the analysis code and real-time visualization software.

I would like to thank Sheng Liu for her terrific input with the spectrometer and other important optics discussions.

I would like to thank Jason Byars for the many helpful discussions regarding sample preparations, electrical engineering, machining, computing, and many other important subjects.

I would like to thank Samantha Schwartz for her instrumental help and expert suggestions in superresolution imaging.

I would like to thank Fang Huang for the many helpful conversations and suggestions in biophysics.

I would like to thank Kevin Cahill for his wonderful instruction, advice, help, and encouragement, all of which will continue to be an invaluable benefit to me going forward.

I would like to thank Shalini Low-Nam for the many helpful and inspiring conversations.

I would like to thank Peter Relich for his contributions in single particle tracking analysis.

I would like to thank John Demoss and Anthony Gravagne for their expert instruction and advice in the machine shop.

Thanks to all of those who have worked with me, and those who have instructed me during these years of my research in biophysics at UNM.

# **HYPERSPECTRAL LINE SCANNING MICROSCOPY FOR HIGH-SPEED MULTICOLOR QUANTUM DOT TRACKING**

**by**

**MICHAEL MALIK**

Ph.D., Physics, University of New Mexico, 2013

M.S., Physics, University of New Mexico, 2006

B.A., Physics, North Central College, 2002

## **ABSTRACT**

One of the challenges in studying protein interactions in live cells lies in the capacity to obtain both spatial and temporal information that is sufficient to extend existing knowledge of the dynamics and interactions, especially when tracking proteins at high density. Here we introduce a high-speed laser line-scanning hyperspectral microscope that is designed to track quantum dot labeled proteins at 27 frames/sec over an area of 28  $\mu\text{m}^2$  using 128 spectral channels spanning the range from 500 to 750 nm. This instrument simultaneously excites 8 species of quantum dots and employs a custom prism spectrometer and high speed EMCCD to obtain spectral information that is then used to distinguish and track individual probes at high density. These emitters are localized to within 10s of nm in each frame and reconstructed trajectories yield information of the protein dynamics and interactions.

This manuscript describes the design, implementation, characterization, and application of a high-speed laser line-scanning hyperspectral microscope (HSM). The intended primary application is that of investigating the dynamics of transmembrane antibody receptors using quantum dot labeled immunoglobulin E (QD-IgE). Several additional examples demonstrate other advantages and applications of this method, including 3D hyperspectral imaging of live cells and hyperspectral superresolution imaging.

# Contents

<b>List of Figures</b>	<b>xiii</b>
<b>List of Tables</b>	<b>xxx</b>
<b>1 Introduction to Fluorescence Nanoscopy. . . . .</b>	<b>1</b>
<b>2 Instrument Design Considerations and Implementation. . . . .</b>	<b>10</b>
<b>2.1 Imaging Modality Design Considerations. . . . .</b>	<b>11</b>
<b>2.1.1 Overview of Commercial Spectral Imaging Systems. . . . .</b>	<b>11</b>
<b>2.1.2 Widefield Filter Based Spectral Imaging. . . . .</b>	<b>12</b>
<b>2.1.3 Confocal Point Scanning Systems. . . . .</b>	<b>13</b>
<b>2.1.4 Confocal Line Scanning Systems. . . . .</b>	<b>14</b>
<b>2.2 HSM System Design Implementation. . . . .</b>	<b>17</b>
<b>2.2.1 Excitation Laser Line. . . . .</b>	<b>17</b>
<b>2.2.2 Excitation Laser Line Intensity. . . . .</b>	<b>21</b>
<b>2.2.3 Excitation Laser Optics &amp; Fiber Coupling. . . . .</b>	<b>24</b>
<b>2.2.4 Optimizing Excitation Laser Line Point Spread Function. . . . .</b>	<b>29</b>
<b>2.2.5 Overall Microscope Layout. . . . .</b>	<b>30</b>
<b>2.2.5.1 Excitation Path. . . . .</b>	<b>31</b>
<b>2.2.5.2 Emission Path. . . . .</b>	<b>33</b>
<b>2.2.6 Selection of Lenses. . . . .</b>	<b>35</b>
<b>2.2.7 Dichroic Mirror. . . . .</b>	<b>40</b>
<b>2.2.8 Scanning Mirror. . . . .</b>	<b>44</b>
<b>2.2.9 System Control and Data Acquisition. . . . .</b>	<b>48</b>

	2.2.10	Signal Timing for Data Acquisition and Mirror Control. . . .	52
	2.2.11	EMCCD Camera. . . . .	54
	2.2.12	Graphical Interface. . . . .	56
	2.2.13	Spectrometer Design. . . . .	59
	2.2.13.1	Equilateral Prism Spectrometer. . . . .	62
	2.2.13.2	Spherical Prism Spectrometer. . . . .	65
	2.2.13.2A	Aplanatic Image Formation of the Spectrometer. . . . .	66
	2.2.13.2B	Calculation of Spectrometer Design. . . .	68
	2.3	Performance Comparison to Commercial Systems. . . . .	70
3		Instrument Calibration and Characterization. . . . .	73
	3.1	AOM Calibration and Control. . . . .	73
	3.2	Magnification. . . . .	75
	3.3	Line Scan Angle. . . . .	79
	3.4	Wavelength Dependence on Localization. . . . .	83
	3.5	4D Point Spread Function. . . . .	85
	3.6	Spectral Calibration. . . . .	89
	3.7	Spectral Distortion and Dispersion. . . . .	90
	3.8	Spectral Resolution. . . . .	93
	3.9	EMCCD Gain Calibration. . . . .	94
	3.10	EMCCD Camera Background and Baseline Correction. . . . .	96
	3.11	Transmission Efficiency. . . . .	96
	3.12	Objective Aperture Acceptance Ratio. . . . .	100



3.13	EMCCD Quantum Efficiency. ....	101
4	Quantum Dot Characterization. ....	104
4.1	Calculation of Quantum Dot Excitation Cross-Sections. ....	104
4.2	Emission Rates and Saturation Effects. ....	107
4.3	Quantum Dot Photostability and Photoluminescence Enhancement .....	112
4.4	Quantum Dot Fluorescence Intermittency. ....	120
4.5	Quantum Dot Emission Spectra, Emission Intensity, and Spectral Shifting. ....	127
	4.5.1 Individual Quantum Dot Emissions. ....	128
	4.5.2 Ensemble Quantum Dot Emission Spectra. ....	129
	4.5.3 Quantum Dot Spectral Shifting. ....	131
5	Fixed and Live Cell Experiments. ....	134
5.1	Localization and Track Reconstruction. ....	134
5.2	Multicolor Single Particle Tracking of Membrane Proteins. ....	137
	5.2.1 Oligomer Dynamics. ....	137
	5.2.2 Interactions with Membrane Components. ....	139
5.3	3D Hyperspectral Scanning of Live Cells. ....	141
5.4	Hyperspectral Superresolution. ....	142
6	Conclusion. ....	153
A	Alignment. ....	156
A.1	Reference Beam. ....	157
A.2	Scanning mirror. ....	161

A.3	Dichroic Mirror. ....	163
A.4	Excitation Path Cage Systems. ....	165
A.5	Excitation Laser Beam. ....	167
A.6	Laser Line Generator Lens. ....	169
A.7	Cylindrical Lens (CYL1) ....	172
A.8	Lenses CYL2 and L1. ....	173
A.9	Overall Excitation Path. ....	173
A.10	Widefield Emission Path. ....	174
A.11	Fine-tuning the Excitation Path. ....	176
A.12	Spectrometer Alignment. ....	177
A.13	Fine-Tuning the Emission Path. ....	181
<b>B</b>	<b>Materials and Methods</b>	
B.1	Imaging of QDs non-specifically adhered to glass. ....	183
B.2	Reagents. ....	183
B.3	Image Acquisition for SPT Experiments on Live Cells. ....	184
B.4	Single Particle Tracking (Preprocessing, Localizations, and Trajectory Building) ....	185
B.5	Cell Culture. ....	186
B.6	Cell Treatment for SPT of QD-IgE. ....	186
B.7	3D-scanning of Live Cells. ....	187
B.8	Hyperspectral Superresolution. ....	188
<b>C</b>	<b>Polarization Effects on PSF. ....</b>	<b>190</b>
<b>D</b>	<b>Quantum Dot Emission Spectra. ....</b>	<b>200</b>

<b>E</b>	<b>Emitter Localization and Track Reconstruction. . . . .</b>	<b>209</b>
<b>E.1</b>	<b>3D Gaussian Fitting. . . . .</b>	<b>209</b>
<b>E.2</b>	<b>Track Reconstruction. . . . .</b>	<b>216</b>

# List of Figures

- 1.1 Diffraction limited resolution. An example Airy pattern (generated in Matlab) from one emitter (blue) is shown with a first local minimum at about  $x = \pm 3.8$  (arbitrary units). It is represented here with one spatial dimension where the actual 2D spatial pattern that is observed would be a surface defined by rotating this curve about the z-axis. The second emitter (green) is positioned such that its peak intensity is centered at the first minimum of the first emitter, where they are considered to be “just resolved”. The observed intensity would be the sum of the two emitters, shown by the dashed magenta line. . . . . 2
- 1.2 Gaussian approximation. The Airy pattern of the first emitter (blue) is shown along with a plot of a Gaussian function that has been fit to the center region bound by the first local minima. Presence of the second emitter (green) would perturb this fit. . . . . 4
- 1.3 Hyperspectral microscope concept. Here, the white spheres in the sample represent fluorophores that remain mostly in the ground state while the colored spheres denote those which are excited. A few simplified example rays are shown of the colored emission light from the fluorophores (more realistic emissions are withheld here for illustration purposes). . . . . 7
- 2.1 Confocal microscope. The green color represents light from an emitter that is in focus, so that light passes through the pinhole that is positioned at a conjugate focal plane. The red color represents light emitted from a fluorophore that is out of focus and is blocked by the pinhole aperture. Additionally, the excitation light is focused, which maximizes in-focus emissions and minimizes out-of-focus excitation. . . . . 14
- 2.2 Laser line produced by a cylindrical lens (shown on a dense sample of 200 nm fluorescent beads,  $150\times 1.45 NA$  objective). Variations in the

	measured intensity profile are caused by the spatial bead distribution on the glass. . . . .	18
2.3	(A) A side view of a line generator lens. The vertical scale is in mm. (B) The laser line produced by a line generator lens (shown on a dense sample of quantum dots). Minor fluctuations of intensity along the line are mostly due to variations in the quantum dot concentration on the glass surface. . . . .	20
2.4	AOM operation in Bragg mode. Here, $\lambda$ is the wavelength of incident light (488 nm for this laser), $\Lambda$ is the distance between pulses in the crystal, $V$ is the velocity of sound in the crystal, $f$ is the frequency of the pulses generated by the transducer, and $\theta_b$ is the Bragg angle. . . . .	22
2.5	Bragg angle calculation. This model shows an incident beam (arrow pointing down to the right) that is interacting with two acoustic pulses in the crystal medium (horizontal lines). The incident beam is composed of many waves, some of which reflect at the first pulse, some reflect at the second pulse, and some continue through. Constructive interference occurs between the reflected beams when their path lengths differ by an integer number of wavelengths, $m$ . The angles are exaggerated here for clarity. . . . .	23
2.6	Laser, AOM, and fiber coupling. The 488 nm diode laser module is anchored to a large piece of custom machined aluminum, used to place the beam at a desired height and also serves as a good heat sink, which is necessary for stable laser power output and for longevity of the laser diode. The beam exits the laser module going to the left through the neutral density filters. The beam is then directed down and then to the left, through the AOM, and then up and to the left, into the objective lens for fiber coupling. . . . .	25
2.7	(A) A calculation to determine the appropriate lens for coupling a free space laser beam into the fiber. (B) A comparison of polarization maintaining fibers and standard single mode fiber. The index of refraction is typically greater in the darker shaded regions. (C) A	

	calculation to determine the appropriate lens for collimating a beam to the desired diameter. *Diagrams (A) and (B) are from <a href="http://www.newport.com/Tutorial-Fiber-Optic-Basics/978863/1033/content.aspx">http://www.newport.com/Tutorial-Fiber-Optic-Basics/978863/1033/content.aspx</a> . . . . .	27
2.8	Partial vs. full use of back aperture of the objective lens. The same power of light (total photons/sec) is the same in both of these example beams. The one on the left is more concentrated at most points along $z$ (shown as the vertical dimension in the drawing), and the one on the right is less concentrated at the objective but goes to the same concentration at the focal point, so the gradient along $z$ is greater, which ultimately reduces out of focus excitation. . . . .	30
2.9	Optical layout. All focal lengths shown are in mm. . . . .	31
2.10	Collimating the laser line. The dashed line intersects the optical axis at the focal point of the cylindrical lens, and this intersection can be at any point on the axis, even inside the line generator lens itself. The important part is that the light is collimated after the cylindrical lens, which can be verified in measuring $h$ at different positions along the optical axis ( $z$ ). The 15-degree fan angle is for the entire distribution, so $\theta$ here is 7.5 degrees. . . . .	38
2.11	Excitation path optics. These diagrams show the overall function of the lenses along the $x$ and $y$ dimensions, where the $y$ -axis is perpendicular to the table surface. The beam is not actually reflected in $y$ (it would actually be into the page, along $x$ ), but is shown here as such only to illustrate the focusing of the line along $y$ at the scanning mirror. The filled solid line lenses are meant to indicate that these components have some influence in that dimension, and the components shown in dashed lines do not. . . . .	40
2.12	Dichroic beam splitter transmission. These three plots are all for the same filter, but show the transmission at different scales. The top is the full range covering the excitation and emission of this instrument. The middle shows the lower range covering the excitation and lower	

wavelength emissions, and the bottom shows the upper wavelength range. ....	43
2.13 Scanning mirror angle calculation. The angles shown here are greatly exaggerated for easier display. ....	46
2.14 System control and data acquisition schematic. The light gray boxes represent physically distinct elements, the dark gray boxes indicate different cards or components in the PC, and the white boxes indicate interfaces within each component or device. The individual lines represent multiple physical wires and/or channels between devices. .	49
2.15 Scanning mirror digital control. The NIDAQ breakout boxes (white) are used to provide and receive analog and digital I/O. The scanning mirror is controlled via digital input from the ribbon cable. The LEDs provide visual confirmation of signal on each channel. ....	52
2.16 Signal timing. The scanning mirror angle is advanced by one step, beginning with the trigger fire pulse, which is sent by the EMCCD upon completion of each frame readout. The readout and exposure times are the same since this is a frame transfer EMCCD. ....	54
2.17 EMCCD camera readout. The actual array in the camera is 128×128 pixels, and for simplicity in this figure the example displayed is a 12×12 array. The green pixel represents a single element in the array that is shifted very quickly to the frame transfer region (darker gray), which is shielded from exposure. The image frame is exposed while the frame transfer region is processed. Immediately after the entire frame transfer region is fully processed, another full frame is shifted into the shielded region. ....	56
2.18 Data acquisition and control interface. ....	57
2.19 Graphical interface for live viewing of hyperspectral data. This example shows one spectral image of a sample containing several varieties of quantum dots. The spectra for the red, green, and blue boxes are shown in their representative colors in the plot below the image. This image is from [9]. ....	59

2.20	Spectrometer prism material. . . . .	61
2.21	Equilateral prism spectrometer design. Inset (A) shows the various angles used for the calculation of the relative angle between the incident and transmitted beams. Inset (B) illustrates the dispersion of light at the EMCCD camera, where the overall sensor size determines the focal lengths of the collimating and focusing lenses. . . . .	62
2.22	Spectral distortion from the equilateral prism spectrometer. Emission light from a spectral calibration light is shown as imaged at the EMCCD. The horizontal axis is the spectral dimension and the vertical axis is the spatial dimension (along the slit, y-axis). . . . .	66
2.23	Spherical prism spectrometer design. (A) Relative positions of each spherical surface of the prism spectrometer. <i>S1</i> (red solid circle) and <i>S2</i> (blue solid circle) are refractive surfaces of the spherical prism, <i>S3</i> (cyan solid circle) is the reflective surface of the concave mirror. The dotted circles are conjugate aplanatic surfaces of <i>S1</i> and <i>S2</i> . (B) Relationship of conjugate aplanatic surfaces (dotted circles) of the refractive spherical surfaces (solid circles). (C) 3D drawing of the spectrometer. (D) Spectrometer design in OSLO (Optics Software for Layout and Optimization). . . . .	68
3.1	AOM calibration. The red vertical lines indicate the minimum and maximum values of output power measured at the free space collimated laser beam after the air objective, before the laser line generator lens. The plot shows input voltages ranging from -0.3 to +0.6 at an offset dial position of 3 (as marked on the driver unit used here). . . . .	74
3.2	Grid target with 10 $\mu\text{m}$ spacing observed with widefield the camera. .	77
3.3	Widefield image of the low-density sample of fluorescent beads. The dashed line shows the region that would be viewed when scanned in hyperspectral mode (using 128 steps per scan). . . . .	78
3.4	Hyperspectral line-scanning mode image of the low-density bead sample. The displacement vectors here are compared to the same ones	



	taken in widefield to obtain the overall magnification, including any amount added by the spectrometer. ....	79
3.5	Laser line angle relative to the scanning direction. Here, the blue rectangle represents the laser line profile as it is projected on the sample plane. Panel (A) shows the ideal case, whereas (B) is the condition to be avoided. ....	80
3.6	An image of emission light from a dense, planar sample of quantum dots fixed to a glass cover slip, excited by the laser line. When the line is correctly aligned with the CCD, the center of the bright region will be centered along a single row of pixels. ....	81
3.7	Maximum projection of a widefield scan of low-density fluorescent beads on a glass cover slip. Each line segment here is the series projection of a single fluorescent bead as the sample is scanned. The brighter lines are likely small clusters of two or more beads. The scan angle is verified using several of these lines at different parts of the field of view. ....	82
3.8	Hyperspectral image of a low-density sample of 100 nm TetraSpeck beads. The upper left quadrant shows the image (summed over the spectral dimension). The upper right and lower left quadrants are used to estimate the pixel location of each bead that is subsequently localized using different spectral regions of the emission light. ....	84
3.9	Wavelength dependence on localization. Scatter plot of 300 localizations of a single 100 nm TetraSpeck bead on glass using three different wavelength ranges. The purpose here is to quantify any chromatic dependence on particle localization. Emitters were 100 nm Tetraspeck beads diluted 2000:1 in 1x PBS and allowed to stick to a glass cover slip. The sample was then scanned 300 times and localizations were obtained for each scan using emitted light from each of three different wavelength ranges. The mean of the localized $x$ -positions varied by $\sim 10$ nm and the mean of the localized $y$ -positions varied by $\sim 8$ nm. (A) Scatter plot of localizations with the mean	

	identified by ‘+’ and listed at the top of the figure. (B) Error bars indicating one standard deviation. . . . .	85
3.10	Theoretical 4D PSF. The 4D PSF is calculated from the theory as described in the text. The spectra and widefield point spread function are based on 100 nm yellow beads. The simulation includes aberrations generated from the phase retrieval process. A linear stretch (A) and log stretch (B) of intensity for projections on the $x$ - $y$ , $x$ - $z$ , and $y$ - $z$ planes are shown along with the $x$ , $y$ , and $z$ vs. wavelength projections (C, D, and E). . . . .	87
3.11	Experimental 4D PSF. The sample is a 100 nm TetraSpeck bead imaged at 100 nm steps in $z$ . A linear stretch (A) and log stretch (B) of intensity for projections on the $x$ - $y$ , $x$ - $z$ , and $y$ - $z$ planes are shown along with the $x$ , $y$ , and $z$ vs. wavelength projections (C, D, and E). The figures show three emission peaks of TetraSpeck bead, 505/515 nm (green), 560/580 nm (orange) and 660/680 nm (dark red). Data were acquired at room temperature, using a 60 $\times$ water objective, $NA=1.2$ . . . . .	88
3.12	Spectral calibration. (A) Image of the calibration lamp on the camera (the vertical axis is the spectral dimension). The calibration lamp is a LightForm multi-ion discharge lamp (MIDL), the slit width is 20 $\mu\text{m}$ , and the camera is an Andor iXon 860 EMCCD with an array size of 128 $\times$ 128, pixel size 24 $\mu\text{m}$ . (B) Spectral curve, generated by the sum projection of (A) along the $x$ dimension; the peak wavelengths are identified from the specification sheet of the calibration lamp. The blue, green, and red lines correspond to the regions in (A) with the same color. All three colored lines almost overlap with each other, which demonstrates a very small distortion in the spectral lines. (C) Dispersion curve, generated from the spectral curve (C), by polynomial fit of specific wavelengths. . . . .	90
3.13	Spectral distortion and dispersion. The distortion and dispersion curves are generated from OSLO. (A) Distortion shows offset of the true image position from the ideal image position at various off axis points. In the	

	HSM setup, the maximum distance from the axis is 1.5 mm, so the designed maximum distortion is 0.4 $\mu\text{m}$ , which is less than 2% of CCD pixel size (24 $\mu\text{m}$ ). (B) Lateral shift shows the dispersion, designed to span a total of 3 mm from 500 nm to 800 nm. It shows dispersions in four relative heights (distance from the optical axis), the four curves are right on top of each other, so the spectral lines are straight, which also indicates a minimal distortion. ....	92
3.14	Spectral resolution. (A) Using the 20 $\mu\text{m}$ slit. (B) Using the 100 $\mu\text{m}$ slit. ....	93
3.15	EMCCD gain calibration. (A) Emission light from green fluorescent reference slide (Chroma Technology Corporation). (B) The sum projection over the horizontal dimension of the image in (A). The 488 long-pass filter has a sharp cutoff at 500 nm that leaves several dark rows that are used in the baseline correction. (C) Example plot of the variance of counts <sup>2</sup> vs. counts and the fit used to determine the gain ( $=1/\text{slope of the line in photoelectrons/ADU}$ ). ....	95
3.16	Transmission efficiency vs. wavelength for the objective lens. This plot is directly from the Olympus website: <a href="http://www.olympusamerica.com/seg_section/img/uis2/graphs/uplsapo_60xw_graph.gif">http://www.olympusamerica.com/seg_section/img/uis2/graphs/uplsapo_60xw_graph.gif</a> . ....	98
3.17	Objective aperture acceptance ratio. In this drawing, the objective lens is represented by the blue region, intended to be a circular area on the surface of a sphere of radius $AB$ . For this case the $z$ -axis is horizontal (along the optical axis of the objective). The angle $\theta$ is determined using the numerical aperture of the objective. The solid angle of acceptance is that of a conic volume defined by rotating triangle $ABC$ about the $z$ -axis. ....	100
3.18	EMCCD Quantum efficiency. <a href="http://www.andor.com/scientific-cameras/ixon-emccd-camera-series/ixon3-860">http://www.andor.com/scientific-cameras/ixon-emccd-camera-series/ixon3-860</a> . ....	102
4.1	Quantum dot emission rate as a function of excitation intensity. These plots were generated using a model that assumes the quantum dots are	

	two state emitters. In this model, excited state saturation appears to occur at or above about 105 W/cm <sup>2</sup> . . . . .	112
4.2	Quantum dot bleaching analysis example plot. Data for Qdot 525 under 15% laser power (8200 W/cm <sup>2</sup> ) is shown in blue and the fitted exponential decay function is shown in red. Similar plots were made for all 8 species of quantum dots, older and newer stocks, for two regions in each sample. . . . .	117
4.3	Photoluminescence enhancement (PLE). The data to the right of the dashed line were fit to an exponential decay curve in order to determine the half-life and rate constant that describe the longer term behavior of the population of quantum dots exposed to the given excitation light intensity. . . . .	119
4.4	Fluorescence intensity trajectory for a single quantum dot. This is the 5×5 subregion pixel sum of intensity over time, showing that the quantum dot “blinks” between “on” and “off” states at various time scales. . . . .	121
4.5	Quantum dot energy state transitions. Black circles represent electrons while the white circles represent “holes”. The green arrow represents absorption of a photon from the excitation light. The dashed black arrow represents relaxation (through phonons in the lattice) to the ground state of the conduction band. The red arrow represents recombination of the electron-hole pair, resulting in fluorescence emission. The magenta arrow represents tunneling into a trap state, with the orange arrow indicating a non-radiative decay from the trap back to the valence band. The white arrow indicates a mechanism for oxidation of selenium atoms, which may contribute to blue shifting and/or photobleaching in addition to a temporary dark state. . . . .	122
4.6	Quantum dot blinking statistics for QD 625. (A) The distribution of probabilities of the “on” times vs. duration of the “on” time is plotted along with the power law fit. (B) The distribution of probabilities of the “off” times vs. duration of the “off” time is plotted along with the power	

	law fit. These data were acquired at 28 FPS, so the $x$ -axis ranges from ~36 msec (1 frame) to 3.6 sec (100 frames). . . . .	124
4.7	Quantum dot blinking statistics for QD 705. (A) The distribution of probabilities of the “on” times vs. duration of the “on” time is plotted along with the power law fit. (B) The distribution of probabilities of the “off” times vs. duration of the “off” time is plotted along with the power law fit. These data were acquired at 28 FPS, so the $x$ -axis ranges from ~36 msec (1 frame) to 3.6 sec (100 frames). . . . .	125
4.8	Individual quantum dot emission spectra. Progressing from blue to red are sum projections of raw data (solid) and Gaussian fits (dashed) for single 525, 565, 585, 605, 625, 655, 705 and 800 nm QDs. . . . .	128
4.9	Ensemble quantum dot emission spectra and observed intensity. QD 565 is shown here as an example. (A) shows spectral features of individual QDs (colored lines; 5 randomly selected spectra) and the ensemble of all individual QDs (black line). (B) is a histogram of fit spectral emission peaks ( $\theta\lambda$ ) identified by 3D Gaussian fitting ( $x,y,\lambda$ ) for individual QDs. The red tick indicates the expected emission peak for the given QD. (C) is a histogram of the fit standard deviation in the spectral dimension ( $\theta\sigma\lambda$ ) identified by 3D Gaussian fitting for individual QDs. (D) is a histogram of fit photons per frame ( $\theta\sigma\lambda$ ) for individual QDs. . . . .	130
4.10	Quantum dot spectral shifting. The color represents the peak emission wavelength, with dark blue indicating about 590 nm and dark red is about 710 nm. The laser intensity was ~27,000 W/cm <sup>2</sup> . . . . .	131
5.1	Quantum dot localization. (A) Progressing from blue to red are sum projections of raw data (solid) and Gaussian fits (dashed) for single 525, 565, 585, 605, 625, 655, 705 and 800 nm QDs. (B) 3D representation of a single hyperspectral time frame with 3D boxes representing sub-volumes identified for further particle localization. Sum projections of the data onto each plane are used to represent the raw data (gray scale). Likewise, 2D projections of each 3D box onto each plane are used to highlight the sub-volumes. Fitting results for the colored sub-volumes	

(color corresponds to the spectral center of the box) in (B) are shown in (C), (D), and (E). In the top figures in (C), (D), and (E) red and green are sum projections of the raw data and fit respectively. Note that the color outlining (C), (D), and (E) correlate with the respective sub-volumes highlighted in (B) with the same color. The localized particles are represented by white ellipsoids in which the radius in each dimension shows 3 standard deviations in the estimated error in the fit using the Cramér Rao Bound and their projection onto each axis is represented by a gray ellipse. The bottom figures in (C), (D), and (E) show raw spectral features (black) and Gaussian fits (color corresponds to fit spectral emission peak). The vertical gray lines represent the spectral cutoffs for independently fit sub-volumes. This figure is from [5]. . . . .136

- 5.2 SPT of 5-colors (565, 585, 605, 625, 655) of QD-IgE on live RBL cells. All subfigures are derived from a single acquisition (27 fps) ~7 minutes after crosslinking with DNP3. (A) 3D ( $x, y, t$ ) depiction of trajectories. The color scheme for the trajectories is dependent on the estimated emission peak of each QD as noted by the color bar. A trimer (565 QD cyan diamond; 605 QD yellow square; 655 QD red up triangle) and dimer (585 QD cyan circle; 605 QD yellow down triangle) are highlighted by their respective symbols. (B) and (C) show localizations for specified time frames. Coloration and symbols correspond to (A). Ellipses in the upper subfigures represent 3 times the localization accuracies over a gray scale projection of the raw data. Red ellipse in the upper left subfigure of (C) is a localized 655 QD that doesn't interact with the dimer. Raw spectra (solid black lines) and Gaussian fit (colored lines with symbols) for individual QDs are shown in the lower subfigures. . . . .138
- 5.3 SPT of 4-colors (605, 625, 655, and 705) of QD-IgE-FcεRI on live RBL cells transiently transfected with GFP-actin acquired at 27 fps. (*left*) Two representative frames are shown. The GFP-actin presented in

	normalized gray scale is the spatially deconvolved portion of the spectrum between 500-570 nm. It is overlaid with Gaussian blobs reconstructed for localized QDs and trajectories for QD-IgE-FcεRI spanning the previous 3.7 s (100 frames; coloration of blobs and trajectories according to emission peak; see color bar). Colored symbols highlight QD-IgE-FcεRI positions at the specified frame, and representative spectra are shown to the right. Text identifiers (D, M1, M2, and M3) are used to indicate monomers (M#) and dimer (D) trajectories. ....	140
5.4	3D scanning of live cells. Change in cell morphology upon activation of IgE-FcεRI by crosslinking with multivalent antigen (DNP-BSA). (A), (B), and (C) show 3D isosurface representations of deconvolved z stacks for a single cell acquired at 1 hyperspectral image stack every 7.72 seconds at several time points before and after activation as indicated. Cells are labeled with Cell Mask orange (blue), Actin-GFP (green), and QD- IgE-FcεRI (red). ....	142
5.5	HSM SR live viewing mode. A raw (not localized) image showing Atto 532 labeled clathrin (green) and Alexa 488 labeled tubulin (blue) in Swiss 3T3 cells. With appropriate blinking statistics and curve resolution methods, multicolor SR image reconstruction should be possible. In this case the z depth is ~500 - 700 nm off of the glass coverslip surface into the sample. ....	144
5.6	High density SR image using the HSM. (A) A sum projection of 1000 frames (line scans) of Alexa 488 labeled tubulin. (B) The same ROI now reconstructed using fitted positions from light in the emission spectrum of Alexa 488. ....	145
5.7	Multicolor SR. (A) A reconstructed image of localized Alexa 488 labeled tubulin from 8000 frames (line scans). (B) The same ROI, but now showing the reconstructed image from localizations of Atto 532 labeled clathrin. (C) A composite image of the Alexa 488 (blue) and Atto 532 (yellow), each localized independently. ....	147

5.8	Five-state blinking dye kinetic model. A given blinking dye molecule has ground state S0, excited singlet state S1, triplet state T1, dark ionic state D1, and photobleached state B. This model describes the populations of states as a laser line is scanned across the molecule. .	149
5.9	Population of states as a function of time. Only states 1 and 4 show appreciable dynamics on this time scale, which is mainly due to the mean lifetime of state 4, the dark ionic state. ....	150
A.1	Reference Beam System. The objective port here is just behind the cage alignment target and 30 mm cage plate. ....	158
A.2	Reference target. When set to a reference beam height this target is used to verify that the beam is parallel to the table by checking it at two or more locations on the table, separated by the largest distance that can be accommodated. It is also useful as a reference height for setting up the 30 mm cage systems that will hold the other optical elements. ....	159
A.3	Alignment of lens L2. The scanning mirror and dichroic are shown, already in position. The z-axis micro-positioner holding the SM1 tube is attached to the 30 mm cage system with the adjuster on the left side (obscured in this view angle). The side port of the microscope base lies just behind the 1/4" black acrylic panel at the top of the figure. The c-mount to SM1 tube adapter attaches to and supports the 30 mm cage to the side port. ....	160
A.4	Emission path offset due to dichroic mirror. The dichroic mirror has a substrate of glass with a thickness of 1 mm. Emission light or alignment beam light (shown here as a blue ray) incident from the bottom of the diagram is refracted at each air-glass interface, resulting in an overall shift of $d = 0.33$ mm. Sizes and angles are exaggerated for easier viewing. For the calculation, $t$ is the thickness of glass traversed by the ray traveling through the dichroic. ....	164
A.5	Excitation path cage system alignment. When properly aligned, the reference beam reflected by the first surface of the dichroic will pass through the center (1 mm) aperture of the alignment target at each end	



- of the cage system. For shorter cages, such as the one that holds lens L1, longer rods are used with an additional post (not shown) in order to maximize the accuracy of the alignment. These extended rods are then replaced one at a time with the shorter ones. . . . . 167
- A.6 Excitation laser beam alignment. Laser light from the fiber (lower left) is collimated by the air objective and propagates in the direction of the blue arrow, towards the first beam steering mirror (top left). The beam is reflected again at the second beam steering mirror, passing through the cage systems, towards the alignment target. When aligned, the green reference beam will pass through the center of the target (from the bottom of the figure) while the blue excitation beam will pass through the same target center from the opposite direction. . . . . 169
- A.7 Laser line generator lens alignment. The blue arrows represent the collimated free space laser beam as it is reflected by the beam steering mirrors, going into the line generator lens. The alignment target is used to verify the  $x$ -position and the angle of the line in the  $x$ - $y$  plane. . . . 172
- A.8 Overall excitation beam alignment. A paper strip is set on the cage plate closest to the objective port in order to see both the excitation beam (coming up from the base) and reference laser beam (directed down from the top of the cage) in alignment with respect to each other and the objective when it is placed. With the excitation laser line centered in the  $x$ - and  $y$ -dimensions along the entire excitation path, the angle and position should be correct up to the objective port. In this figure, the green laser is somewhat difficult to see against the blue line, but this is much easier when observing it directly. . . . . 174
- A.9 Widefield emission path. Lens L3 ( $f = 175$  mm, achromatic doublet) is mounted in an SM1 lens tube held in a 30 mm cage system that extends from the cage cube holding the dichroic mirror. The flip-mount mirror is shown in the down position, directing the light into the widefield CCD camera, which is mounted on a 30 mm rotation plate. The entrance slit

	to the spectrometer is shown near the top of the figure, and is positioned at the focal point of lens L3. . . . .	175
A.10	Spectrometer layout and alignment. The diagram shown in (A) illustrates the positioning of the elements in the $x$ - $z$ plane ( $x$ -axis is along the vertical direction and the $z$ -axis is horizontal). The transmitted reference beam projected onto a reference target that is placed between the spherical prism and concave mirror is depicted in (B). The dashed line represents the possible positions of the beam on the target as the spherical prism is rotated in the $x$ - $y$ plane. The left side shows the beam when the prism is not at the correct angle and the right side is the desired result. . . . .	179
A.11	Spectrometer and EMCCD. The spectrometer components are all mounted to a removable breadboard to facilitate the setup and it allows the entire spectrometer to be removed as a single unit while maintaining the relative positions of the components. The emission light path just clears the mounting hardware for the planar mirror by several mm (more than the required aperture of $\sim 1$ mm at that position). . . . .	180
C.1	Polarization effect on the point spread function. . . . .	190
C.2	Simulation showing a dipole emitter at $\theta = \pi/4$ and $\phi$ can be any value from zero to $2\pi$ (shown at zero). The pink arrow indicates the dipole orientation. On the right side, the modified PSF is simulated on a $128 \times 128$ pixel camera at the image plane, where the top figure shows a log stretch and the bottom figure shows the normal values. . . . .	199
D.1	QD 525 ensemble emission spectra and observed intensity. . . . .	201
D.2	QD 565 ensemble emission spectra and observed intensity. . . . .	202
D.3	QD 585 ensemble emission spectra and observed intensity. . . . .	203
D.4	QD 605 ensemble emission spectra and observed intensity. . . . .	204
D.5	QD 625 ensemble emission spectra and observed intensity. . . . .	205
D.6	QD 655 ensemble emission spectra and observed intensity. . . . .	206
D.7	QD 705 ensemble emission spectra and observed intensity. . . . .	207
D.8	QD 800 ensemble emission spectra and observed intensity. . . . .	208

- E.1 3D Gaussian model. (A) 3D pixelated Gaussian model for a single QD with Poisson noise. (B) The standard deviation in parameter estimates from 500 fits of simulated data with Poisson noise (open circles) agree well with the theoretical standard deviation (square root of the Cramér Rao Bound;  $x$ ). No blinking was included in this simulation. (C) and (D) show results for fitting. Simulations of 2 QDs with a fixed spatial separation (0.5 pixels or  $\sim 60$  nm) and variable spectral separation (0 to 50 nm) are fit with a 2 QD model. (C) The relative accuracies (absolute error ( $\epsilon$ ) normalized by the pixel size) for positional parameters for QD 1 (solid lines;  $\theta_{x1}$ ,  $\theta_{y1}$ ,  $\theta_{\lambda1}$ ) and QD 2 (dashed lines;  $\theta_{x2}$ ,  $\theta_{y2}$ ,  $\theta_{\lambda2}$ ). (D) The percent of divergent fits (yielded unreasonable parameter estimates). . . . . 212
- E.2 Multi-QD fitting routine. QD fitting is performed sequentially for 1 to  $N$  QDs. Figure adapted from Huang et al. More details about the fitting steps are included in the text. . . . . 213
- E.3 (A) Localizations for a single QD605 overlaid on the sum projection of raw data. Coloration of localizations corresponds to the localized emission peak (color bar). The estimated intensity (left axis; blue) and spectral emission peak (right axis; green) are shown over time ( $\sim 3.8$  fps) in (B). Note the blue shifting of the QD is observed in (A) and (B). Localizations were binned by intensity in (C) and the standard deviation of the localization parameters were compared to the square root of the CRB in (D), (E), and (F). The standard deviation in the line dimension (E) corresponds well to the theoretical lower bound. The standard deviation in the scanning dimension (D) and the spectral dimension (F) do not correspond well with theory. This is attributed to QD blinking during the line scan and QD blue shifting respectively. . . . . 216
- E.4 Spectral information improves trajectory connections. Hyperspectral image data (100 frames) with diffusing QDs were simulated (QD simulation parameters attained from the characterization of QDs) and localized (Appendix E). Trajectories were subsequently built either

using (solid colored lines) or ignoring spectral information (solid black lines). Localizations are shown in ellipsoids (size of the ellipsoid corresponds to 3x the estimated localization accuracy), and solid colored lines correspond to the connected trajectories. Dashed colored lines represent the ‘true’ simulated trajectories. The black line with circles identifies trajectories built from connecting localizations without spectral information. Black diamonds represent positions where tracks jump from one true underlying track to another. . . . . 218

# List of Tables

2.1	Parts Reference. . . . .	34
2.2	Spectrometer Dimensions of each surface in OSLO design. . . . .	70
3.1	Transmission efficiency of emission path. . . . .	99
4.1	Quantum dot cross-sections for an excitation source wavelength of 488 nm. . . . .	106
4.2	Quantum dot photobleaching half-life and rate constants. The naming convention used for the quantum dot stocks is the peak emission wavelength and the shelf age of the lot, where “Old” refers to a stock that is 1-year in aqueous solution, and “New” implies that the lots were about 1 month of age. . . . .	118
4.3	Quantum dot emission spectra and observed intensity. Statistics for results shown in Figure 4.9 are summarized in this table. Additional descriptions of the model parameters are included in Appendix E. . .	130
5.1	Rate constants used in simulation. . . . .	150
E.1	Gaussian fitting variables. . . . .	210

# Chapter 1

## Introduction to Fluorescence Nanoscopy

Understanding the mechanisms of cellular signaling is an important goal in cell biology and is required for understanding aspects of dysregulation that can lead to diseases such as cancer or allergies. One key aspect in the study of cell signaling involves the examination of membrane protein interactions in living cells. Signaling processes are often initiated by dimerization or oligomerization of the membrane proteins, and these interactions occur at scales of tens of nanometers or less. The study of membrane protein dynamics is a challenge for biologists since the diffraction limit of visible light (described below) is at least an order of magnitude larger than this size. Individual proteins can be localized and tracked within this scale ( $\sim 10$  nm), but observing the dynamics of multiple particles interacting within this extent is difficult and requires the implementation of more advanced methods. The focus of the research described here is on the development of one such method that enables further study of membrane protein dynamics by tracking multiple proteins at spatial and temporal resolutions necessary to make new observations.

Microscopes are optical systems designed to magnify objects for observation or imaging and are composed of lens elements that typically have a circular aperture. Light that is focused to a point through a circular aperture, as in the case of the microscope objective lens, produces a diffraction pattern known as an Airy pattern [1] at the focal point. Likewise, light that is emitted from a point source at the focal plane of the objective produces an image of the Airy pattern at the image plane of the microscope (after the

eyepieces or at an imaging sensor element, such as in a camera). This unavoidable distribution of the light limits the overall resolution of the microscope. When using the human eye as a detector and without any additional analysis techniques, the maximum resolution where two point sources are just far enough apart to be considered as barely resolved, occurs when the first Airy pattern minimum of one emitter coincides with the maximum of the other one (see **Figure 1.1**).

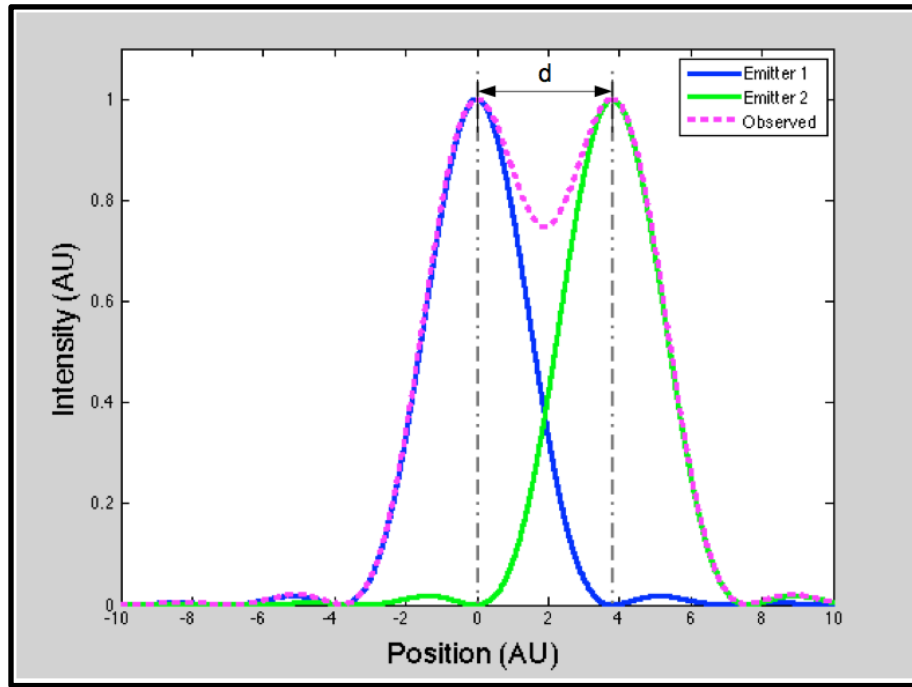


**Figure 1.1: Diffraction limited resolution.** An example Airy pattern (generated in Matlab) from one emitter (blue) is shown with a first local minimum at about  $x = \pm 3.8$  (arbitrary units). It is represented here with one spatial dimension where the actual 2D spatial pattern that is observed would be a surface defined by rotating this curve about the z-axis. The second emitter (green) is positioned such that its peak intensity is centered at the first minimum of the first emitter, where they are considered to be “just resolved”. The observed intensity would be the sum of the two emitters, shown by the dashed magenta line.

In microscopes, this diffraction-limited distance  $d$  (known as the Rayleigh criterion) [2] is

$$d = \frac{1.22 \lambda}{2 NA}$$

Here,  $\lambda$  is the wavelength of emitted light and  $NA$  is the numerical aperture of the objective lens,  $NA = n \sin \theta$  ( $n$  is the index of refraction of the medium between the emitter and the objective and  $\theta$  is half of the aperture angle of the objective). In order to minimize  $d$ , microscope designs attempt to maximize  $NA$  and minimize  $\lambda$ . The  $NA$  is maximized by using the highest possible index of refraction and accepting the widest possible angle into the objective lens aperture. Water immersion objectives with  $NA \sim 1.2$  are commonly used for imaging at depth within living cells (the index of refraction here is just that of water,  $n=1.33$ ), and visible or near infrared light (400 - 800 nm) is often used since it is non-invasive (it doesn't kill or significantly perturb the living cells being studied) and the cells and medium are mostly transparent in this range ( $\sim 600$  nm). These constraints impose a resolution limit of  $d \sim 300$  nm. It is important to note that this is much larger than typical protein molecules ( $\sim 20$  nm) and other components within living cells, and this limit is due to the wavelength, the index of the medium, and the aperture of the objective lens and is independent of the magnification (i.e. increasing magnification only increases the observed Airy pattern size at the detector).

When using more advanced sensors where an intensity pattern can be digitally recorded and analyzed, the Rayleigh criterion is incomplete and far more precise localizations for point-like emitters are possible by fitting the known point spread function (PSF) of the microscope to the data collected [3]. In a perfect optical system with a circular aperture and the emitter perfectly in focus this would normally be a fit to the Airy pattern or more complicated models for high  $NA$  objectives, but this analysis can be complicated and computationally expensive, so an approximation is commonly made where the center peak out to the first minimum of the Airy pattern is approximated as a 2D Gaussian



distribution (**Figure 1.2**). The limit of the localization precision for fitting an individual emitter scales with the square root of the number of photons detected [4].

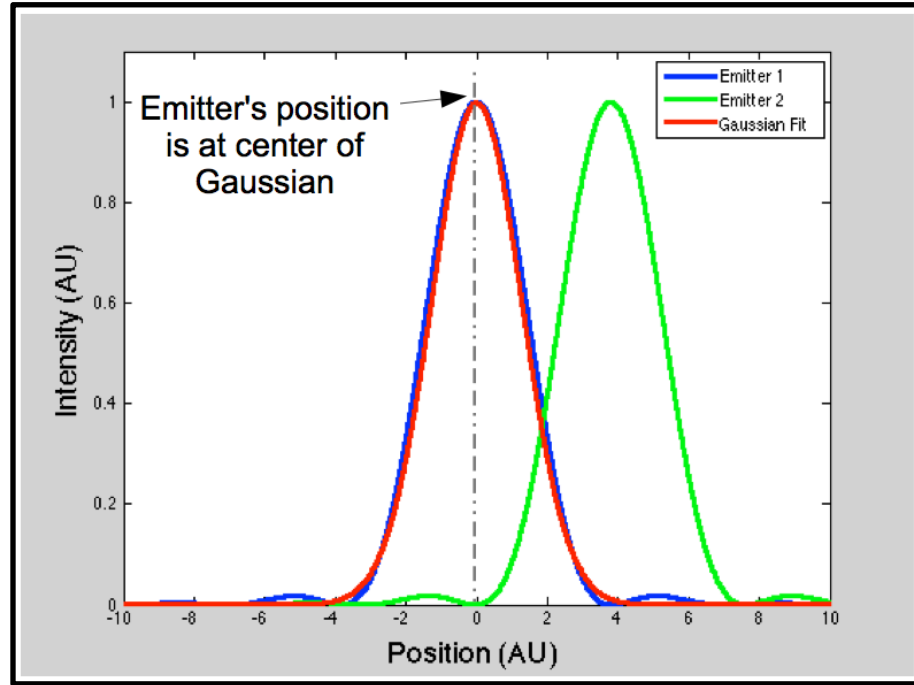


Figure 1.2: Gaussian approximation. The Airy pattern of the first emitter (blue) is shown along with a plot of a Gaussian function that has been fit to the center region bound by the first local minima. Presence of the second emitter (green) would perturb this fit.

The diffraction limit (and thus sub-diffraction limit localization) is achievable when individual point sources can be observed and analyzed independently from the other components in the living cells, and only if there is no prohibitive overlap of the intensity pattern from indistinguishable emitters in a given proximity.

Fluorescence nanoscopy has proven to be a useful means of making observations of individual fluorescent emitters (fluorophores), which can be single molecules or

nanoparticles that are chemically bound to protein molecules or other cellular components. Conventional fluorescence microscopes exploit the Stokes shift of one or more given dyes, where the shorter wavelength excitation light is filtered from the longer wavelength emission light. Similarly, background auto-fluorescence from proteins can be reduced by filtering a given spectrum, and multiple fluorophore varieties can be used with multiple filters (spectral imaging) so that emissions are distinguishable and multiple emitters (and thus multiple protein molecules) can be localized in proximity well below the diffraction limit.

Other imaging methods, such as electron microscopy (EM), can produce very high resolution images, but they are restricted to samples that are fixed (treated with a crosslinking agent that renders most of the proteins stationary and/or inert) [5,6]. Superresolution (SR) microscopy is another method where the on/off blinking nature of fluorophores is used as a means of enabling localizations of individual emitters at high densities. If two emitters are within the diffraction limit of each other, but only one of the two is observed emitting during one frame and the other is observed emitting at some other time, the two can be localized individually and a superresolution image can be reconstructed from the localizations performed for each of the different exposures. These SR techniques [7–9] can also reveal nanometer-scale protein distributions, yet these measurements are inherently slow, making the observation of dynamic events difficult.

For experiments that are designed to study fast processes, such as diffusing protein molecules in living cells, the highest possible spatial and temporal resolutions are desired,

and a video rate of at least  $\sim 30$  Hz is required for membrane protein tracking. In these experiments, fluorescent molecules or nanoparticles are directly attached to individual protein molecules and tracked over time. The tracks are reconstructed from localized emitter positions in each frame, and since the proteins are moving, higher temporal sampling (frame rates) will provide more reliable trajectories (i.e. the motion of a particle during and/or between frames will add uncertainty to track reconstruction). As noted earlier, the localization precision for a given emitter depends on the number of photons detected above the background levels, and fluorescent molecules and nanoparticles have finite emission rates, so using a very high frame rate alone will not achieve the best possible trajectory resolution. It is essential that the maximum number of photons are captured and that the emissions of each fluorophore are much higher than background as detected, and that the emission light is as distinguishable as possible if multiple types of fluorophores are used. None of the commercial confocal microscope systems available at the time of this writing are suitable for high-speed multicolor single particle tracking.

In order to address these concerns and to acquire new data on the dynamics of transmembrane receptor proteins involved in cell signaling using single particle tracking (SPT), we have designed and implemented a high-speed laser line scanning hyperspectral microscope (HSM) that is capable of resolving and tracking eight or more spectrally distinct fluorescent probes. The basic concept of the microscope is shown in **Figure 1.3**. The excitation beam (optics not shown) is reflected by a dichroic mirror and forms a laser line focused at the sample plane by the objective, concentrating the excitation light to a high intensity at the focal plane. The emitted light passes through the dichroic mirror and into a spectrometer, which distributes the light onto an electron-multiplying charge

coupled device (EMCCD) camera such that each exposure captures information of wavelength and position along the line. The entrance slit on the spectrometer also serves to reject out-of-focus light, providing a confocal ability for imaging at any depth in the sample. A scanning mirror (not shown) advances the line position by one back-projected pixel length on the sample and another exposure is acquired. One hyperspectral “frame” (spectral image) is a reconstructed series of these steps, performed in post processing to form an image data cube with dimensions  $x$ ,  $y$ , and  $\lambda$ . A time series of these hyperspectral frames is acquired at ~30 FPS, providing spatial, spectral, and temporal resolution that enables localized single molecule tracking of multiple emitters within a given diffraction limited volume. For a more detailed description of the instrument, see **Chapter 2**, Instrument Design.

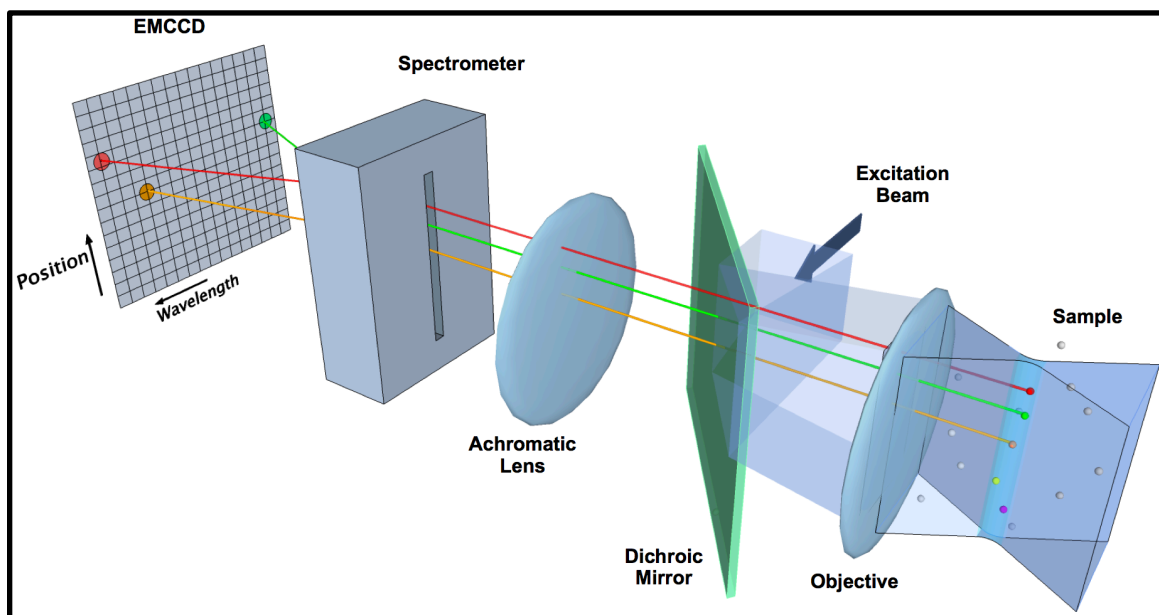


Figure 1.3: Hyperspectral microscope concept. Here, the white spheres in the sample represent fluorophores that remain mostly in the ground state while the colored spheres denote those which are excited. A few simplified example rays are shown of the colored emission light from the fluorophores (more realistic emissions are withheld here for illustration purposes).

The remaining chapters of this manuscript describe the instrument design (**Chapter 2**), the instrument calibration and characterization (**Chapter 3**), characterization of the fluorescent quantum dots used (**Chapter 4**), and experiments that demonstrate the capabilities of the microscope (**Chapter 5**). **Appendix A** provides an alignment and setup procedure, **Appendix B** contains sample preparation procedures, **Appendix C** describes the effects of dipole orientation on the PSF (for stationary dye molecules), **Appendix D** is a summary of individual and ensemble quantum dot emission spectra, and **Appendix E** describes the localization and track reconstruction algorithms that are used in analyzing the HSM data.

## References

1. Airy GB (1834) Transactions of the Cambridge Philosophical Society: “on the Diffraction of an Object-glass with Circular Aperture”. Cambridge: Biodiversity Heritage Library. Available: <http://www.biodiversitylibrary.org/item/19829>.
2. Born M, Wolf E (1999) Principles of Optics. 7th ed. Cambridge, U.K.: Cambridge Univ. Press.
3. Ram S, Ward ES, Ober RJ (2006) Beyond Rayleigh’s criterion: a resolution measure with application to single-molecule microscopy. Proceedings of the National Academy of Sciences of the United States of America 103: 4457–4462. Available: <http://www.pnas.org/content/103/12/4457>.
4. Ober RJ, Ram S, Ward ES (2004) Localization accuracy in single-molecule microscopy. Biophysical journal 86: 1185–1200. Available: <http://www.pubmedcentral.nih.gov/articlerender.fcgi?artid=1303911&tool=pmc&entrez&rendertype=abstract>.

5. Wilson BS, Pfeiffer JR, Oliver JM (2000) Observing FcεRI Signaling from the Inside of the Mast Cell Membrane. *J Cell Biol* 149: 1131–1142 ST – Observing FcεRI Signaling from the. Available: <http://jcb.rupress.org/cgi/content/abstract/149/5/1131>.
6. Wilson BS, Pfeiffer JR, Surviladze Z, Gaudet EA, Oliver JM (2001) High resolution mapping of mast cell membranes reveals primary and secondary domains of FcεRI and LAT. *The Journal of Cell Biology* 154: 645–658. Available: <http://jcb.rupress.org/content/154/3/645.abstract>.
7. Hell SW (2007) Far-field optical nanoscopy. *Science (New York, NY)* 316: 1153–1158. Available: <http://www.ncbi.nlm.nih.gov/pubmed/17525330>.
8. Schermelleh L, Heintzmann R, Leonhardt H (2010) A guide to super-resolution fluorescence microscopy. *The Journal of cell biology* 190: 165–175. Available: <http://jcb.rupress.org/content/190/2/165.full>.
9. Lidke DS, Lidke KA (2012) Advances in high-resolution imaging--techniques for three-dimensional imaging of cellular structures. *Journal of cell science* 125: 2571–2580. Available: <http://jcs.biologists.org/content/125/11/2571.long>.

## Chapter 2

# Instrument Design Considerations and Implementation

As discussed in Chapter 1, the goal of this instrument is to perform multicolor single particle tracking of individual protein molecules with the highest possible frame rate and spatial resolution. The specific design goals include tracking eight spectrally distinct fluorophores at video frame rates ( $\sim 30$  FPS), as the protein molecules they are attached to diffuse about on the cell membrane. The fluorophores chosen for this application are quantum dots since they can all be excited by a single laser wavelength (less than about 500 nm), they have narrow emission spectra with little overlap, they are more photostable and have higher excitation cross-sections than most of the organic dyes, and they can be conjugated to various proteins of interest. A 488 nm laser was chosen due to availability of filters and dichroic mirrors. The overall system design is a 488 nm laser line scanning hyperspectral microscope that has a fast imaging and scanning speed and has the highest possible transmission efficiency.

The remaining sections of this chapter discuss the overall system design and the details of the system components – why they were chosen and how they were implemented. First, an overview is given (2.1) of other spectral imaging methods and the important factors that have lead us to the current design choice. This is followed by more specific

descriptions of the system components (2.2), and finally a brief performance comparison to commercially available spectral imaging systems (2.3).

## **2.1 Imaging Modality Design Considerations**

A survey of existing methods and technologies is necessary before arriving at a final system design. This section provides a basic overview of various spectral imaging systems and the relevant performance characteristics.

### **2.1.1 Overview of Commercial Spectral Imaging Systems**

At the time of this writing, there are several commercial microscope systems that use confocal spectral imaging methods (described below). Some use photomultiplier tubes (PMTs) that can have fairly fast scan speeds with pixel dwell times on the order of microseconds, but with quantum efficiencies (QE) of only about 20-45%. All of the following models use several different excitation laser sources from 405 to 670 nm, including various diode, diode pumped solid state (DPSS), and gas lasers (such as multi-line argon and helium neon lasers). The Zeiss LSM 780 uses a diffraction grating with a 32-channel gallium arsenide phosphide (GaAsP) PMT array, which is a newer technology that achieves up to 45% QE, with maximum scan rates of 8-250 FPS (image sizes from 512×512 to 512×16). The Nikon A1R uses a diffraction grating with a 32-channel PMT, and spectral imaging has a maximum frame rate of 4 FPS on a 256×256 region. The Leica SP5 also uses a PMT array (QE ~25%), but with a prism and a series of sliding mirrors to capture 5 spectral channels, allowing it to have a higher frame rate (25 FPS at 512×512). The Olympus FluoView FV1200 has a 3-channel PMT array and diffraction



grating with selectable wavelength ranges from 1-1000 nm, and a scan speed of ~1 FPS @ 512×512. There are also liquid crystal based filter systems, such as the Perkin-Elmer Nuance (EX, FX, VX) that uses a CCD camera (Sony ICX285: 1360×1024) with a maximum frame rate of 60 FPS for 256×1024, but this is filtering on each frame for a specific wavelength range (in 20 nm steps), so this rate decreases linearly with the number of channels desired, and this system uses filtered white light as the excitation source.

### **2.1.2 Widefield Filter-Based Spectral Imaging**

In filter-based systems, imaging more than one variety of fluorophores requires the use of several emission filters with bandpass regions centered around each emission peak. This is typically accomplished using dichroic filters arranged in series in the emission path, where each wavelength channel is reflected to a different sensor or region of a charge coupled device (CCD) pixel array, and the localization analysis is performed on emitters independently in each of the spectral channels. Each channel provides the same field of view of the sample, and a small amount of light is lost in each dichroic filter (~95% transmission for each dichroic). Besides the loss of emission light from the filters, a disadvantage is that the field of view position offset in each channel has to be well known and remain consistent throughout experiments, which becomes increasingly more difficult with the number of spectral channels used. In addition to this, specific dichroic filters are required for the dyes used. In some applications there is spectral overlap since the emission spectra of fluorophores can be broad enough to span more than one of the

spectral channels defined by the dichroic filters, and this also becomes more challenging as the number of spectral channels are increased.

### **2.1.3 Confocal Point Scanning Systems**

Methods in fluorescence microscopy have greatly improved in recent years, with the specific goal of maximizing the detection of emitted light from in-focus probes (the signal), while minimizing the detection of light from background sources (the noise). One successful approach is referred to as confocal microscopy, where a pinhole aperture is placed at a conjugate focal plane such that most of the out-of-focus light is blocked (see **Figure 2.1**). The excitation light is also focused at the sample, and an image is created by raster scanning this “point” over a region of interest and then reconstructing the data in post-acquisition processing. The small  $z$ -depth spanned by the focused and detected light provides the opportunity to image at various depths in the sample, and doing this at many different planes along the  $z$ -axis (called  $z$ -sectioning or optical sectioning) allows the set of 2D images to be reconstructed into a three dimensional image.

Other optical components, such as filters, lenses, or beam splitters can be placed after the pinhole, or the sensor can be positioned directly behind the pinhole aperture itself (at the conjugate focal plane). If the sensor is an array of pixels (such as a CCD or CMOS camera), the pinhole aperture can be defined with a virtual mask instead of a physical entity, whereby a subset of pixels is accepted while all of the others are rejected. Another modified design uses many pinholes on a spinning disk (and another disk with many microlenses for focusing the excitation and emission light) to multiplex the acquisition, a method referred to as spinning disk microscopy.

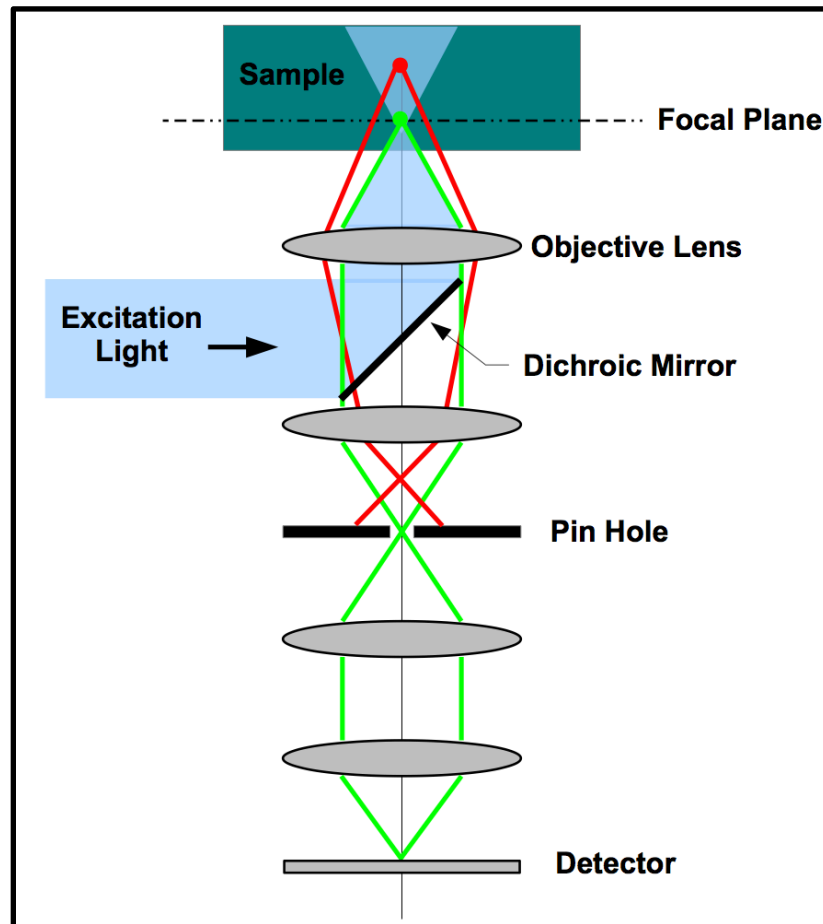


Figure 2.1: Confocal microscope. The green color represents light from an emitter that is in focus, so that light passes through the pinhole that is positioned at a conjugate focal plane. The red color represents light emitted from a fluorophore that is out of focus and is blocked by the pinhole aperture. Additionally, the excitation light is focused, which maximizes in-focus emissions and minimizes out-of-focus excitation.

## 2.1.4 Confocal Line Scanning Systems

Instead of a pinhole aperture, a thin slit can be used and the excitation source can be focused to a line at the sample instead of a point, with the line having the same orientation as the slit. This reduces the 2D raster scanning to that of a 1D line scan, possibly providing a significant performance gain in the overall frame rate (quantified

below). This confocal line-scanning system has a slit that blocks light along one spatial dimension instead of two, so the optical sectioning is not quite as good as a point scanning system, but it still has a good enough PSF to image well at any depth in a living or fixed cell.

## Comparison of Line- and Point-Scanning System Performance

The number of photons that can be captured in a given frame limits the localization accuracy for each emitter in each frame for a given optical system. Fluorescent dyes and quantum dots have a finite excited state mean lifetime,  $\tau$ , which ultimately bounds the emission rate to  $1/\tau$  in the limit of very large excitation intensities. This maximum emission rate is commonly referred to as the saturation rate (i.e. a sample of emitters is exposed to excitation light of such high intensity that essentially none are ever in the ground state as they are immediately excited).

For emission wavelength  $\lambda_{em}$ , numerical aperture  $NA$ , overall optical efficiency of the emission path  $\gamma$ , emission rate  $A$ , and exposure time  $t$ , the theoretical best possible localization accuracy [6] is given by:

$$\delta = \frac{\lambda_{em}}{2\pi(NA)\sqrt{\gamma At}}$$

In the limit of excited state saturation,  $A = 1/\tau$  photons/sec,

$$\delta = \frac{\lambda_{em}}{2\pi(NA)\sqrt{\frac{\gamma t}{\tau}}}$$

If we desire some approximate localization accuracy  $\delta$ , and wish to find the minimum exposure time required to achieve that, we can rearrange the equation, solving for  $t$ :

$$t = \left( \frac{\lambda_{em}}{2\pi(NA)\delta} \right)^2 \frac{\tau}{\gamma}$$

If we consider a single emitter species, say quantum dot 625, with a peak emission wavelength of 625 nm and mean excited state lifetime of 20 ns, a system with a numerical aperture of 1.2, and overall optical transmission efficiency of 0.04 (including detector efficiency and solid angle acceptance of the objective), then a desired localization accuracy of 10 nm would require an exposure time of  $\sim 31 \mu\text{s}$  for that emitter.

A point scanning system would use the required exposure time as the pixel dwell time (the amount of time the excitation beam must stay at each  $(x,y)$  pixel position on the sample). Since a point scanning system raster scans the point over the sample region of interest one  $(x,y)$  pixel position at a time, the maximum overall frame rate is

$$r_{point} = \frac{1}{(t * N_x * N_y)}$$

where  $N_x$  is the number of pixels in  $x$  and  $N_y$  is the number of pixels in  $y$ . A line scanning system will have the same dwell time, but this will be for an entire row (or column) of pixels, so the frame rate is

$$r_{line} = \frac{1}{(t * N_x)}$$

In the case where we have a region of interest that is composed of  $128 \times 128$  spatial pixels, for the desired localization accuracy and system described above,  $r_{point}$  is  $\sim 2$  FPS and  $r_{line}$

is ~250 FPS (where one frame is actually a reconstructed image from each scan, e.g. 250×128 camera exposures per second). This illustrates not only a performance advantage of line scanning over point scanning systems, but also that the theoretical frame rate is much higher than currently possible with camera technology that is available at the time of this writing, and this is a key area of potential improvement as camera speeds increase.

## **2.2 HSM System Design Implementation**

The ability to image proteins on the apical surface of the cell (away from a glass cover slip surface) allows the study of motion that is free from any interference resulting from the interaction of the glass with the cell. This requires a confocal property that can reject the out-of-focus light, so a laser line-scanning system is chosen for this attribute along with the need for high-speed scanning that includes spectral information. This section first introduces the laser line generation methods, then the overall layout of the instrument, and finally the individual components of the excitation and emission paths that are discussed in the layout. This order is intended to introduce the line generation optics separately, as the other components are somewhat independent of this topic.

### **2.2.1 Excitation Laser Line**

The first task in creating the HSM is to form a laser line that will be scanned over the sample area. While a line-like geometry can be produced using a cylindrical lens, this

provides a very non-uniform distribution of intensity along the line, as is seen in the image of **Figure 2.2**.

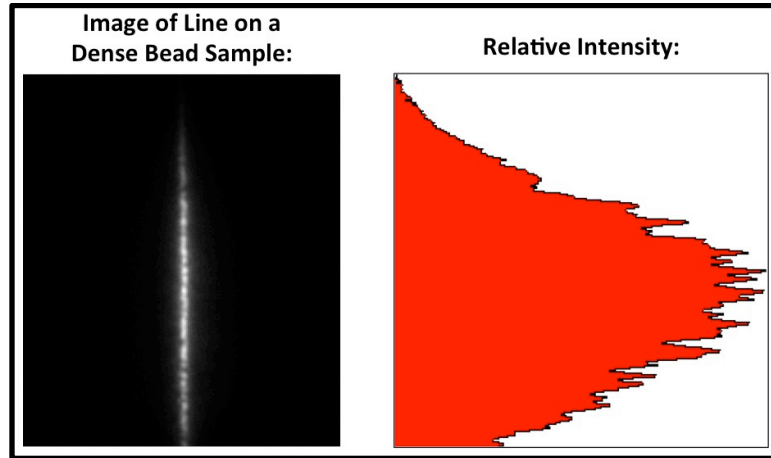


**Figure 2.2:** Laser line produced by a cylindrical lens (shown on a dense sample of 200 nm fluorescent beads, 150 $\times$  1.45 *NA* objective). Variations in the measured intensity profile are caused by the spatial bead distribution on the glass.

This image shows the light emitted from a dense sample of yellow-green fluorescent beads excited by a 472 nm diode laser. The line was created using a cylindrical lens with a focal length of 25.4 mm. The light from this lens diverges along the line dimension, so it was collimated with another cylindrical lens and then directed into a microscope base (tube lens and objective) and onto the sample. On the emission path the light was filtered to remove the excitation light and the remaining light was captured with a CCD camera (Andor Luca). This non-uniform intensity distribution would cause fluorescent particles (fluorophores) to be excited at varying degrees along the line. The result would be that if the fluorophores near the edges were bright enough to be localized well, the region near the center would receive far more light than necessary, which could lead to photobleaching and/or higher backgrounds than would be necessary. Conversely, if the

fluorophores near the middle of the line receive adequate excitation intensity, the ones near the edges will not.

For this reason most laser line scanning applications in microscopy require a uniform line intensity. In order to accomplish this a laser line generator lens (also known as a Powell lens) is used to produce the line starting from a free space beam [8]. Line generator lenses have an aspheric surface (typically hyperbolic along one dimension) and are designed to accept Gaussian laser beam profiles (TEM 00 mode = Transverse Electric and Magnetic fields with no field components along the direction of propagation and with zero horizontal and vertical orders in the pattern) with specific  $1/e^2$  beam diameters – a common method of describing the beam profile as having the diameter be defined as the distance between points where the intensity is  $1/e^2$  of the maximum value.

For this system the chosen lens was designed to accept a 0.8 mm beam diameter. It is important not only to approach this size, but also to have a uniform Gaussian distribution of the beam (in both  $x$  and  $y$ ) that is well collimated before the line generator lens. For creating this symmetric distribution, the laser was coupled into single mode fiber, which acts as a good spatial filter and also helps in the organization of the optics table layout since the laser can be placed at any position.

**Figure 2.3A** shows a side view model of a Powell lens. The actual lens is a cylindrical shape oriented along the beam line with a flat circular aperture on one end and a hyperbolic surface that projects along the dimension that is into and out of the page as drawn (i.e. that surface has the same shape along the diameter of the cylinder). A few example rays have been drawn to represent the laser beam profile and the intersection for



each ray at the hyperbolic surface was used to calculate the refraction angle into the glass using Snell's Law ( $n_1 \sin \theta_1 = n_2 \sin \theta_2$ , with  $n_1 = 1$  for air and  $n_2 = 1.5$  for glass), and then the same thing was done at the flat surface of the lens, going from glass into air. This illustrates the overall effect of the lens – a collimated incoming Gaussian beam is converted into an isotropic divergence along one dimension (and the beam is still Gaussian along the other dimension). The diverging beam is collimated with a cylindrical lens (discussed later). **Figure 2.3B** shows a laser line from a Powell lens projected on a dense planar sample of quantum dots, and shows a much flatter intensity profile than the line produced from a cylindrical lens as in **Figure 2.2**.

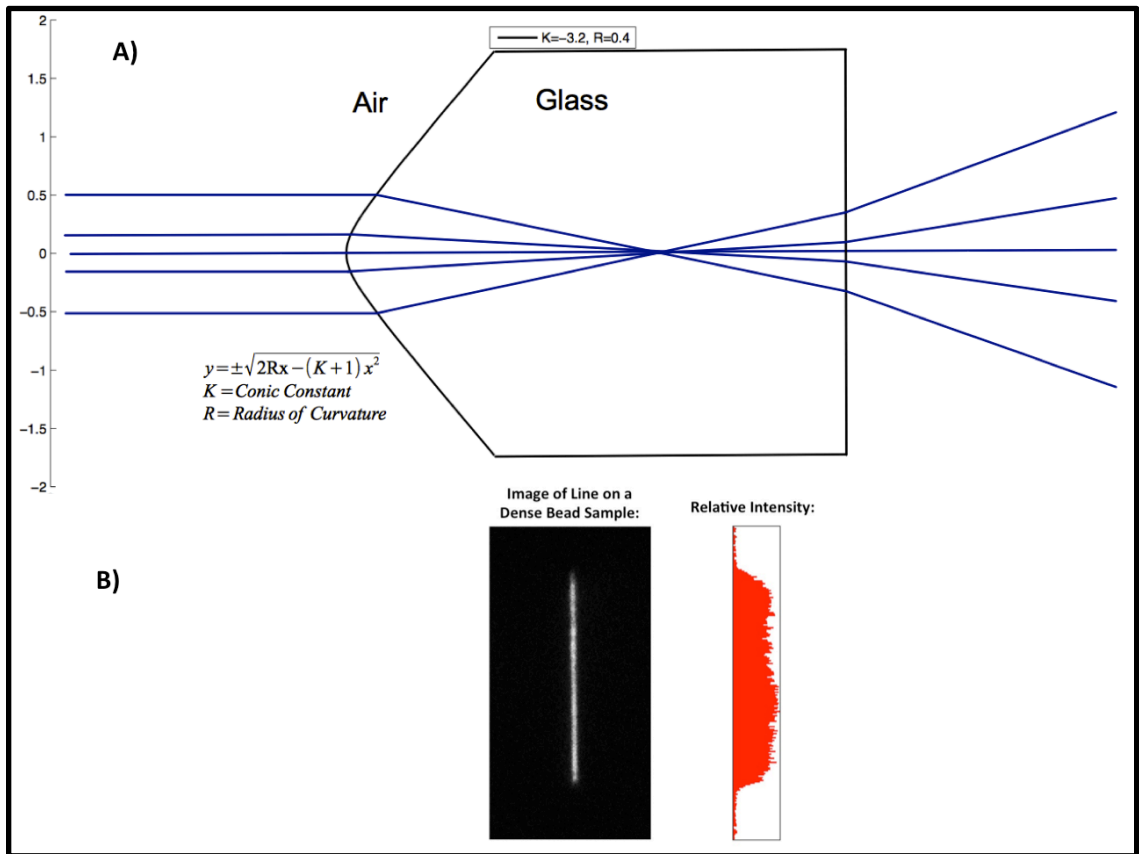


**Figure 2.3:** (A) A side view of a line generator lens. The vertical scale is in mm. (B) The laser line produced by a line generator lens (shown on a dense sample of quantum dots). Minor fluctuations of intensity along the line are mostly due to variations in the quantum dot concentration on the glass surface.

### 2.2.2 Excitation Laser Line Intensity

Another important design consideration is having control over the laser power. Course-grain control is provided by two neutral density filter wheels that rotate (manually), placing different filters into the beam path as desired. In addition to this, an acousto-optic modulator (AOM, IntraAction Corp. Model AOM-402AF1) is used as a Bragg device, where diffracted beams are created. In the AOM, a piezoelectric transducer is attached to a solid crystal medium and creates acoustic plane waves in the medium with sufficient amplitude to change the index of refraction at the traveling pulse positions in the crystal. The interaction of incident light waves with this pattern of refractive index changes from the acoustic waves is such that the AOM can act like a diffraction grating. When the AOM is set at the appropriate angle to the incident beam and with optimal acoustic wave amplitude, approximately 80% of the incident light can be diffracted into the first order beam that emerges at a constant angle from the incident beam. **Figure 2.4** shows the basic concept of the AOM operating as a Bragg device and **Figure 2.5** shows the calculation of the Bragg angle.

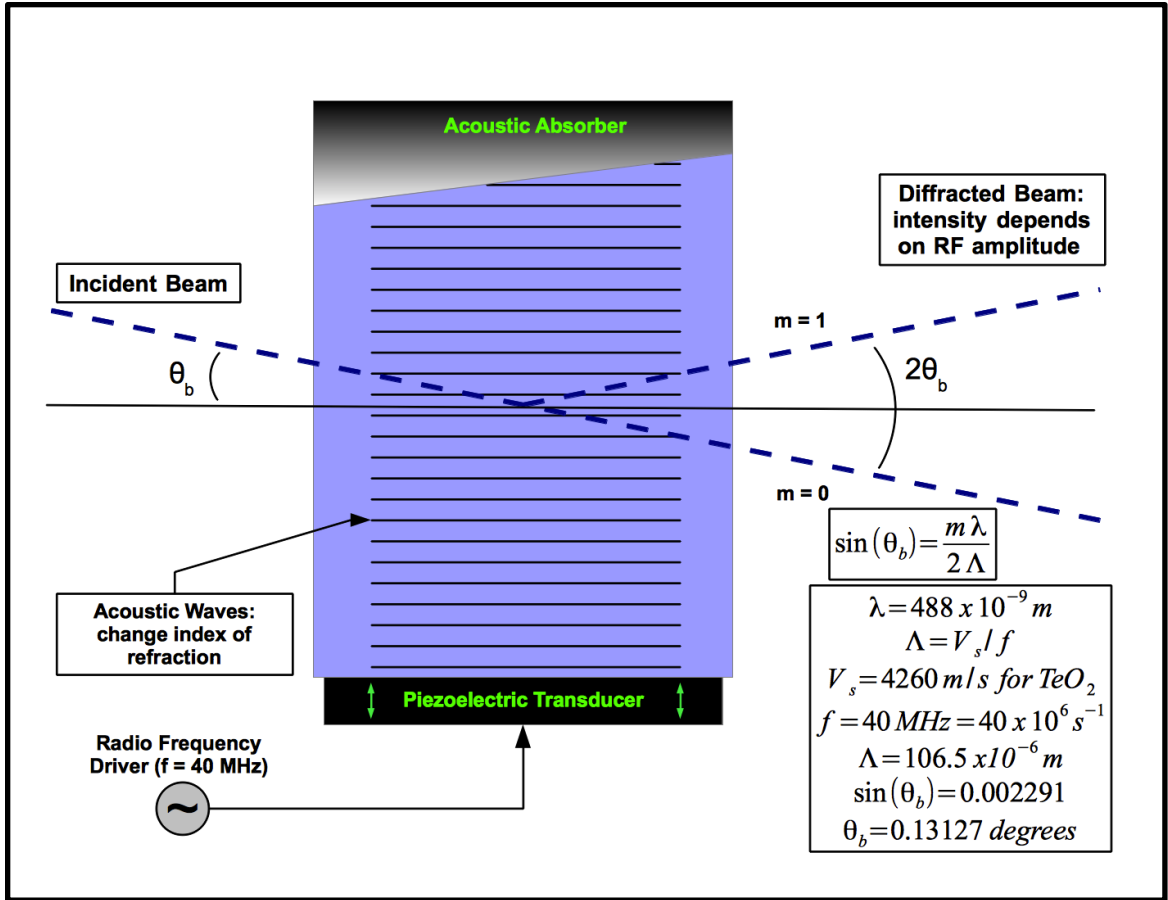
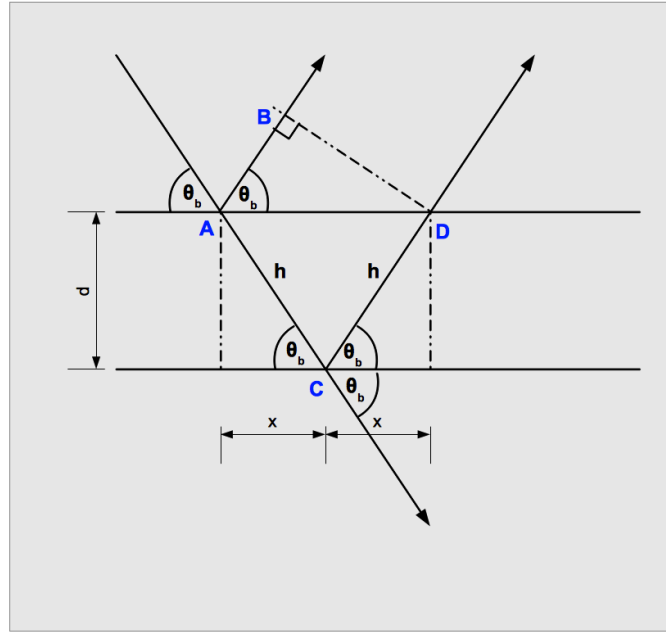


Figure 2.4: AOM operation in Bragg mode. Here,  $\lambda$  is the wavelength of incident light (488 nm for this laser),  $\Lambda$  is the distance between pulses in the crystal,  $V$  is the velocity of sound in the crystal,  $f$  is the frequency of the pulses generated by the transducer, and  $\theta_b$  is the Bragg angle.

### Bragg Angle Calculation:



$$\begin{aligned}
 AC + CD - AB &= m\lambda \\
 AC &= CD = h \\
 \sin(\theta_b) &= d/h \\
 2h &= \frac{2d}{\sin(\theta_b)} \\
 x &= h \cos(\theta_b) \\
 AD &= 2x = 2h \cos(\theta_b) \\
 \cos(\theta_b) &= \frac{AB}{2x} \\
 AB &= 2x \cos(\theta_b) \\
 AB &= 2h \cos(\theta_b) \cos(\theta_b) \\
 AB &= \frac{2d \cos^2(\theta_b)}{\sin(\theta_b)} \\
 m\lambda &= \frac{2d}{\sin(\theta_b)} - \frac{2d \cos^2(\theta_b)}{\sin(\theta_b)} \\
 m\lambda &= \frac{2d}{\sin(\theta_b)} (1 - \cos^2(\theta_b)) \\
 m\lambda &= \frac{2d}{\sin(\theta_b)} (\sin^2(\theta_b)) \\
 m\lambda &= 2d \sin(\theta_b) \\
 \sin(\theta_b) &= \frac{m\lambda}{2d}
 \end{aligned}$$

Figure 2.5: Bragg angle calculation. This model shows an incident beam (arrow pointing down to the right) that is interacting with two acoustic pulses in the crystal medium (horizontal lines). The incident beam is composed of many waves, some of which reflect at the first pulse, some reflect at the second pulse, and some continue through. Constructive interference occurs between the reflected beams when their path lengths differ by an integer number of wavelengths,  $m$ . The angles are exaggerated here for clarity.

When the acoustic amplitude is zero (i.e. the AOM is off) there is no light in the first order beam (all of the light follows the zero-order path, parallel to the incident beam). It is the first order diffracted beam which is coupled into the single mode fiber, and since the coupling efficiency is strongly dependent on both the angle and position of the incident light, a very small fraction of the light will propagate through the fiber when the AOM is in the off state. A signal processor (IntraAction Corp. model ME-402) drives the AOM with a fixed carrier frequency of 40 MHz and the acoustic wave amplitude is controlled by applying a DC voltage to a BNC input on the signal processor. Varying

this voltage allows between 0 and 80% of the original laser light to be focused into the fiber. This input voltage is produced by an analog output from a data acquisition and control card in a computer, which is operated by the user through a custom software interface (see **Chapter 3** for a more detailed description of this GUI and the AOM and signal processor calibration).

### **2.2.3      Excitation Laser Optics & Fiber Coupling**

**Figure 2.6** shows the actual layout of the elements for the excitation beam generation up to and including the fiber launch. Starting in the top center of the photo, the 40 mW, 488 nm (CW) diode laser (Newport Spectra Physics 488 Cyan, Model PC14011) is directed to the right with the beam emerging parallel to the table surface. The beam passes through two neutral density filter wheels and onto a pair of beam steering mirrors. Using two mirrors that each have fine adjusters for controlling the angles both parallel and perpendicular to the table, one can accurately steer the beam in both position and angle through a target aperture. In this case, we steer the beam into the AOM. Note that this was actually done by first setting the beam to be parallel to the table at the desired beam height and then placing the AOM in the path since it is held in a fixed mount. During setup the AOM was carefully rotated to achieve the greatest amount of power in the first diffracted mode beam and then anchored to the table. After the AOM the beam is steered again using a pair of mirrors, this time into the objective that focuses the light into the fiber.

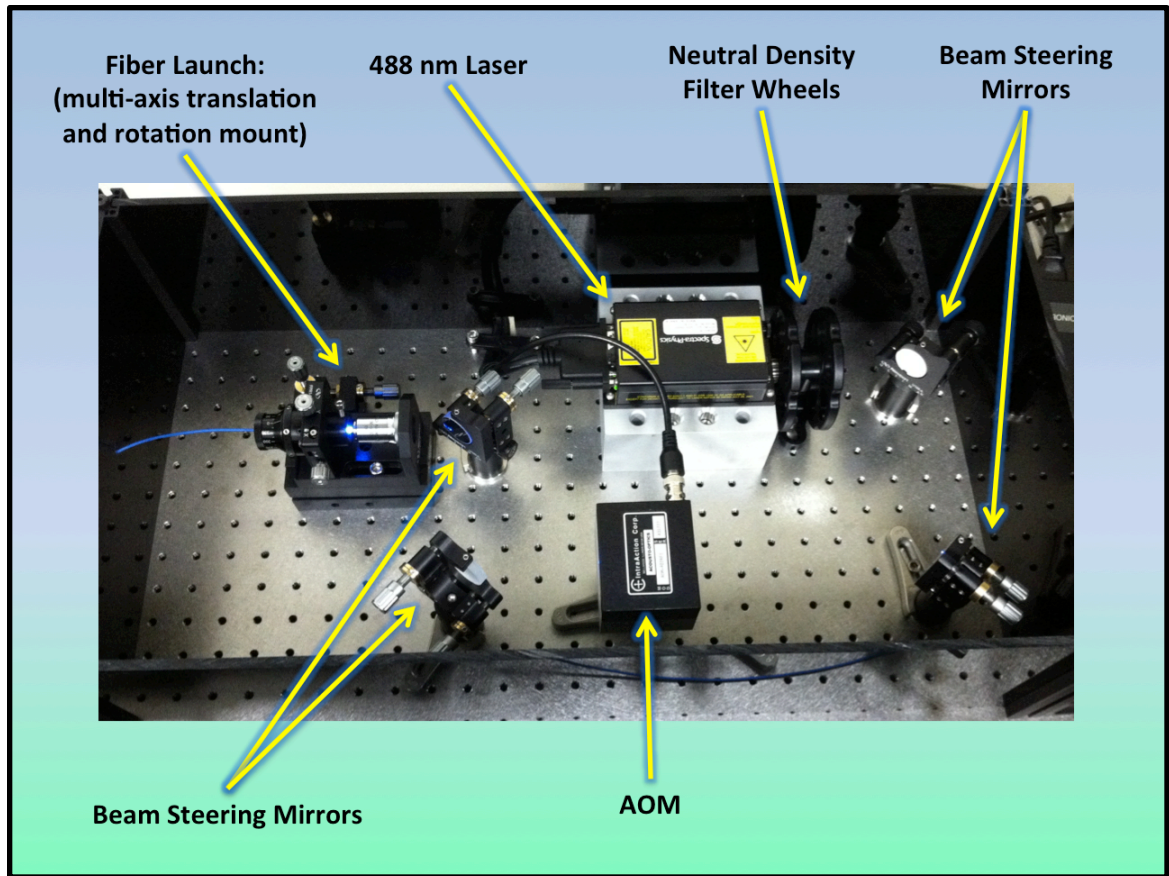


Figure 2.6: Laser, AOM, and fiber coupling. The 488 nm diode laser module is anchored to a large piece of custom machined aluminum, used to place the beam at a desired height and also serves as a good heat sink, which is necessary for stable laser power output and for longevity of the laser diode. The beam exits the laser module going to the left through the neutral density filters. The beam is then directed down and to the left, through the AOM, and then up and to the left, into the objective lens for fiber coupling.

While the light of the first diffracted mode from the AOM is what is actually coupled into the fiber, zero mode light is also reflected toward the objective by the mirrors since the angle is small – in fact small enough such that one cannot determine which mode is centered by eye. A power meter is used to measure the light out of the fiber, and by varying the acoustic amplitude one can infer which mode is coupled into the fiber. When the AOM is off we expect no light out from the  $m=1$  mode, and when in the first mode we expect up to 80% of the initial light to be available.

In order to couple the free space laser beam into the fiber, first a lens (typically an objective lens) is chosen. The focal length of the lens is determined by the calculation shown in **Figure 2.7A**. For the fiber used in this system, we have  $d = 3.6 \mu\text{m}$ ,  $\lambda = 488 \text{ nm}$ ,  $D = 0.9 \text{ mm}$  (approximate, after the AOM), and numerical aperture  $NA = 0.1 - 0.13$ , which gives us a focal length range from  $3.96 - 4.24 \text{ mm}$ . Choosing an affordable objective lens from those that were available at the time of this design, the best match happened to be a Newport M-40x, which has  $f = 4.5 \text{ mm}$ , and a working distance of  $0.6 \text{ mm}$  (the former being important for the actual coupling, and the latter being an inconvenience in that the actual metal fiber connector had to be machined to expose the tip such that it was within the working distance of the lens).

The fiber alignment is an iterative process of fine adjustments involving several degrees of freedom ( $x, y, z, \theta$ , and  $\phi$ ) between the objective, fiber, and incoming beam. In order to make adjustments in each of these dimensions, a single-mode fiber coupler assembly was used, specifically the Newport F-91-C1. The fiber core diameter is very small, in this case (using Newport F-PM480-C-2FC fiber) it is  $3.6 \text{ microns}$ , which is a very small target on which to focus and there is usually no easy way to see the focal point relative to the fiber core, especially with a small working distance between the lens and fiber tip. The alignment procedure involves trying to place the fiber tip at first just somewhere inside the conic region of focused light (getting at least some light into the fiber, also adjusting the angle of the tip relative to the incoming beam), and then moving it just barely out of the cone along  $z$ , then adjusting the  $x, y$  position until it seems centered, and then again moving it just barely out of the cone and repeat until the greatest amount of light is coupled into the fiber (i.e. the fiber tip is right at the point of focus of the laser

light). The overall coupling efficiency is determined by measuring the power of the free space beam (after the AOM, before the coupling objective) and then again where the light exits the fiber.

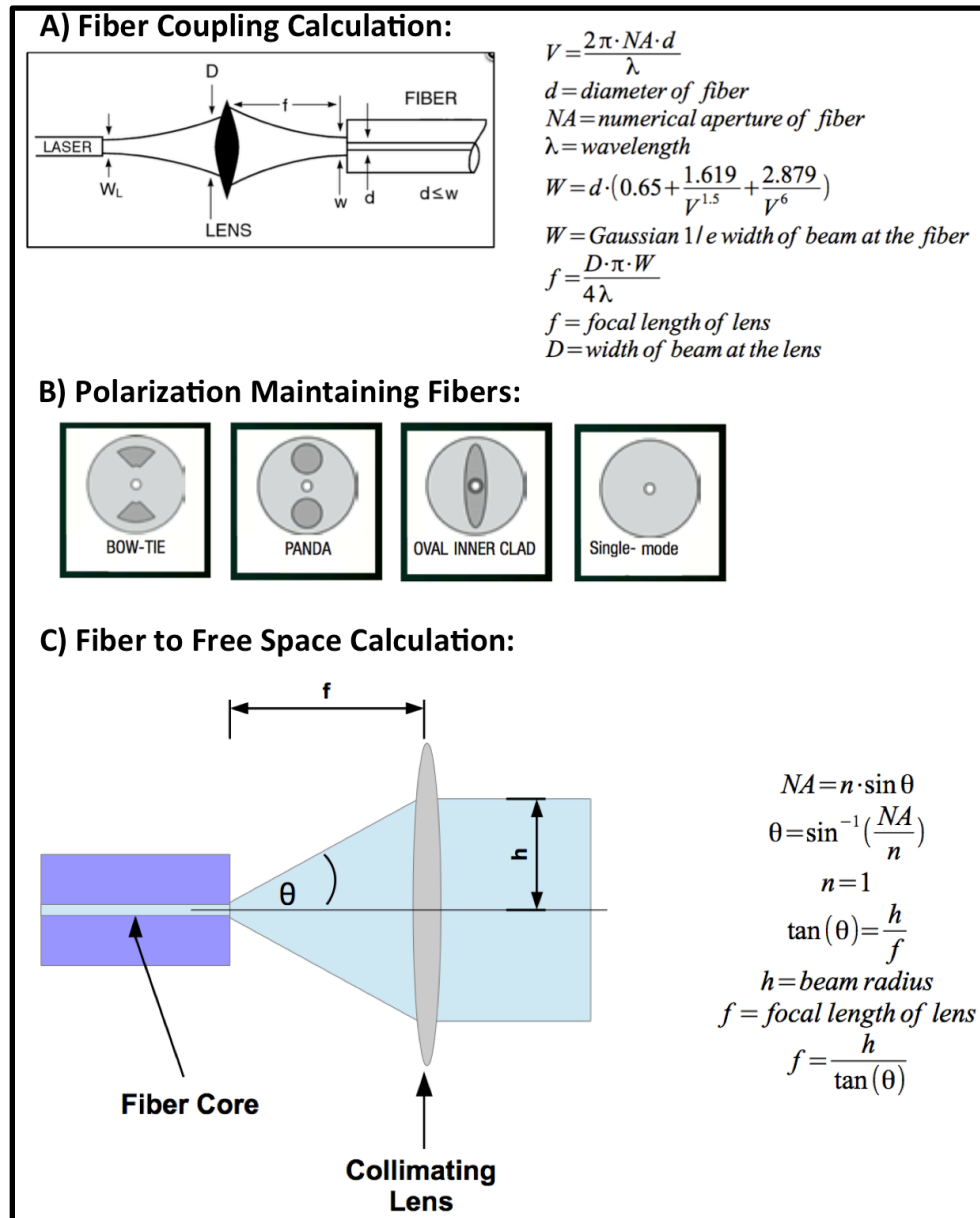


Figure 2.7: (A) A calculation to determine the appropriate lens for coupling a free space laser beam into the fiber. (B) A comparison of polarization maintaining fibers and standard single mode fiber. The index of refraction is typically greater in the darker shaded regions. (C) A calculation to determine the appropriate lens for collimating a beam to the desired diameter. \*Diagrams (A) and (B) are from <http://www.newport.com/Tutorial-Fiber-Optic-Basics/978863/1033/content.aspx>



The fiber used here maintains the linear polarization of light and so the fiber alignment chuck must also have the ability to rotate the fiber about the optical axis so that the polarization axis matches the laser polarization (which happens to be perpendicular to the table surface in this case). The fiber polarization axis has regions where the index of refraction is slightly higher than the rest of the core, which causes the medium to have a birefringence characteristic such that light that is linearly polarized that is not perfectly oriented along the slow or fast axis will be converted to an elliptical polarization state. **Figure 2.7B** shows various types of polarization maintaining fibers. The performance difference between the geometries is not significant for this particular setup and the panda style happens to be the variety used here.

The light out of the fiber is collimated to the beam diameter desired for input to the line generator lens. This is done by calculation using the numerical aperture of the fiber to determine the angle of divergence from the fiber tip. The appropriate lens can then be chosen, with a focal length that will produce the desired beam width and with a numerical aperture that will accommodate the divergence angle (i.e. none of the diverging light is blocked). It is a good practice to exceed the numerical aperture of the fiber by at least 50%, which will ensure that at least 99% of the light is collimated. Since there are few choices in objective lenses for collimation using this fiber (with  $NA = 0.1-0.13$ ), the closest possible match is selected, which give a beam diameter that is somewhere in the range of 0.92 to 1.21 mm. While this is larger than the value desired by the line generator lens, one can adjust the focal distance between the fiber tip and the objective to make the light converge slightly to produce a good line and the distance between the objective and

the line generator lens is large enough to make the convergence angle so small that there is no noticeable impact after the line is produced.

Up to this point, these components (488 nm diode laser, neutral density filters, AOM, fiber, and Powell lens) provide a collimated laser line with the light polarized along the length of the line and with the ability for the user to smoothly control the intensity of the beam. We ultimately seek the ability to scan the line across some region of a living (or fixed) biological cell, with the intention of studying individual protein interactions. The line should be as narrow as possible in order to excite only the fluorophores that are in focus along the line. Having the light linearly polarized along the line also helps accomplish this by increasing the probability density for excitations along the line, while minimizing the probability distribution perpendicular to the line.

#### **2.2.4 Optimizing Excitation Laser Line Point Spread Function**

In addition to minimizing the line width, it is also preferable to minimize the depth of the excitation to reduce the amount of light contributed by out of focus fluorophores and auto-fluorescent materials in the sample. This is achieved by using the full back aperture of objective to use the widest possible focusing angle, concentrating the light as quickly as possible along the  $z$  dimension. **Figure 2.8** illustrates the effect of making use of the full back aperture and comparing it to a case that uses only half of that beam width going into the lens. In order to fill the back of the objective, the collimated laser line beam is expanded along the  $x$ -dimension (perpendicular to the line) with a cylindrical lens. In this

case, a concave cylindrical lens ( $f = -100$  mm) was chosen over the convex variety due to space restrictions imposed by the necessary placement of other optical elements.

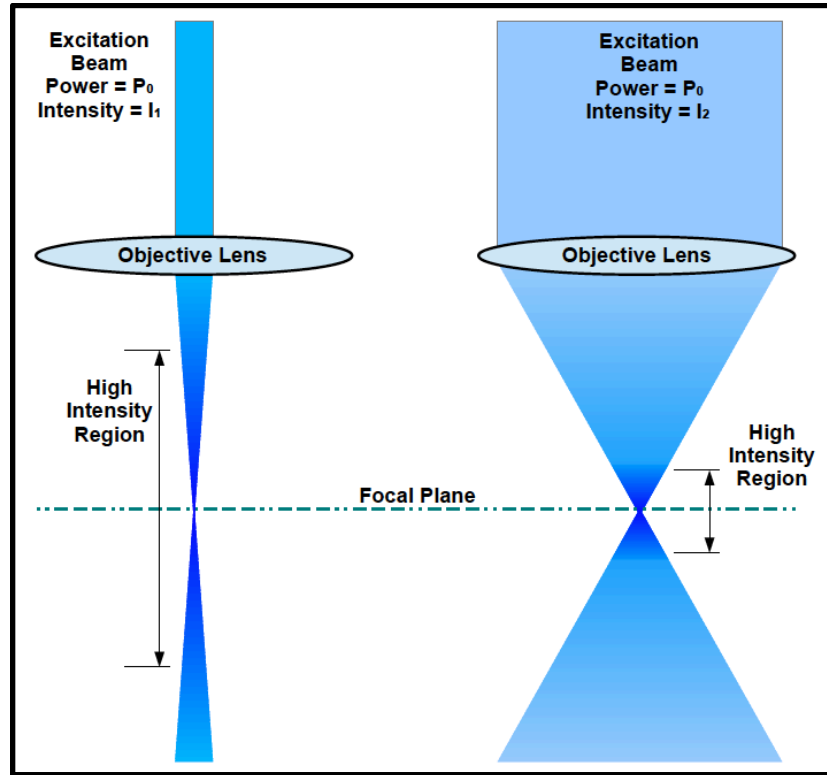


Figure 2.8: Partial vs. full use of back aperture of the objective lens. The same power of light (total photons/sec) is the same in both of these example beams. The one on the left is more concentrated at most points along  $z$  (shown as the vertical dimension in the drawing), and the one on the right is less concentrated at the objective but goes to the same concentration at the focal point, so the gradient along  $z$  is greater, which ultimately reduces out of focus excitation.

## 2.2.5 Overall Microscope Layout

As the laser line generation optics are mostly separable from the remaining system, it is useful at this point to present the overall layout of the microscope components and then discuss the details of each one independently in the sections that follow.

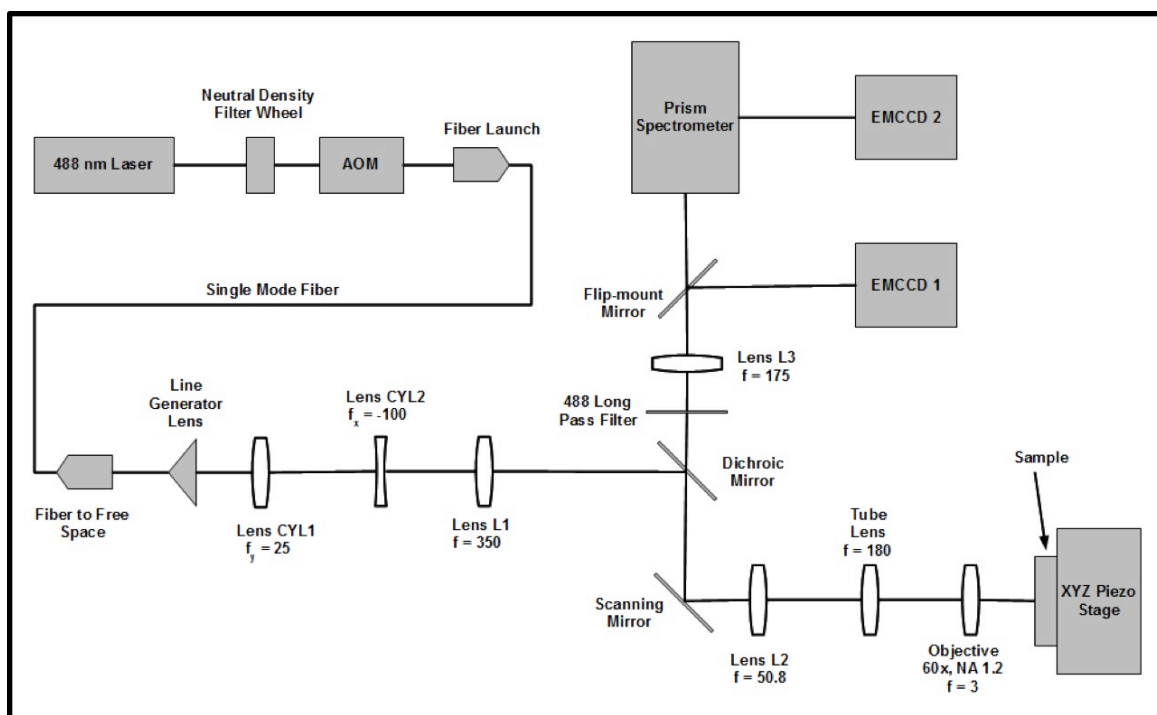


Figure 2.9: Optical layout. All focal lengths shown are in mm.

Unless otherwise specified, the spatial dimensions will be defined such that the  $z$ -axis is along beam line, the  $y$ -axis will be perpendicular to the optics table surface, and the  $x$ -axis will be parallel to the optics table surface. Beam steering mirrors, mounts, and micro-adjusters are omitted to simplify the diagram. The numbers in brackets  $\{\}$  are references to parts listed in **Table 2.1**, below the text.

### 2.2.5.1 Excitation Path

Starting with the 488 nm laser (**Figure 2.9** upper left,  $\{1\}$ ) the beam is 40 mW which turns out to be much more than needed for some experiments so neutral density filters ( $\{2\}$ ,  $\{3\}$ ) are used for course adjustment of the initial laser power. The beam is steered (using mirrors  $\{4\}$ ,  $\{5\}$ ) through an acousto-optic modulator (AOM,  $\{6\}$ ) and the first

order diffracted beam is coupled into the fiber {7}, {8}. The amount of laser light in the that beam depends on the radio frequency (RF) power in the AOM, which can be smoothly and quickly controlled, providing a good mechanism for modulation and tuning the power of the laser light as desired. The AOM power is controlled by providing a voltage to the signal processor unit. This voltage signal is provided by an analog output from a data acquisition and control PC card {9} that is controlled via software. The fiber is single-mode, polarization preserving and is used as a means to control intensity as well as for acting as a good spatial filter since light emitted from the fiber is collimated (via objective {10}) into a good approximation of a Gaussian beam TEM 00 mode with an  $1/e^2$  diameter of  $\sim 0.8$  mm. The polarization is maintained such that the light which is focused to create the laser line has the  $E$  field oriented along the length of the line at the focal plane so that the line has the minimum possible width.

The free space Gaussian beam is steered into a laser line generator lens {11} that has a 15-degree fan angle in the  $y$ -dimension and distributes the light evenly over the angle. This light is then collimated with a cylindrical lens (CYL1, {12}). Lens CYL2 {13} is a concave cylindrical lens oriented along the  $x$ -axis, which serves to expand the beam along the  $x$ -axis such that the beam will ultimately fill the back aperture of the objective lens, which reduces the excitation focal volume along the  $z$ -axis. Lenses L1 {14} and L2 {17} are used as a telescope to reduce the size of the line before entering the microscope base {18}, such that the line will be  $\sim 15$   $\mu\text{m}$  in length on the sample (which is also the approximate length of one column of 128 CCD pixels back-projected on the sample). L1 focuses the light onto the scanning mirror {16} after being reflected off of the dichroic mirror {15}, which is fixed at a 45-degree angle to the beam. The excitation line is finally

reduced and focused onto the sample by the combination of the tube lens (which is part of the microscope base and has a focal length of 180 mm) and the objective lens.

#### **2.2.5.2 Emission Path**

The light emitted from a fluorophore excited by the laser line will be distributed over all angles and the light that is accepted by the aperture of the objective lens {29} will then be collimated and will propagate to the tube lens. The tube lens will focus the light to an image plane which is also the focal plane of lens L2, so it will then be collimated and de-scanned by the mirror, which causes the emission light to match the axis of excitation light for all scan angles, allowing fixed positions of the remaining optical elements.

The emitted light then passes through the dichroic mirror and a 488 nm long pass filter {22}, which has the purpose of further reducing any amount of excitation light that may have passed through the dichroic filter. Lens L3 {23} then focuses this light onto the entrance slit {24} of the spectrometer, which also serves as a line-scanning confocal slit that blocks much of the light from sources that are out of focus.

The custom-made prism spectrometer {27}, described fully in [9], focuses the light onto the CCD pixel array (see **Figure 2.17** for a more detailed description of operation). This provides a  $128 \times 128$  array of data from the CCD {28} that consists of  $y$ -position (along the laser line and slit) and wavelength along the other dimension. As the line is scanned across the sample another  $128 \times 128$  ( $y, \lambda$ ) array is taken for each line position (one angle step in the  $x$ -dimension). The full field of view ( $x, y$ ) is then reconstructed into a data set of ( $x, y$ , and  $\lambda$ ) for one scan or “spectral image”.

Other (some not shown in diagram): 3D scanning is enabled by the  $x, y, z$  piezo stage {19}. Widefield excitation (used for finding regions of interest within a sample) is performed using a white light source {20} and filter cube set {21}. The electromechanical flip-mount mirror {25}, changes the emission path into the widefield CCD {26} and is controlled through the DAQ GUI.

## Table 2.1: Parts Reference

1. Laser: Newport Spectra Physics 488 Cyan, Model PC14011
2. ND Filters: Newport FRQ-ND03, FRQ-ND07, FRQ-ND10, FRQ-ND15, and FRQ-ND20
3. ND Filter Wheels: Newport FWM1X12
4. Mirrors: Newport 10D20ER.1
5. Mirror Mounts: Newport U100-A with precision actuators AJS100-0.5
6. AOM: IntraAction Corp. Model AOM-402AF1 with signal processor from IntraAction Corp. model ME-402
7. Fiber: Newport F-PM480-C-2FC
8. Fiber Coupler: Newport F-91-C1 with objective lens M-40X
9. DAQ Card: National Instruments PCIe-6343 X Series Data Acquisition Card (P/N 781047-01) with BNC-2110 shielded connector block (P/N 777643-01) and SHC68-68-EPM 5m cable (P/N 192061-05).
10. Fiber to Collimated Free Space Beam: Newport L-40X ( $f = 4.6$  mm,  $NA = 0.66$ ), Thorlabs HPT1 X,Y Translator (holds FC connector), Thorlabs SM1Z Z-Axis Translator (holds the objective)
11. Laser line generator lens: Edmund Optics 46632 (15-degree fan angle)
12. CYL1: Edmund Optics 48353 ( $f = 25$  mm,  $d = 12.5$  mm,  $MgF_2$  Coated)
13. CYL2: Thorlabs LK1743R-A ( $f = -100$  mm,  $d = 25.4$  mm, BK7)
14. Lens L1: Newport KPX114AR.14 ( $f = 350$  mm,  $d = 25.4$  mm)
15. Dichroic: Semrock LPD01-488RU-25x36x2.0

16. Scanning Mirror: Cambridge Technology 6210H
17. Lens L2: Newport PAC040AR.14 ( $f = 50.8$  mm,  $d = 25.4$  mm)
18. Microscope Base: Olympus IX71
19. X,Y,Z Piezo Stage: Mad City Labs Nano-LPS200
20. Widefield Lamp: X-cite 120Q
21. Widefield Filter Cube Set: Chroma Z473-10x (excitation), Semrock LPD01-488RS-25x36x2.0 (dichroic), Semrock LP02-488RU-25 (emission).
22. Long Pass Filter: Semrock LP02-488RU-25
23. Lens L3: Newport PAC061AR.14 ( $f = 175$  mm,  $d = 25.4$  mm)
24. Spectrometer Entrance Slit: Thorlabs S100R (100 +/- 4  $\mu$ m wide, 3mm tall)
25. Flip-Mount Mirror: Thorlabs MFF001
26. EMCCD1: Andor Luca R
27. Prism Spectrometer: Custom Design, Rainbow Optics
28. EMCCD2: Andor iXon 860
29. Objective Lens: Olympus UPLSAPO 60XW (60x Water Immersion,  $NA=1.2$ )

## 2.2.6 Selection of Lenses

The actual selection of lenses used in the design is somewhat of a juggling act. Availability of lenses with desired characteristics (such as focal length, achromatic doublets, antireflective coatings, diameter, thickness, etc.), physical space limitations, and available mounting hardware with required degrees of freedom for adjustment are some of the primary concerns that limit the selection. The excitation and emission paths share some components, namely lens L2, the tube lens, and the objective lens, as well as the scanning mirror and dichroic mirror, and this shared path imposes restrictions on the



choices for the other components. Lastly, the total size and scan angle of the line must also be small enough to avoid aperture conflicts and to minimize the impact of any spherical aberration.

The selection process begins with a look at the overall hard requirements of the system. First, since this is a system that acquires spectral information, all lenses in the emission path must be achromatic doublets selected for the emission spectrum (achromatic implies that the different wavelengths have the same focal point; doublet means that the lens is made of two optical elements), and this happens to be the most limiting characteristic in terms of available focal lengths for common lenses, so this is a good place to start the selection. The back projected dimensions of the CCD pixel array need to be such that the length along one of the dimensions (128 pixels) is equal to whatever the length of the line is on the sample. If anything, the excitation line may actually slightly exceed this, but we want it to be close so that wasted light and background levels are minimized. The desired line length is approximately 15  $\mu\text{m}$  long on the sample, which would allow coverage over an area that would be adequate for observing cell membrane protein dynamics (interactions and/or diffusion) for times of perhaps minutes, and other structures (such as the actin cytoskeleton filaments) within the field of view. The CCD has an actual pixel size of 24  $\mu\text{m}$ , so 128 pixels is 3.1 mm, which means that the overall emission path must provide about  $207\times$  magnification ( $3,100 \mu\text{m} / 15 \mu\text{m}$ ).

The objective and tube lens combination provides  $60\times$ , so the ratio of focal lengths of L3 to L2 must be about 3.41 (assuming 1:1 magnification in the spectrometer). Noting that L2 will need to be positioned such that the scanning mirror will be at the focal point, and that the dichroic requires about 50 -75 mm of clearance with mounting hardware, and in

order to allow spatial tolerance for focusing (clearing the scanning mirror and its necessary mounting hardware), L2 and L3 were chosen with focal lengths of 50.8 and 175 mm respectively, and both of which are achromatic doublets.

On the excitation path, CYL1 was chosen such that the expanding laser line would be collimated as quickly as reasonably possible (minimizing the length of the line to reduce the amount of required demagnification with a telescope) while providing sufficient working distance between itself and the line generator mounting hardware. **Figure 2.10** shows the calculation for determining the length of the collimated laser line. The line generator lens produces a fan angle (15 degrees for this lens) for a specified  $1/e^2$  input beam diameter (which is 0.8 mm in this case). The lens manufacturers do not typically provide detailed design specifications beyond the basic characteristics (fan angle, input beam diameter required, overall length, and overall lens diameter), but one does not need this information to choose an appropriate collimating lens (or to determine the collimated line length if one is already chosen). Instead, the fan angle alone can be used to make the lens selection (or length calculation). One does not need to know where the actual focal point of the cylindrical lens happens to lie (it may even be inside the line generator lens), as long as the line is collimated after it and there is sufficient working distance to accommodate mounting hardware. In this case, CYL1 was chosen with a focal length of 25.4 mm, and with a circular mounting surface for use in common 1" mounts, which enabled the use of a continuous rotation mount in a 30 mm cage system.

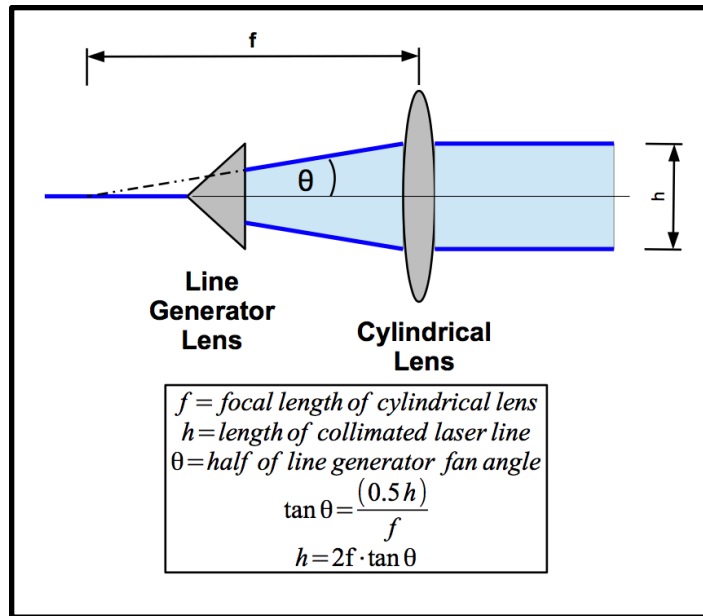


Figure 2.10: Collimating the laser line. The dashed line intersects the optical axis at the focal point of the cylindrical lens, and this intersection can be at any point on the axis, even inside the line generator lens itself. The important part is that the light is collimated after the cylindrical lens, which can be verified in measuring  $h$  at different positions along the optical axis ( $z$ ). The 15-degree fan angle is for the entire distribution, so theta here is 7.5 degrees.

Knowing the length of the line, the next task is to select a lens for L1 that will work in combination with L2 to get the line to be the desired length going into the microscope base. The line should be  $\sim 15 \mu\text{m}$  long at the sample plane, and with a  $60\times$  magnification between the objective and tube lens combination, which gives 0.9 mm. At the time when this system was designed, the most reasonable lens choice available was one with a focal length of 350 mm. This yields a collimated line between the L1 and the tube lens with a length of 0.97 mm, which then gives a length of  $16.2 \mu\text{m}$  at the sample plane.

The final lens to be selected in the excitation path is CYL2, mentioned previously in section 2.5, used to expand the line width to fill the back aperture of the objective lens,

which happens to be about 10 mm. This would then require a width (along  $x$ ) of about 2.8 mm between L1 and L2.

**Figure 2.11** shows the overall layout of excitation path. Some of the more important sizes are shown: Along the  $y$ -dimension,  $h_1$  is the collimated laser line length after CYL1,  $h_3$  is the line length at the conjugate image plane, and  $h_5$  is the length of the laser line at the sample plane; Along the  $x$ -dimension,  $h_2$  is the modified width of the laser line that is then expanded by L1 and L2 to fill the back aperture of the objective,  $h_4$ . Focal lengths at the time of this design are (in units of mm):  $f_{\text{CYL1}} = 25.4$ ,  $f_{\text{CYL2}} = -100$ ,  $f_{\text{L1}} = 350$ ,  $f_{\text{L2}} = 50.8$ ,  $f_{\text{TubeLens}} = 180$ , and  $f_{\text{Obj}} = 3$ . The distance between CYL1 and CYL2 can be arbitrary since the beam is collimated in both  $x$  and  $y$  in that region. All other lenses in the system are at fixed separations with common focal planes.

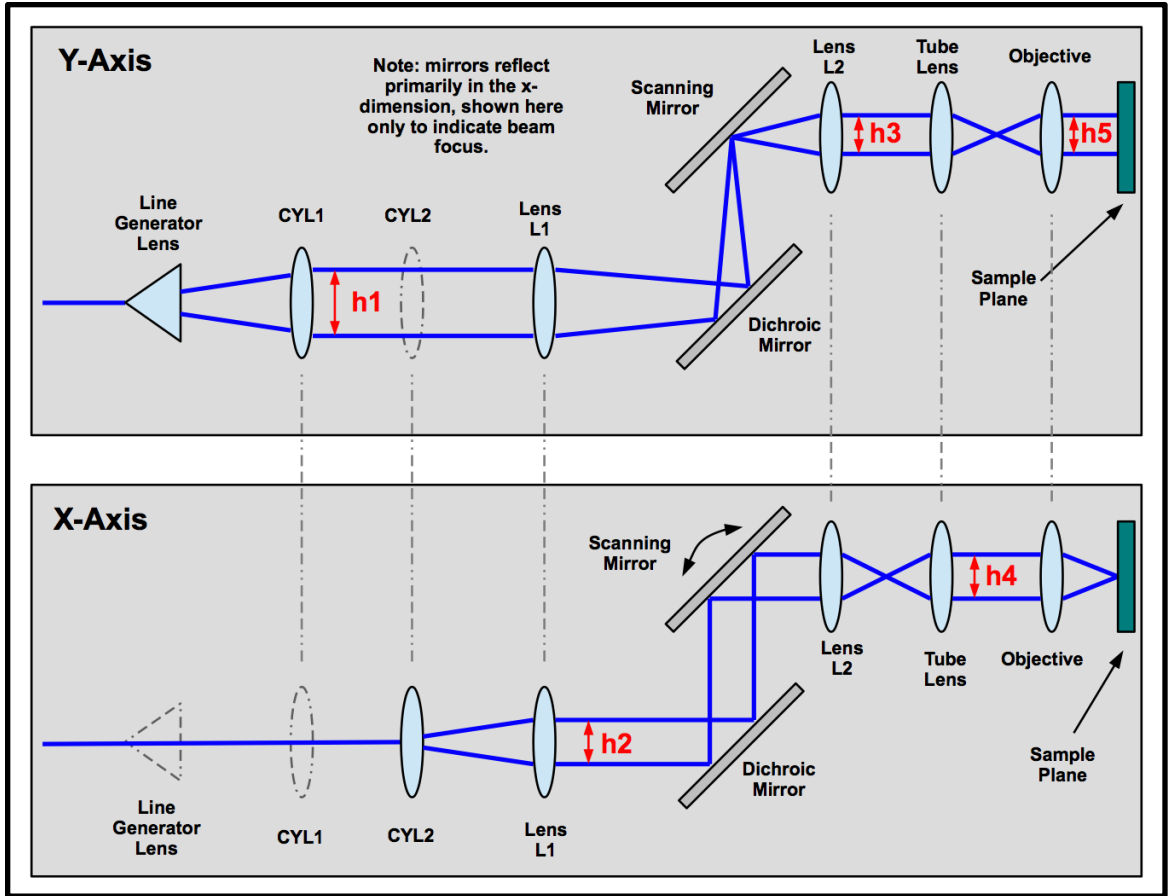


Figure 2.11: Excitation path optics. These diagrams show the overall function of the lenses along the  $x$  and  $y$  dimensions, where the  $y$ -axis is perpendicular to the table surface. The beam is not actually reflected in  $y$  (it would actually be into the page, along  $x$ ), but is shown here as such only to illustrate the focusing of the line along  $y$  at the scanning mirror. The filled solid line lenses are meant to indicate that these components have some influence in that dimension, and the components shown in dashed lines do not.

Given the current system design, assuming the beam diameter of the collimated free space excitation laser is 0.8 mm, then  $h_1 = 6.69$  mm,  $h_3 = 0.97$  mm,  $h_5 = 16.2$   $\mu\text{m}$ ,  $h_2 = 2.8$  mm, and  $h_4 = 9.92$  mm.

## 2.2.7 Dichroic Mirror

The dichroic mirror is a key component in the system that allows the excitation beam to share a common optical path with the emission light. This is important in fluorescence

microscopy, and especially with line scanning systems because the scanning mirror can then be placed somewhere in this shared path and be used for both scanning and de-scanning without having to worry about synchronizing the step angles for each exposure and this also allows the emission path optics to remain in a fixed position (the scanned image is reconstructed later in post-processing based on the camera frame sequence). The dichroic functions as a beam splitter that is reflective for the shorter wavelength excitation beam, and transparent for the longer wavelength emissions. The dichroic filter functions based on principles of thin film interference and is made of a glass substrate with many thin layers (applied via vacuum deposition) that have precisely controlled thicknesses that selectively cause certain wavelengths to be reflected while allowing transmission of others. Most dichroic beam splitters are designed to operate at an orientation of 45 degrees to the incident beam. In this case, the laser wavelength is 488 nm, which was chosen in part for the market availability of filters that have reached a significant maturity in the development cycle, and this is especially important where there are potentially several orders of magnitude of difference in intensity of the excitation vs. emission light.

While it is important to have a low transmission for the excitation laser, it is essential to have the highest possible transmission efficiency for the emission light since the number of photons captured imposes a limit on the overall resolution that can be obtained with the instrument. This microscope is primarily designed to track quantum dots and other probes that have emission wavelengths in the visible spectrum, specifically from about 500 to 800 nm. **Figure 2.12** shows the plot of the transmission efficiency vs. wavelength for the dichroic mirror selected for this system design. It is important to note that the

transmission is very small at 488 nm and well over 90% from 500 to 780 nm, however, it does drop off very rapidly above 800, which will remove some of the emission from quantum dot 800.

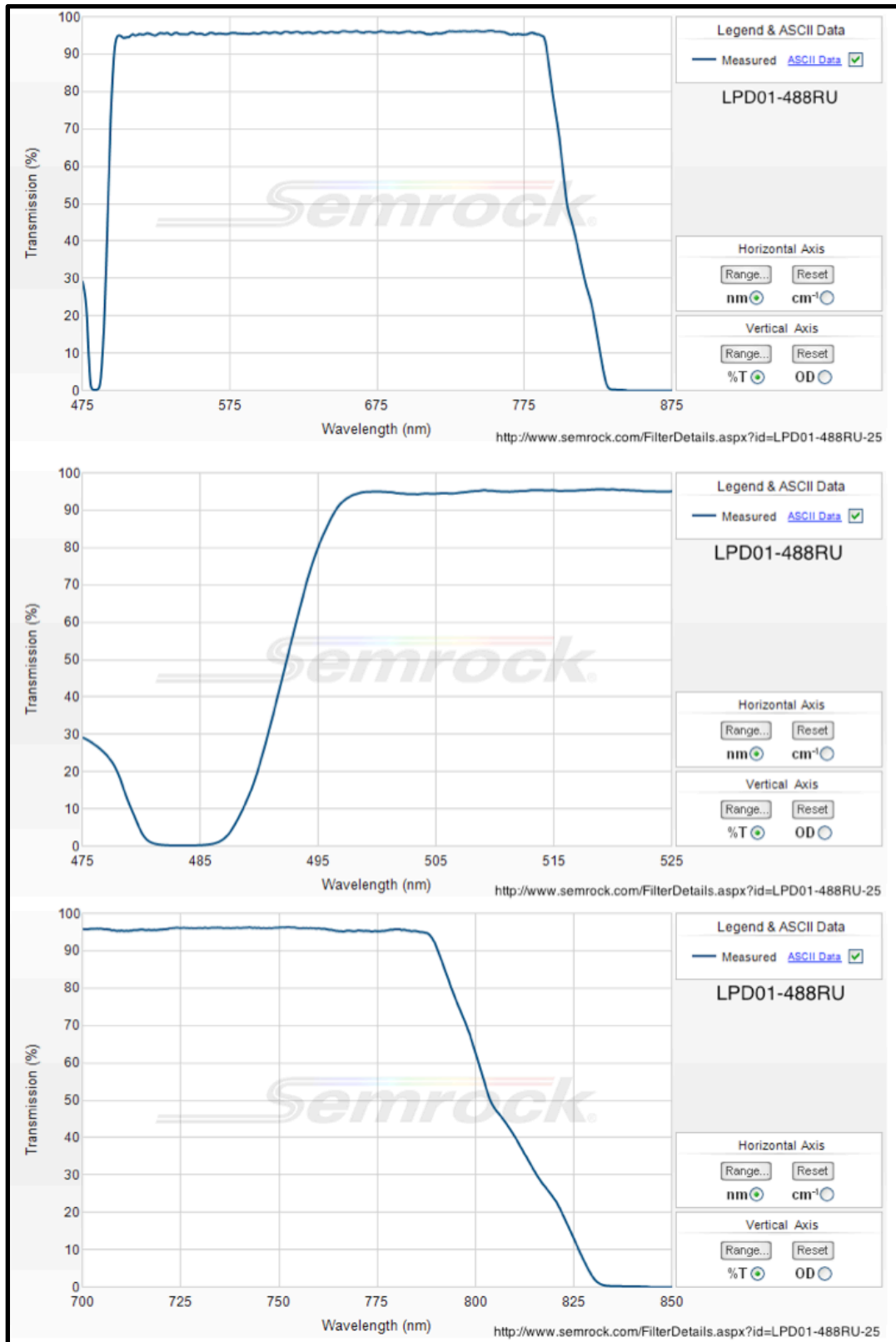




Figure 2.12: Dichroic beam splitter transmission. These three plots are all for the same filter, but show the transmission at different scales. The top is the full range covering the excitation and emission of this instrument. The middle shows the lower range covering the excitation and lower wavelength emissions, and the bottom shows the upper wavelength range.

## 2.2.8 Scanning Mirror

Scanning mirrors used in microscopy applications typically require very accurate, fast angular motion over small steps with very repeatable step-wise angular positioning and low response times. For these reasons, galvanometer actuated mirrors have been a common choice. The actual design of the galvanometer scanner can be quite complicated, but in the most basic description, electrical currents through a wire coil fixed to one part induce a magnetic field that interacts with some permanent magnets fixed to another part and the forces induce relative motion between the two parts and position feedback is accomplished via some kind of internal sensor. There are several design varieties [10] (p.52), some allow the coil to move and some allow the magnets to move. In either case, the mirror is attached to the rotor, which moves relative to the stator, which is fixed relative to the chassis.

Continuous rotation at a constant angular velocity results in a nonlinear reflected beam angle as a function of time and would require multiple mirror surfaces with precise alignment to reduce the temporal interruption of the data acquisition as the mirror is rotated (and even multi-faceted mirrors would cause brief interruptions as the edges traverse the beam. Galvanometer scanners have been developed that oscillate about an angle, using a torsion spring that opposes the motion, with either resonance or linear motion. Resonance scanners oscillate through a fixed total angle at several kHz and

above, and linear scanners can go to a position and hold it for an arbitrary amount of time. The latter has been chosen for this system since it can move the line to a desired position and keep it there for the duration of an exposure of the CCD before moving the line to the next position between frames.

The selection of the specific model of scanning mirror will depend on several key factors, including the total scan angle, step size, step frequency, and fly-back timing. The scanning mirror angle calculation is shown in **Figure 2.13**. It is important to note that the scanning mirror will only affect the beam angle along the x-dimension, and this diagram is oriented such that positive  $x$  is up, and positive  $z$  is to the right. Also, it is important to note that while this calculation will be a simple ray trace that assumes perfect, thin lenses for the angle response estimate necessary to select a scanning mirror, the actual angle response will be measured and the mirror control calibrated using the actual (imperfect, thick) lenses after the setup and alignment (see **Chapter 3**).

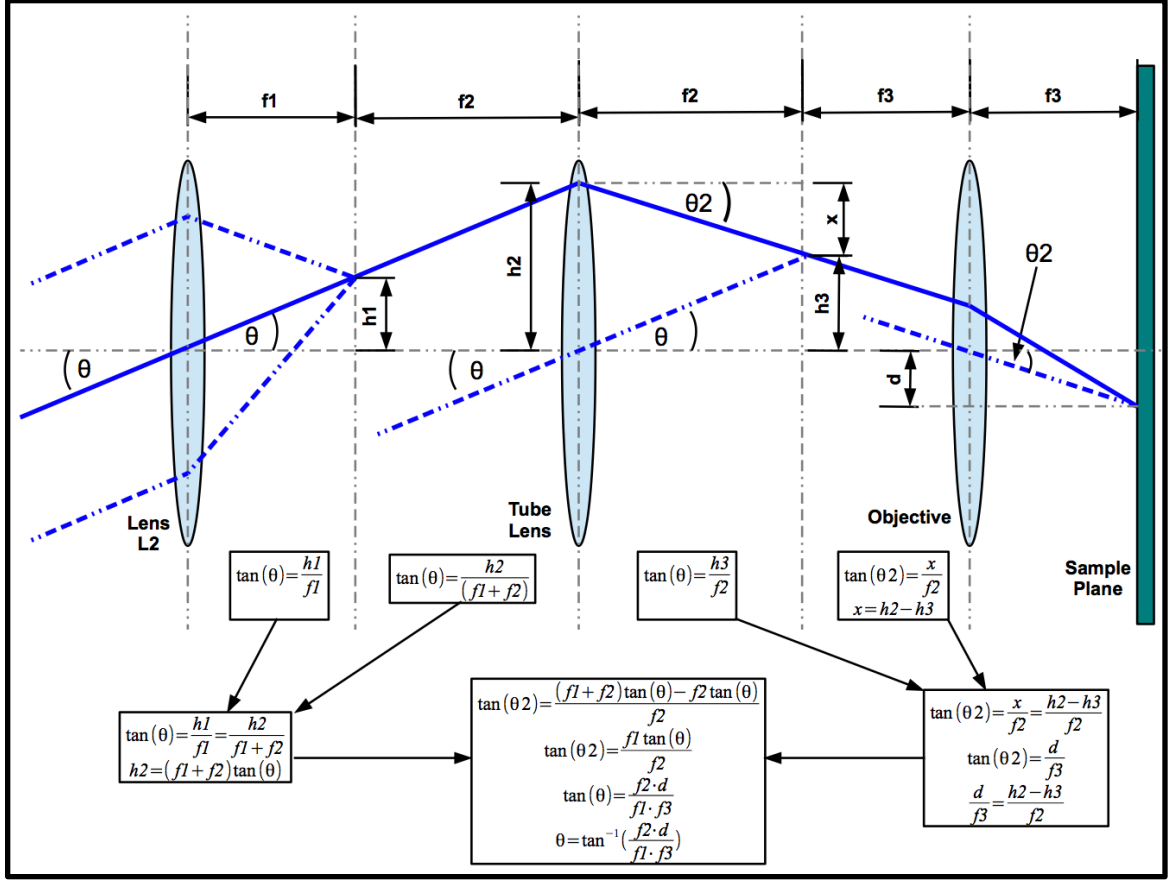


Figure 2.13: Scanning mirror angle calculation. The angles shown here are greatly exaggerated for easier display.

Starting on the left, consider an incident beam that is set at an angle  $\theta$  with respect to the  $z$ -axis (this is any angle the scanning mirror will impose), and we seek the angle and position change at the sample plane that this will cause. The beam will enter this lens system collimated in the  $x$ -dimension. The ray represented by the solid blue line that goes through the lens L2 at the  $z$ -axis will continue on unaltered to the focal plane, where the other previously parallel rays will converge at the focal point. The same solid blue ray will pass through the focal point and will be refracted by the tube lens. In order to find the tube lens focal point that it will pass through on the right, consider an incident ray

parallel to the solid blue ray that crosses the  $z$ -axis at the lens, thus it continues to the focal point to the right of the tube lens where the solid blue ray will converge. A similar consideration is made at the objective lens to determine that focal point as well. The simple geometric calculations are shown in **Figure 2.13**, with the result showing the relation between the mirror angle ( $\theta$ ), the spatial displacement of the laser line ( $d$ ), and the focal lengths of lenses L2 ( $f1$ ), tube lens ( $f2$ ), and objective lens ( $f3$ ).

For this system,  $f1 = 50.8$  mm,  $f2 = 180$  mm, and  $f3 = 3$  mm, so a desired line scan of  $14.9\text{ }\mu\text{m}$  on the sample (which is 128 CCD pixels back projected on the sample) would yield a total scan angle of 1.01 degrees, which would be the necessary fly-back angle (the total angle that we need to cover in one step between scans). Note that this 128-pixel scan is likely to be the upper limit for most single molecule tracking applications with this system due to the exposure time for the CCD. Replacement of the camera would require a re-evaluation of the scanning mirror requirements. The step size of  $0.1161\text{ }\mu\text{m}$  (1 CCD pixel back projected on the sample) implies a scan angle step of 0.0079 degrees. We seek a scanning mirror that will take these tiny steps at least as fast as the total exposure rate of the CCD camera, which is about 1kHz when the line length is set to 64 pixels.

The first mirror selected for this application (based on cost and availability) was a Thorlabs GVS001. The desired specifications were provided to the vendor, who stated that this scanning mirror would perform to those specifications. After installation (with custom machined mounting bracket, wiring, and control software implemented) and optical path alignment it was noticed that while the mirror would respond to these individual small step angle movements, the fly-back step response was too slow, resulting in several blurred pixels at one edge of the 2D reconstructed ( $x,y$ ) image. It was later

confirmed with the vendor that this mirror did not have the appropriate torque to handle the inertial mass of the mirror and rotor at this frequency and scan range. A second vendor (Cambridge Technology) was contacted and provided the same specifications and a replacement scanner (6210H) was implemented (again, with custom machined mounting hardware, wiring, control software, and optical alignment) and found to perform as expected. This was a major setback in the overall project, in terms of time (about 6 months from order to delivery of the new scanner, not including installation, alignment, calibration, etc.), effort, and equipment cost, and was not easily foreseen. This underscores the importance of not only scanning mirror performance, but in identifying risks in possible overall project costs and estimated time to completion, even when the most reasonable care is given in preparation.

### **2.2.9 System Control and Data Acquisition**

The overall system control and data acquisition schematic is shown in **Figure 2.14**. The fire out signal from the camera is used as the clock to advance the scanning mirror, stepping through a list of 16-bit digital words provided to the scanning mirror control board. The AOM controller accepts analog DC voltage input and controls the RF power output to the AOM's piezoelectric transducer. The flip-mount controller toggles the mirror position with a single 5V pulse. The XYZ Piezo-stage controller applies a z-position change based on analog DC voltage input and returns position information to an analog voltage input on the DAQ board. The secondary camera (used for widefield viewing to center a sample or select ROI) uses a single USB connection.

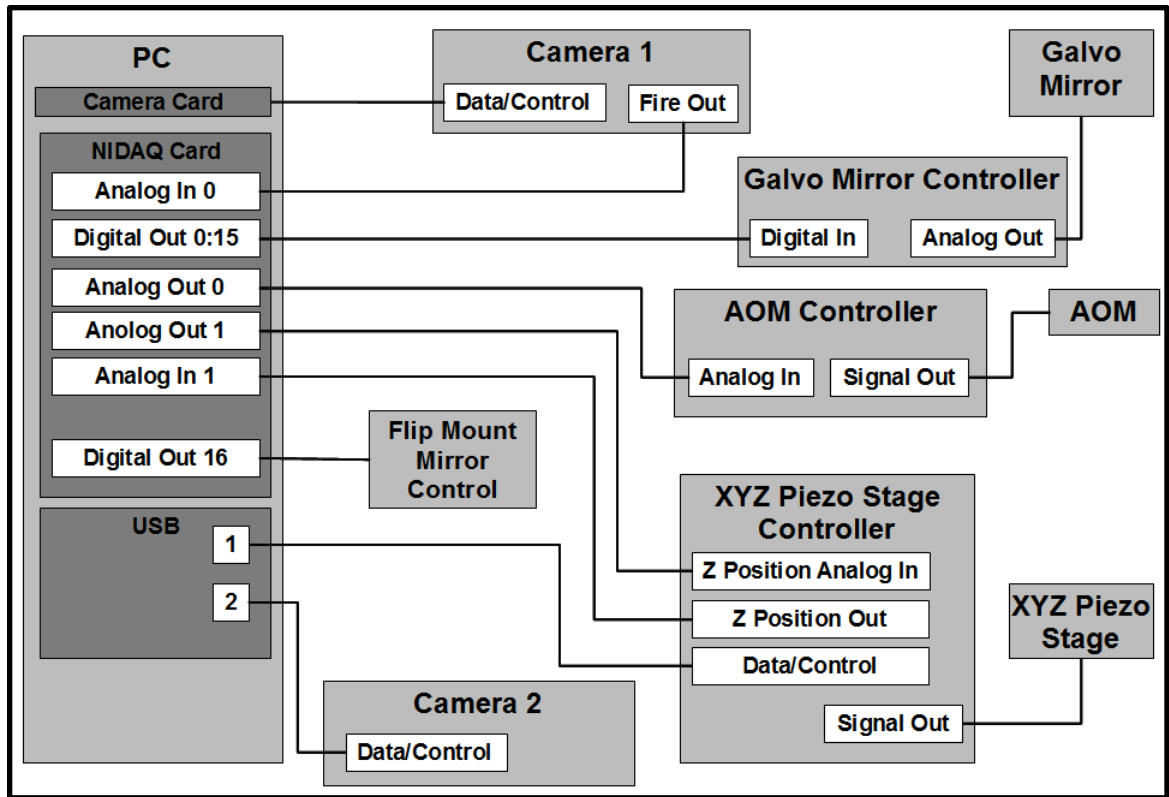


Figure 2.14: System control and data acquisition schematic. The light gray boxes represent physically distinct elements, the dark gray boxes indicate different cards or components in the PC, and the white boxes indicate interfaces within each component or device. The individual lines represent multiple physical wires and/or channels between devices.

The scanning mirror control board (Cambridge Technology 67121HHJ-1 with digital input module 6757) was calibrated by the vendor for this specific scanning mirror such that it controls the mirror movement between -15 and +15 degrees from the center position with a linear response to analog voltage from the DAC board ( $\pm 10\text{ V} = \pm 15$  degrees). The DAC board has a digital input that accepts a 16-bit binary word to set the analog voltage that is accepted by the scanning mirror controller that applies the appropriate current to set the angular position of the mirror. A word of all zeros gives a voltage of -10 V, which gives a position of -15 degrees and all ones gives a voltage of +10 V, which gives a position of +15 degrees. This may seem like an unnecessary layer

of complexity, but it removes a potential source of noise by having the digital conversion happen in a shielded, close proximity to the analog input, which nearly eliminates a potential source of noise that could be important at the very small voltage steps taken in this system design.

The 16 binary bits provides 65,536 positions over the 30 degrees of motion, which implies an angular resolution of 0.000458 degrees, and this is below the required angle step size of 0.0079 degrees by a factor of about 17. To position the mirror at a given angle, the 16-bit word is created by a simple conversion function:

```

N = 16;                % Number of bits for the digital word.
In = 15;               % Upper bound of source value.
in = -15;              % Lower bound of source value.
Out = (2^N) - 1;       % Upper bound of destination range.
out = 0;               % Start at 0 (go from 0 to 65,365 for 16-bit N).
                       % This can be an offset.
x = 0.0079;           % Step size in degrees.

AffineDigital = (x - in)/(In - in)*(Out - out)+out; % Make a decimal number to
                                                    % be converted to binary (e.g. 0 to 65,365 for 16-bit).
AffineDigitalRounded = round(AffineDigital);      % Make sure it's an integer.
Word1 = dec2bin(AffineDigitalRounded,N);          % The N here tells dec2bin
                                                    % that is needs to keep all N bits, even if there are leading zeros.

```

The example code above was written for Matlab (R2012a, Natick, Massachusetts USA), but can be easily implemented in any language. The function *dec2bin* is a Matlab function that converts a decimal number into binary. In this case, Word1 happens to be 10000000000010001, which would be one angle step from zero (1 back-projected CCD camera pixel of displacement of the laser line on the sample, in the positive x-direction = 0.0079 degrees).

Before scanning a sample (acquiring hyperspectral images), the scanning parameters (set by the user in the GUI) are accepted as inputs used to create a series of pre-calculated mirror positions. These parameters include the number of steps per scan (which defines the width of the image) and the total number of scans, which is the number of hyperspectral image frames  $(x,y,\lambda)$ . One mirror position is calculated (using a Matlab function called by the GUI script) for each angle step and this series of steps is repeated by the total number of scans to produce an overall scan position matrix composed of binary words. Each of the 16 bits in each word is converted to a TTL (transistor-transistor logic) signal that is output from the NI-DAQ card (PCIe-6343) in the PC. The 16 wires are patched from the NI-DAQ break-out panel (BNC-2110) to the ribbon cable that connects to the scanning mirror DAC board via a custom made interface board that displays the signal status of each wire with a simple LED. **Figure 2.15** shows the actual implementation of the scanning mirror control. Three colors of LEDs are in a staggered configuration to allow easier reading with the given space limitations.



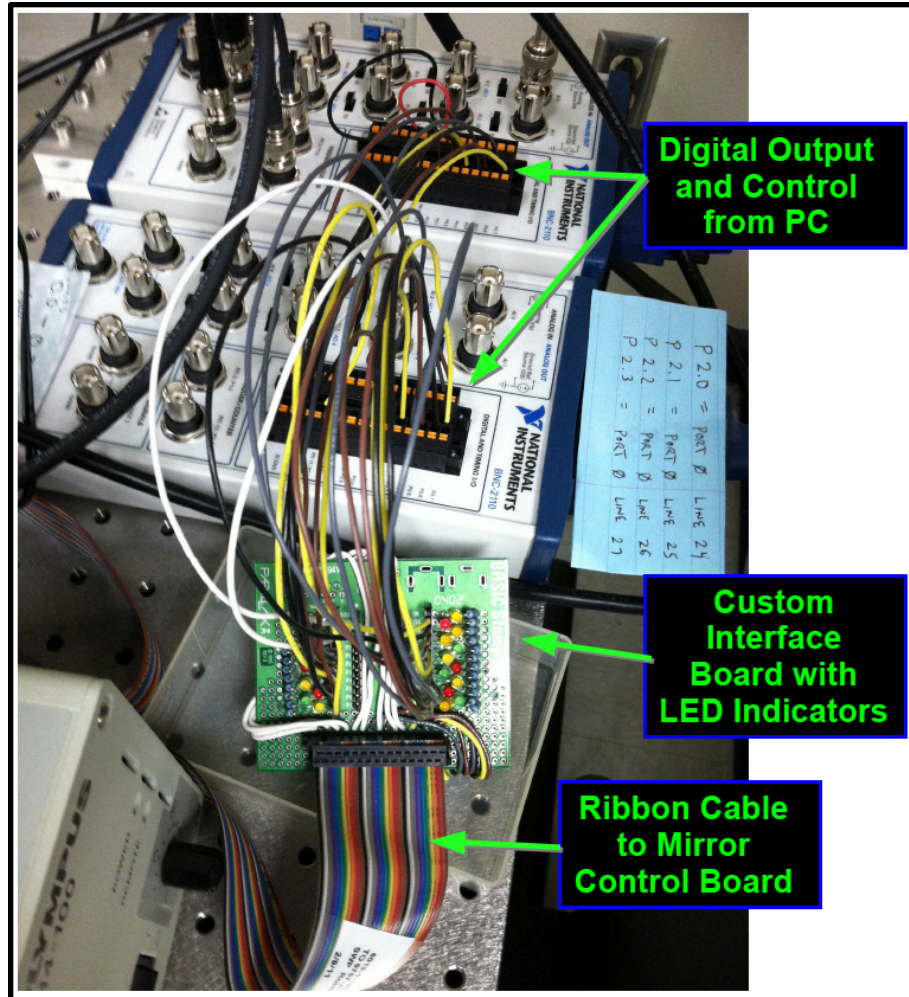


Figure 2.15: Scanning mirror digital control. The NIDAQ breakout boxes (white) are used to provide and receive analog and digital I/O. The scanning mirror is controlled via digital input from the ribbon cable. The LEDs provide visual confirmation of signal on each channel.

## 2.2.10 Signal Timing for Data Acquisition and Mirror Control

**Figure 2.16** shows the signal timing for the data acquisition and mirror angle control. (A) As the camera finishes an exposure the falling edge trigger is used as a clock to advance the mirror scan angle by one step. (B) Scans are completed after a set number of steps, where the mirror angle is returned to the starting position. (C) In fast 3D scans, as a

single scan is completed the  $z$  stage is translated by one step. (D) As the  $z$  steps are completed through the depth of the region of interest, the piezoelectric stage is returned to the starting position to begin another pass. It is important to note that (B) and (C) show scan profiles with only 8 steps per scan, which would actually cover a very small sample space that is not typical (32, 64, or 128 steps/scan would be more common) – the small number of steps was chosen here only to simplify these diagrams. Likewise, (D) shows a 3D scan having only five different  $z$ -positions, whereas a typical case would be more than 10.

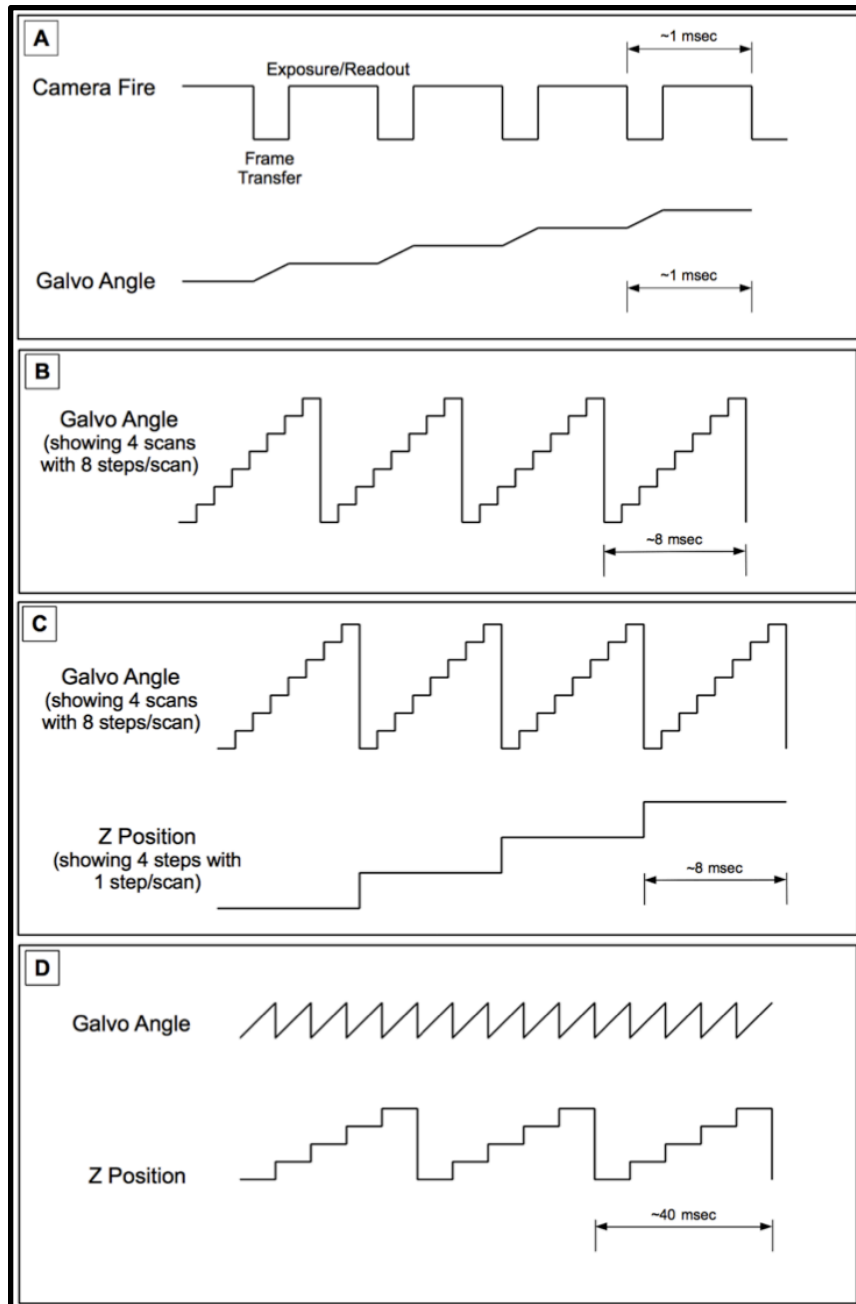


Figure 2.16: Signal timing. The scanning mirror angle is advanced by one step, beginning with the trigger fire pulse, which is sent by the EMCCD upon completion of each frame readout. The readout and exposure times are the same since this is a frame transfer EMCCD.

## 2.2.11 EMCCD Camera

The Andor iXon 860 EMCCD camera was selected for its high frame rate, low noise, and high quantum efficiency (up to ~90%, see **Figure 3.19**). This is one of the more

important components in the system as it is where the photons are ultimately detected. This model is capable of over 500 FPS at frame sizes of  $128 \times 128$ , and almost 1 kHz at  $64 \times 128$ . This is accomplished by using an acquisition method known as frame transfer mode (**Figure 2.17**). The image area (shown in the figure as a white grid) is exposed to emission light that is focused to this pixel plane, with wavelength along the horizontal axis and line position along the vertical axis. The photoelectrons produced in this region during the exposure time are very quickly transferred to the storage area (or frame transfer region, shown in the figure as a gray grid). The frame transfer region is read line-by-line until all rows have been read, and while this readout is happening the image frame is acquiring a new image. When all of the rows in the frame transfer region are read, the image region is once again very quickly transferred to the storage region and the process continues for the desired number of frames in the series.

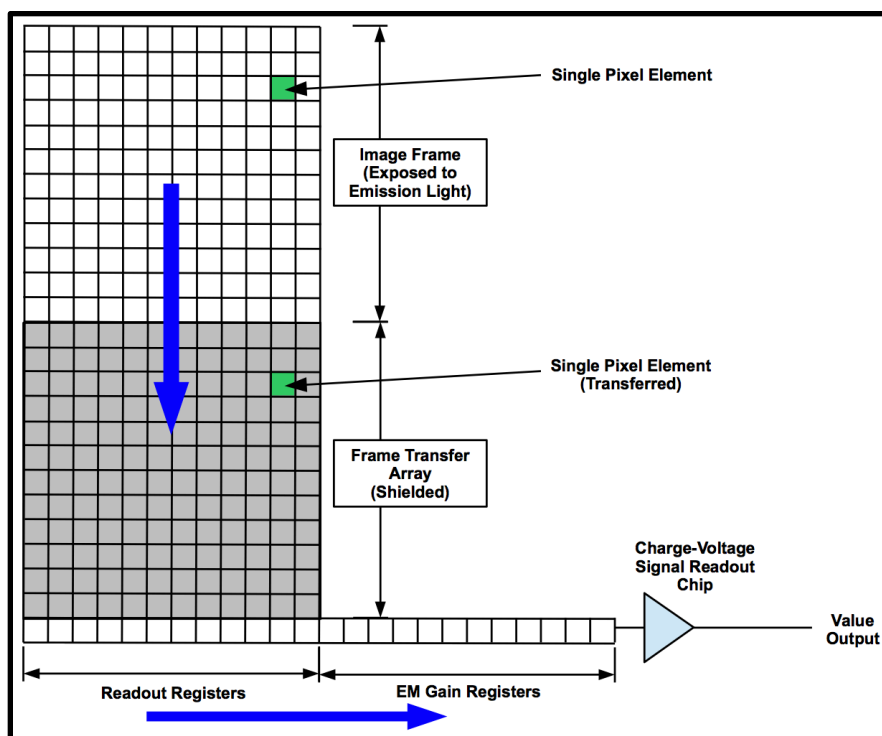


Figure 2.17: EMCCD camera readout. The actual array in the camera is 128×128 pixels, and for simplicity in this figure the example displayed is a 12×12 array. The green pixel represents a single element in the array that is shifted very quickly to the frame transfer region (darker gray), which is shielded from exposure. The image frame is exposed while the frame transfer region is processed. Immediately after the entire frame transfer region is fully processed, another full frame is shifted into the shielded region.

## 2.2.12 Graphical Interface

The data acquisition and control GUI (**Figure 2.18**) allows for efficient adjustment and optimization of acquisition parameters for experiments. The AOM control panel (upper left) is used to set the laser intensity. Just to the right of the AOM control is the Luca CCD Settings panel used for controlling the widefield viewing (enabled by clicking the flip-mount mirror toggle near the bottom center). The iXon CCD Settings panel provides control for the high speed EMCCD camera used for hyperspectral data acquisition. The MCL NanoDrive panel allows for control of the piezoelectric stage as well as high-speed 3D hyperspectral imaging (iXon Scan Z-Stack). The Scanning Parameters panel allows

the user to define the size of the ROI and the number of spectral images to be acquired in the series. The Save Info panel sets the destination for the data files and allows the user to enter some comments about the sample being imaged. The CCD Initialization/Shutdown panel starts and stops the cooling function of the camera sensors, loads/unloads the appropriate drivers, and provides scan and image performance information.

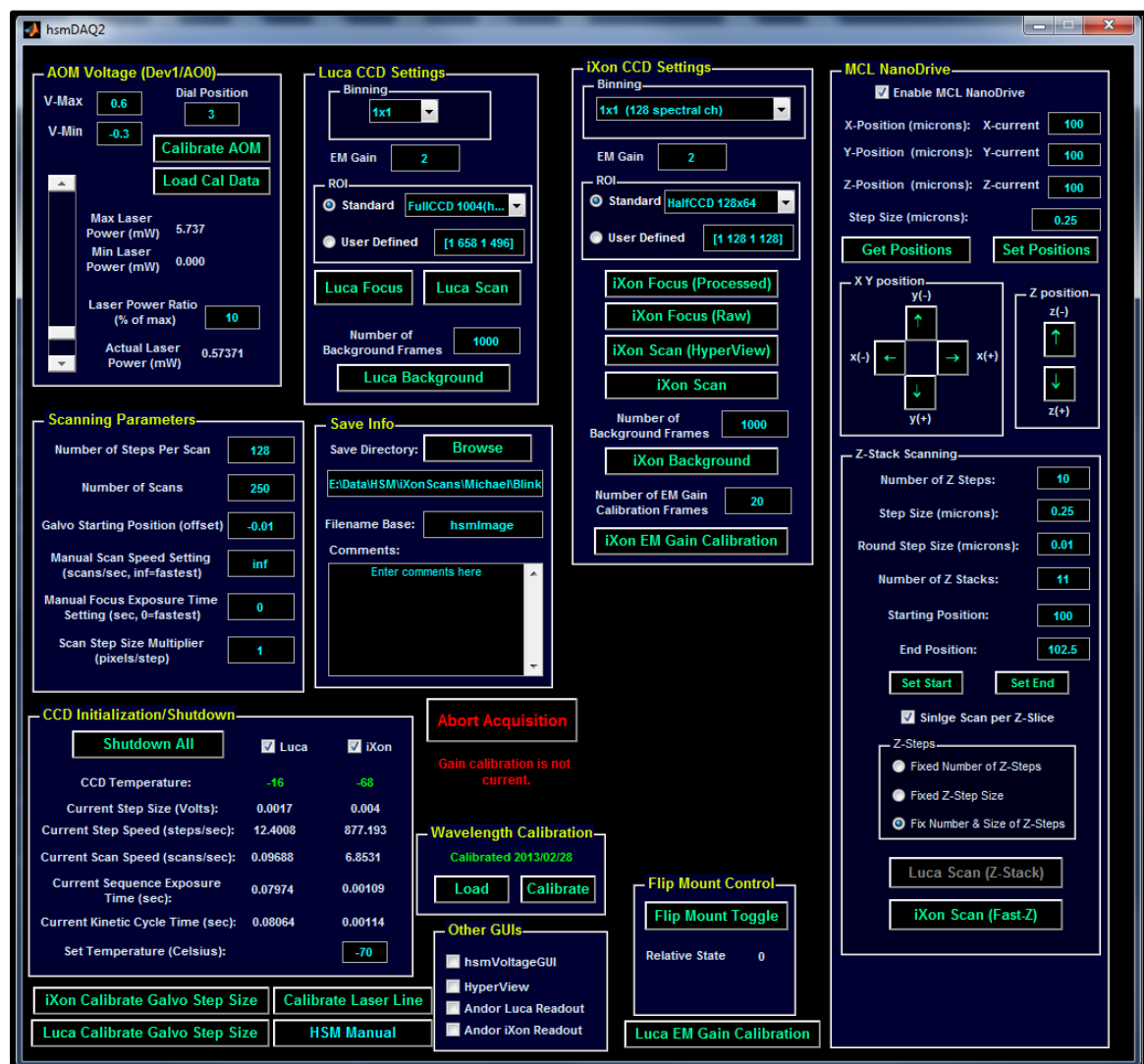


Figure 2.18: Data acquisition and control interface.

The hyperspectral viewing GUI (**Figure 2.19**) provides real-time feedback for instrument control (focusing, ROI determination, etc.) and experimental observations (sample quality, QD labeling density, etc.). The GUI can also be used for preliminary investigations of data in post processing. For example, the blue, green, and red boxes in the RGB image (top left of GUI) highlight single 565, 625, and 800 nm QDs respectively. Spectra for pixels within those boxes are shown in the axes below the RGB image. The GUI provides flexibility in the coloration scheme for the RGB image. For the default RGB representation, each spectral channel is assigned an RGB color progressing from blue to green to red. RGB values for each spatial pixel are determined by relative contributions from of RGB values from each spectral channel.

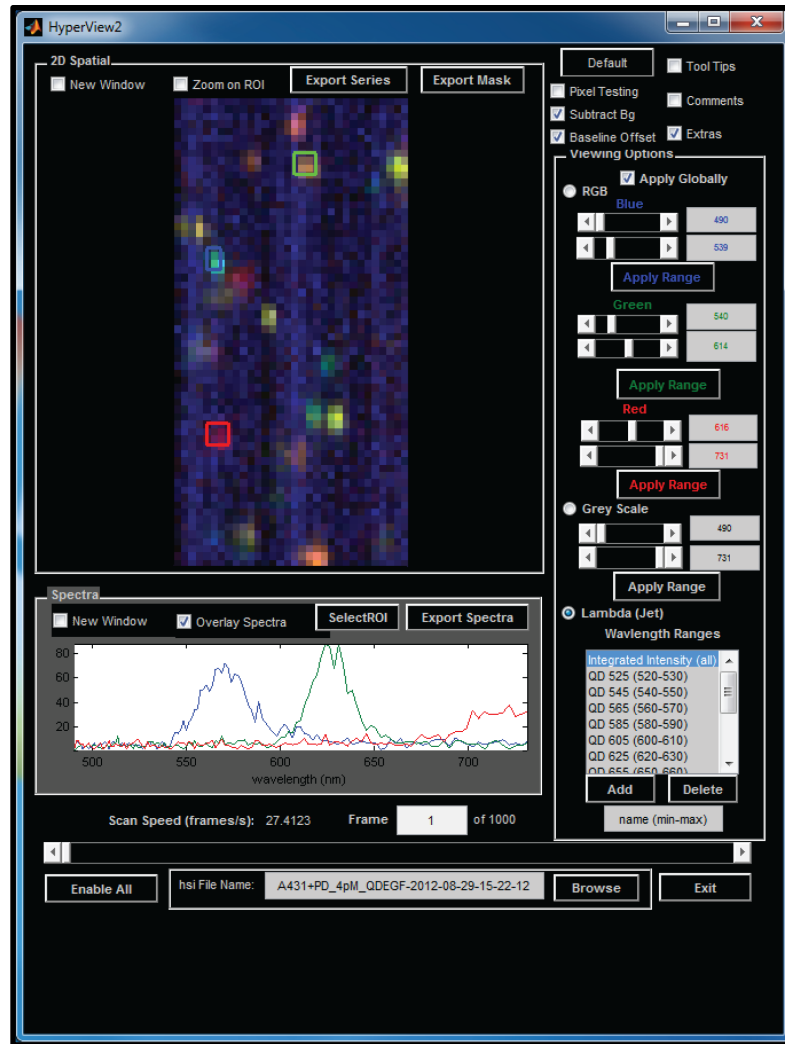


Figure 2.19: Graphical interface for live viewing of hyperspectral data. This example shows one spectral image of a sample containing several varieties of quantum dots. The spectra for the red, green, and blue boxes are shown in their representative colors in the plot below the image. This image is from [9].

### 2.2.13 Spectrometer Design

The localization precision of single fluorophores is proportional to the square root of the number of photons captured [6] and therefore, for throughput efficiency, a prism spectrometer is used as the dispersing element. Prism spectrometers have slightly higher transmission efficiency than diffraction gratings over the spectral range of emission light for this system design (500 to 800 nm) [11], so they are more suitable for this application.



The original spectrometer implemented in this system was that of a simple equilateral prism design (described below in **2.2.13.1**), with plans to later upgrade it to a more advanced aplanatic spherical prism model (part of the 3<sup>rd</sup> year budget for this microscope project). The newer, more advanced prism design has been implemented and is described below in **2.2.13.2**. The prism itself is composed of a dispersive material (the index of refraction is dependent on wavelength). Some of the most common types are N-SF11, F2, calcium fluoride, and germanium, however only F2 provides very high transmission efficiency in the 500-800 nm range (see **Figure 2.20**).

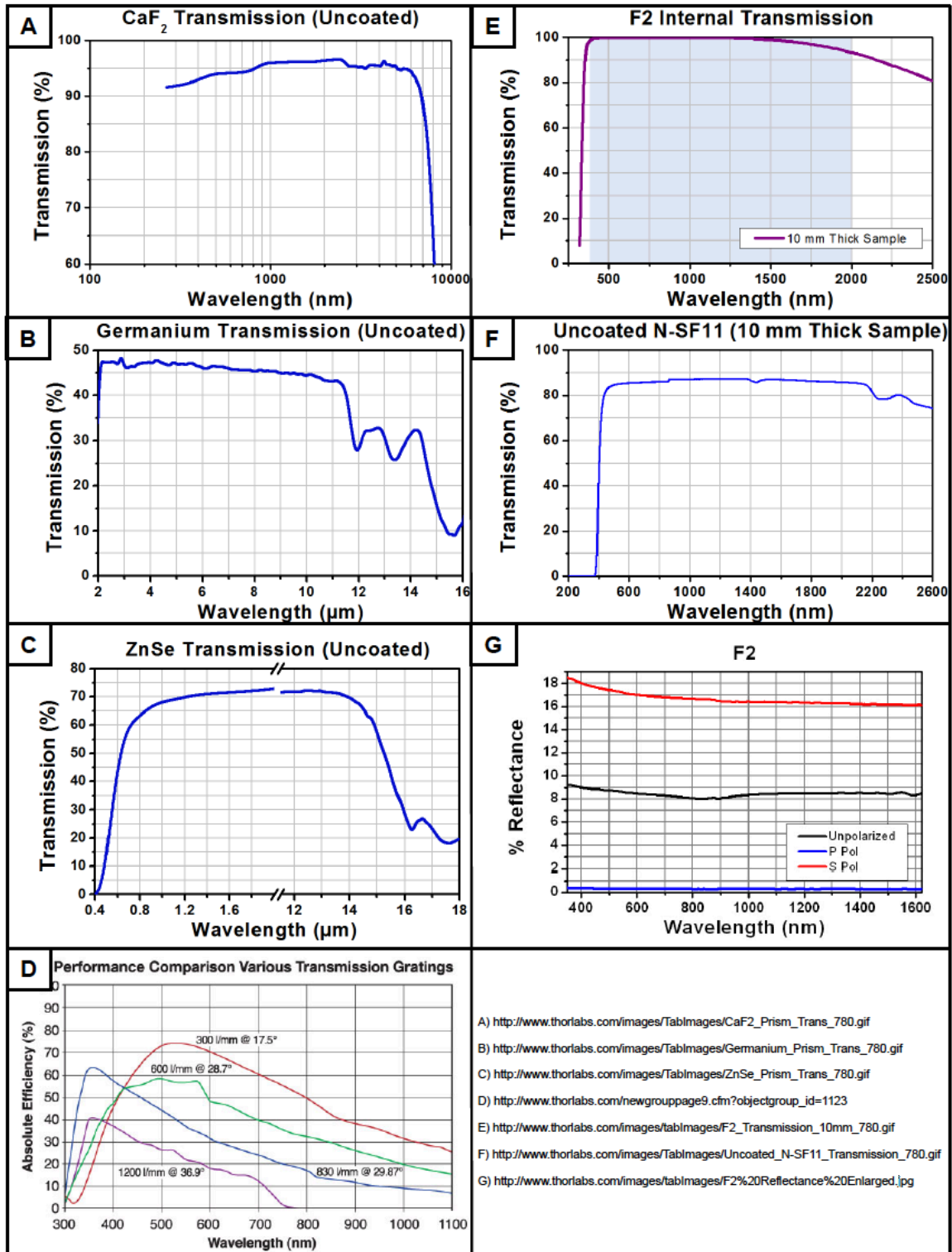


Figure 2.20: Spectrometer prism material.

### 2.2.13.1 Equilateral Prism Spectrometer

The equilateral prism is oriented for transmission efficiency, with the angle set at the minimum deviation, approaching Brewster's angle (where ~100% of the p-polarized light is transmitted). Some of the s-polarized light is still reflected, but this is minimized by using an antireflective coating on the prism.

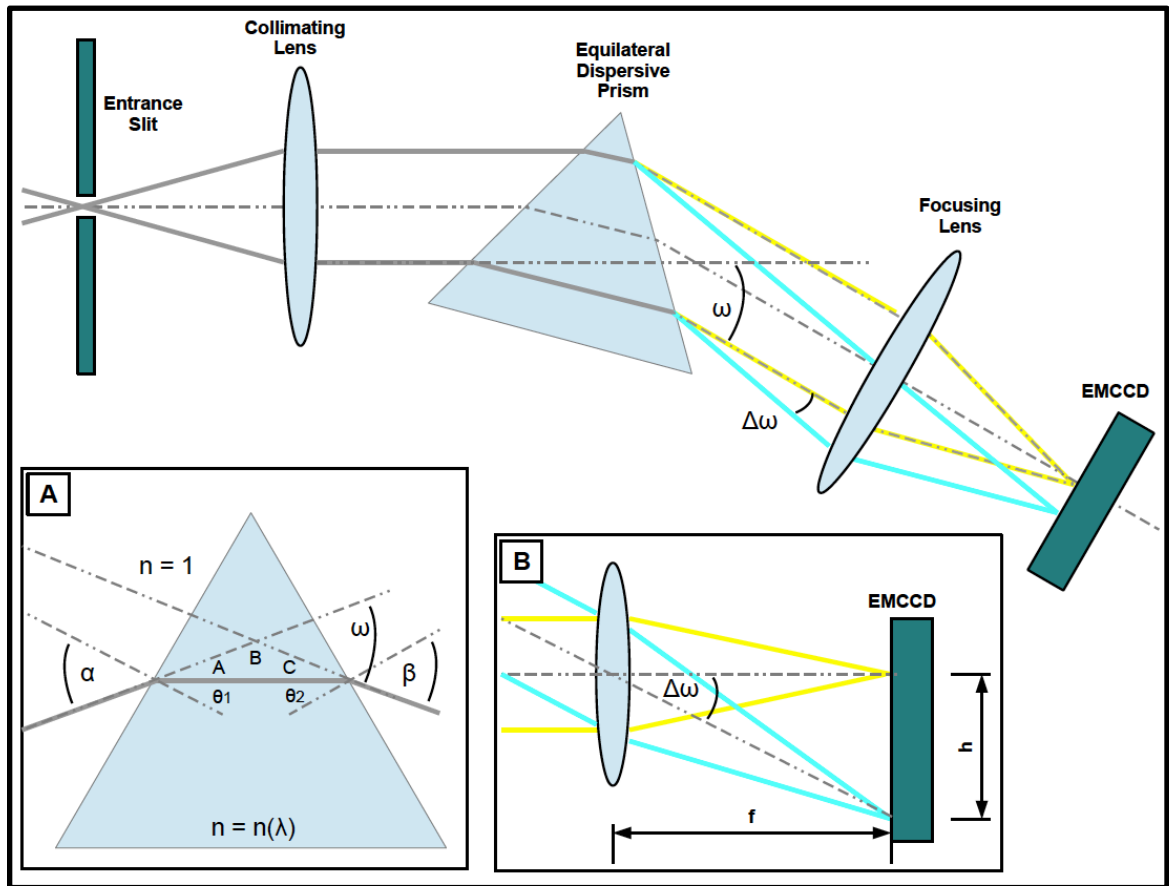


Figure 2.21: Equilateral prism spectrometer design. Inset (A) shows the various angles used for the calculation of the relative angle between the incident and transmitted beams. Inset (B) illustrates the dispersion of light at the EMCCD camera, where the overall sensor size determines the focal lengths of the collimating and focusing lenses.

Considering a ray incident from the left side of **Figure 2.21A**, the angle of the incident ray relative to the normal of the surface is  $\alpha$ . After the surface the ray is refracted, resulting in angle  $\theta_1$  to the normal of the first surface and angle  $\theta_2$  relative to the normal of the second surface, and these angles will be wavelength dependent since the medium has a wavelength dependent index of refraction. Looking at the triangle defined by the ray and the two sides of the prism:

$$(90^\circ - \theta_1) + (90^\circ - \theta_2) + 60^\circ = 180^\circ \rightarrow \theta_1 + \theta_2 = 60^\circ$$

Angles  $A$ ,  $B$ , and  $C$  will sum to  $180^\circ$ , as will  $B$  with  $\omega$ :

$$\alpha = A + \theta_1 ; \beta = C + \theta_2 ; A + B + C = 180^\circ$$

$$B + \omega = 180^\circ$$

Plugging these back in:

$$(\alpha - \theta_1) + (180^\circ - \omega) + (\beta - \theta_2) = 180^\circ$$

Using Snell's Law at the first interface:

$$\sin \alpha = n \sin \theta_1 \rightarrow \alpha = \sin^{-1}(n \sin \theta_1)$$

$$\sin \beta = n \sin \theta_2 \rightarrow \beta = \sin^{-1}(n \sin \theta_2)$$

The minimum angle of deviation  $\alpha$  is such that a ray inside the prism is parallel to the bottom surface (as drawn in **Figure 2.21A**). Finding this angle for the longest wavelength in the range of emission spectra (800 nm), and then fixing the prism angle relative to this incident emission path ray, the angle  $\omega$  can then be determined for any of the other

wavelengths. At the minimum angle of deviation (for  $\lambda = 800 \text{ nm}$ , where  $n = 1.60839$  for F2):

$$\theta_1 = \theta_2 = 30^\circ ; \alpha_{min} = \beta_{min}$$

$$\omega_{min} = 2\alpha_{min} - 60^\circ \rightarrow \alpha_{min} = \frac{\omega_{min} + 60^\circ}{2}$$

$$\sin \alpha_{min} = n \sin \theta \rightarrow \sin \frac{\omega_{min} + 60^\circ}{2} = n \sin 30^\circ$$

$$\omega_{min} = 2 \sin^{-1}(n \sin 30^\circ) - 60^\circ$$

$$\omega_{min}(\lambda = 800 \text{ nm}) = 47.065^\circ$$

$$\alpha = 53.5525^\circ$$

$$\theta_1(\lambda = 500 \text{ nm}) = \sin^{-1}\left(\frac{\sin \alpha}{n(\lambda)}\right) = 29.57^\circ$$

$$\theta_1 + \theta_2 = 60^\circ \rightarrow \theta_2(\lambda = 500 \text{ nm}) = 30.428^\circ$$

$$\beta(\lambda = 500 \text{ nm}) = \sin^{-1}(n \sin \theta_2) = 55.6385^\circ$$

$$\omega(\lambda = 500 \text{ nm}) = \alpha - \theta_1(\lambda = 500 \text{ nm}) + \beta(\lambda = 500 \text{ nm}) - \theta_2(\lambda = 500 \text{ nm})$$

$$\omega(\lambda = 500 \text{ nm}) = 49.193^\circ$$

The dispersion angle  $\Delta\omega$  is then used to calculate the desired focal length for each of the lenses used in the spectrometer. The sensor on the EMCCD camera has an active pixel array composed of  $128 \times 128$  pixels that are each  $24 \times 24 \text{ }\mu\text{m}$  in size, which means that the total sensor area is  $3.072 \times 3.072 \text{ mm}$ . The lenses should be chosen

such that  $\Delta\omega$  will span the active sensor region along the wavelength dimension ( $x$ -axis) as shown in **Figure 2.21B**:

$$\tan(\Delta\omega) = \frac{h}{f} \rightarrow f = \frac{h}{\tan(\Delta\omega)}$$

$$\Delta\omega = 2.128^\circ$$

$$f = 82.67 \text{ mm}$$

The closest achromatic doublet lenses that were commonly available at the time of this spectrometer implementation had a focal length of 76.2 mm, which implies that a slightly greater spectral range is covered (shorter focal length increases  $\Delta\omega$  up to  $\sim 2.3$  degrees).

### 2.2.13.2 Spherical Prism Spectrometer

The equilateral prism design introduces a spatial distortion in the spectrum that is caused by the spherical lens used for focusing after the prism. Off-axis light that is refracted by the prism is focused to a slightly different position at the image plane (EMCCD), resulting in an effect commonly referred to as “smile”. An example of this is shown in **Figure 2.22**, where the light from a spectral calibration lamp is imaged at the EMCCD. The vertical axis is the spatial dimension and the horizontal axis is the spectral dimension. The distortion effect is the slight curvature of these emission lines. The spherical prism spectrometer design described in this section addresses this problem, eliminating the need to characterize and apply a correction factor in post-processing of the data.

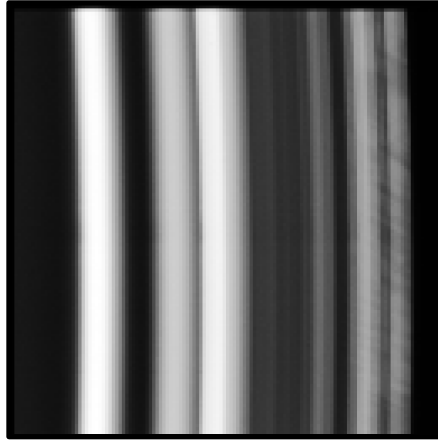


Figure 2.22: Spectral distortion from the equilateral prism spectrometer. Emission light from a spectral calibration light is shown as imaged at the EMCCD. The horizontal axis is the spectral dimension and the vertical axis is the spatial dimension (along the slit,  $y$ -axis).

This section describing the spherical prism spectrometer design is from [9], and the research was primarily performed by Sheng Liu at UNM.

### 2.2.13.2A Aplanatic Image Formation of the Spectrometer

In **Figure 2.23A**,  $S_1$  and  $S_2$  are the front and rear spherical surfaces of the spherical prism.  $S_3$  is the surface of the concave mirror.  $I_1$  is the object point at the entrance slit.  $I_6$  is the image point at the spectral plane.  $I_2$ - $I_5$  are intermediate image points.  $I_1$ - $I_6$  are on the concentric spherical surfaces of  $S_1$  and  $S_2$ . Since the concentric surfaces are an aplanatic pair of image and object conjugates, the spectrometer is aplanatic. Those concentric surfaces satisfy the relationship  $n_1^2 R_1 = n_2^2 R_2 = n_1 n_2 R$  in **Figure 2.23B**.

The detailed image formation of the spectrometer is:

(1) The front surface of prism  $S_1$  forms a virtual image of object  $I_1$  at the position of its aplanatic conjugates  $I_2$ .  $C_1$  is the center of surface  $S_1$ .

(2) Notice that  $I_2$  also lies on the aplanatic conjugate surface of the rear prisms spherical surface  $S_2$ , which forms the virtual image of  $I_2$  at position  $I_3$ .  $C_2$  is the center of surface  $S_2$ .

(3) Mirror  $S_3$  forms a virtual image of  $I_3$  at position  $I_4$  by reflection. Since  $I_3$  and  $I_4$  are near the center of  $S_3$ , the magnification is 1:1.

(4) Notice that  $I_4$  is still at the aplanatic conjugate surface of  $S_2$ , which relays  $I_4$  to  $I_5$ .

(5) Although  $I_5$  doesn't lie on the inner aplanatic conjugate of  $S_1$ , it is near the intersection and  $S_1$  can still form the real image  $I_6$  at the outer aplanatic conjugate of  $S_1$ . Therefore, this last refraction is still near aplanatic.



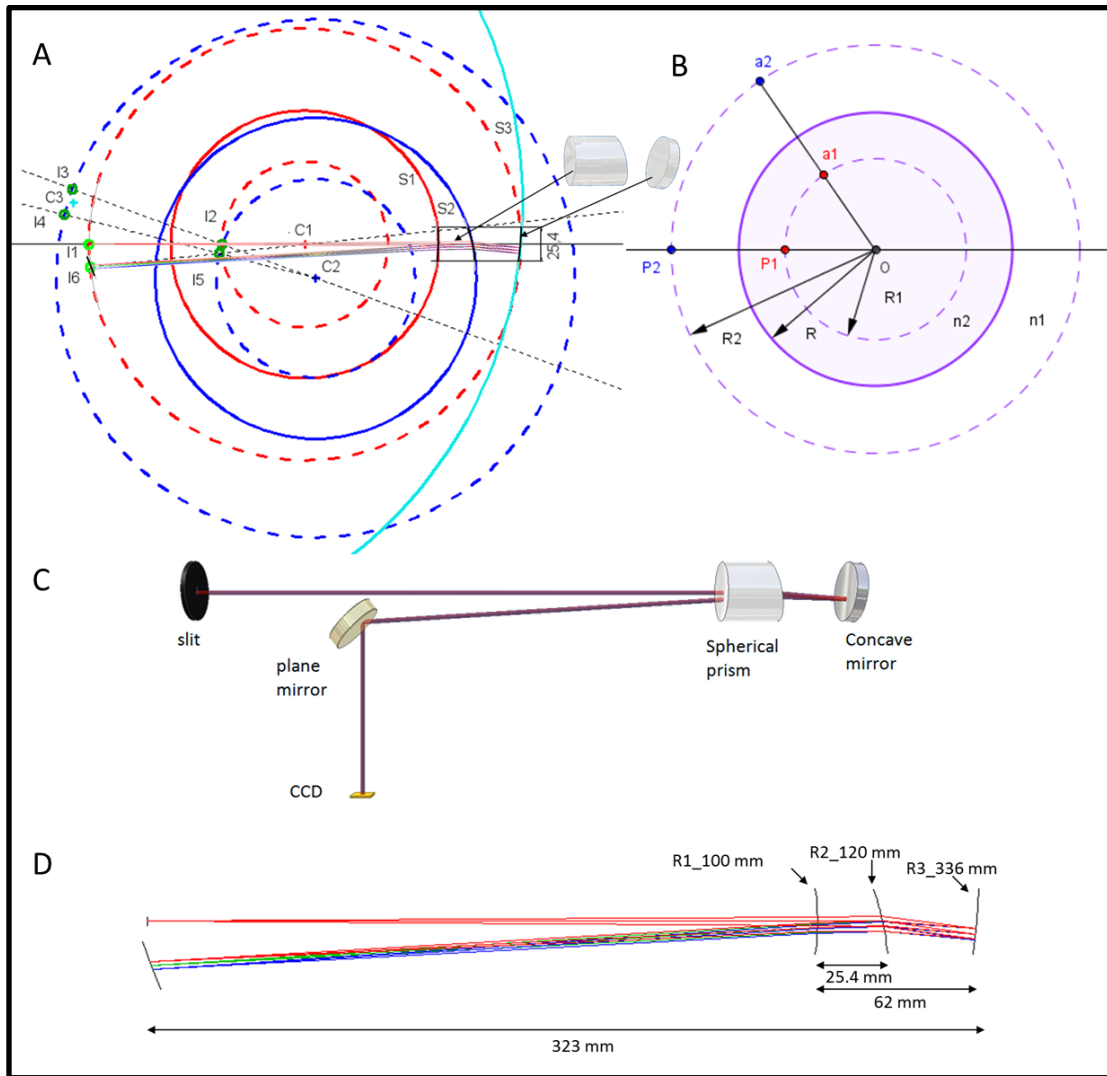


Figure 2.23: Spherical prism spectrometer design. (A) Relative positions of each spherical surface of the prism spectrometer.  $S1$  (red solid circle) and  $S2$  (blue solid circle) are refractive surfaces of the spherical prism,  $S3$  (cyan solid circle) is the reflective surface of the concave mirror. The dotted circles are conjugate aplanatic surfaces of  $S1$  and  $S2$ . (B) Relationship of conjugate aplanatic surfaces (dotted circles) of the refractive spherical surfaces (solid circles). (C) 3D drawing of the spectrometer. (D) Spectrometer design in OSLO (Optics Software for Layout and Optimization).

### 2.2.12.2B Calculation of Spectrometer Design

First, given an approximate size of the spectrometer 300 mm, we choose  $R_1=100$  mm, and  $R_2=120$  mm (**Figure 2.23D**), the glass type of prism is F2, which has a refractive

index  $n_c=1.615$  (the refractive index at 656.3 nm). All the calculations follow the aplanatic rule.

$$I_1C_1 = nR_1 = 1.615 \times 100 = 161.5 \text{ mm}$$

$$I_2C_1 = \frac{R_1}{n} = \frac{100}{1.615} = 62 \text{ mm}$$

$$I_5C_2 = \frac{R_2}{n} = \frac{120}{1.615} = 74.3 \text{ mm} *$$

\*It is 74.56 mm in the final design, so there is a little offset from the perfect image

$$I_3C_2 = nR_2 = 1.615 \times 120 = 193.8 \text{ mm}$$

$R_3$  is decided by making  $I_3$  near  $C_3$ . Since  $I_4$  should also be on the outer dotted blue circle,  $C_3$  should be near the midpoint of  $I_3$  and  $I_4$ .  $R_3 = I_3C_2 + R_2 + L$ , where  $L$  is an arbitrary distance. For a starting value, we choose  $L = 25 \text{ mm}$  which gives  $R_3 = 338.3 \text{ mm}$  ( $R_3 = 336 \text{ mm}$  in the final design).

These numbers are chosen to be the starting point of the prism spectrometer design in the optics design program called Optics Software for Layout and Optimization (OSLO). The radius and angle of the surfaces  $S_2$ ,  $S_3$ , and the distance between the three surfaces are adjusted to minimize aberrations (mainly astigmatism, coma, and distortion). The table below shows the dimensions of the optimized spectrometer design in OSLO.

**Table 2.2      Dimensions of each surface in OSLO design**

Surface	Radius	Thickness	Glass	Notes
object	0.00	261.50	Air	
1	-100.00	25.40	F2	Tilt 0.00 deg
2	-120.00	36.69	Air	Position then tilt (Y-tilt, clockwise) - 12.200 deg
3	-336.00	-36.69	Reflect	Position then tilt (Y-tilt, clockwise) 5.458 deg
4	-120.00	-25.4	F2	Same as S2
5	-100.00	-259.94	Air	Same as S1
image	0.00	0.00	Air	Position then tilt (Y-tilt, clockwise) - 20.879 deg, global coordinate: Y is - 17.14, Z is -259.94, origin is at S1

Units are mm.

## **2.3 Performance Comparison to Commercial Systems**

The performance advantages of this HSM system over existing commercial systems are multifold. In this design, a high-speed back illuminated EMCCD camera is used instead of a PMT array like those used in many of the commercial spectral imaging microscopes. While the EMCCD has relatively high quantum efficiency (QE) of the detector (~90%) compared to the lower 20-45% QE of available PMT arrays, it is effectively reduced by a noise factor introduced from impact ionizations in the gain registers [7], which essentially scales the effective QE down by ~2. This leaves the EMCCD QE at about 45%, similar to that of the best PMTs. The main advantage is that the EMCCD also allows for 128

spectral channels per spatial pixel (and with 64 spatial pixels per frame), compared to 32 spectral channels (and no spatial component) found on commercial systems. Also, the pixels within the EMCCD are essentially contiguous, so no part of the spectrum is lost, whereas PMT arrays and filter-based systems typically have some losses from gaps in the acquired spectrum (and this is one of the important distinguishing traits of a hyperspectral system – many contiguous spectral channels without gaps, as opposed to multispectral systems). Also, this HSM design uses a custom made spherical prism spectrometer, which has a higher transmission efficiency than diffraction gratings for this spectral range (from 500 to 800 nm).

## References

1. Wilson BS, Pfeiffer JR, Oliver JM (2000) Observing FceRI Signaling from the Inside of the Mast Cell Membrane. *J Cell Biol* 149: 1131–1142 ST – Observing FceRI Signaling from the. Available: <http://jcb.rupress.org/cgi/content/abstract/149/5/1131>.
2. Wilson BS, Pfeiffer JR, Surviladze Z, Gaudet EA, Oliver JM (2001) High resolution mapping of mast cell membranes reveals primary and secondary domains of FceRI and LAT. *The Journal of Cell Biology* 154: 645–658. Available: <http://jcb.rupress.org/content/154/3/645.abstract>.
3. Hell SW (2007) Far-field optical nanoscopy. *Science (New York, NY)* 316: 1153–1158. Available: <http://www.ncbi.nlm.nih.gov/pubmed/17525330>.
4. Schermelleh L, Heintzmann R, Leonhardt H (2010) A guide to super-resolution fluorescence microscopy. *The Journal of cell biology* 190: 165–175. Available: <http://jcb.rupress.org/content/190/2/165.full>.

5. Lidke DS, Lidke KA (2012) Advances in high-resolution imaging--techniques for three-dimensional imaging of cellular structures. *Journal of cell science* 125: 2571–2580. Available: <http://jcs.biologists.org/content/125/11/2571.long>.
6. Ober RJ, Ram S, Ward ES (2004) Localization accuracy in single-molecule microscopy. *Biophysical journal* 86: 1185–1200. Available: <http://www.pubmedcentral.nih.gov/articlerender.fcgi?artid=1303911&tool=pmcentrez&rendertype=abstract>.
7. Robbins MS, Member S, Hadwen BJ (2003) The Noise Performance of Electron Multiplying Charge-Coupled Devices. *IEEE Transactions on Electron Devices* 50: 1227–1232.
8. Powell I (1987) Design of a laser beam line expander. *Applied optics* 26: 3705–3709. Available: <http://www.ncbi.nlm.nih.gov/pubmed/20490126>.
9. Malik MD, Cutler PJ, Liu S, Byars JM, Lidke DS, et al. (2013) Multi-color Quantum Dot Tracking using a High-Speed Hyperspectral Line-Scanning Microscope. Manuscript in review.
10. Pawley JB (2006) *Handbook of Biological Confocal Microscopy* (Third Edition). 3rd ed. Pawley JB, editor Springer.
11. Lerner JM (2006) Imaging spectrometer fundamentals for researchers in the biosciences--a tutorial. *Cytometry Part A : the journal of the International Society for Analytical Cytology* 69: 712–734. Available: <http://www.ncbi.nlm.nih.gov/pubmed/16615140>.

## Chapter 3

### Instrument Calibration and Characterization

Calibration and characterization are a vital part of the overall system implementation. This chapter investigates the methods used for each component and describes the results found for the configurations implemented at the time of this writing. Calibrations include the AOM (for laser power), magnification before and after the spectrometer, line scan angle (orientation of the laser line relative to the scan direction at the sample), color dependence on localization (spectrometer alignment), the 4D point spread function (theoretical and measured), spectral calibration, spectral distortion and dispersion, spectral resolution, EMCCD gain calibration, EMCCD background and baseline correction, measured transmission efficiency, objective aperture acceptance ratio, and the EMCCD quantum efficiency vs. wavelength.

#### 3.1 AOM Calibration and Control

The AOM and signal processor are calibrated together to obtain a plot of the overall output laser power for each value of voltage applied to the input of the signal processor unit (see **Figure 3.1**). This is measured with a power meter at the collimated free space laser beam near the air objective. The DC offset is adjusted by altering the front panel level control until the optimal response is achieved, providing the maximum output laser power as input voltage is varied. The minimum and maximum input voltages are set in the hsmDAQ GUI AOM control box, finding the most ideal values for each, where

clearly identified local minimum and maximum values are observed at smooth regions of the curve (as shown in **Figure 3.1**). Once a satisfactory driver offset level and input voltage range are found, the response curve is then generated in the control GUI (hsmDAQ) to obtain the desired output laser power as a percentage of the maximum for each input voltage value. An average is taken over three passes of 100 voltage steps with a delay between steps to allow the AOM to stabilize. This provides the GUI with information necessary to adjust the laser power as a percentage of the maximum power value. The laser power out is also displayed to the user in mW (see **Figure 2.17**).

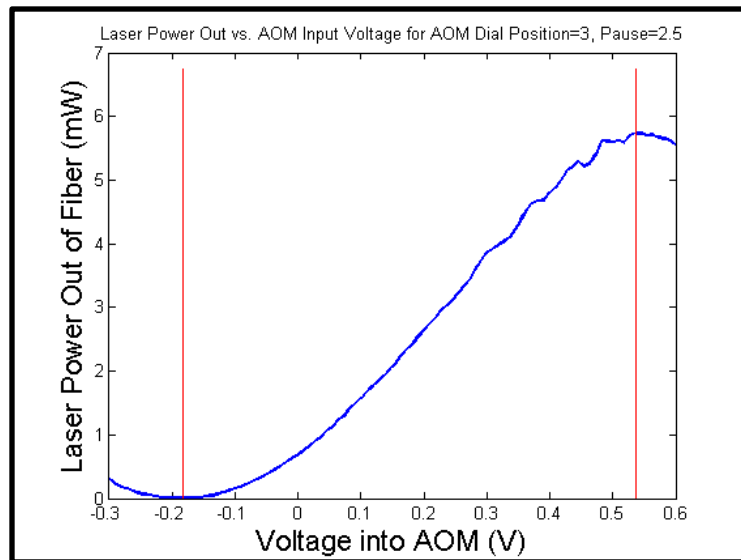


**Figure 3.1: AOM calibration.** The red vertical lines indicate the minimum and maximum values of output power measured at the free space collimated laser beam after the air objective, before the laser line generator lens. The plot shows input voltages ranging from -0.3 to +0.6 at an offset dial position of 3 (as marked on the driver unit used here).

## 3.2 Magnification

The expected overall magnification is calculated by multiplying the 60 $\times$  value from the objective and tube lens combination by the ratio of focal lengths of lenses L3 and L2, i.e.

$$M = 60 \times (f_{L3}/f_{L2}) = 60 \times (175/50.8) = 60 \times 3.44 = 206.7 \text{ (overall magnification).}$$

This calculation assumes perfect lenses and that all of them are in perfect focus with each other. There may be some variation in the actual lenses and their placement, so a measurement is necessary in order to determine the real value, especially for knowing the actual back projected CCD pixel size on the sample, which is used in many other applications, include the 3D point spread function measurement. The original system design is such that there should be minimal magnification in the spectrometer path (from the entrance slit to the CCD pixel array surface), so a measurement is first made by imaging a grid target of known spacing with the widefield camera. This will provide the magnification from the objective, tube lens, lens L2, and lens L3.

**Figure 3.2** shows one widefield image of the grid target (ThorLabs R1L3S3P Grid Array; 500, 100, 50, 10  $\mu\text{m}$  Grids, 3''  $\times$  1''), looking at the 10  $\mu\text{m}$  grid. In this case, the camera used was the Andor Luca R model, which has a pixel size of 8  $\mu\text{m}$ . While an attempt was made to align the grid array with the CCD, the orientation of the grid target relative to the CCD pixel array is not perfect since this is a glass microscope slide that rests in a mount with some freedom to move relative to the mount, so the magnification must be measured by calculating the vector magnitude between points of known spacing in the image, comparing the distance observed on the camera to the actual distance based on the grid spacing (10  $\mu\text{m}$ ). This is done for both the vertical and horizontal directions to get a



measure of the magnification along each of those dimensions.

First, finding the magnitude of the vector  $R_1$  (shown in green in **Figure 3.2**), the distance between points  $(x_1, y_1)$  and  $(x_2, y_2)$  is found in terms of pixels and then converted to microns ( $1 \text{ pixel} = 8 \text{ } \mu\text{m}$ ). These points were chosen because, in theory, they are spaced apart by  $30 \text{ } \mu\text{m}$  on the target, which reduces the impact of being off by perhaps one pixel when a smaller spacing is used, and the corners of the boxes were chosen in order to simplify the estimation of the start and ending pixel positions (the desired distance vector needs to be perpendicular to the pseudo-vertical lines). The procedure is repeated for a total of three horizontal vectors  $R_1$ ,  $R_2$ , and  $R_3$ , and three vertical vectors  $R_4$ ,  $R_5$ , and  $R_6$  (the latter two not shown in the figure) in the image and each of these horizontal and vertical sets are averaged to obtain the mean magnifications of 209.2 for the horizontal dimension and 210.4 for the vertical dimension. Running this procedure several times on different regions of the grid array confirmed consistency in the measurement, so unless there is some constant non-uniformity between the vertical and horizontal spacing of the grid (which is not easily tested in this system since the slide holder has a fixed orientation due to spatial constraints in the  $x,y,z$  Piezo stage), these magnifications should be fairly accurate.

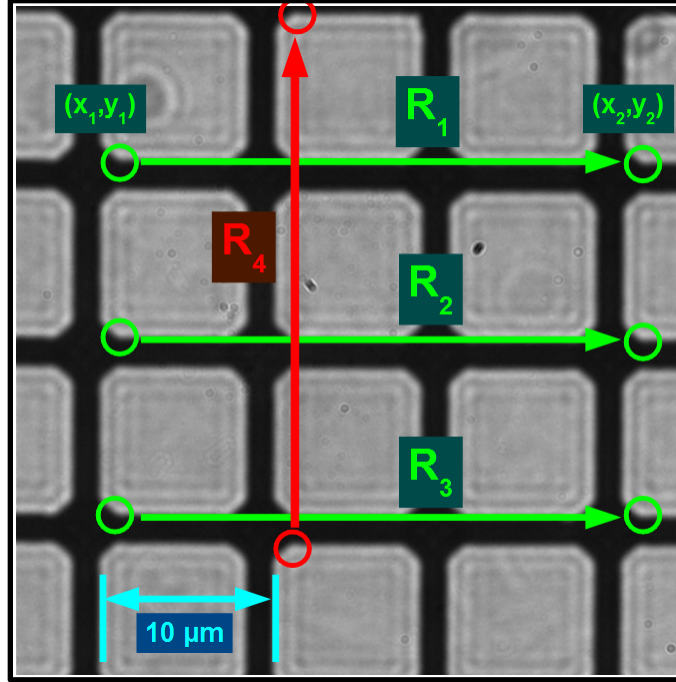
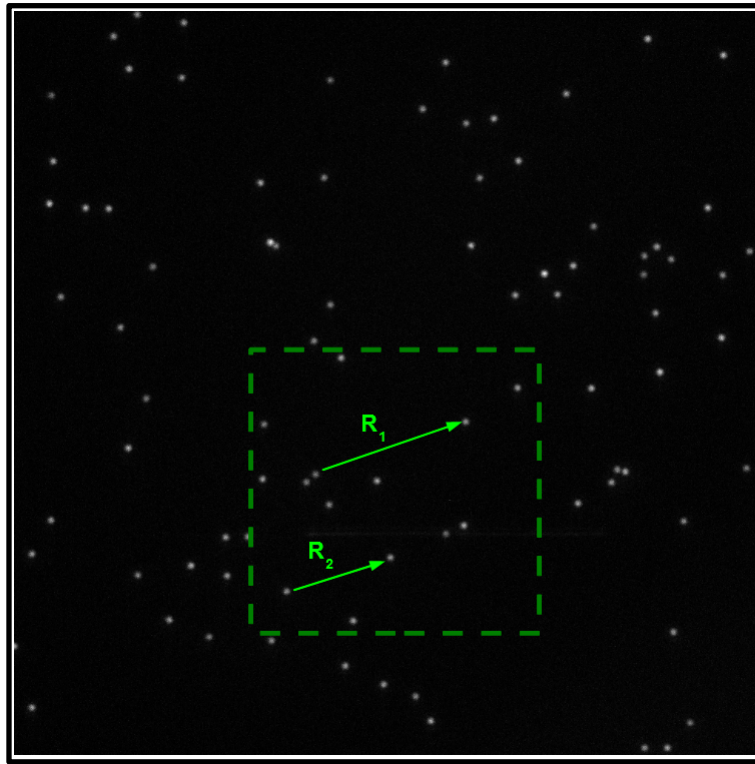


Figure 3.2: Grid target with 10  $\mu\text{m}$  spacing observed with widefield the camera.

The next step is to get the overall magnification of the system, including the spectrometer. This was done by using a low-density sample of fluorescent beads fixed to the surface of a glass coverslip and obtaining the real vector distance between two of the beads using the known magnification of the widefield mode, and then switching to hyperspectral line-scanning mode and measuring the observed pixel distance between the same beads, then converting to microns (at the CCD) using that each pixel of the CCD camera on the hyperspectral path (Andor iXon 860) is 24  $\mu\text{m}$ . The ratio of the real distance (inferred from the widefield measurement) to that measured at the CCD gives the overall magnification. This roundabout method was necessary because the grid target is not fluorescent and the field of view of the CCD camera used on the hyperspectral path is much smaller, so 30  $\mu\text{m}$  of spacing is not observable in one field of view (in fact only

$\sim 15\text{ }\mu\text{m}$  at most), and the pixels are also larger so the impact of guessing the location of a corner is worse), and also that estimating the center pixel of a fluorescent bead is much easier than a corner of the grid. A more straightforward (and possibly more accurate) measurement would be to have a fluorescent grid target or, perhaps even better, fluorescent beads that are placed at known distances from each other on a glass substrate, maybe where the spacing is exactly 1 or 2 microns.



**Figure 3.3:** Widefield image of the low-density sample of fluorescent beads. The dashed line shows the region that would be viewed when scanned in hyperspectral mode (using 128 steps per scan).

**Figure 3.3** shows an image of the low-density fluorescent bead sample captured using the widefield CCD camera. The dashed green line indicates the approximate field of view using the hyperspectral line-scanning mode. The magnitudes of  $R_1$  and  $R_2$  are calculated

and converted into distance on the sample plane. **Figure 3.4** shows the same sample using the hyperspectral line-scanning mode. The magnitudes of  $R_1$  and  $R_2$  are calculated using this path and the overall system magnification is obtained by comparing the distance on the sample plane to the distance on the camera. This procedure was done for several different sets of points within this image and for other selected regions of the bead sample, and the mean value of the overall magnification was found to be 205.4, which implies that a small negative magnification is introduced by the spectrometer. This implies that one back-projected pixel of the EMCCD camera used in the hyperspectral line-scanning mode is approximately 117 nm at the sample plane.

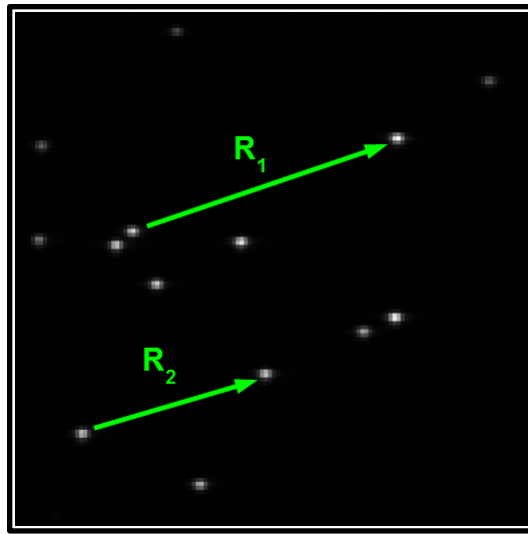


**Figure 3.4:** Hyperspectral line-scanning mode image of the low-density bead sample. The displacement vectors here are compared to the same ones taken in widefield to obtain the overall magnification, including any amount added by the spectrometer.

### 3.3 Line Scan Angle

One of the important system alignment parameters to verify is the orientation of the laser line relative to the scan direction. **Figure 3.5** illustrates the potential problem, showing the desired condition (A) and the case where the line has a slight angle relative to the scan direction (B), which could result in a slight blurring of the image. If it exists, the condition can be corrected by rotating the line generator lens and the two cylindrical lenses in the excitation path, iteratively making adjustments and then checking the orientation until a satisfactory convergence in the alignment is achieved.

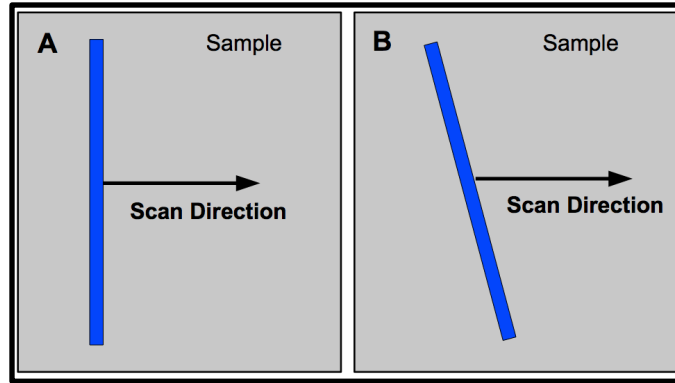


**Figure 3.5: Laser line angle relative to the scanning direction.** Here, the blue rectangle represents the laser line profile as it is projected on the sample plane. Panel (A) shows the ideal case, whereas (B) is the condition to be avoided.

The first step is to set the orientation of the widefield camera to be aligned with the laser line, which can be accomplished by having the camera supported by a rotation mount. This line is projected onto a dense, planar sample of quantum dots fixed to a glass cover slip (preferably with a variety of quantum dots that have a low bleaching rate and an emission spectrum that is visible through the eye-pieces for easy focusing), and the camera orientation is set such that the laser line is parallel to the rows of pixels. **Figure 3.6** shows a widefield image of light emitted from the planar sample of quantum dots

excited by the laser line. The center peak of the line intensity (in the vertical sense in this image) is in the same horizontal row of pixels at  $(x_1, y_1)$  as at  $(x_2, y_2)$ . Once confirmed, the camera orientation is secured and the sample is changed to a low-density sample of fluorescent beads that will be used to measure the scan direction.

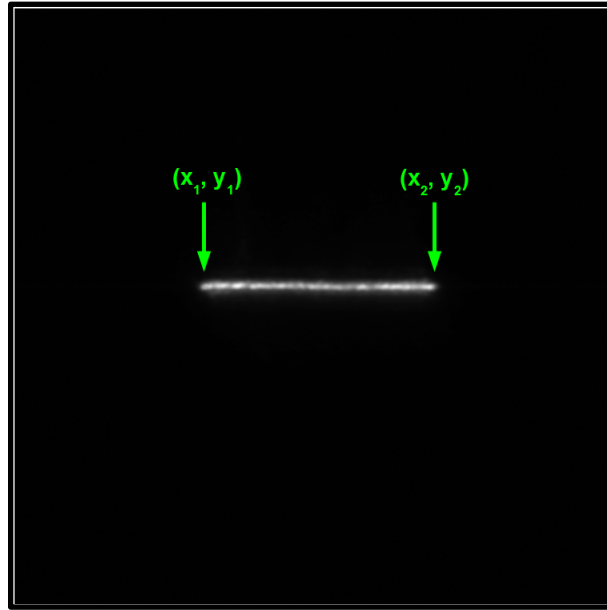


Figure 3.6: An image of emission light from a dense, planar sample of quantum dots fixed to a glass cover slip, excited by the laser line. When the line is correctly aligned with the CCD, the center of the bright region will be centered along a single row of pixels.

**Figure 3.7** shows a maximum pixel projection of a scan of a low-density fluorescent bead sample taken in widefield mode. An exposure is captured at each step in the scan and the acquired series of images is analyzed for the maximum value of each pixel throughout the series, producing a result that is similar to a sum projection over the series (in this case the sum projection was not used since the intensity scale was skewed by a few very bright bead aggregates). The scan direction (relative to the widefield CCD) is determined by finding the vector defined by starting and ending points of a bead position

in the projected image (**Figure 3.7**). With the CCD aligned to the axis of the laser line, and the scan direction relative to the CCD determined, a minor adjustment can be made to the line and CCD (if necessary) to correct any angle in the line relative to the scan direction (the latter taking precedent over the former since the scan direction has previously been determined relative to the optics table and the other components).

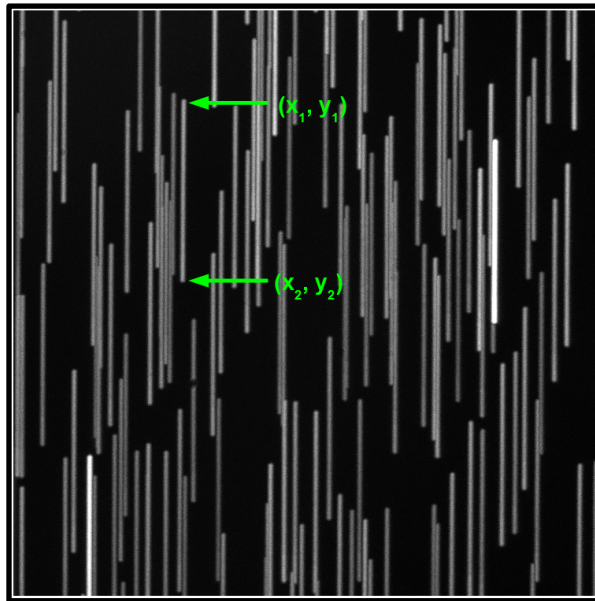


Figure 3.7: Maximum projection of a widefield scan of low-density fluorescent beads on a glass cover slip. Each line segment here is the series projection of a single fluorescent bead as the sample is scanned. The brighter lines are likely small clusters of two or more beads. The scan angle is verified using several of these lines at different parts of the field of view.

### **3.4 Wavelength Dependence on Localization (Spectrometer Alignment)**

Ideally, there should be no wavelength dependence on the position found for a given emitter. For example, if two fluorescent dye molecules or nanocrystals with different emission spectra have formed a dimer, with perhaps less than a few nanometers distance between them, it should be possible in post processing to localize them in each frame (and track them in a series) to within tens of nanometers, which would result in such dimers appearing to be co-localized. If, on the other hand, there were some wavelength dependence to the localized positions, then the emitters would appear to have some distance between them. If there is any systematic error introduced in the form of a wavelength dependent shift in position, this should be measured and corrected in post processing.



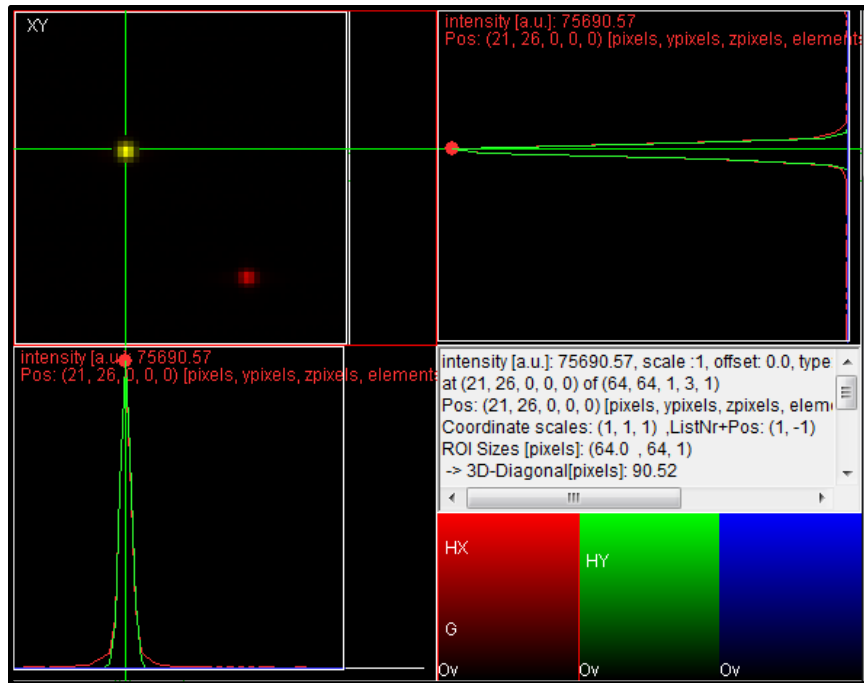


Figure 3.8: Hyperspectral image of a low-density sample of 100 nm TetraSpeck beads. The upper left quadrant shows the image (summed over the spectral dimension). The upper right and lower left quadrants are used to estimate the pixel location of each bead that is subsequently localized using different spectral regions of the emission light.

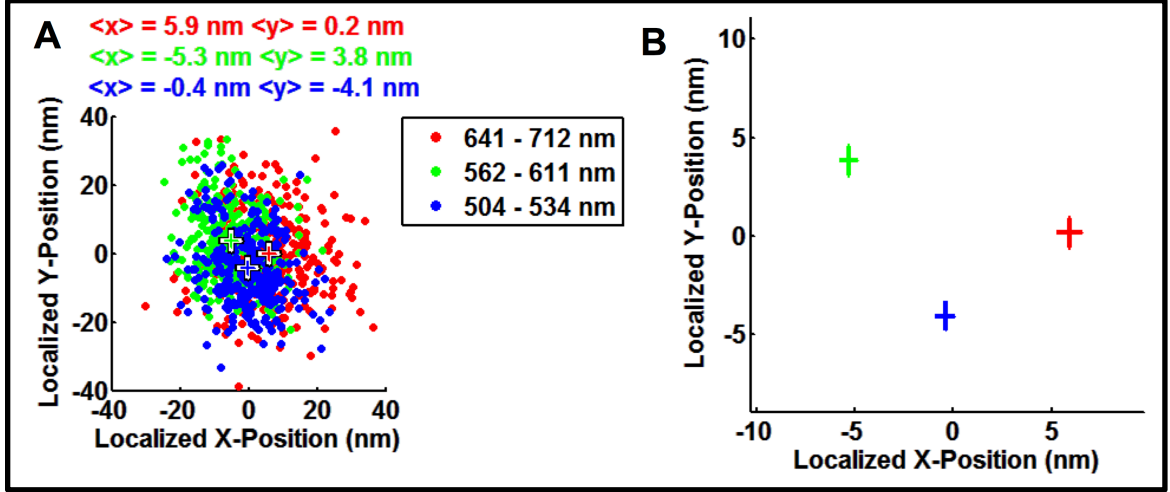


Figure 3.9: Wavelength dependence on localization. Scatter plot of 300 localizations of a single 100 nm TetraSpeck bead on glass using three different wavelength ranges. The purpose here is to quantify any chromatic dependence on particle localization. Emitters were 100 nm Tetraspeck beads diluted 2000:1 in 1x PBS and allowed to stick to a glass cover slip. The sample was then scanned 300 times and localizations were obtained for each scan using emitted light from each of three different wavelength ranges. The mean of the localized x-positions varied by  $\sim 10$  nm and the mean of the localized y-positions varied by  $\sim 8$  nm. (A) Scatter plot of localizations with the mean identified by '+' and listed at the top of the figure. (B) Error bars indicating the standard error of the mean.

### 3.5 4D Point Spread Function

The theoretical point spread function derivation has been performed by Sheng Liu at UNM, and is included in a manuscript currently in review, [1].

In the HSM, the excitation path is the same as a line scanning confocal microscope. On the sample plane, assuming that a single fluorophore is at point  $(0,0,z)$ , the excitation laser line is along the y-axis at position  $x$ . The excitation field at the fluorophore is

$$U_{\text{ex}}(0 - x, z).$$

We use  $U$  for magnitude point spread function, and  $PSF$  for intensity point spread function.  $U_{\text{ex}}$  is a line spread function, assuming the intensity along y-axis is uniform. In

the emission path, after light passes through the slit, the emission field at slit will be dispersed along  $x$ -axis by spectrometer at the image plane. The field at image plane is generated by shifting the slit field along the  $x$ -axis (spectral dimension) and multiplying each shifted field by the spectral function at the corresponding wavelength. We define the spectral function as  $SP(x_\lambda)$ , which depends on the spectrum of the sample. The field at position  $(x_\lambda, y)$  on image plane is

$$\int_l U_{\text{em}}(x - \xi, y, z) L(\xi) SP(x_\lambda + \xi) d\xi.$$

$U_{\text{em}}(x, y, z)$  is the wide field emission point spread function, and  $L(x)$  is the slit shape function along  $x$  axis, which is a rectangular function with the width equal to the slit width  $l$ . The above expression is the convolution of  $U_{\text{em}}(x, y, z)$  with  $L(x)SP(x_\lambda)$ . Combining the excitation and emission fields gives the magnitude point spread function of the HSM

$$U_{\text{HSM}}(x, y, z, x_\lambda) = U_{\text{ex}}(-x, z) \int_l U_{\text{em}}(x - \xi, y, z) L(\xi) SP(x_\lambda + \xi) d\xi.$$

$U_{\text{ex}}(-x, z)$  is the wide field excitation line spread function.  $U_{\text{HSM}}$  is a 4D point spread function, with spatial dimension  $x, y, z$ , and spectral dimension  $x_\lambda$ . The intensity point spread function is

$$PSF_{\text{HSM}} = |U_{\text{HSM}}|^2.$$

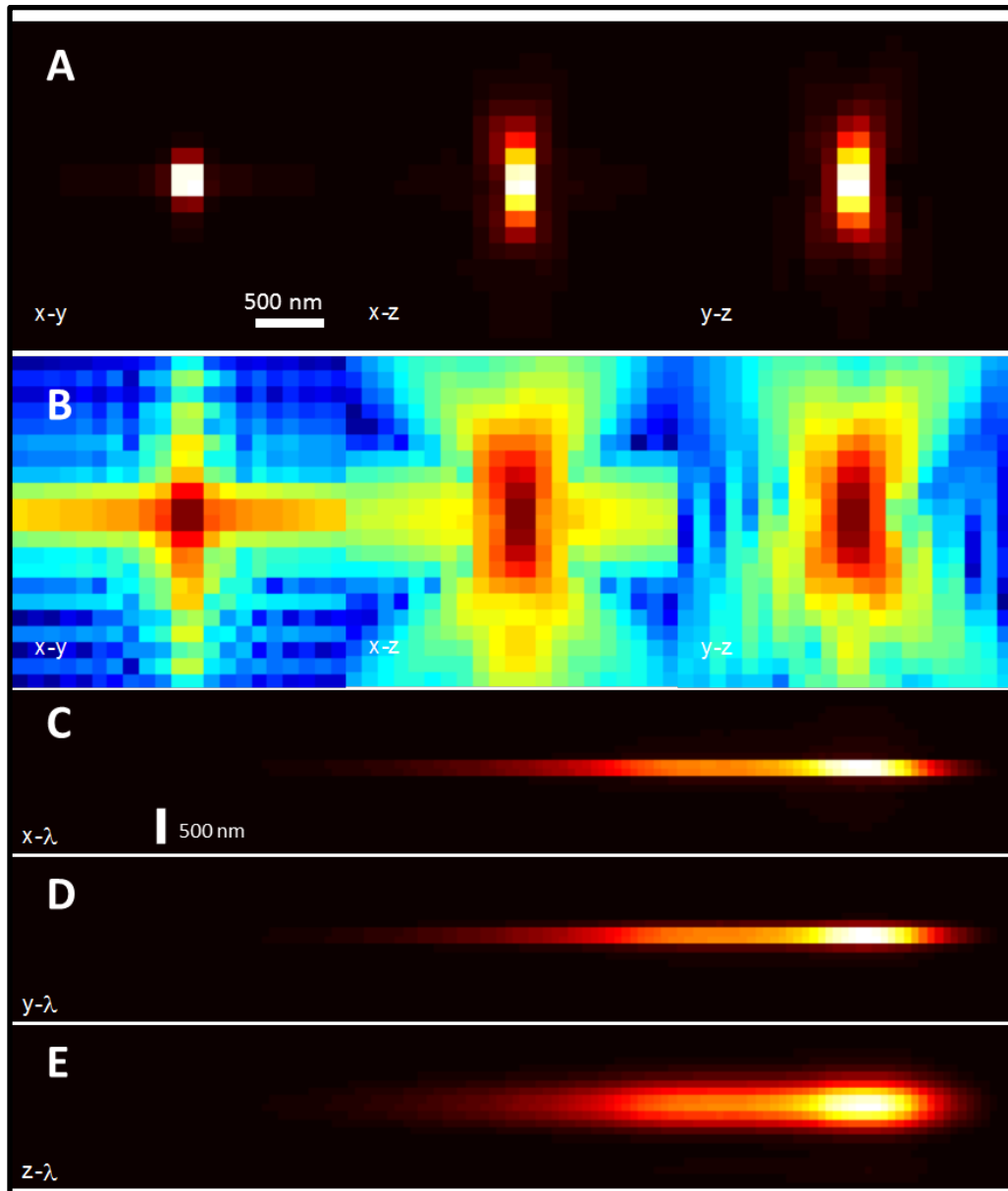
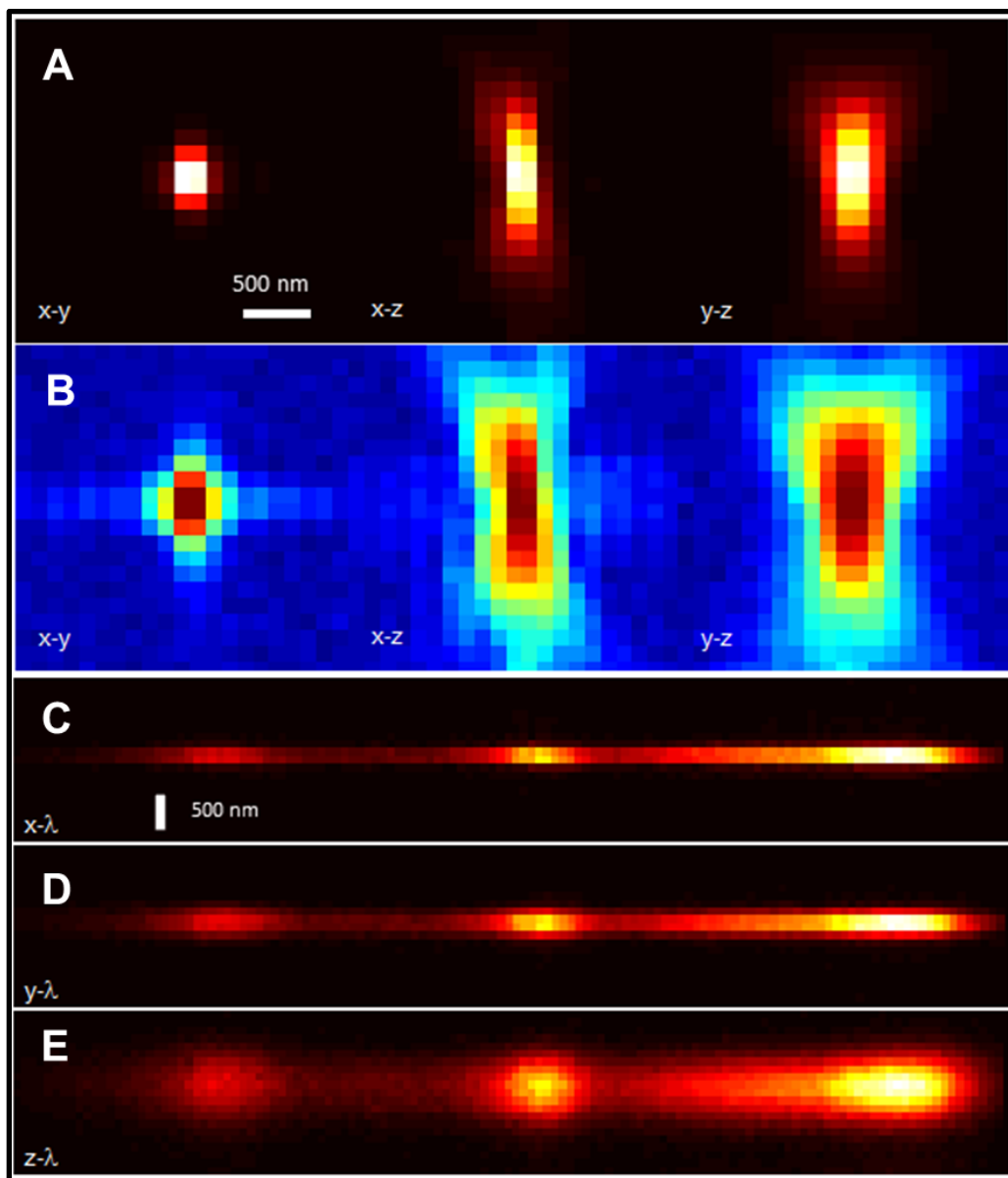


**Figure 3.10: Theoretical 4D PSF.** The 4D PSF is calculated from the theory as described in the text. The spectra and widefield point spread function are based on 100 nm yellow beads. The simulation includes aberrations generated from the phase retrieval process. A linear stretch (A) and log stretch (B) of intensity for projections on the  $x$ - $y$ ,  $x$ - $z$ , and  $y$ - $z$  planes are shown along with the  $x$ ,  $y$ , and  $z$  vs. wavelength projections (C, D, and E).

**Figure 3.11** shows the measured 4D  $(x, y, z, \lambda)$  microscope point spread function (PSF) that seems to be in good agreement with that expected for a diffraction limited system.



### 3.6 Spectral Calibration

Spectral calibration was performed using a spectral calibration lamp (MIDL® Wavelength Calibration Lamp) and the 543 nm and 633 nm lines from HeNe lasers. There is no observable curvature in the spectral lines with respect to the spatial axis (**Figure 3.12**). While the normal slit width used during hyperspectral imaging is 100  $\mu\text{m}$ , the initial characterization shown here was performed using a 20  $\mu\text{m}$  wide slit to more accurately check for distortion. The calibration lamp was placed on the microscope sample stage and imaged (without scanning) using an air objective and camera exposure times that were set to be long enough to provide good fits to the emission peaks (typically 0.01 – 0.05 sec). Using the most distinguished emission peaks, a polynomial fit was used to calibrate the spectrometer.

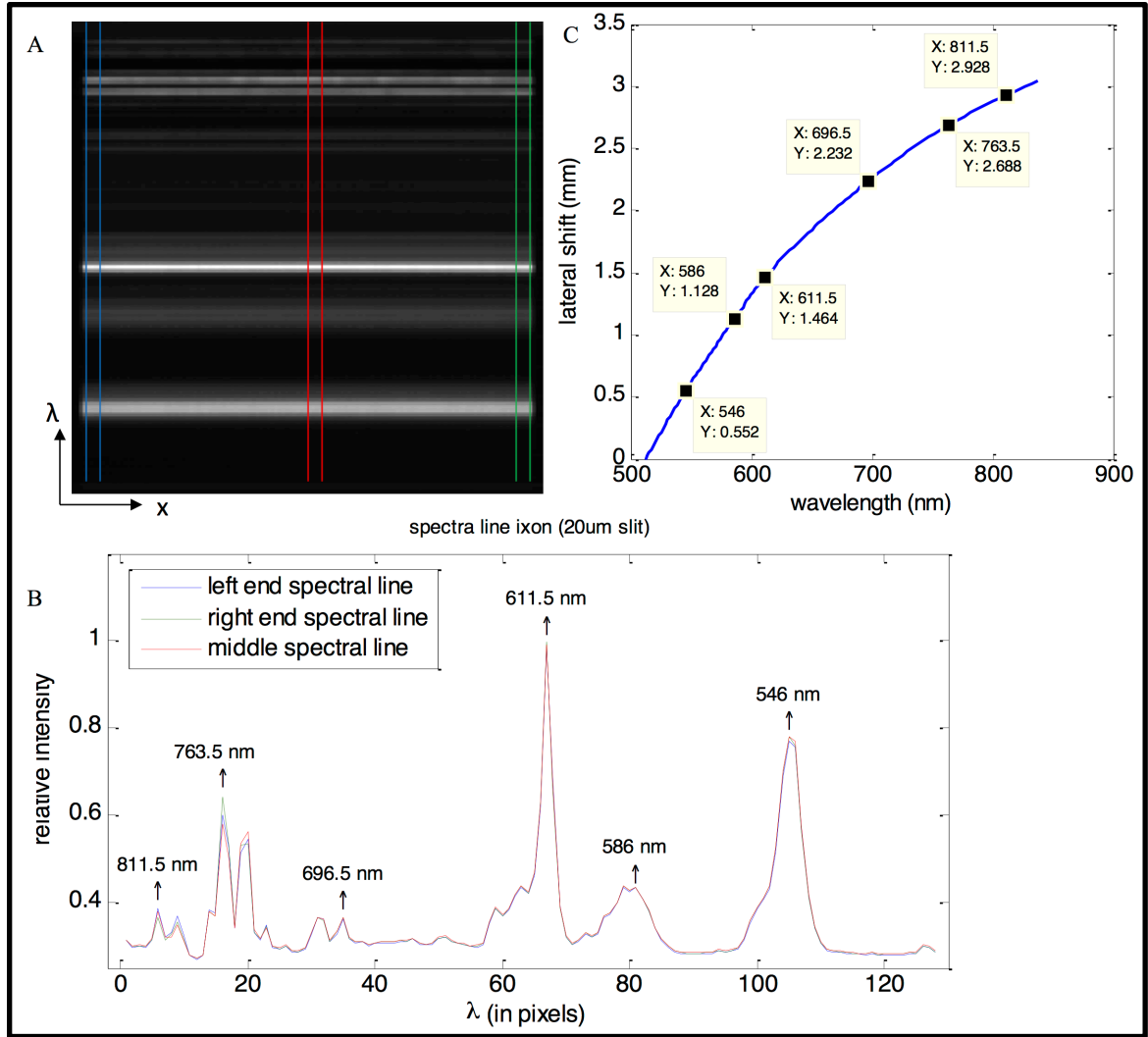


**Figure 3.12: Spectral calibration.** (A) Image of the calibration lamp on the camera (the vertical axis is the spectral dimension). The calibration lamp is a LightForm multi-ion discharge lamp (MIDL), the slit width is 20  $\mu\text{m}$ , and the camera is an Andor iXon 860 EMCCD with an array size of 128 $\times$ 128, pixel size 24  $\mu\text{m}$ . (B) Spectral curve, generated by the sum projection of (A) along the  $x$  dimension; the peak wavelengths are identified from the specification sheet of the calibration lamp. The blue, green, and red lines correspond to the regions in (A) with the same color. All three colored lines almost overlap with each other, which demonstrates a very small distortion in the spectral lines. (C) Dispersion curve, generated from the spectral curve (C), by polynomial fit of specific wavelengths.

### 3.7 Spectral Distortion and Dispersion

Using optical design software, the theoretical distortion and dispersion are plotted in **Figure 3.13**. The dispersion curve is very similar to that measured (shown above in

**Figure 3.12).** The distortion plot is also in agreement with the measured value, where it is worth noting that the units on the vertical axis in **Figure 3.13A** are in  $\mu\text{m}$ , so this results in no observable distortion since each pixel is  $24 \times 24 \mu\text{m}$ , and the total shift is less than one  $\mu\text{m}$ .



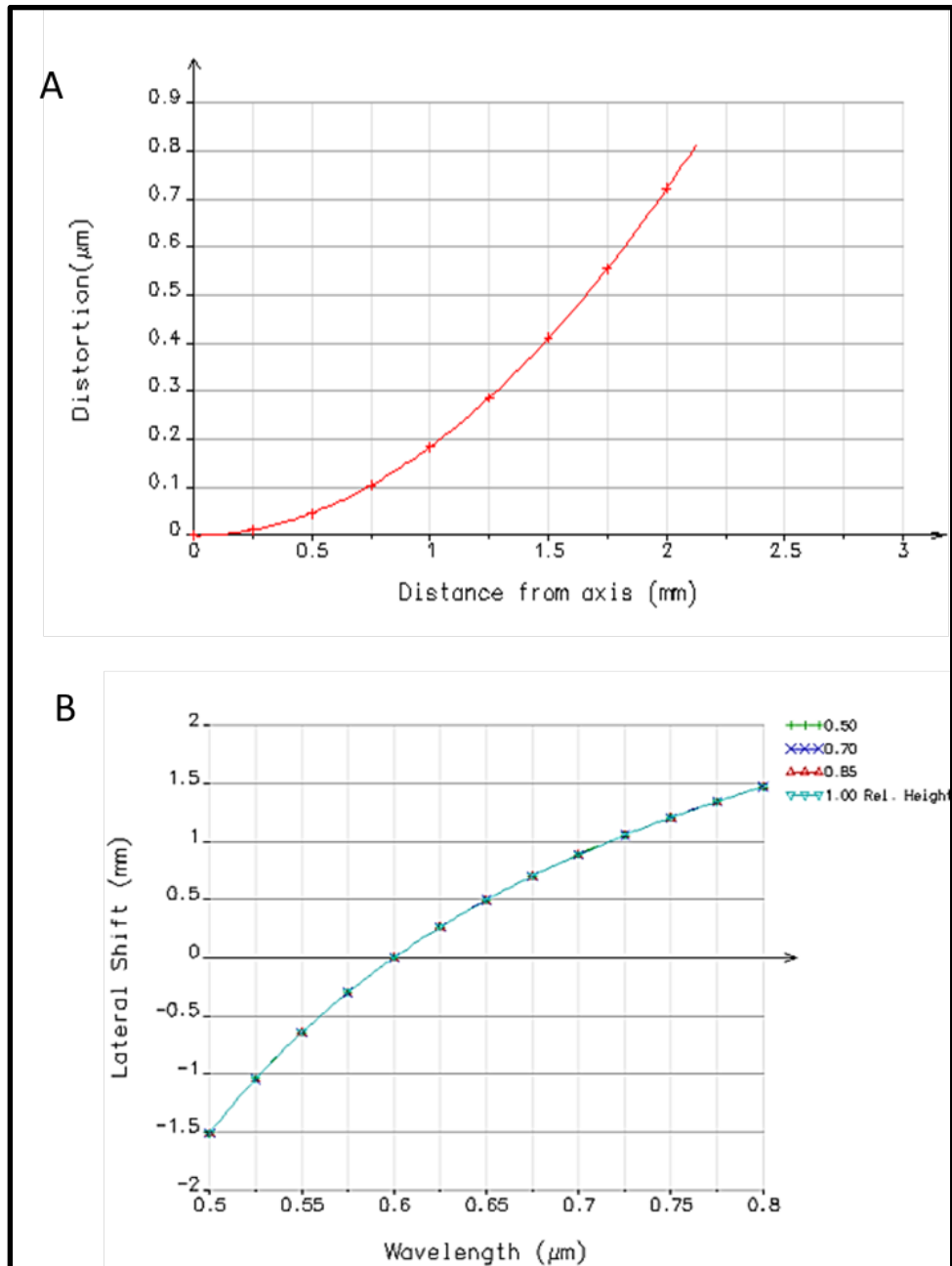
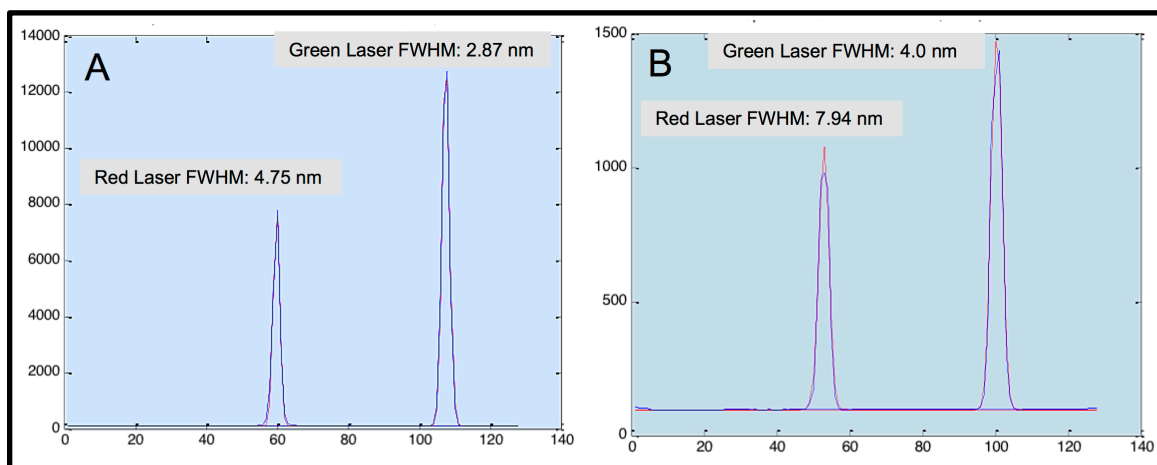


Figure 3.13: Spectral distortion and dispersion. The distortion and dispersion curves are generated from OSLO. (A) Distortion shows offset of the true image position from the ideal image position at various off axis points. In the HSM setup, the maximum distance from the axis is 1.5 mm, so the designed maximum distortion is  $0.4 \mu\text{m}$ , which is less than 2% of CCD pixel size ( $24 \mu\text{m}$ ). (B) Lateral shift shows the dispersion, designed to span a total of 3 mm from 500 nm to 800 nm. It shows dispersions in four relative heights (distance from the optical axis), the four curves are right on top of each other, so the spectral lines are straight, which also indicates a minimal distortion.

### 3.8 Spectral Resolution

The spectral resolution was measured using the red and green HeNe laser emissions (633 and 543 nm respectively) by directing the diverging light from a single mode fiber tip into the microscope objective (without collimation), which keeps the intensity low enough to avoid saturating the EMCCD. The results are shown in **Figure 3.14**. The full width at half max (FWHM) is measured by the intensity pattern on the EMCCD pixels, which are converted to a length (using the pixel size of 24  $\mu\text{m}$ ), and then into the corresponding wavelength range using the spectral dispersion curve. The FWHM is found at each wavelength using both the 20 and 100  $\mu\text{m}$  slits.



**Figure 3.14: Spectral resolution. (A) Using the 20  $\mu\text{m}$  slit. (B) Using the 100  $\mu\text{m}$  slit.**

While this only provides specific values at two wavelengths, a qualitative verification can be made that the resolution is sufficient for this system by looking at the emission spectra of all eight species of quantum dots and noting that the emission peaks are narrow enough as measured to allow individual fitting (see **Chapter 4** and **Appendix D**).

### 3.9 EMCCD Gain Calibration

The EM gain calibration is required in order to determine the number of photoelectrons captured in a given pixel from the counts that are read out by the camera after the gain registers. The important parameters that have an effect on this are the temperature, preamp gain, and EM gain, so it is important to use the same settings for these as in the intended experiment, and that the EMCCD had cooled and stabilized. The method used to perform the gain calibration is from van Vliet, et al [2]. The procedure involves taking a background image, and then a gain calibration image, where there is a smooth distribution of light intensity from bright to dark. An example is shown in **Figure 3.15**. *Cal\_readnoise.m* is a Matlab dipimage function that calculates the gain value, read noise, background variance, and mean background using the background image set and this image of distributed intensities.

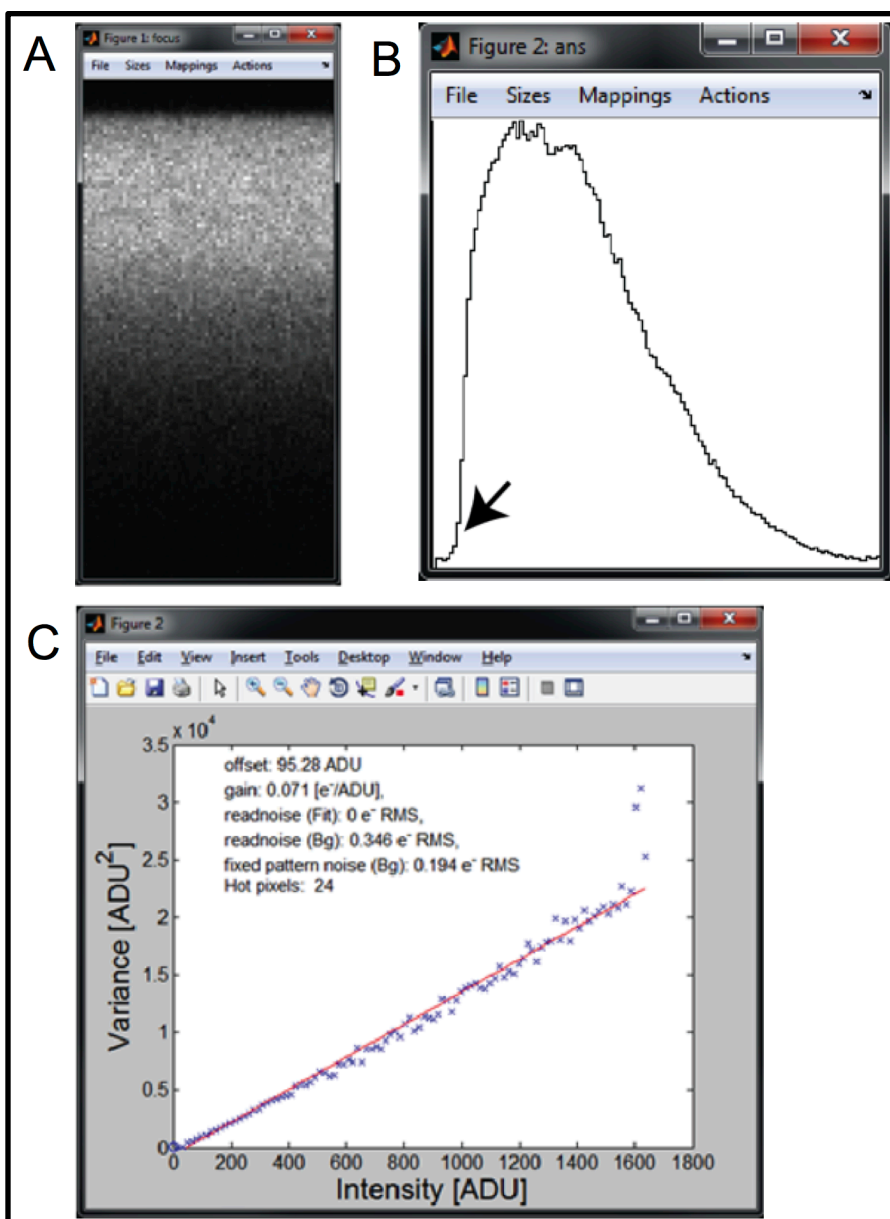


Figure 3.15: EMCCD gain calibration. (A) Emission light from green fluorescent reference slide (Chroma Technology Corporation). (B) The sum projection over the horizontal dimension of the image in (A). The 488 long-pass filter has a sharp cutoff at 500 nm that leaves several dark rows that are used in the baseline correction. (C) Example plot of the variance of counts<sup>2</sup> vs. counts and the fit used to determine the gain (=1/slope of the line in photoelectrons/ADU).

## **3.10 EMCCD Camera Background and Baseline Correction**

Internal camera background noise, whatever the sources may be, can be removed in post processing. Before each hyperspectral scan series is initiated, a sequence of exposures (a default of 1000 frames) is acquired with the shutter closed, using the chosen scan parameters that will be used in the actual imaging (ROI, binning, horizontal and vertical shift speeds, vertical shift voltage, preamp gain, frame transfer mode, baseline clamp, exposure time, and EM gain). The mean value for each pixel is found for the background series and may be later subtracted from acquired data.

Baseline correction is intended to fix an overall level offset for each camera frame. The EMCCD camera used here (Andor iXon 860) is designed to maintain a consistent frame level by using a built-in feature known as the baseline clamp, but while this reduces the offset, it does not eliminate it entirely. The baseline correction is performed on each frame in post processing, where several rows of intentionally dark pixels are used in the correction. The dark pixel rows are created by arrangement of the camera position in the spectral dimension such that it extends into the region blocked by the long-pass filter (at ~500 nm).

## **3.11 Transmission Efficiency**

The transmission efficiency is the ratio of total light power that is transmitted through a given system compared to that of the incident light. Losses are caused by reflections at element surfaces as well as scattering and/or absorption within element material, and the

degree of loss often has a significant dependence on the wavelength, and sometimes on the polarization of the light. To mitigate losses due to reflection, lenses are treated with anti-reflective coatings that are designed for specific wavelengths (such as the 488 nm excitation source) or spectral ranges (such as the visible and near infrared spectrum used in the emission path of this system design). Optical filters, such as the dichroic mirror and long-pass filter, have been chosen specifically for high transmission efficiency in the spectral range of the expected quantum dot emissions (from 500 to 800 nm).

In order to measure the transmission efficiency of the emission path, the collimated alignment laser is mounted to the objective turret via RMS to SM1 adapter, without going through the objective lens, and the transmitted light is measured with a power meter at various points along the emission path. The free space laser beam used for alignment has a  $1/e^2$  beam diameter of about 2 mm, so even if the objective would accept the full beam, the diameter would be magnified over 200 times, far exceeding the aperture of any part of the emission path. Focusing the light into the objective would require another objective positioned such that the two are exactly centered and in perfect focus. Instead, the measurements are made without the objective, and the efficiency of the objective (Olympus UPLSAPO60XW) is assumed to be that quoted by the manufacturer (see **Figure 3.16**). The overall transmission efficiency found here without the objective would then need to be scaled by the appropriate value from the plot (~90% at 543 nm).

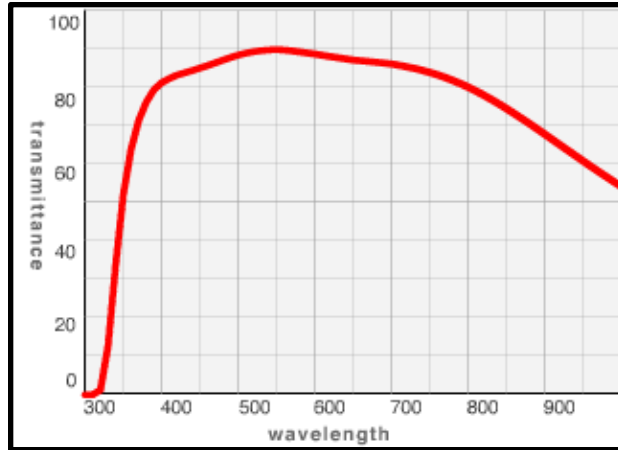


Figure 3.16: Transmission efficiency vs. wavelength for the objective lens. This plot is directly from the Olympus website: [http://www.olympusamerica.com/seg\\_section/img/uis2/graphs/uplsapo\\_60xw\\_graph.gif](http://www.olympusamerica.com/seg_section/img/uis2/graphs/uplsapo_60xw_graph.gif)

The laser power was measured with a power meter (Thorlabs PM100D with S121C silicon photodiode sensor, 400-1100 nm, 500 nW - 500 mW, 10 nW resolution, +/- 3% measurement uncertainty), which was configured for the laser wavelength of 543 nm. To allow for fluctuations in laser power and sensor uncertainty, the detector was held in position for several seconds and an average reading over the interval was estimated. This procedure was repeated several times and the results were averaged to obtain the values for power measurements and transmission efficiencies shown in **Table 3.1**. The laser power of the collimated free space beam (out of the fiber), just before the objective was about 175  $\mu$ W.

Position of the Measurement	Power (μW)	Relative to the Original Beam	Relative Efficiency
1) Free Space Beam at Objective Port	175	100%	N/A
2) Between L2 and Scanning Mirror	156	89%	89%
3) Between Scanning Mirror and Dichroic	155	89%	99.3%
4) After Dichroic, Long Pass, and L3	140	80%	90.3%
5) After Prism, Before Spherical Mirror	136.33	78%	97.4%
6) At the EMCCD Camera	131.33	75%	96.3%

**Table 3.1: Transmission efficiency of emission path.**

The overall excitation path transmission efficiency was calculated using the 488 nm laser power measurements taken directly out of the fiber (collimated by the 40× air objective) and directly out of the 60× water objective in the microscope base. This was done at several different laser powers set by the AOM control via the graphical interface (HSMDAQ). The measured power at 5, 10, 15, and 20% of the full laser power was measured to be 0.287, 0.574, 0.861, and 1.147 mW respectively in the collimated free-space beam, before the excitation optics, and 0.095, 0.189, 0.287, and 0.382 mW respectively out of the water objective, after all excitation optics. This indicates that the overall excitation path has a transmission efficiency of 33%. Due to spatial constraints imposed by some of the mounting hardware it is difficult to measure the power at several of the positions to determine the losses of some of the individual elements. The combination of the laser line generator lens and CLY1 produce obvious artifacts that likely contribute the majority of the power loss. Using a lower fan angle along with a longer focal length cylindrical lens may mitigate the issue by reducing the sensitivity to imperfections on the surface of the cylindrical lens that collimates the laser line. These components have been acquired and mounted, but not yet implemented at the time of this



writing. Importantly, even with the lower than expected transmission ratio on the excitation path, more than enough laser power is ultimately delivered to the sample for imaging, to the point where neutral density filters are required under most experimental observations.

### 3.12 Objective Aperture Acceptance Ratio

The numerical aperture of the objective lens will determine the number of photons that are captured and ultimately observed with the camera. If one assumes that a fluorophore emits uniformly in all directions, then the ratio of photons accepted by the objective is just that of the solid angle ( $\Omega$ ) defined by the aperture divided by the full  $4\pi$  steradians.

**Figure 3.17** displays the geometry used in this calculation.

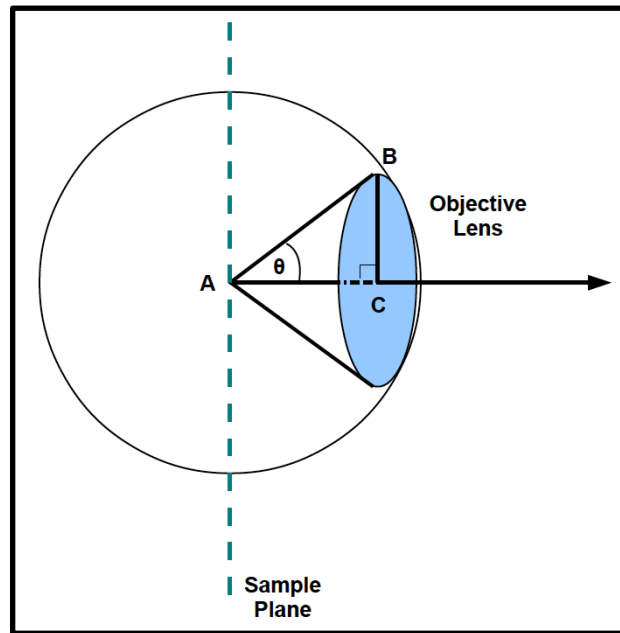


**Figure 3.17:** Objective aperture acceptance ratio. In this drawing, the objective lens is represented by the blue region, intended to be a circular area on the surface of a sphere of radius  $AB$ . For this case the  $z$ -axis is horizontal (along the optical axis of the objective). The angle  $\theta$  is determined using the numerical aperture of the objective. The solid angle of acceptance is that of a conic volume defined by rotating triangle  $ABC$  about the  $z$ -axis.

An element of solid angle is

$$d\Omega = \sin \theta \, d\theta \, d\varphi$$

Integrating this yields the solid angle:

$$\Omega = \int d\Omega = \int_0^\theta \int_0^{2\pi} \sin \theta' \, d\theta' \, d\varphi = 2\pi[1 - \cos \theta]$$

And so the ratio of accepted photons is this partial solid angle over the full solid angle:

$$\text{Acceptance Ratio} = \frac{\Omega}{4\pi} = \frac{[1 - \cos \theta]}{2}$$

The numerical aperture of the objective is:

$$NA = n \sin \theta$$

The objective used at the time of this writing is a water immersion objective ( $n = 1.33$ ) with  $NA = 1.2$ , which implies that  $\theta = 64.5^\circ$ , yielding an acceptance ratio of 0.2844. This indicates that at most, 28.44% of the light emitted (uniformly in all directions) by a fluorophore will be captured by the objective lens.

### 3.13 EMCCD Quantum Efficiency

**Figure 3.18** shows the quantum efficiency of the EMCCD vs. wavelength, as quoted by the manufacturer. It is important to note that while this QE is true, the signal to noise

ratio for EMCCD cameras with the gain enabled, induces a noise factor of  $\sim\sqrt{2}$  from the impact ionizations in the gain registers [3], where there is a statistical fluctuation in the overall number of electrons from a given starting number of photoelectrons, and this multiplicative noise scales down the effective QE about by a factor of  $\sim 2$ .

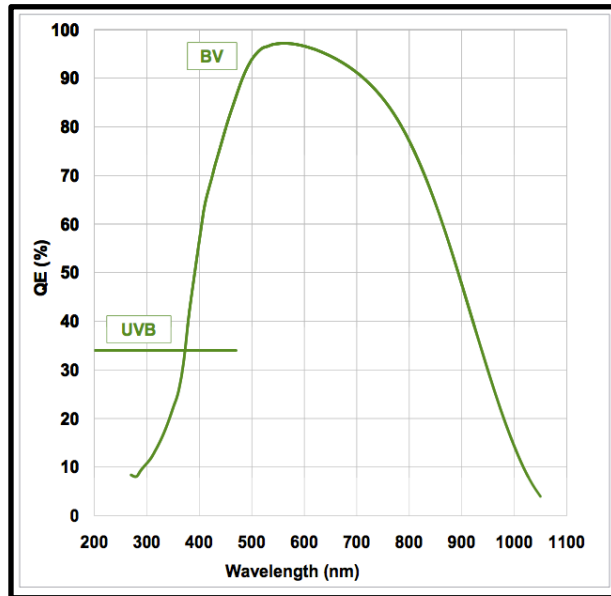


Figure 3.18: EMCCD Quantum efficiency. <http://www.andor.com/scientific-cameras/ixon-emccd-camera-series/ixon3-860>

## References

1. Malik MD, Cutler PJ, Liu S, Byars JM, Lidke DS, et al. (2013) Multi-color Quantum Dot Tracking using a High-Speed Hyperspectral Line-Scanning Microscope. Manuscript in review.
2. Van Vliet LJ, Sudar D, Young IT (1998) Digital fluorescence imaging using cooled charge-coupled device array cameras. In: Celis JE, editor. Cell Biology. A laboratory handbook. Academic Press, Vol. III. pp. 109–120.

3. Robbins MS, Member S, Hadwen BJ (2003) The Noise Performance of Electron Multiplying Charge-Coupled Devices. IEEE Transactions on Electron Devices 50: 1227–1232.

## Chapter 4

### Quantum Dot Characterization

The hyperspectral microscope described in this manuscript is capable of using just about any variety of fluorescent probes that are excited with 488 nm light, but quantum dots have narrow emission spectra which allows individual emitter localizations and tracking at high density, and they are more resilient to photobleaching, making them the preferred probe type to be used in this system for studying protein interactions in live cells. However, quantum dots have some other complicated characteristics that arise from some lesser-known aspects of their electronic structure and kinetics. This chapter attempts to characterize and model several traits of the quantum dots that are important in the context of single protein molecule localizations and tracking in live cells using this microscope system.

#### 4.1 Calculation of Quantum Dot Excitation Cross-Sections

The overall emission rate ( $R$ ) of a given fluorophore is often useful to know for many aspects of system design and expected experimental observations (e.g. the achievable localization accuracy for a given fluorophore within a given time frame depends on the number of photons detected at the sensor [1]). This overall emission rate depends on the intensity of the excitation light ( $I$ ) and on the excitation cross-section of the fluorophore ( $\sigma$ ). Without considering any effect of excited state lifetime (i.e. if the excited state lifetime is taken to be zero, or if the excitation intensity is very low), the emission rate  $R$

(photons  $\cdot$  sec<sup>-1</sup>) =  $I$  (photons  $\cdot$  sec<sup>-1</sup>  $\cdot$  cm<sup>-2</sup>)  $\sigma$  (cm<sup>2</sup>). Fluorophore manufacturers often provide extinction coefficients (also known as molar absorptivity; units are M<sup>-1</sup> cm<sup>-1</sup>) for some of the common excitation laser wavelengths. In order to obtain the individual emitter cross-section, one can use the Beer-Lambert Law [2]. The assumptions needed for validity of the Beer-Lambert Law are (1) that the individual absorbers act independently, (2) the absorbing medium is homogeneous, (3) the medium doesn't elastically scatter photons such that power is radiated away from the propagation direction without being absorbed, (4) the incident beam is collimated and normal to the surfaces of the volume containing the absorbing medium, (5) the incident beam is monochromatic, and (6) the light is not invasive to the medium such that the absorption characteristic is changed by the light itself. Considering a medium of absorbers in a volume that has a thickness  $l$  (cm), extinction coefficient  $\epsilon$  (M<sup>-1</sup> cm<sup>-1</sup>), concentration of absorbers  $c$  (moles L<sup>-1</sup>), absorption cross-section  $\sigma$  (cm<sup>2</sup>), and volume density of absorbers  $N$  (cm<sup>-3</sup>), the transmissivity is

$$T = \frac{I_1}{I_0} = 10^{-\epsilon lc} = e^{-\sigma lN}$$

$$N = \frac{c (\text{moles} \cdot \text{L}^{-1})(6.02 \times 10^{23} \text{ absorbers} \cdot \text{moles}^{-1})}{1000 \text{ cm}^3 \text{ L}^{-1}}$$

$$= c (6.02 \times 10^{20}) \text{ absorbers} \cdot \text{cm}^{-3}$$

$$T = 10^{-\epsilon lc} = e^{-\sigma lN}$$

Taking the natural logarithm of both sides,

$$\ln(10^{-\epsilon lc}) = -\sigma lN$$

Noting that  $10^x = \exp[x \ln(10)]$ ,

$$\ln(10^{-\varepsilon lc}) = \ln[e^{-\varepsilon lc \ln 10}] = -\varepsilon lc \ln 10$$

Which then gives the relation between absorption (excitation) cross-section and extinction coefficient (molar absorptivity):

$$\sigma = \frac{-\varepsilon lc \ln 10}{-l N} = \frac{\varepsilon \ln 10}{6.02 \times 10^{20}} \text{ (cm}^2\text{)}$$

The units were chosen here for the convenience in calculation, since excitation beam intensities are commonly specified in  $\text{W cm}^{-2}$ . **Table 4.1** lists the extinction coefficients and the corresponding excitation cross-sections for the eight varieties of quantum dots available from Invitrogen Corporation as of this writing. It is important to note that the actual fluorescence emission rate (observed in the spectrum of the excited state primary decay channel) depends on the rate of that specific transition, and there may be non-radiative decays, or those that do not fall within the spectrum of the fluorescence emission. Because of the non-fluorescent decay channels, the extinction coefficient (or the cross-section) alone is not sufficient to accurately estimate the emission rate.

Quantum Dot	Extinction Coefficient ( $\text{cm}^{-1} \text{ M}^{-1}$ ) for $\lambda = 488 \text{ nm}$	Cross-Section ( $\text{cm}^2$ )
525	130000	4.97E-16
565	290000	1.11E-15
585	530000	2.03E-15
605	1100000	4.21E-15
625	2700000	1.03E-14
655	2900000	1.11E-14
705	3000000	1.15E-14
800	3000000	1.15E-15

Table 4.1: Quantum dot cross-sections for an excitation source wavelength of 488 nm.

## 4.2 Emission Rates and Saturation Effects

Fluorescent molecules or nano-particles have excited state mean lifetimes that are typically on the order of nanoseconds or tens of nanoseconds. With sufficiently large excitation intensity these fluorophores will spend almost all of the time in the excited state (i.e. once they drop to the ground state they are immediately excited again due to the high excitation intensity). While in this excited state, the probes cannot be excited further with light of the same wavelength (at least not in a way that yields the same emission spectrum for the given emitter). It is sometimes useful to know where this saturation regime is for a given probe in order to apply the appropriate power to the excitation beam, providing enough light but not exceeding the saturation level, which would only add unnecessary background from auto-fluorescence in the sample. Also, one may wish to intentionally supply a saturation level intensity for some reason, such as for adding structure to the emission profile as the beam traverses the probe, and this more structured emission could result in better fluorophore localization [3]. For these, and possibly other reasons, a basic calculation is made here to determine the emission rate of a fluorophore (in photons/sec) for a given excited state mean lifetime, cross-section, and excitation beam intensity. In the limit of total saturation, one would expect the emission rate to be the inverse of the mean excited state lifetime. The following is a model of emission rates from a population of simple two-state systems.



Consider a population of fluorophores that are exposed to an excitation beam of some intensity,  $I$ . The total population ( $N$ ) will consist of the sum of the number in the ground state ( $N_1$ ) and the number in the excited state ( $N_2$ ).

$$N = N_1 + N_2$$

The change in the number of fluorophores that are in the excited state per unit time is equal to the rate of those that are excited minus those that emit a photon and drop back to the ground state:

$$\frac{dN_2}{dt} = (I\sigma N_1) - \left(\frac{N_2}{\tau}\right)$$

Here, the intensity ( $I$ ) is in units of photons/(sec  $\cdot$  cm<sup>2</sup>), the absorption cross-section ( $\sigma$ ) is in units of cm<sup>2</sup>, and the mean lifetime ( $\tau$ ) is in units of seconds. Substituting for  $N_1$  and collecting constant terms,

$$\begin{aligned}\frac{dN_2}{dt} &= I\sigma(N - N_2) - \left(\frac{N_2}{\tau}\right) \\ &= I\sigma N - I\sigma N_2 - \left(\frac{N_2}{\tau}\right) \\ &= I\sigma N - \left(\frac{1}{\tau} + I\sigma\right) N_2\end{aligned}$$

To clean things up a bit, let  $\alpha = (1/\tau + I\sigma)$ , and then take the second derivative to eliminate the time-independent term:

$$\frac{dN_2}{dt} = I\sigma N - \alpha N_2$$

$$\frac{dN_2}{dt} + \alpha N_2 = I\sigma N$$

$$\frac{d(N_2 e^{\alpha t})}{dt} = I\sigma N e^{\alpha t}$$

$$N_2 e^{\alpha t} - N_2(0) = \frac{I\sigma N}{\alpha} (e^{\alpha t} - 1)$$

$$N_2 = \frac{I\sigma N}{\alpha} (1 - e^{-\alpha t}) + N_2(0) e^{-\alpha t}$$

$$N_2 = \frac{I\sigma N}{\alpha} - \left[ \frac{I\sigma N}{\alpha} - N_2(0) \right] e^{-\alpha t}$$

Finally, replacing  $\alpha$  with  $(1/\tau + I\sigma)$ :

$$N_2 = \frac{I\sigma N}{\left(\frac{1}{\tau} + I\sigma\right)} - \left[ \frac{I\sigma N}{\left(\frac{1}{\tau} + I\sigma\right)} - (N_2)_{t=0} \right] \exp \left[ - \left( \frac{1}{\tau} + I\sigma \right) t \right]$$

The total emission rate (for the whole population of emitters) is then given by

$$\begin{aligned} E &= \frac{N_2}{\tau} \\ &= \frac{I\sigma N}{(1 + I\sigma\tau)} - \left[ \frac{I\sigma N}{(1 + I\sigma\tau)} - \frac{(N_2)_{t=0}}{\tau} \right] \exp \left[ - \left( \frac{1}{\tau} + I\sigma \right) t \right] \end{aligned}$$

A single fluorophore will then have an emission rate

$$R = \frac{E}{N} = \frac{I\sigma}{(1 + I\sigma\tau)} - \left[ \frac{I\sigma}{(1 + I\sigma\tau)} - \frac{(N_2)_{t=0}}{N\tau} \right] \exp \left[ - \left( \frac{1}{\tau} + I\sigma \right) t \right]$$

In the case where  $t \gg \tau$ , as would be the case for a constant excitation beam or for durations of typical exposure times of most cameras used in fluorescence microscopy, the exponential term goes to zero. This simplifies the emission rate to:

$$R = \frac{I\sigma}{(1 + I\sigma\tau)}$$

In the limit where the intensity is very large (i.e. saturation of the excited state), this simplifies to an emission rate of  $1/\tau$ , as expected.

As an example, consider a case where there is a 50 mW laser with a wavelength of 488 nm that is made into a line on the sample plane that is  $0.250 \times 10 \mu\text{m}$  in size (assuming a rectangular profile for simplicity), and that we have fluorophores with a cross-section of  $\sigma = 4.97 \times 10^{-16} \text{ cm}^2$  and a mean excited state lifetime of  $\tau = 20 \text{ ns} = 2 \times 10^{-8} \text{ sec}$ , then

$$\begin{aligned} E_{\text{photon}} &= \frac{hc}{\lambda} \\ &= \frac{(6.626 \times 10^{-34} \text{ J} \cdot \text{sec})(3 \times 10^8 \text{ m/sec})}{488 \times 10^{-9} \text{ m}} \\ &= 4.0705 \times 10^{-19} \text{ J} \end{aligned}$$

The area of the line on the sample is

$$A = (0.25 \times 10^{-4} \text{ cm})(10 \times 10^{-4} \text{ cm}) = 2.5 \times 10^{-8} \text{ cm}^2$$

The profile of the laser line on the sample plane is actually Gaussian along the x-axis, but for this calculation a much simpler estimate is used, where the line is approximated as a rectangular region with diffraction limited width. So the intensity of the laser line is then

$$\begin{aligned}
I &= \frac{50 \times 10^{-3} W}{2.5 \times 10^{-8} cm^2} \\
&= 2 \times 10^6 W/cm^2 \\
&= (2 \times 10^6 Jcm^{-2} sec^{-1}) \left( \frac{1 photon}{4.0705 \times 10^{-19} J} \right) \\
&= 4.913 \times 10^{24} photons \cdot cm^{-2} \cdot sec^{-1}
\end{aligned}$$

Which then gives an individual fluorophore emission rate that is

$$R = \frac{(4.913 \times 10^{24} photons \cdot cm^{-2} \cdot sec^{-1})(4.97 \times 10^{-16} cm^2)}{[1 + (4.913 \times 10^{24} photons \cdot cm^{-2} \cdot sec^{-1})(4.97 \times 10^{-16} cm^2)(2 \times 10^{-8} sec)]}$$

$$R = 4.9 \times 10^7 photons \cdot sec^{-1}$$

It is important to note that this model calculates the average individual fluorophore emission rate where there are only two states (excited and ground state). If there are other states of the system (e.g. dark states that cause the effect known as blinking), these emission rates will be different and another model would be required to more accurately quantify an expected observation. In addition, under very high intensity the fluorophores will have much higher probabilities of photobleaching, being permanently converted to a dark state, so the emission rate of a given population of fluorophores would be affected by that bleaching rate. Nonetheless, this calculation may offer a good starting point for estimating emission rates and/or choosing the laser intensity for a given application, and some probes, such as giant quantum dots [4], do not display fluorescence intermittency (blinking) or photobleaching behaviors. **Figure 4.1** shows the emission rates of eight varieties of quantum dots using this two-state emitter model.

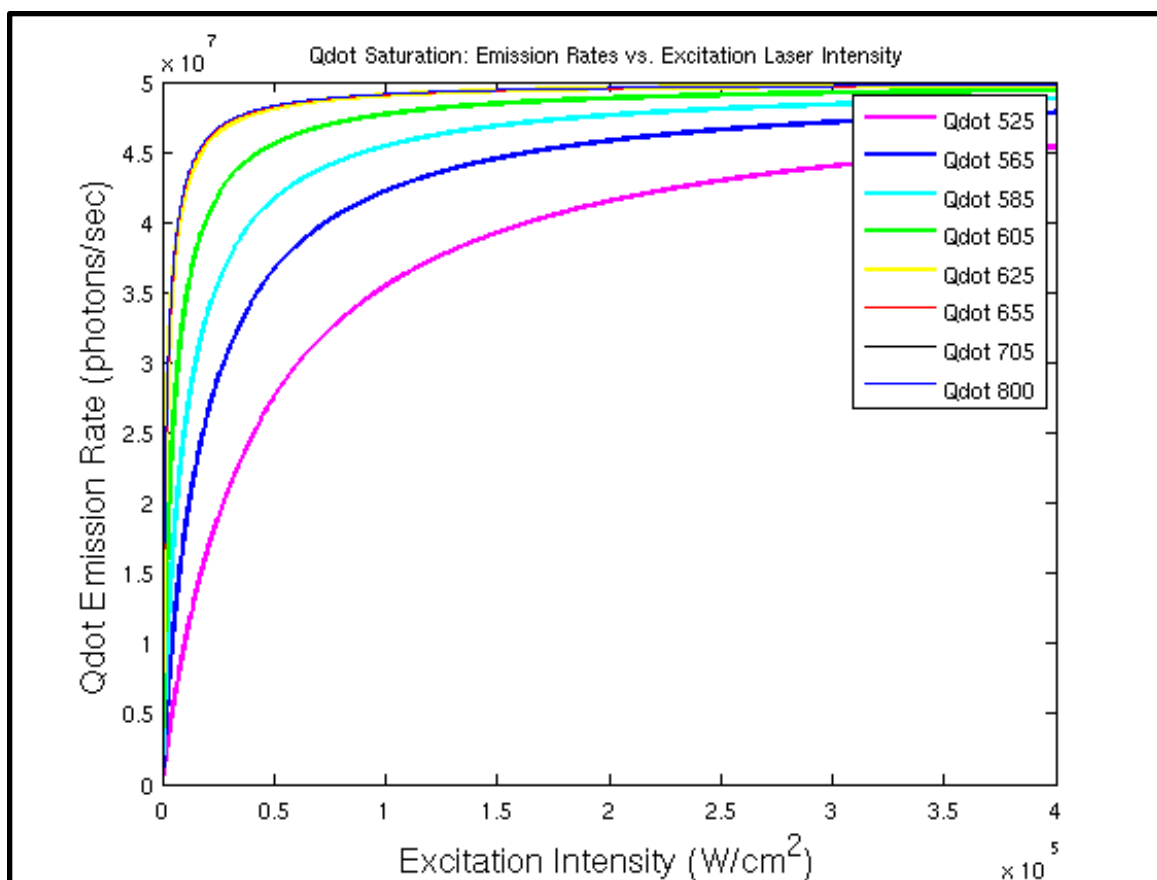


Figure 4.1: Quantum dot emission rate as a function of excitation intensity. These plots were generated using a model that assumes the quantum dots are two state emitters. In this model, excited state saturation appears to occur at or above about  $10^5 \text{ W}/\text{cm}^2$ .

### 4.3 Quantum Dot Photostability and Photoluminescence Enhancement

By comparison to many other organic dyes, quantum dots are very resilient to photobleaching. However, they do in fact experience transitions to a permanent dark state at the laser intensities typically used in this hyperspectral microscope system, and so a study of the bleaching rates was performed for each of the eight varieties of quantum dots used. Even without quantification, it becomes fairly obvious when using this microscope

that there is a significant difference in the photobleaching rate for each type of quantum dot.

For single particle tracking experiments that use several different species of quantum dots, the concentration over time of each type may be important. For example, if an experimenter labels two proteins, each with a different type of quantum dot and wishes to quantify aggregations of each type over time, it is important to know what percentage of the original population remains actively emitting as a function of time. Also, if one wishes to have a mixture of quantum dots with equal concentrations at some point in time, one must select the appropriate starting concentrations and have some knowledge of the bleaching rate. Experimenters in both of these examples may also have to contend with the possibility that quantum dots may diffuse into the region being exposed to excitation light, where they were previously not exposed, and likewise proteins labeled with quantum dots that photobleached during exposure may diffuse out of the field of view. These and other concerns are specific to each experiment, so instead of quantifying all of the different possibilities, a more general approach was examined where the half-life (and rate constant) was determined for each species of quantum dots and for different lot numbers (and shelf ages) of the quantum dot stocks.

Planar samples of each of the eight quantum dots were prepared by diluting stock solutions into ~10 nM concentrations in 1x phosphate buffered saline (PBS), at pH 7.4, approximating some of the fixed and live-cell chemical environments that may be used. 400  $\mu$ L of this dilution was added to each well of an 8-well chamber slide and allowed to aggregate for ~12 hours (which is much longer than required for a sufficient number to adhere to the glass surface). The concentrated quantum dot solution was then removed

and replaced with 1x PBS, leaving a thin, concentrated layer of quantum dots adsorbed onto the glass surface, but very few in the solution above – this removes any effect of the quantum dots diffusing into or out of the field of view. Each of these samples were then placed on the microscope and imaged for 2000 scanned frames (spectral images), where each image was  $(x,y,\lambda) = (64,42,128)$  in size.

Since different experiments may require various laser line intensities, the samples were measured using several laser powers. The laser power out of the objective was measured at AOM settings of 5, 10, 15, and 20%, and these values were found to be 0.095, 0.189, 0.287, and 0.382 mW. The laser intensity is determined using this power divided by the area of the beam. At the sample plane, the laser line is expected to be diffraction limited in width, where the diameter is  $d \sim 0.61\lambda/NA = 250 \text{ nm} = 2.5 \times 10^{-5} \text{ cm}$  and a length of about  $L = 14 \text{ }\mu\text{m} = 1.4 \times 10^{-3} \text{ cm}$ . Approximating the intensity as constant across the width (it is actually closer to being Gaussian, but this crude approximation is made here since the line is scanned and the relative integrated intensity is compared at different powers), the rectangular area of the line is  $A = d*L = 3.5 \times 10^{-8} \text{ cm}^2$ . This gives laser line intensities of 2714, 5400, 8200, and 10,914 W/cm<sup>2</sup> for laser powers of 5, 10, 15, and 20% respectively. It is useful to use these crudely approximated intensities since the actual laser power out of the AOM may change, or the coupling efficiency into the fiber may be adjusted, or some other component may change, but one can always measure the laser power out of the objective and assume the laser line geometry and then compare the data collected here with future samples for characterizing quantum dot stocks.

For each sample, two different regions were selected to verify that a given region was free from any obvious anomaly. Samples of both “old” and “new” quantum dots were

analyzed, where the older stocks were stored for about 1 year at 4° C in the solution in which they were shipped from Invitrogen corporation (1 M betaine, 50 mM borate, and 0.05% sodium azide at pH 8.3), and the newer stocks were stored in the same way for about 1 month. The “old” and “new” samples had different lot numbers, so this analysis cannot necessarily distinguish traits by age apart from production lots, and this points out another experiment that can be performed.

To model the population of emitters as a function of time  $N(t)$ , a basic exponential decay is assumed, with initial population  $N_0$  (the number of emitters within the scanned region) and decay constant  $r$ :

$$N(t) = N_0 e^{-rt}$$

The actual scan-integrated intensity observed,  $I(t)$  will include a background ( $B$ ), possibly from some population that is just outside of the region being scanned that is excited by scattered excitation light (or possibly from some other effect), and the integrated intensity from the original population,  $A$ , so the observed integrated intensity as a function of time will be:

$$I(t) = A e^{-rt} + B$$

Here,  $B$  is considered as a constant and that any photobleaching of the sample outside of the directly scanned region from scattered excitation light, or any other background source is negligible. The half-life is the time required for the sample population to be reduced by a factor of two, so  $I(t)$  becomes  $A/2 + B$  and then the half-life is

$$t_{1/2} = \frac{\ln 2}{r}$$



While the half-life is helpful in illustrating the resilience of a given sample of emitters, the rate constant is more useful if one has several species and desires some specific concentration of each at some point in time. In this case, one would begin by selecting the stocks with the closest possible half-life values to maintain the closest concentration ratios and then the rate constants can be used with the exponential decay function to provide the desired initial labeling concentrations for the experiment (plug in  $r$  and  $t$ , set  $N_1(t) = N_2(t)$ , and find the ratio for  $N_{0\_1}$  to  $N_{0\_2}$ ).

**Figure 4.2** shows an example plot of the measured scan-integrated intensity of quantum dot 525, over 2000 scans (spectral images). The data were analyzed by summing over the spectral and spatial dimensions for each frame and then fitting to an exponential decay, providing the rate constant ( $r$ ), initial population intensity ( $A$ ), and background level ( $B$ ). **Table 4.2** shows the results for eight types of quantum dots, each with two different lot numbers and shelf ages of the stock. Each of the results is a mean value taken from two data sets (two different regions analyzed on the planar sample).

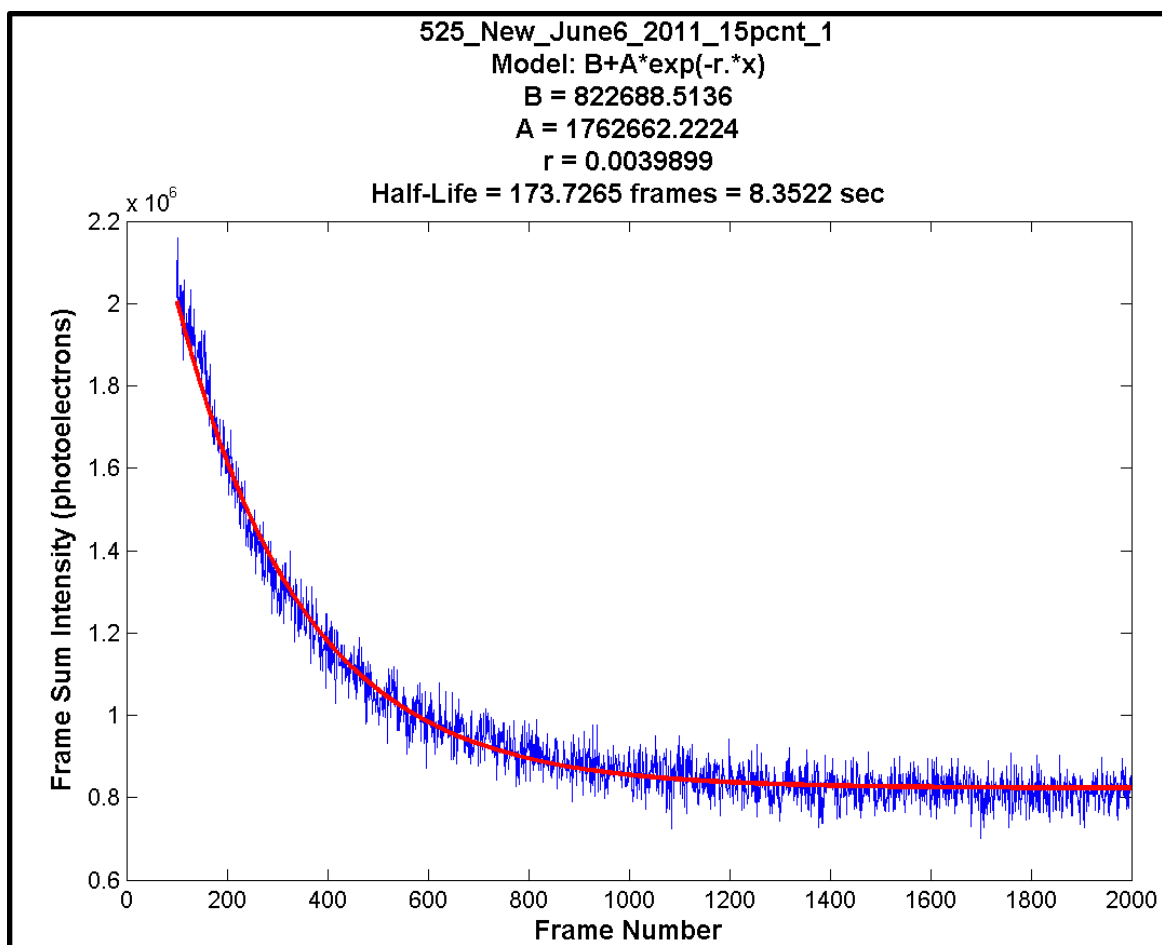


Figure 4.2: Quantum dot bleaching analysis example plot. Data for Qdot 525 under 15% laser power ( $8200 \text{ W/cm}^2$ ) is shown in blue and the fitted exponential decay function is shown in red. Similar plots were made for all 8 species of quantum dots, older and newer stocks, for two regions in each sample.

Laser Power 5% (0.095 mW), Intensity 2714 W/cm <sup>2</sup>			Laser Power 15% (0.287 mW), Intensity 8200 W/cm <sup>2</sup>		
Quantum Dot Stock	Half-Life (s)	Rate Constant (r)	Quantum Dot Stock	Half-Life (s)	Rate Constant (r)
525 New	20.3	0.034	525 New	7.7	0.090
525 Old	45.7	0.015	525 Old	10.8	0.064
565 New	41.3	0.017	565 New	8.6	0.081
565 Old	56.3	0.012	565 Old	6.4	0.108
585 New	43.2	0.016	585 New	8.2	0.085
585 Old	55.2	0.013	585 Old	10.7	0.065
605 New	13.8	0.050	605 New	3.7	0.187
605 Old	10	0.069	605 Old	3.8	0.182
625 New	44.4	0.016	625 New	9.4	0.074
625 Old	33.4	0.021	625 Old	11.1	0.062
655 New	10.3	0.067	655 New	5.6	0.124
655 Old	14.1	0.049	655 Old	6.7	0.103
705 New	N/A	N/A	705 New	82.8	0.008
705 Old	21.7	0.032	705 Old	16.5	0.042
800 New	24.2	0.029	800 New	23.4	0.030
800 Old	25.3	0.027	800 Old	28.1	0.025

Laser Power 10% (0.189 mW), Intensity 5400 W/cm <sup>2</sup>			Laser Power 20% (0.382 mW), Intensity 10,914 W/cm <sup>2</sup>		
Quantum Dot Stock	Half-Life (s)	Rate Constant (r)	Quantum Dot Stock	Half-Life (s)	Rate Constant (r)
525 New	11.4	0.061	525 New	6.1	0.114
525 Old	15	0.046	525 Old	9.2	0.075
565 New	10.3	0.067	565 New	4.8	0.144
565 Old	12	0.058	565 Old	4.4	0.158
585 New	12.1	0.057	585 New	4.7	0.147
585 Old	14.2	0.049	585 Old	6.7	0.103
605 New	4.9	0.141	605 New	2.9	0.239
605 Old	4.8	0.144	605 Old	2.2	0.315
625 New	14	0.050	625 New	7.9	0.088
625 Old	14.1	0.049	625 Old	8.4	0.083
655 New	8.8	0.079	655 New	4.7	0.147
655 Old	9.7	0.071	655 Old	4.8	0.144
705 New	113	0.006	705 New	52.8	0.013
705 Old	16.6	0.042	705 Old	16.1	0.043
800 New	22	0.032	800 New	23.4	0.030
800 Old	31.7	0.022	800 Old	30.9	0.022

Table 4.2: Quantum dot photobleaching half-life and rate constants. The naming convention used for the quantum dot stocks is the peak emission wavelength and the shelf age of the lot, where “Old” refers to a stock that is 1-year in aqueous solution, and “New” implies that the lots were about 1 month of age.

For most samples, there was an obvious initial increase in the integrated intensity for up to several hundred frames (see **Figure 4.3**). The causes for this photoluminescence enhancement (PLE), while not yet known, may be due to a number of mechanisms, including water molecule induced passivation of surface traps and photoinduced

modification of the surface material [5,6] in the nanocrystal solid. Most of the current models suggest a reduced effect from dark states that results in an overall increase in the quantum yield. The possibly multifold causes of the PLE compete with the mechanisms that induce the dark states of the quantum dots under excitation light. In order to provide the best fit of the data to an exponential decay (and thus obtain more reliable values for half-life and rate constant), the frames where obvious enhancement effects occurred were excluded from the fitting.

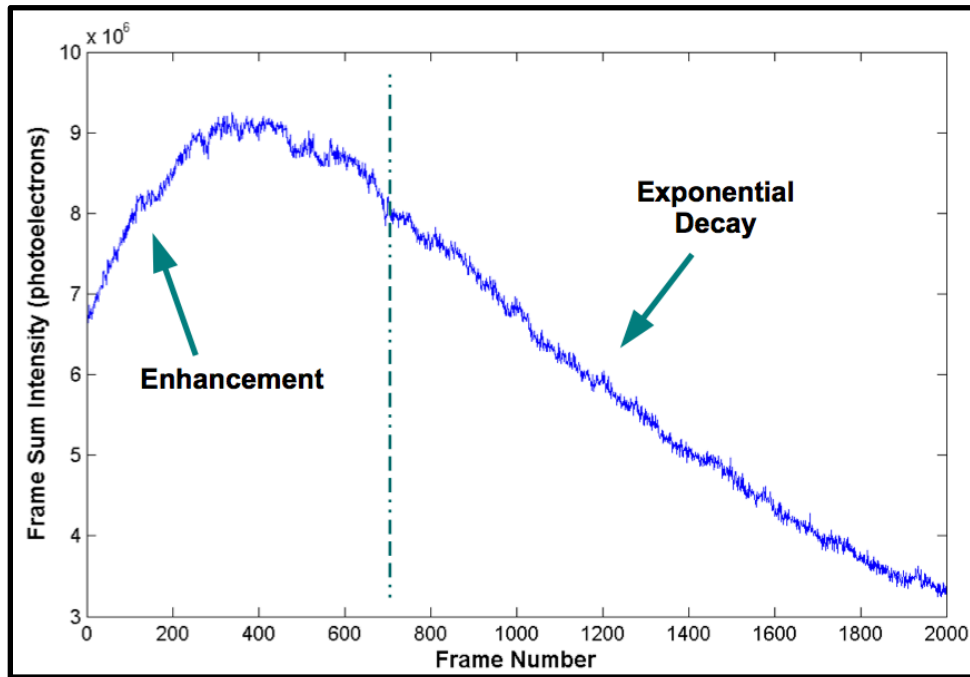


Figure 4.3: Photoluminescence enhancement (PLE). The data to the right of the dashed line were fit to an exponential decay curve in order to determine the half-life and rate constant that describe the longer term behavior of the population of quantum dots exposed to the given excitation light intensity.

## 4.4 Quantum Dot Fluorescence Intermittency

While both organic dyes and quantum dots exhibit fluorescence intermittency, they each have very different underlying electronic mechanisms responsible for the dark states that present this effect. This on-off blinking behavior reduces the steady state quantum yield and can introduce difficulties in single particle tracking experiments, where the off state would result in a loss of information that could cause reduced particle localizations or incomplete trajectory reconstruction. **Figure 4.4** shows an example plot of the integrated intensity vs. time (frame #) of a 5×5 pixel subregion that contains a single quantum dot (in this case QDot 625). This example shows that the quantum dot is sometimes “off” for tens of consecutive frames, and sometimes “on” for over a hundred consecutive frames.

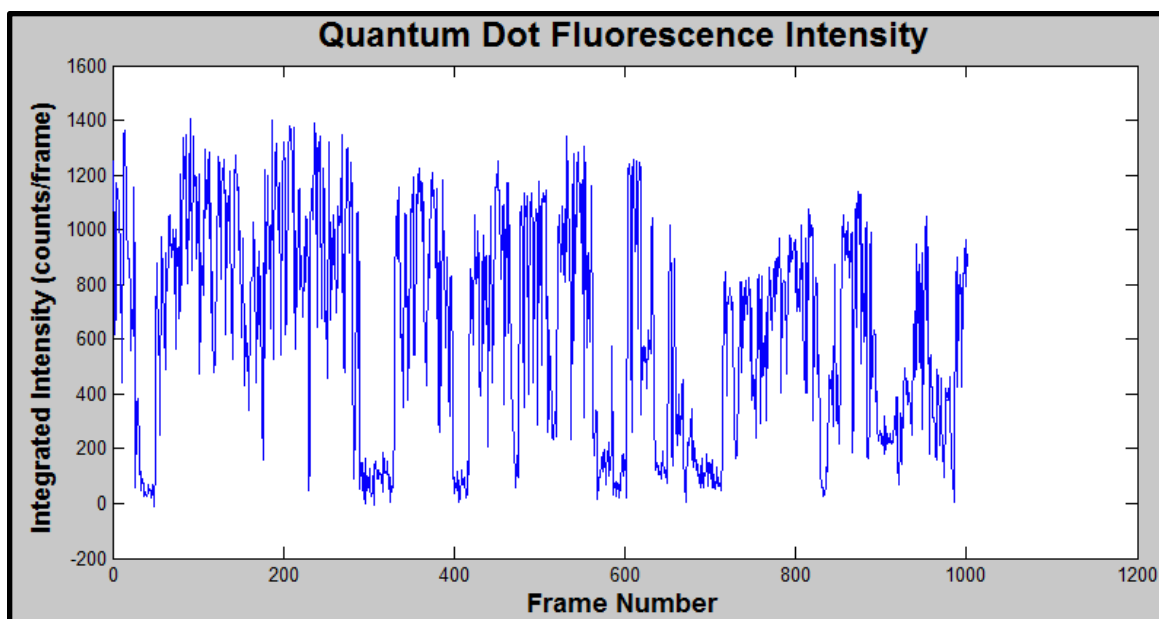


Figure 4.4: Fluorescence intensity trajectory for a single quantum dot. This is the 5×5 subregion pixel sum of intensity over time, showing that the quantum dot “blinks” between “on” and “off” states at various time scales.

It is important to note that the “on” states here are such that the emission is not quite constant – there is actually some blinking behavior at shorter time scales, possibly within the individual frames. This strange blinking behavior has been studied [7,8] and has even been used in super-resolution techniques [9,10], and is still a topic of interest since there are many possible mechanisms that may be responsible for this effect. Many of the models of dark states point to a charged nanocrystal core due to surface traps or defects in the lattice. These non-radiative transitions may be modeled in the simplified energy diagram shown in **Figure 4.5**.

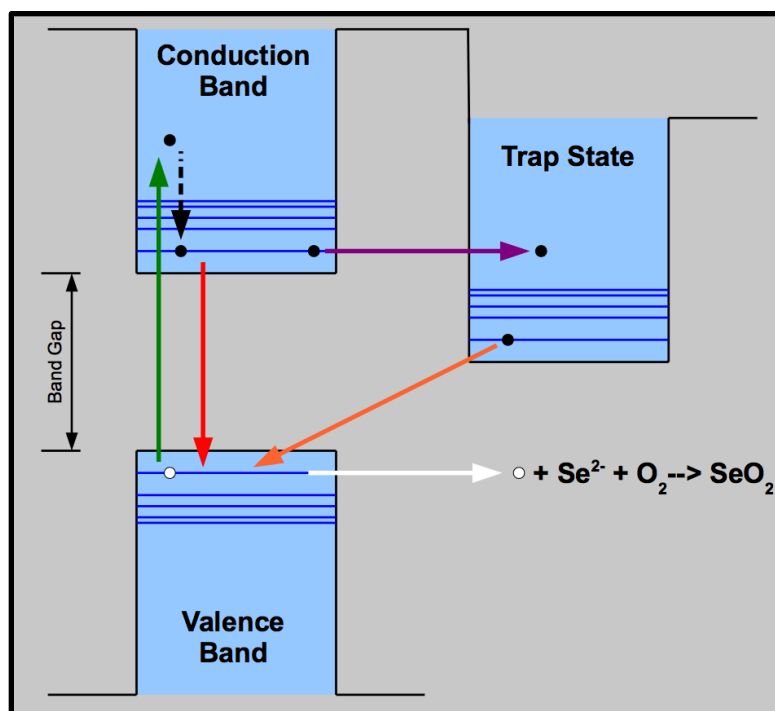


Figure 4.5: Quantum dot energy state transitions. Black circles represent electrons while the white circles represent “holes”. The green arrow represents absorption of a photon from the excitation light. The dashed black arrow represents relaxation (through phonons in the lattice) to the ground state of the conduction band. The red arrow represents recombination of the electron-hole pair, resulting in fluorescence emission. The magenta arrow represents tunneling into a trap state, with the orange arrow indicating a non-radiative decay from the trap back to the valence band. The white arrow indicates a mechanism for oxidation of selenium atoms, which may contribute to blue shifting and/or photobleaching in addition to a temporary dark state.

In this model, the trap states leave the nanocrystal charged, unable to absorb and emit light through the normal excitation and emission paths. There may be several types of these traps at mid band-gap energies, with various lifetimes that account for different time scales observed for the “on” and “off” states. Interactions with ions from the nearby environment may further complicate the model and some evidence suggests that the dark states are not entirely caused by a charged core alone [11]. The study of the mechanisms behind the observed fluorescence intermittency is not the goal of the research described in this manuscript, but the implications of the behavior can be important in the context of single particle tracking, thus a basic characterization is warranted. While the individual

quantum dots will each have unique blinking characteristics, a statistical analysis of ensemble observations may be useful in selecting appropriate probes for a given experiment, perhaps among other reasons. Example blinking characterizations were performed on samples of quantum dot 625 and 705 (the “best” and “worst” in terms of blinking and overall duty cycle). The results are shown in **Figures 4.6** and **4.7**.



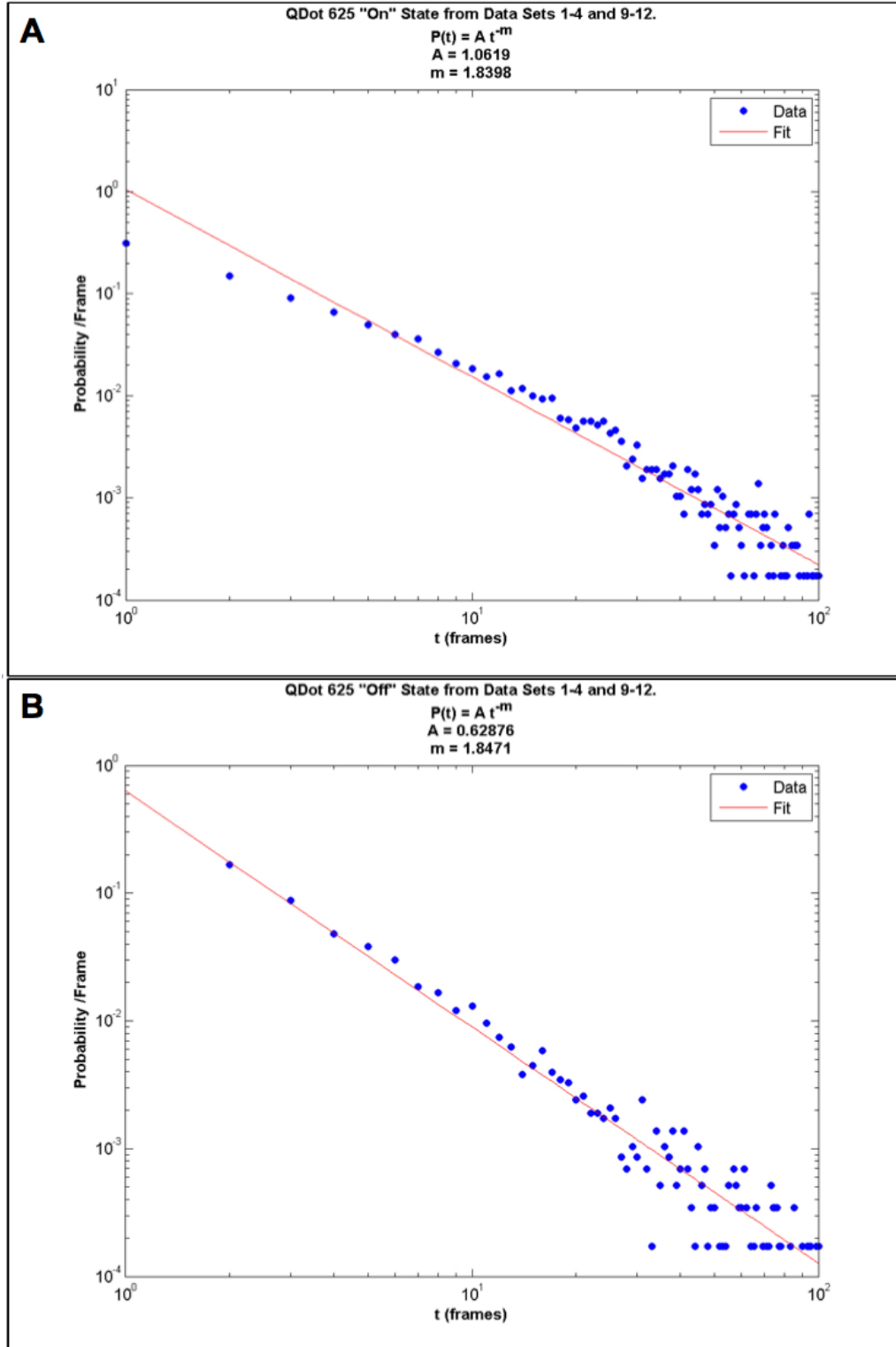


Figure 4.6: Quantum dot blinking statistics for QD 625. (A) The distribution of probabilities of the “on” times vs. duration of the “on” time is plotted along with the power law fit. (B) The distribution of probabilities of the “off” times vs. duration of the “off” time is plotted along with the power law fit. These data were acquired at 28 FPS, so the x-axis ranges from ~36 msec (1 frame) to 3.6 sec (100 frames).

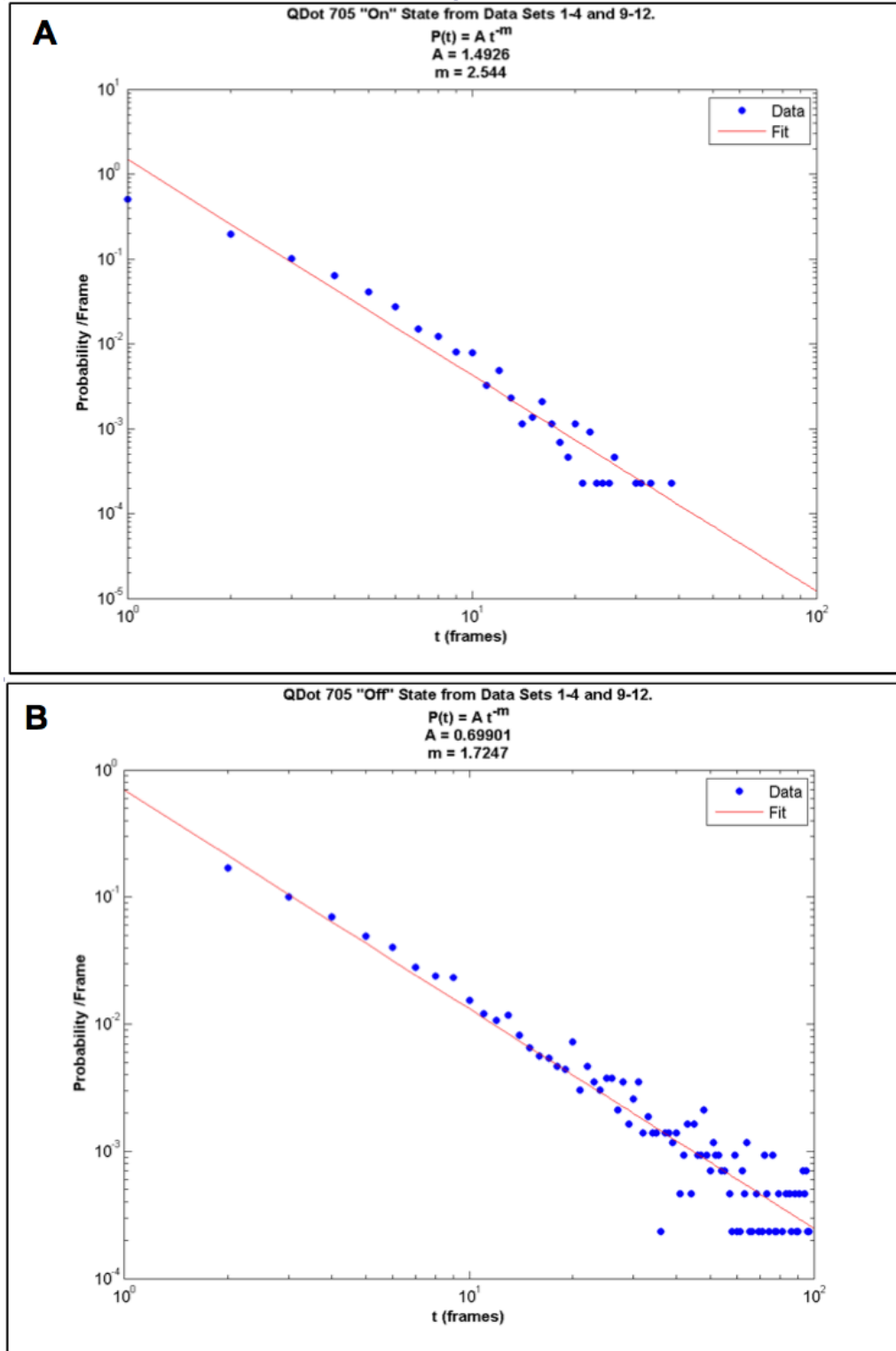


Figure 4.7: Quantum dot blinking statistics for QD 705. (A) The distribution of probabilities of the "on" times vs. duration of the "on" time is plotted along with the power law fit. (B) The distribution of probabilities of the "off" times vs. duration of the "off" time is plotted along with the power law fit. These data were acquired at 28 FPS, so the x-axis ranges from ~36 msec (1 frame) to 3.6 sec (100 frames).

In these experiments, 20 pM quantum dot samples were prepared by dilution into 1x PBS (pH 7.4) and placed into 8-well chamber slides for 2+ hrs. The dilution was then replaced with 1x PBS, leaving only a sparse population of quantum dots on the glass surface. Eight regions were imaged for each of the samples (QD 625 and 705) and 4 individual quantum dots were selected from each region for analysis. The on/off data were compiled from the 32 individual quantum dots for each species by selecting a threshold where all frame intensities above this value were considered “on” and were assigned a value of 1, and all intensities below the threshold were considered “off” and assigned a value of zero. The number of consecutive zeros and ones in this series were counted and binned by frequency of occurrence, and then finally normalized into a probability density. These probabilities were then plotted vs. number of frames on (or off) on a log-log scale and fits were made to power law distributions,  $P(t) = A * t^{-m}$ , where  $P(t)$  is the probability density (per frame) of the emitter being in the on or off state for  $t=1,2,3,\dots,n$  consecutive frames. Values for  $A$  and  $m$  were found from these fits and provide some basic information about the blinking behaviors of each ensemble. Larger  $m$  values indicate a larger slope to the “line” representing the fit, which means that there would be fewer consecutive on (or off) times. The duty cycle is defined as the ratio of “on” frames to the total frames and was found to be 56.6% for QD 625 and 17.3% for QD 705. The lower value for  $m$  along with the higher duty cycle confirms the previous qualitative observation that QD 625 is much more desirable for single particle tracking experiments than QD 705. In many cases, as in high density SPT, the number of colors of quantum dots may be more important than the blinking behavior, but a much better solution would be to use probes that do not blink or have dramatically suppressed blinking, such as the

“giant” multishell quantum dots that have recently been developed by Hollingsworth, et al. [4]. Additionally, it has been reported [7] that adding  $\beta$ -mercaptoethanol to a final concentration of 1 mM reduces blinking to such an extent that about 60% of a given population of commercial streptavidin-coated quantum dots exhibits essentially no blinking over an imaging period of 80 s.

## **4.5 Quantum Dot Emission Spectra, Emission Intensity, and Spectral Shifting**

As noted above, each quantum dot will have a different fluorescence intermittency and overall emission rate, and it is also expected that there will be some variance in the spectral emission peaks and distributions of the spectra, both between species and within each one. For example, the spectral peak, distribution, and observed emission rate of one individual quantum dot 565 will be different from that of another QD 565, and there will be a difference in the QD 565 ensemble emission rates and spectral distributions compared to those of QD 655. These properties have been measured and are summarized in this section. In addition, there is the possibility of spectral shifting during exposure to the excitation light [7], but this effect is not as problematic in single particle tracking since the track reconstructions use frame-to-frame connections using Gaussian fits of the spectral emissions, and under the laser intensities used in the single particle tracking experiments typically performed with this system the blue shifting happens at a rate that does not have a significant impact on the tracking.

## 4.5.1 Individual Quantum Dot Emissions

Shown in **Figure 4.8**, the emission spectra profiles of individual quantum dots are well modeled by a Gaussian distribution. Here, solid colored lines represent the measured emissions from individual QDs and the dashed colored lines represent the Gaussian fits. These data were collected from a sparse sample of eight different species of quantum dots (525, 565, 585, 605, 625, 705, and 800) non-specifically adsorbed onto a glass cover slip surface in a solution of 1x PBS (pH 7.4). Individual emitter subregions were selected and the sum of spatial pixels in each subregion was plotted along the spectral dimension (128 pixels). The excitation laser line intensity was about 5400 W/cm<sup>2</sup> (50% total laser power with neutral density filter transmissivity of 0.2), and the scan speed was set (via region size) to that of the typical SPT experiment (27.4 hyperspectral images per second).

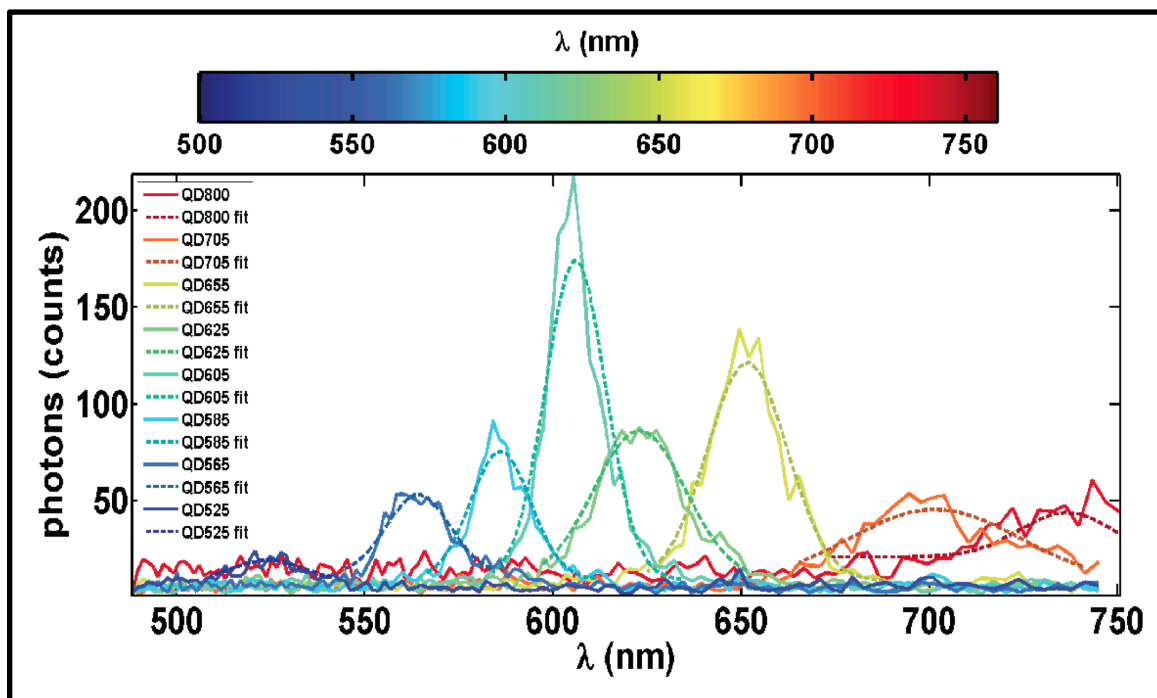


**Figure 4.8: Individual quantum dot emission spectra.** Progressing from blue to red are sum projections of raw data (solid) and Gaussian fits (dashed) for single 525, 565, 585, 605, 625, 655, 705 and 800 nm QDs.

Some of the features worth noting here are the low emission rate of QD 525 (mainly due to its small cross-section, but also detector and transmission efficiency is smaller for this part of the spectrum), and that QD 800 does not show a very good fit due to the cutoff in spectral range at around 750 nm – the peak may be at or above 750 nm, and the distribution is larger than any other emitter in this set.

#### **4.5.2 Ensemble Quantum Dot Emission Spectra**

A good characterization requires analyzing a large number of emitters. The same sample discussed above was used, where eight different regions were scanned and 1000 hyperspectral images were acquired for each region, at the laser intensity and frame rate described above ( $5400 \text{ W/cm}^2$  at 27.4 FPS). Subregions were selected that contained only a single emitter, and the spectra were analyzed for each emitter in each frame. Results for quantum dot 565 are plotted as an example in **Figure 4.9**, and **Table 4.3** shows the values found for all eight types of quantum dots. **Appendix D** shows the plots (similar to Figure 4.9) for all of the quantum dot species. Note that the expected emission peak for QD800 is significantly different from the histogram. This is attributed to the spectral range of the instrument (i.e. only the tail of the spectrum is observed on the camera). The total number of spectra used to compute each ensemble is included in **Table 4.3**.

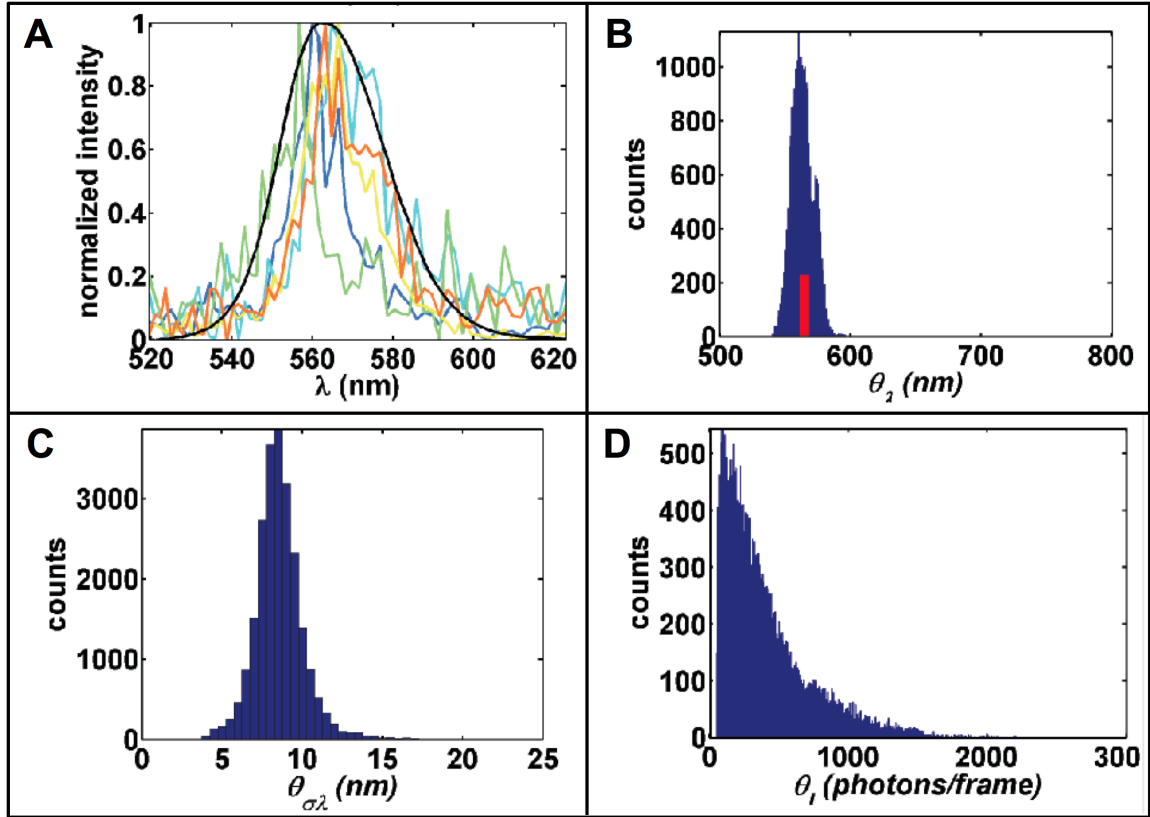


Figure 4.9: Ensemble quantum dot emission spectra and observed intensity. QD 565 is shown here as an example. (A) shows spectral features of individual QDs (colored lines; 5 randomly selected spectra) and the ensemble of all individual QDs (black line). (B) is a histogram of fit spectral emission peaks ( $\theta_\lambda$ ) identified by 3D Gaussian fitting ( $x, y, \lambda$ ) for individual QDs. The red tick indicates the expected emission peak for the given QD. (C) is a histogram of the fit standard deviation in the spectral dimension ( $\theta_{\sigma_\lambda}$ ) identified by 3D Gaussian fitting for individual QDs. (D) is a histogram of fit photons per frame ( $\theta_I$ ) for individual QDs.

Invitrogen QDot species	Number of localizations	$\theta_\lambda$ (nm) <i>mean</i>	$\theta_\lambda$ (nm) <i>stdev</i>	$\theta_{\sigma_\lambda}$ (nm) <i>mean</i>	$\theta_{\sigma_\lambda}$ (nm) <i>stdev</i>	$\theta_I$ (counts) <i>mean</i>
QD525	1527	525	7	8	2	208
QD565	23053	563	9	9	2	411
QD585	28777	587	10	9	2	541
QD605	36216	607	7	8	2	956
QD625	52666	622	9	10	2	800
QD655	17147	653	8	11	2	1218
QD705	25731	696	17	17	4	412
QD800	5795	733	15	15	4	209

Table 4.3: Quantum dot emission spectra and observed intensity. Statistics for results shown in Figure 4.9 are summarized in this table. Additional descriptions of the model parameters are included in Appendix E.

### 4.5.3 Quantum Dot Spectral Shifting

Due to confinement, the size of the quantum dot core dictates the emission frequency. If the core size is reduced, possibly from photo-induced oxidation, the observed result is a spectral shift to shorter wavelengths. This mechanism would lead to an irreversible blue shift, and under continued illumination, would ultimately result in a permanently photobleached state. **Figure 4.10** displays several quantum dot trajectories that appear to be examples of this behavior.

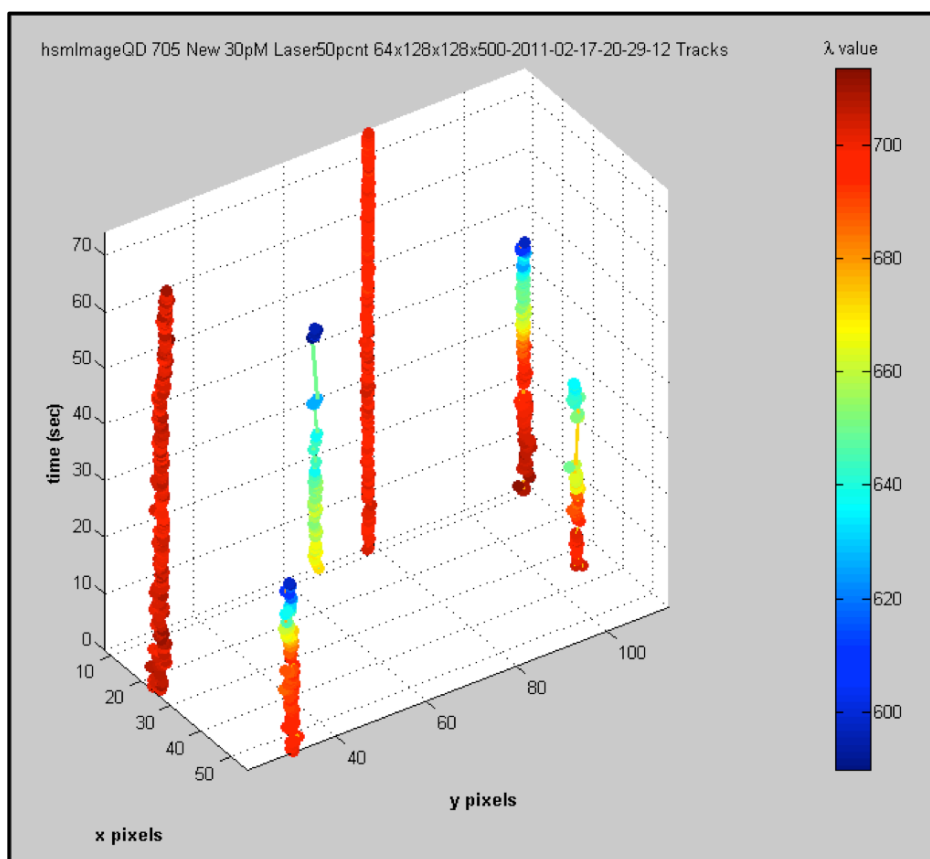


**Figure 4.10: Quantum dot spectral shifting.** The color represents the peak emission wavelength, with dark blue indicating about 590 nm and dark red is about 710 nm. The laser intensity was  $\sim 27,000 \text{ W/cm}^2$ .



Overall, when one is selecting quantum dot stocks to use in a given experiment, it may be important to consider (and possibly measure) the photostability (bleaching rate), the fluorescence intermittency and duty cycle, the emission rate (when in the “on” state), and the individual and ensemble spectral peaks and distributions. Quantifying, or even estimating each of these properties may lead one to more appropriate starting concentrations of each type to be used for the given experiment, and even some buffer modifications can be made to mitigate the fluorescence intermittency.

## References

1. Ober RJ, Ram S, Ward ES (2004) Localization accuracy in single-molecule microscopy. *Biophysical journal* 86: 1185–1200. Available: <http://www.pubmedcentral.nih.gov/articlerender.fcgi?artid=1303911&tool=pmc&entrez&rendertype=abstract>.
2. Swinehart DF (1962) The Beer-Lambert Law. *Journal of Chemical Education* 39: 333. Available: <http://pubs.acs.org/doi/abs/10.1021/ed039p333>.
3. Gustafsson MGL (2005) Nonlinear structured-illumination microscopy: wide-field fluorescence imaging with theoretically unlimited resolution. *Proceedings of the National Academy of Sciences of the United States of America* 102: 13081–13086. Available: <http://www.pubmedcentral.nih.gov/articlerender.fcgi?artid=1201569&tool=pmc&entrez&rendertype=abstract>.
4. Chen Y, Vela J, Htoon H, Casson JL, Werder DJ, et al. (2008) “Giant” multishell CdSe nanocrystal quantum dots with suppressed blinking. *J Am Chem Soc* 130: 5026–5027. Available: <http://www.ncbi.nlm.nih.gov/pubmed/18355011>.
5. Jones M, Nedeljkovic J, Ellingson RJ, Nozik AJ, Rumbles G (2003) Photoenhancement of Luminescence in Colloidal CdSe Quantum Dot Solutions.

The Journal of Physical Chemistry B 107: 11346–11352. Available: <http://pubs.acs.org/doi/abs/10.1021/jp035598m>.

6. Pechstedt K, Whittle T, Baumberg J, Melvin T (2010) Photoluminescence of Colloidal CdSe/ZnS Quantum Dots: The Critical Effect of Water Molecules. The Journal of Physical Chemistry C 114: 12069–12077. Available: <http://pubs.acs.org/doi/abs/10.1021/jp100415k>.
7. Lee SF, Osborne M a (2009) Brightening, blinking, bluing and bleaching in the life of a quantum dot: friend or foe? Chemphyschem : a European journal of chemical physics and physical chemistry 10: 2174–2191. Available: <http://www.ncbi.nlm.nih.gov/pubmed/19691081>.
8. Galland C, Ghosh Y, Steinbrück A, Sykora M, Hollingsworth J a, et al. (2011) Two types of luminescence blinking revealed by spectroelectrochemistry of single quantum dots. Nature 479: 203–207. Available: <http://www.ncbi.nlm.nih.gov/pubmed/22071764>.
9. Lidke KA, Heintzmann R (2007) LOCALIZATION FLUORESCENCE MICROSCOPY USING QUANTUM DOT BLINKING Keith A . Lidke University of New Mexico Department of Physics and Astronomy Albuquerque , NM 87131 , USA Rainer Heintzmann King ' s College London Randall Division of Cell and Molecular Biop. 2007 4th IEEE International Symposium on Biomedical Imaging: From Nano to Macro: 936–939.
10. Hoyer P, Staudt T, Engelhardt J, Hell SW (2011) Quantum dot blueing and blinking enables fluorescence nanoscopy. Nano letters 11: 245–250. Available: <http://www.ncbi.nlm.nih.gov/pubmed/21128678>.
11. Zhao J, Nair G, Fisher BR, Bawendi MG (2010) Challenge to the Charging Model of Semiconductor-Nanocrystal Fluorescence Intermittency from Off-State Quantum Yields and Multiexciton Blinking. Physical Review Letters 104: 157403. Available: <http://link.aps.org/doi/10.1103/PhysRevLett.104.157403>.

## Chapter 5

### Fixed and Live Cell Experiments

The experiments discussed in this chapter are meant to demonstrate the application of the HSM to the study of several biological systems of interest. They are not meant to be fully comprehensive investigations, but rather as examples of the potential of the HSM system applied in these contexts. An overview of the necessary analysis methods is provided in section 5.1, an example of multicolor SPT experiments is discussed in 5.2, 3D hyperspectral imaging is shown in 5.3, and hyperspectral superresolution is demonstrated in 5.4. It is important to note that this is by no means an exhaustive list of potential experiments using the HSM.

#### 5.1 Localization and Track Reconstruction

The following localization and particle tracking methods are not the primary focus of this research, but are described here since they are necessary in making experimental observations using the HSM and these analysis methods have been developed at UNM by Patrick Cutler, Keith Lidke, and Fang Huang.

Single particle tracking is carried out by the localization of single molecules and the subsequent building of trajectories from those localizations [1]. The light emitted from a point source (such as a fluorescently tagged protein) is distributed on the detector according to the PSF of the microscope. The 2D  $(x,y)$  spatial PSF is well modeled by a 2D Gaussian distribution [2] and the emission spectra profiles of QDs are also well

modeled by a Gaussian shape (**Figure 5.1A**). The position of QDs are found by performing a maximum likelihood estimate of spatial position, intensity and spectral peak position using a 3D  $(x,y,\lambda)$  Gaussian PSF model and a Poisson noise model (**Appendix E**). Localizations are performed using an iterative update method [3] that includes the possibility of fitting multiple point emitters within a diffraction limited area [4]. As with previous work [3,4], the analysis is implemented on graphics processing units in a parallel fashion in order to take advantage of modern graphical processing unit's (GPU) high computational performance (**Figure E.2, Appendix E**).

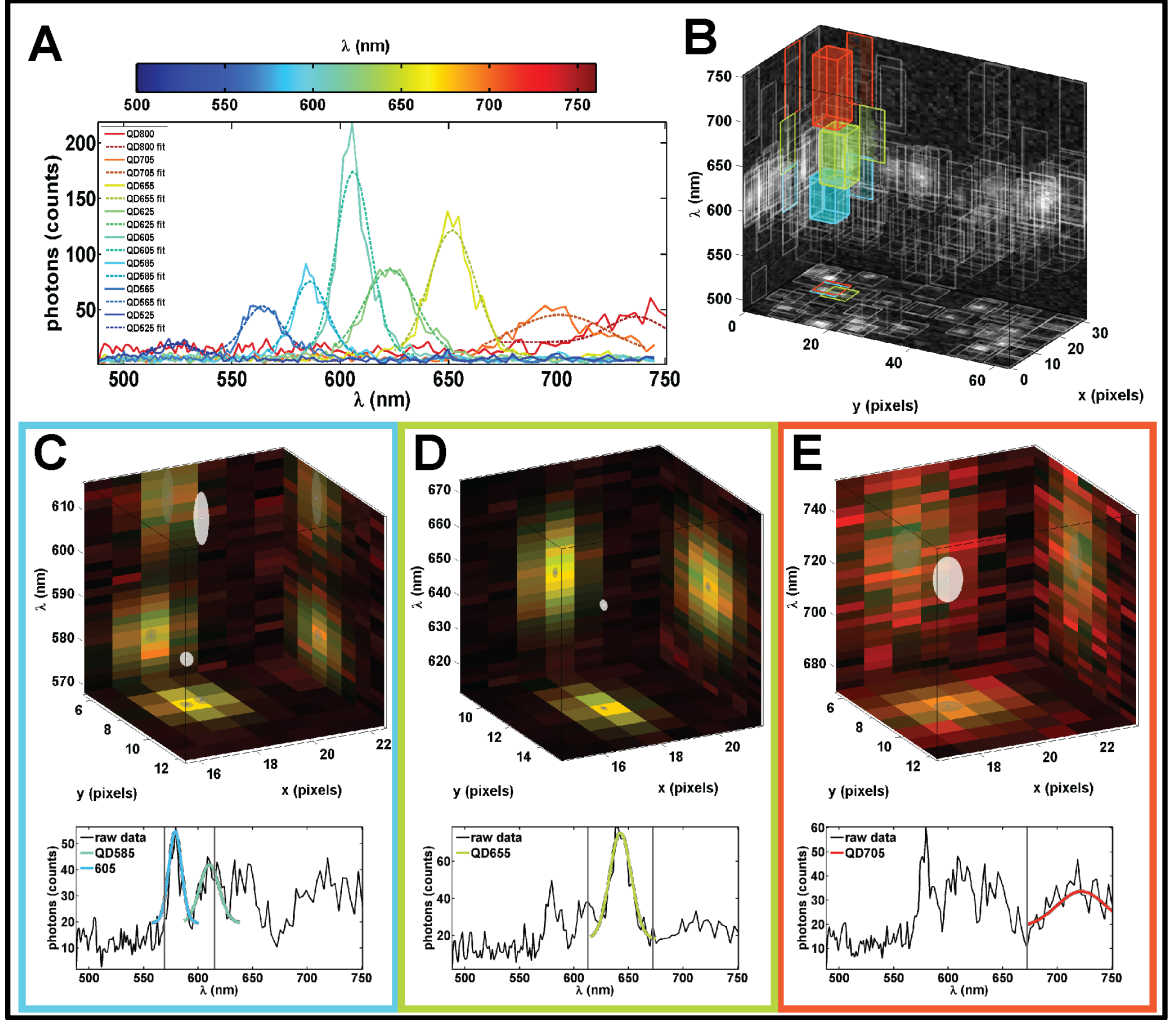


**Figure 5.1: Quantum dot localization.** (A) Progressing from blue to red are sum projections of raw data (solid) and Gaussian fits (dashed) for single 525, 565, 585, 605, 625, 655, 705 and 800 nm QDs. (B) 3D representation of a single hyperspectral time frame with 3D boxes representing sub-volumes identified for further particle localization. Sum projections of the data onto each plane are used to represent the raw data (gray scale). Likewise, 2D projections of each 3D box onto each plane are used to highlight the sub-volumes. Fitting results for the colored sub-volumes (color corresponds to the spectral center of the box) in (B) are shown in (C), (D), and (E). In the top figures in (C), (D), and (E) red and green are sum projections of the raw data and fit respectively. Note that the color outlining (C), (D), and (E) correlate with the respective sub-volumes highlighted in (B) with the same color. The localized particles are represented by white ellipsoids in which the radius in each dimension shows 3 standard deviations in the estimated error in the fit using the Cramér Rao Bound and their projection onto each axis is represented by a gray ellipse. The bottom figures in (C), (D), and (E) show raw spectral features (black) and Gaussian fits (color corresponds to fit spectral emission peak). The vertical gray lines represent the spectral cutoffs for independently fit sub-volumes. This figure is from [5].

The procedure for localizing QDs using hyperspectral data is demonstrated with all 8 colors of QDs in a single acquisition (**Figures 3B-E**). See **Appendix B, Materials and**

**Methods** for more details. The simultaneous localization of two highly spatially and spectrally overlapping QDs (QD585 and QD605) is highlighted in **Figures 3C** and **3F**. Additionally, a total of four highly spatially overlapping QDs are localized simultaneously. This is highlighted by the colored boxes in **Figure 3B** and the corresponding fits in **Figures 3C, 3D** and **3E**. The fit precision for each parameter is estimated from the Cramér-Rao Bound (CRB) however, it is important to note that QD blinking during line scanning can contribute to higher than expected error in QD localization in the line-scanning dimension of the data (**Figure E.3, Appendix E**). Trajectories are constructed from found QD  $(x,y,\lambda)$  positions (**Figure E.4, Appendix E**); manuscript in preparation Relich P, Cutler PJ, Huang F, Lidke KA)[6]. The use of spectral information to build trajectories helps to improve the overall accuracy of the trajectory building process (**Figure E.4, Appendix E**).

## **5.2 Multicolor Single Particle Tracking of Membrane Proteins**

### **5.2.1 Oligomer Dynamics**

Previous studies of FcεRI have shown that receptor mobility is a function of antigen dose and valency, and consequently aggregate size [7]. However, in these experiments, the size of aggregates could not be directly determined since a mixture of dark and QD-labeled IgE (QD-IgE) was used to maintain SPT density. Using the HSM to perform mcSPT of QD-IgE-FcεRI on live cells captures not only the dynamics of IgE-FcεRI complexes, but also reveals the number of proteins in the aggregate based on spectral signature. **Figure 5.2** shows the results of mcSPT of QD-IgE-FcεRI approximately 7

minutes after the addition of a crosslinking agent (DNP<sub>3</sub>). DNP<sub>3</sub> (manuscript in preparation Mahajan A, Barua D, Cutler P, Lidke DS, et al.) is a small trimer of peptides that presents three DNP moieties for crosslinking DNP-specific IgE, which was synthesized by AnaSpec (Fremont, CA). Several long-lived complexes are observed that demonstrate correlated motion.

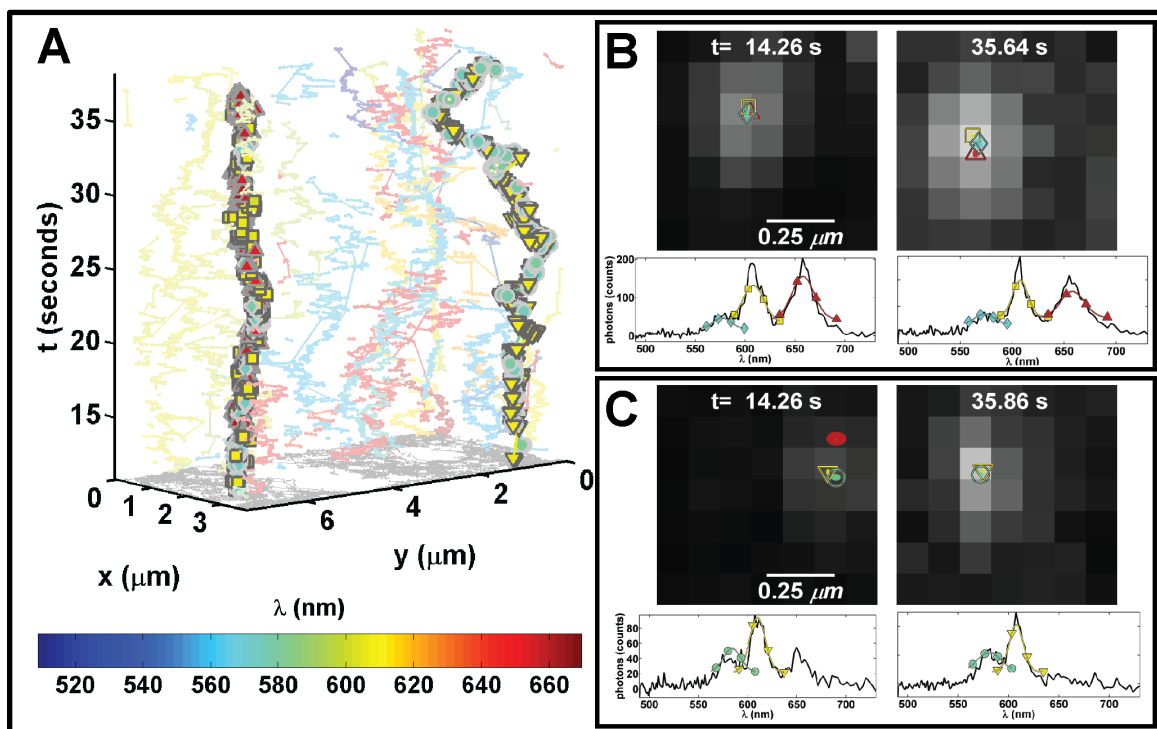


**Figure 5.2:** SPT of 5-colors (565, 585, 605, 625, 655) of QD-IgE on live RBL cells. All subfigures are derived from a single acquisition (27 fps) ~7 minutes after crosslinking with DNP<sub>3</sub>. (A) 3D ( $x$ ,  $y$ ,  $t$ ) depiction of trajectories. The color scheme for the trajectories is dependent on the estimated emission peak of each QD as noted by the color bar. A trimer (565 QD cyan diamond; 605 QD yellow square; 655 QD red up triangle) and dimer (585 QD cyan circle; 605 QD yellow down triangle) are highlighted by their respective symbols. (B) and (C) show localizations for specified time frames. Coloration and symbols correspond to (A). Ellipses in the upper subfigures represent 3 times the localization accuracies over a gray scale projection of the raw data. Red ellipse in the upper left subfigure of (C) is a localized 655 QD that doesn't interact with the dimer. Raw spectra (solid black lines) and Gaussian fit (colored lines with symbols) for individual QDs are shown in the lower subfigures.

**Figure 5.2A** highlights the observation of a trimer and dimer. Spectral separation is further beneficial for accurate quantification of diffusion of QD-IgE-FcεRI oligomeric complexes due to their high degree of spatial and spectral overlap (**Figures 5.2B** and **5.2C**). Note that the localization of the QDs in these complexes would not be possible

using single color SPT represented by the gray scale projection in **Figures 5.2B** and **5.2C**. The red ellipse in **Figure 5.2C** (upper left subfigure) is a QD655-IgE-FcεRI that comes in close proximity but does not interact with the observed dimer. The spectral features of the QD655-IgE-FcεRI are observed in the raw spectrum (**Figure 5.2C**; lower left subfigure; solid black line). In a two color SPT experiment, the proximity of a third QD to an observed dimer would disrupt one of the trajectories in the dimer. The diffusion coefficients of the individual trimer and dimer seen in this example are 0.013 and 0.024  $\mu\text{m}^2/\text{s}$ , respectively. These results demonstrate the ability of mcSPT to investigate the dynamics and composition of protein complexes.

### **5.2.2 Interactions with Membrane Components**

The dynamics of membrane proteins may be influenced by membrane-associated structures such as actin [8], clathrin [9] or other microdomains [10] and interaction with such structures could be correlated with oligomerization state. The HSM allows the simultaneous observations of several colors of QDs at the same time as other fluorescent probes that can be excited efficiently with 488 nm light, such as GFP. Here mcSPT is demonstrated using 4 colors of QD-IgE-FcεRI (605, 625, 655, and 705 nm) while simultaneously imaging GFP-actin. Imaging was performed on RBL-2H3 cells transiently transfected with GFP-actin. **Figure 5.3** provides observations that highlight several advantages of this technique.



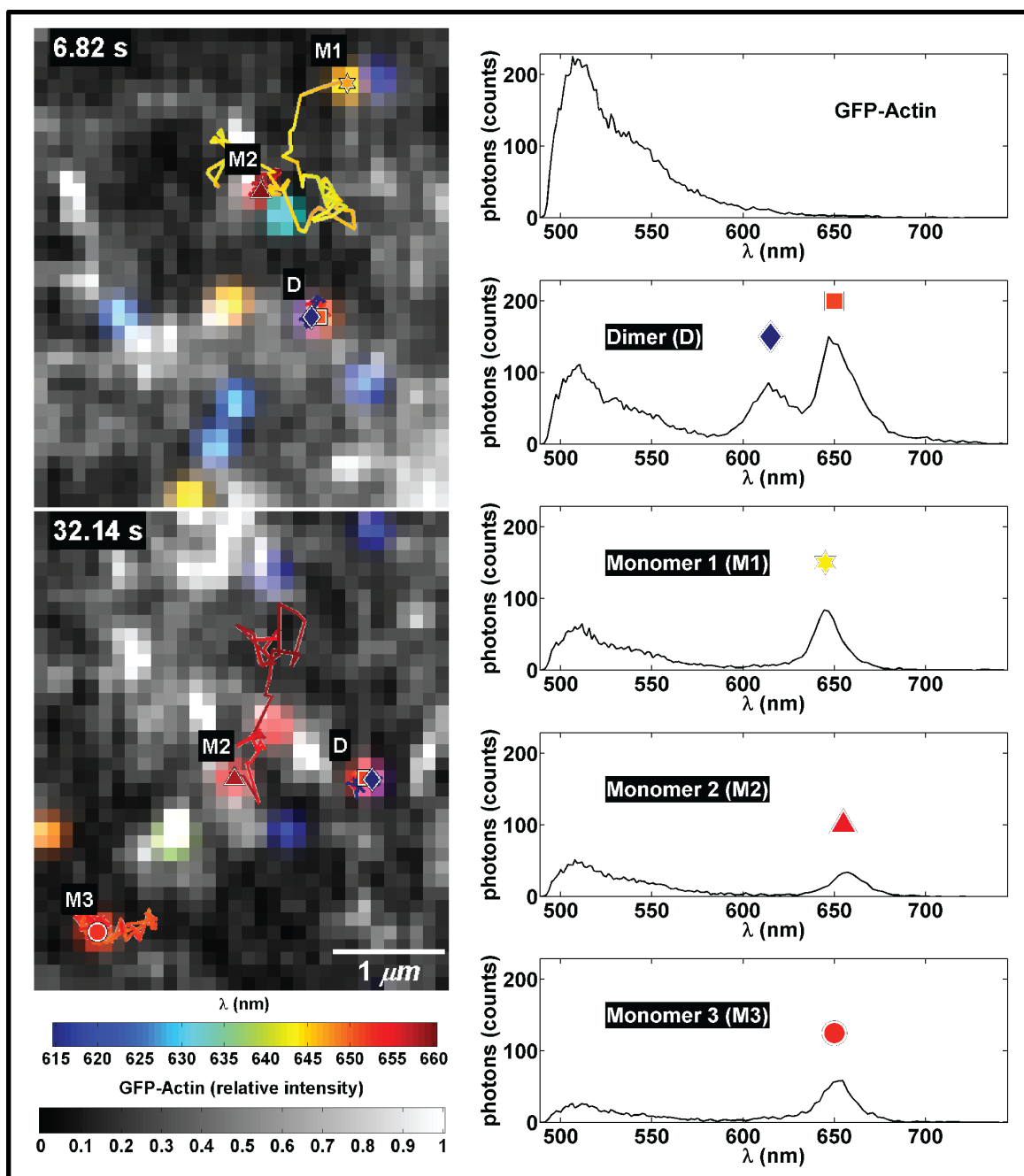


Figure 5.3: SPT of 4-colors (605, 625, 655, and 705) of QD-IgE-Fc $\epsilon$ RI on live RBL cells transiently transfected with GFP-actin acquired at 27 fps. (left) Two representative frames are shown. The GFP-actin presented in normalized gray scale is the spatially deconvolved portion of the spectrum between 500-570 nm. It is overlaid with Gaussian blobs reconstructed for localized QDs and trajectories for QD-IgE-Fc $\epsilon$ RI spanning the previous 3.7 s (100 frames; coloration of blobs and trajectories according to emission peak; see color bar). Colored symbols highlight QD-IgE-Fc $\epsilon$ RI positions at the specified frame, and representative spectra are shown to the right. Text identifiers (D, M1, M2, and M3) are used to indicate monomers (M#) and dimer (D) trajectories.

Comparison of the actin structure in the top and bottom images demonstrates how dynamic the actin structure is over the time course of this acquisition. Actin corralling of QD-IgE-Fc $\epsilon$ RI is also observed (red triangle and red circle in the bottom image). These results are consistent with previous reports of actin corralling first observed by tracking QD655-IgE-Fc $\epsilon$ RI with respect to GFP-actin [8]. However, these previous studies were limited to tracking in TIRF at the adherent surface since wide field imaging of actin structures at the apical surface was insufficient and point scanning confocal was too slow for tracking. Using the HSM, one can perform fast confocal imaging while simultaneously tracking single quantum dots. Moreover, the increased number of spectrally distinct QDs allow for tracking of many receptors simultaneously such that their interactions within the actin domains can be observed. The mobility of the dimer complex ( $0.004 \mu\text{m}^2/\text{s}$ ; purple blue diamond and red square, top and bottom) is less than that of highlighted monomers ( $0.044 \mu\text{m}^2/\text{s}$ ). A transition of the mobility of a monomer from relatively immobile (red triangle, top) to relatively mobile (red triangle, bottom) is observed. Crossing trajectories are appropriately connected due to the spectral information (red triangle and yellow star).

### **5.3 3D Hyperspectral Scanning of Live Cells**

Since this instrument is a line scanning system with optical sectioning capability, the microscope can be used to obtain hyperspectral z-slices of a sample. Using the fast scanning ability and a piezoelectric stage, the HSM can make three dimensional observations of samples with hyperspectral information, providing 5D data sets with spatial ( $x,y,z$ ), spectral ( $\lambda$ ), and temporal ( $t$ ) dimensions. A demonstration of live cell, 5D

imaging of three cellular markers is shown in **Figure 5.4** (see **Appendix B** for sample preparation and experimental methods).

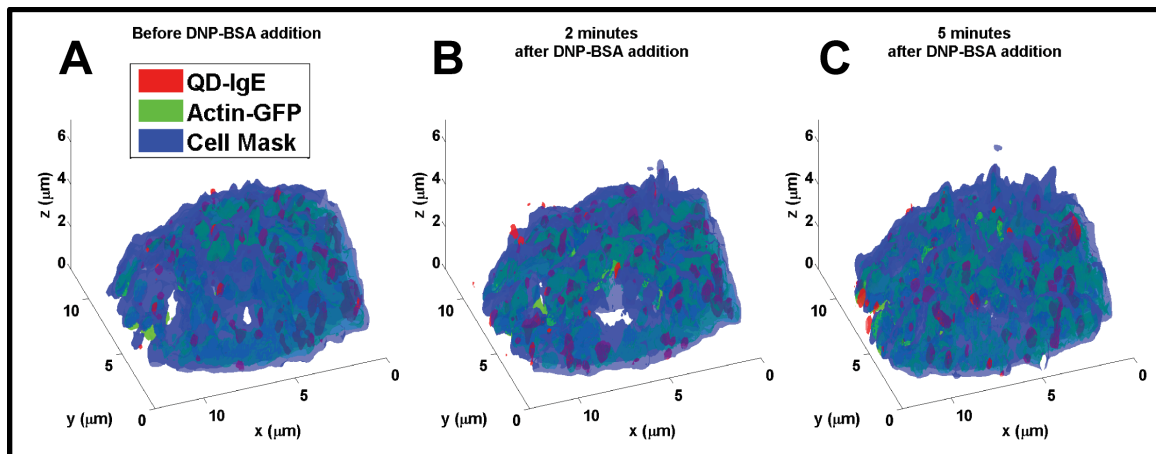


**Figure 5.4:** 3D scanning of live cells. Change in cell morphology upon activation of IgE-Fc $\epsilon$ RI by crosslinking with multivalent antigen (DNP-BSA). (A), (B), and (C) show 3D isosurface representations of deconvolved z stacks for a single cell acquired at 1 hyperspectral image stack every 7.72 seconds at several time points before and after activation as indicated. Cells are labeled with Cell Mask orange (blue), Actin-GFP (green), and QD-IgE-Fc $\epsilon$ RI (red).

## 5.4 Hyperspectral Superresolution

The purpose of this experiment was to determine if multicolor superresolution was plausible using the HSM. The challenge here is that there is only a single excitation laser source, which is the 488 nm laser line, and therefore in traditional STORM (stochastic optical reconstruction microscopy) the dyes used must either have significantly different emission spectra or more advanced analysis techniques must be used for spectral unmixing (such as multivariate curve resolution MCR [11,12]). Additionally, all dyes used must be excited by 488 nm and exhibit photoluminescence intermittency (blinking) using the same buffer composition, all while having sufficient photostability in a density appropriate for image reconstruction. The benefits are that this line scanning system is

semi-confocal and can therefore image at depth in the cell, and the hyperspectral ability adds spectral dimension for analyzing composition and density in the reconstructed images. Additionally, while not shown in this experiment, the high scan speed of this instrument may enable 3D multicolor hyperspectral superresolution images by taking a sufficient number of z-stacks while the oxygen scavenging buffer is still effective at keeping the dyes stable and blinking (typically about 1 hour with our current methods).

Sample preparations and imaging parameters for these experiments are described in **Appendix B. Figure 5.5** shows a live-view image of a Swiss 3T3 cell, fixed and labeled with Atto 532 clathrin and Alexa 488 tubulin. The spectra of each component are shown below the image for selected regions that likely contain mostly clathrin (green box, green plot, green color value in the image) and tubulin (red box, red plot, blue color value in the image), and the overall image spatial sum spectrum (blue plot).

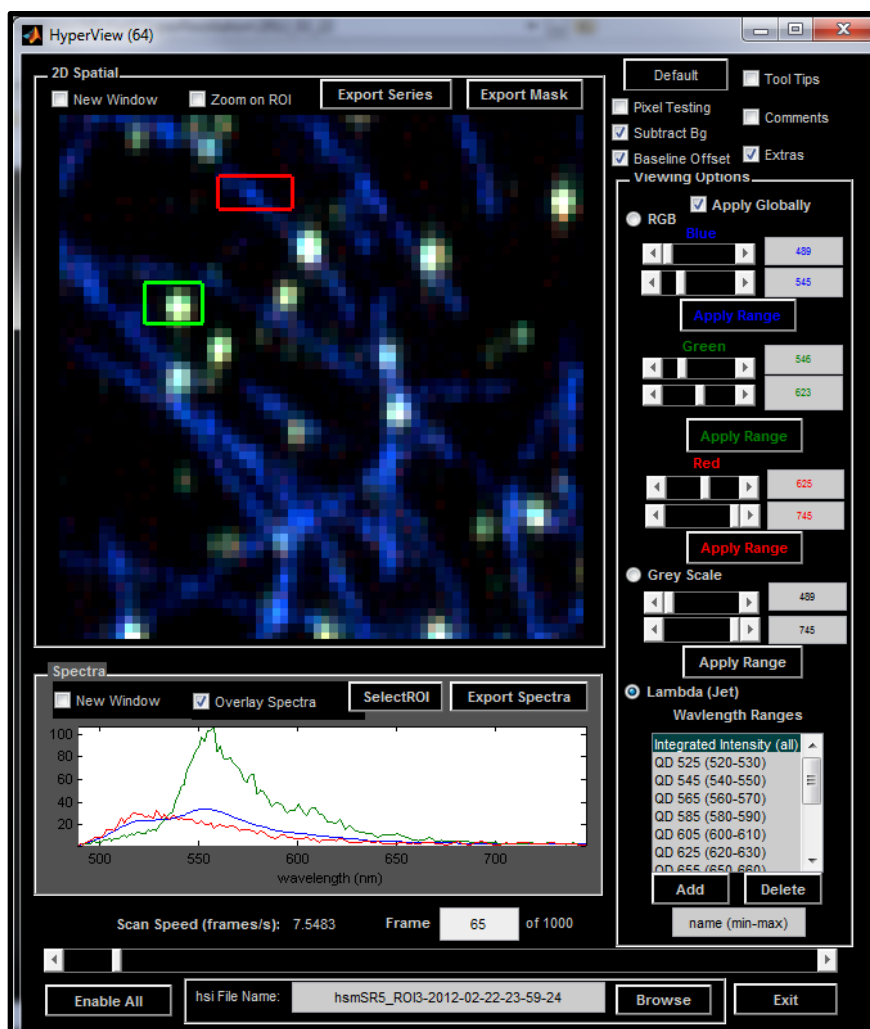
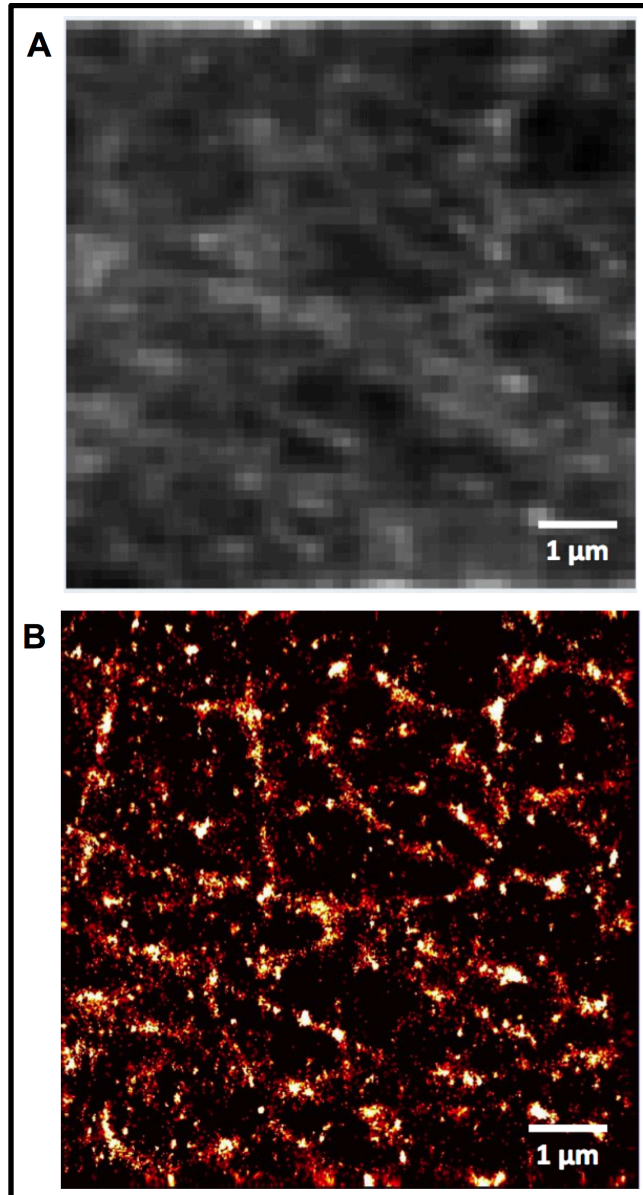


Figure 5.5: HSM SR live viewing mode. A raw (not localized) image showing Atto 532 labeled clathrin (green) and Alexa 488 labeled tubulin (blue) in Swiss 3T3 cells. With appropriate blinking statistics and curve resolution methods, multicolor SR image reconstruction should be possible. In this case the z depth is ~500 - 700 nm off of the glass coverslip surface into the sample.

Figure 5.6 shows a sample of a Swiss 3T3 cell with tubulin that is labeled with Alexa 488. The sum projection of 1000 scans is shown, as well as the composite image made from the fitted positions of individual emitters. Selecting only the emission from Alexa 488 reduces background (a smoothly selectable “filter” range out of the 128 spectral channels), illustrating a key benefit of the HSM. The analysis parameters used here may

not have been perfectly optimized, so a better image may be possible, but the technique establishes a first order proof-of-concept for SR using the HSM.



**Figure 5.6:** High density SR image using the HSM. (A) A sum projection of 1000 frames (line scans) of Alexa 488 labeled tubulin. (B) The same ROI now reconstructed using fitted positions from light in the emission spectrum of Alexa 488.

**Figure 5.7** shows an example of two-color SR using the HSM. Tubulin in Swiss 3T3 cells was labeled with Alexa 488 via secondary antibody, and clathrin was labeled with

Atto 532, as described in **Appendix B**. The observed emission spectra for each of these dyes are shown in **Figure 5.5**. Individual emitter localizations were performed after separating the spectra, once again by using a selected range from the 128 available spectral channels. Reconstructed images for each dye are shown in addition to a composite. Once again, the fitting parameters used here may possibly be improved, or more advanced fitting methods such as MCR may offer better results, but even with a coarse, pseudo-filter approach, it seems that multicolor SR is possible using this HSM system.

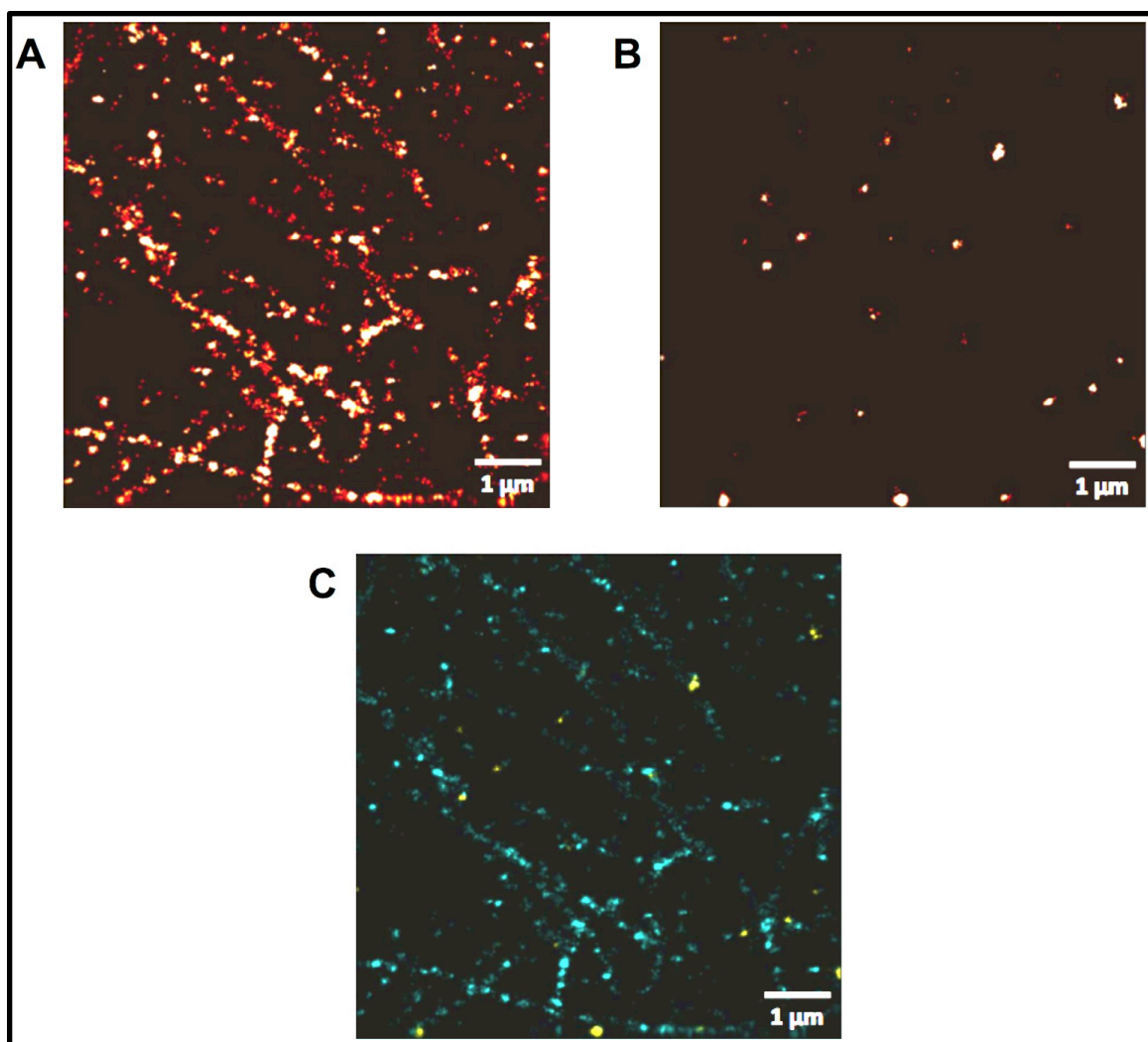


**Figure 5.7: Multicolor SR.** (A) A reconstructed image of localized Alexa 488 labeled tubulin from 8000 frames (line scans). (B) The same ROI, but now showing the reconstructed image from localizations of Atto 532 labeled clathrin. (C) A composite image of the Alexa 488 (blue) and Atto 532 (yellow), each localized independently.

During this experiment, there was some difficulty in getting more than two types of dyes to blink reliably without significant photobleaching. The high excitation intensity of the laser line along with the hyperspectral information would make this system well suited for performing multicolor SR experiments, as long as the probes can function under these conditions for up to an hour. A multi-state model was developed to try and gain some insight into the kinetics of the dyes during exposure to the excitation beam as the laser



line scans over the molecules. This model may help in selecting appropriate concentrations of the OSB components. **Figure 5.8** illustrates the model developed for this purpose. Starting with the initial conditions where all emitters are in the ground state at  $t=0$  and laser intensity zero, and then solving the system at one time step of  $t=\Delta t$  and the first step of the Gaussian of the laser line profile (each step is  $\sim 115$  nm at the sample for this system), then solve again using the new populations for the initial conditions, and continue stepping through the laser line intensity profile to simulate one scan over a given fluorophore.

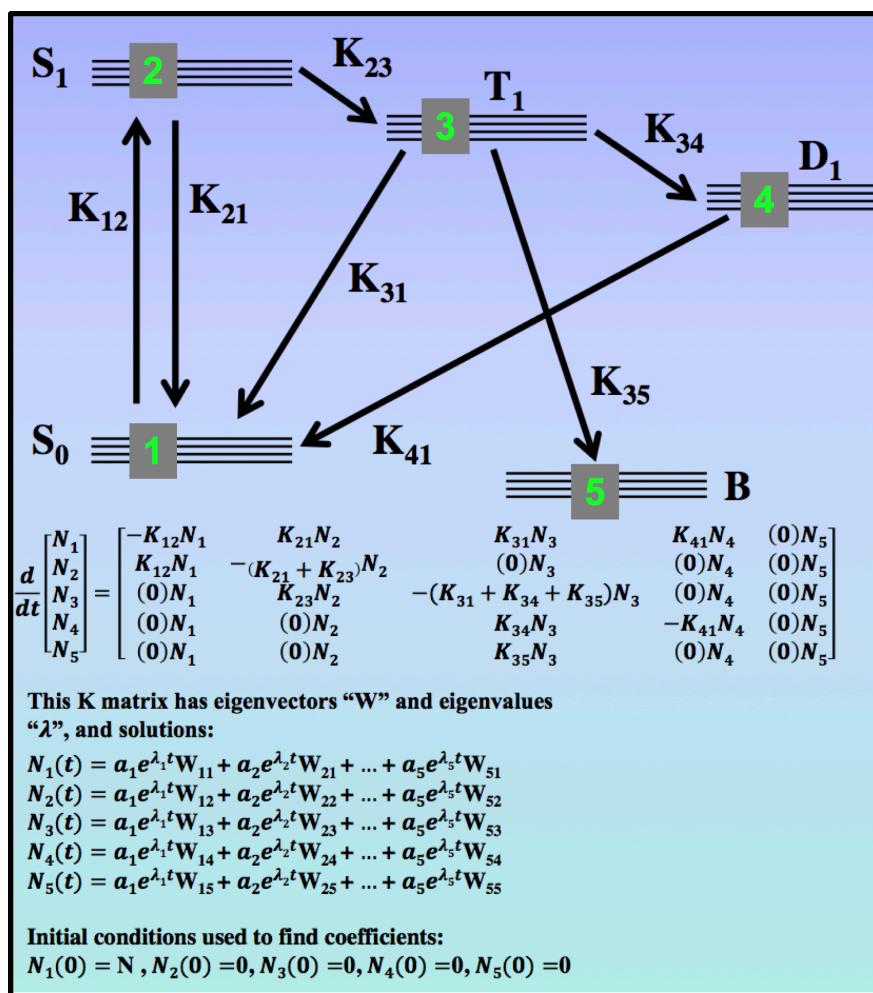


Figure 5.8: Five-state blinking dye kinetic model. A given blinking dye molecule has ground state S0, excited singlet state S1, triplet state T1, dark ionic state D1, and photobleached state B. This model describes the populations of states as a laser line is scanned across the molecule.

Figure 5.9 shows the results of a simulation of Atto 488, using the extinction coefficient at 488 nm excitation and the rate constants (K) found by Heveker, et al. [13]. The unknown rates were estimated and a summary is provided in Table 5.1. The low value for  $K_{41}$  dominates at this time scale, and the overall population (of 1000 emitters in the example) is found mostly in this long-lived dark state.

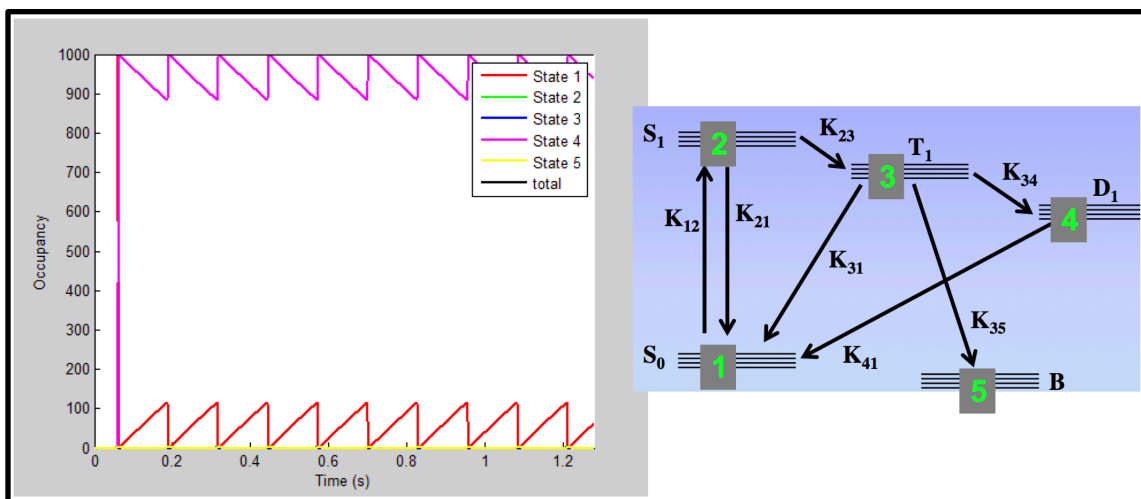


Figure 5.9: Population of states as a function of time. Only states 1 and 4 show appreciable dynamics on this time scale, which is mainly due to the mean lifetime of state 4, the dark ionic state.

Rate	Value	Source
K12	1.10E+07	I*sigma
K21	3.33E+08	1/lifetime
K23	1.00E+05	unknown, estimated
K31	2.00E+05	Hevekerl, et al. 2011
K34	2.00E+06	Hevekerl, et al. 2011
K35	1.00E+01	unknown, estimated
K41	1.00E+00	unknown, estimated

Table 5.1: Rate constants used in simulation.

## References

1. Cheezum MK, Walker WF, Guilford WH (2001) Quantitative comparison of algorithms for tracking single fluorescent particles. *Biophysical journal* 81: 2378–2388. Available: [http://www.cell.com/biophysj/fulltext/S0006-3495\(01\)75884-5](http://www.cell.com/biophysj/fulltext/S0006-3495(01)75884-5).
2. Zhang B, Zerubia J, Olivo-Marin J-C (2007) Gaussian approximations of fluorescence microscope point-spread function models. *Applied Optics* 46: 1819. Available: <http://www.opticsinfobase.org/abstract.cfm?uri=ao-46-10-1819>.
3. Smith CS, Joseph N, Rieger B, Lidke K a (2010) Fast, single-molecule localization that achieves theoretically minimum uncertainty. *Nature methods* 7: 373–375. Available: <http://www.pubmedcentral.nih.gov/articlerender.fcgi?artid=2862147&tool=pmc&rendertype=abstract>.
4. Huang F, Schwartz SL, Byars JM, Lidke KA (2011) Simultaneous multiple-emitter fitting for single molecule super-resolution imaging. *Biomed Opt Express* 2: 1377–1393.
5. Malik MD, Cutler PJ, Liu S, Byars JM, Lidke DS, et al. (2013) Multi-color Quantum Dot Tracking using a High-Speed Hyperspectral Line-Scanning Microscope. Manuscript in review.
6. Jaqaman K, Loerke D, Mettlen M, Kuwata H, Grinstein S, et al. (2008) Robust single-particle tracking in live-cell time-lapse sequences. *Nat Meth* 5: 695–702. Available: <http://dx.doi.org/10.1038/nmeth.1237>.
7. Andrews NL, Pfeiffer JR, Martinez a M, Haaland DM, Davis RW, et al. (2009) Small, Mobile FcεRI Receptor Aggregates Are Signaling Competent. *Immunity* 31: 469–479. Available: <http://www.pubmedcentral.nih.gov/articlerender.fcgi?artid=2828771&tool=pmc&rendertype=abstract>.
8. Andrews NL, Lidke K a, Pfeiffer JR, Burns AR, Wilson BS, et al. (2008) Actin restricts FcεRI diffusion and facilitates antigen-induced receptor immobilization. *Nature cell biology* 10: 955–963. Available: <http://dx.doi.org/10.1038/ncb1755>.
9. Wilson BS, Pfeiffer JR, Oliver JM (2000) Observing FcεRI Signaling from the Inside of the Mast Cell Membrane. *J Cell Biol* 149: 1131–1142 ST – Observing FcεRI

Signaling from the. Available:  
<http://jcb.rupress.org/cgi/content/abstract/149/5/1131>.

10. Kusumi A, Nakada C, Ritchie K, Murase K, Suzuki K, et al. (2005) PARADIGM SHIFT OF THE PLASMA MEMBRANE CONCEPT FROM THE TWO-DIMENSIONAL CONTINUUM FLUID TO THE PARTITIONED FLUID: High-Speed Single-Molecule Tracking of Membrane Molecules. *Annual Review of Biophysics and Biomolecular Structure* 34: 351–378. Available:  
<http://arjournals.annualreviews.org/doi/abs/10.1146/annurev.biophys.34.040204.144637>.
11. Haaland DM, Timlin J a., Sinclair MB, Van Benthem MH, Martinez MJ, et al. (2003) Multivariate Curve Resolution for Hyperspectral Image Analysis: Applications to Microarray Technology. *Proc SPIE* 4959: 55–66. Available:  
<http://proceedings.spiedigitallibrary.org/proceeding.aspx?articleid=891233>.
12. Jones HDT, Haaland DM, Sinclair MB, Melgaard DK, Collins AM, et al. (2012) Preprocessing strategies to improve MCR analyses of hyperspectral images. *Chemometrics and Intelligent Laboratory Systems* null: 1–10. Available:  
<http://linkinghub.elsevier.com/retrieve/pii/S0169743912000226>.
13. Hevekerl H, Spielmann T, Chmyrov A, Widengren J (2011) Förster resonance energy transfer beyond 10 nm: exploiting the triplet state kinetics of organic fluorophores. *The journal of physical chemistry B* 115: 13360–13370. Available:  
<http://www.ncbi.nlm.nih.gov/pubmed/21928769>.

## Chapter 6

### Conclusion

We have implemented a new high-speed laser line scanning hyperspectral microscope that is custom built specifically for multicolor single particle tracking of quantum dot labeled cell membrane proteins. This system simultaneously excites eight different species of quantum dots and uses their emission spectra as a means of independent sub-diffraction limited localizations. This enables the identification and tracking of multiple emitters within and through regions on the order of  $\sim 10$  nm, at a frame rate of 27 Hz, a spatial and temporal resolution necessary to observe various dynamics and interactions of membrane protein molecules in living cells. The primary goals of the system have been achieved by integrating several key components, including a 488 nm excitation laser line, a high-speed scanning mirror, fast EMCCD camera, and prism spectrometer.

The instrument has been calibrated and characterized for laser power (via AOM control), magnification, line scan angle, wavelength dependence on localization, 4D point spread function measurement, spectral calibration, spectral distortion and dispersion, spectral resolution, EMCCD gain calibration, EMCCD background and baseline correction, transmission efficiency, and aperture acceptance ratio. Quantum dot characterization has been performed, including calculations for cross-section and emission rates with saturation modeling, photostability and photoluminescence enhancement, fluorescence intermittency, emission spectra, intensity, and spectral shifting. Demonstrative experiments have been performed, including multicolor single particle tracking

(membrane protein oligomer dynamics and interactions with cytoskeletal actin), 3D hyperspectral scanning of live cells, and hyperspectral superresolution.

## **Future Directions and Improvements**

The HSM seems to be well suited for various experiments in quantum dot measurements. All of the quantum dot characterizations discussed in this document were performed with the intent of applying and using the information within the context of the biological experiments (the primary focus of the system). Thus, these studies were not thorough investigations, they were only extended to the degree necessary to enable protein tracking and further work is possible using the HSM. The high-speed scanning enables the study of blinking with good temporal resolution, the spectrometer enables spectral observations (individual and ensemble), and sensitive EMCCD and controllable laser offer numerous possible studies of quantum dots and other nanoparticles.

The 3D hyperspectral imaging of live cells discussed here was just a single experiment of this type using the HSM, and there can be a number of things to investigate on this front. While the overall 3D image rate is not fast enough to perform 3D multicolor SPT for membrane proteins (with the detail achieved in 2D experiments), slower processes can be observed, including cytoskeletal response, endocytosis, and exocytosis. Hyperspectral superresolution is another exciting opportunity. The methods described in this document are very preliminary to this emerging concept. More stable blinking dyes, improvements in imaging buffers, and MCR analysis methods may offer significant improvements. 3D hyperspectral superresolution seems to be achievable with at least two of the organic dyes already tested.

The HSM itself has room for improvement, including faster cameras, such as the complementary metal–oxide–semiconductor (CMOS) systems available at the time of this writing. Since the readout rate of the camera is the limiting factor in frame rate, improvement in this component should directly translate into higher acquisition rates. The HSM can also benefit from a line generator lens that has a lower fan angle since the cylindrical lens used to collimate the expanded line has a fairly short focal length (25 mm) compared to the line size at the lens, and this introduces some aberrations that ultimately result in loss of laser power in the excitation path. A line generator with a 5-degree fan angle (as opposed to the current 15-degrees) would change the required focal length of the cylindrical lens to 75 mm, and this should result in higher laser intensity and possibly reduced background from unintended excitation at the sample.

Overall, this new laser line scanning hyperspectral microscope design has been successfully implemented and demonstrated to operate with the intended performance, providing exciting new opportunities for observations in cell biology and nanotechnology.



# Appendix A

## Alignment

A good alignment of the optical components of the line scanning hyperspectral microscope is essential for obtaining high quality data that can be subsequently analyzed to achieve sub-diffraction limited spatial information with high temporal resolution. A number of assumptions are made regarding some of the trusted reference geometries, namely that the optics table is uniformly flat, that the microscope base components are aligned properly (objective, tube lens, ports, and other mounting hardware on and within the base unit) and that the base unit frame is aligned with the optics table such that the optical axis of the side port tube lens is parallel to the table surface. It is also assumed here that three lasers (red HeNe, green HeNe, and the blue 488 nm diode laser) have been coupled into single-mode fibers with FC connectors. References will be made to optical elements and parts using the conventions and diagrams found in **Chapter 2**. Unless otherwise specified, the  $z$ -axis will be along the beam (or emission light path), the  $x$ -axis will be parallel to the table surface, and the  $y$ -axis will be perpendicular to the table surface; and this convention will be relative to the beam path for each section (the  $x$ -axis in one section may be parallel to the  $z$ -axis in another if the beam has been reflected 90 degrees by a mirror, so the coordinate system will be relative to the beam or emission path optical axis).

## A.1 Reference Beam

The first step is to make a reference beam using the green HeNe laser that will be centered and collimated going into the objective port (RMS threaded) on the microscope base (Olympus IX-71). The purpose for this is to direct the reference beam out of the tube lens (through the side port) in order to align the remaining components to a good first approximation. A beam that is fairly well collimated and approximately centered relative to the objective port will provide a good reference optical axis. Excitation light that is propagating along this path into the microscope base will be centered on the back of the objective and emission light that is propagating along this path outward from the sample will continue to follow along the path as long as all other external optical elements are centered on this axis.

In order to make this reference beam, a 12-inch long cage system is created with four cage plates used to hold it straight and to make checking the beam centering with a cage alignment target (Thorlabs CPA1) quicker and easier. A longer alignment cage allows a more centered beam that is parallel to the intended optical axis. A micrometer adjusted  $x$ - $y$  translator stage is used to position the collimating lens relative to the fiber tip in order to provide the necessary accuracy when centering the beam. The collimating lens is held inside the SM1 threaded (thicker) part of the translator. The translator is attached to a cage plate on then end of the 12-inch cage system with an SM1 male to SM1 male lens tube adapter. The other end of the cage system has an SM1 male to RMS male adapter that will be attached to the objective turret on the microscope base (after removal of the  $x$ - $y$ - $z$  peizo stage. **Figure A.1** shows a picture of the reference beam system mounted to

the microscope base objective turret. A reference target (consisting of a post, post holder, cage plate, short cage rods, and cage alignment target, **Figure A.2**) can be used to verify that the beam exiting from the side port is parallel to the table surface, and minor adjustments can be made if necessary. This reference target should be locked at the beam height and kept aside for future system alignment.

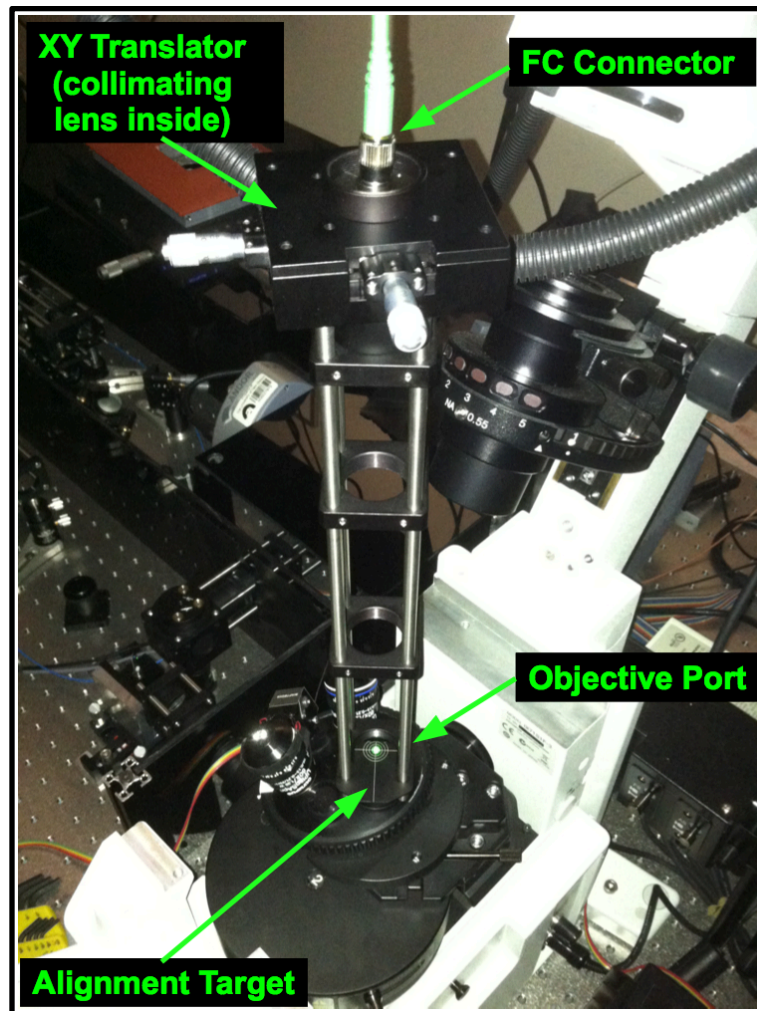


**Figure A.1: Reference Beam System.** The objective port here is just behind the cage alignment target and 30 mm cage plate.

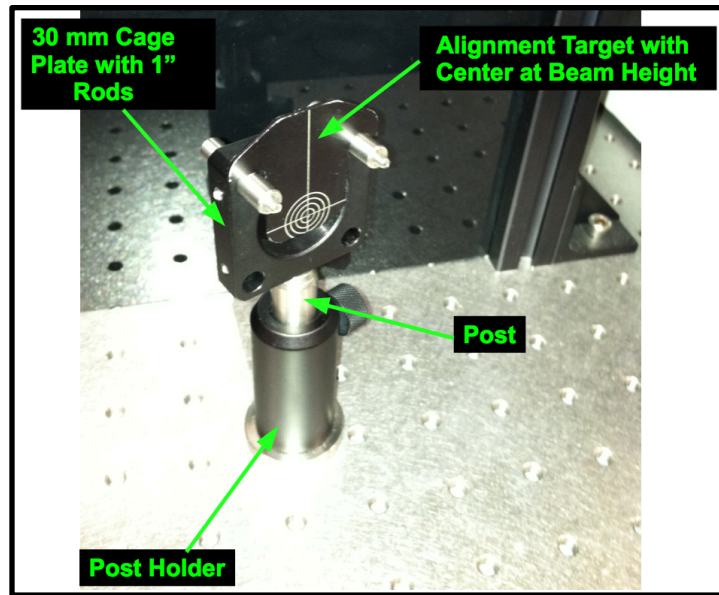


Figure A.2: Reference target. When set to a reference beam height this target is used to verify that the beam is parallel to the table by checking it at two or more locations on the table, separated by the largest distance that can be accommodated. It is also useful as a reference height for setting up the 30 mm cage systems that will hold the other optical elements.

With a centered, collimated beam projected into the objective port, the remaining elements can be aligned. Since there is a tube lens ( $f = 180$  mm) in the path, the light will be diverging out of the side port of the microscope base. Since a collimated beam is preferred for aligning the cage systems, the first element to align will be the achromatic doublet lens L2 ( $f = 50.8$  mm). If no other setup has been performed and there are no obstructions to the beam along the length of the optics table, one can use the reference target to check that a collimated beam going into the objective port will be once again collimated after lens L2 when that lens is positioned correctly along the  $z$  dimension. The part of the alignment does not need to be exact at this stage, and accurate alignment is difficult since the beam will be demagnified by the combination of the tube lens and L2 (beam diameter will be reduced by a factor of  $180/50.8 = 3.54$ ). Lens L2 is mounted in a

30 mm cage via SM1 tube attached to a z-axis micro-adjuster, and the cage is attached to the microscope base side port using a c-mount to SM1 tube adapter that is coupled to the 30 mm cage system (see **Figure A.3**).

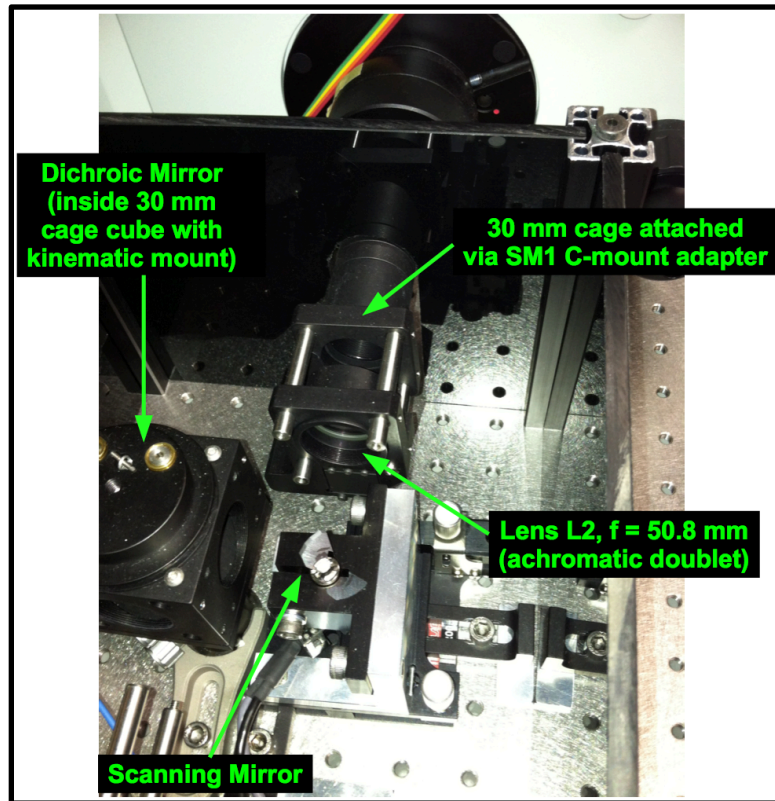


Figure A.3: Alignment of lens L2. The scanning mirror and dichroic are shown, already in position. The z-axis micro-positioner holding the SM1 tube is attached to the 30 mm cage system with the adjuster on the left side (obscured in this view angle). The side port of the microscope base lies just behind the ¼" black acrylic panel at the top of the figure. The c-mount to SM1 tube adapter attaches to and supports the 30 mm cage to the side port.

Lens L2 should now be centered along the x- and y-axes, and this can be verified using the reference beam and target, checking for beam height and angle at several positions along the path. If the scanning mirror and dichroic are already positioned correctly, one only needs to verify the beam along the excitation path. If the spectrometer is not already

positioned, one can also verify the beam using the reference target on that side as well. Since the scanning mirror and dichroic mirror can easily accommodate a minor angle within the  $x$ - $z$  plane, the more important thing to check here is that the beam is parallel to the optics table surface (zero  $y$ -axis component to the beam vector). This should be checked on the emission path as well (if those components are installed at this point), which will verify that the scanning mirror is set at the correct angle for the rotation axis (along the  $y$ -axis).

## **A.2        Scanning mirror**

If no other components are installed (besides lens L2), the scanning mirror is placed such that the focal point of lens L2 (and that of lens L1 when it is in position) is at the reflective surface of the mirror, centered on the axis of mirror rotation. During alignment, the mirror should be switched on and holding an angle in the center of the scanning range (zero degrees if the range is between -15 and +15 degrees). The mirror itself (Cambridge Technology 6210H) has a rated angular excursion of 40 degrees, but the mirror control board (Cambridge Technology 67121HHJ-1) allows for 30 degrees of rotation. However, the total scan required for this application is just a little over 1 degree, so there is plenty of room for an offset angle to be applied later (i.e. the angle in the  $x$ - $z$  plane does not need to be perfect at this point), but the basic idea here is to make a 90 degree angle, directing the reference beam coming from the microscope base side port into the dichroic mirror (or where it will be when it is positioned). While centering the rotational axis of the mirror with respect to the reference beam is fairly straightforward, positioning the mirror along the  $z$ -axis is not. The scanning mirror needs to be placed at the focal points of

lenses L1 and L2 to avoid any off-axis translation of the reflected light along the scanning dimension ( $x$ -axis), but those components have not been placed accurately yet so a first guess is made and then an iterative alignment procedure will be necessary since changing the  $z$ -position of the mirror will change the  $x$ -position of the excitation path between the dichroic and the fiber. After the dichroic is installed, if its angle is not changed, the dichroic can be translated along  $x$  and  $z$  to accommodate a  $z$ -translation of the scanning mirror, maintaining the beam alignment with the other excitation path elements. A first approximation for the scanning mirror  $z$ -position is made by measuring the distance from closest surface of lens L2, placing the mirror's reflective surface at the specified working distance from that side of the lens. This position will be verified later using the excitation beam.

It is extremely important for the scanning mirror's axis of rotation to be exactly parallel to the  $y$ -axis, with zero  $x$ - and  $z$ -components. For this reason, the mirror is mounted to a multi-axis kinematic base via a custom machined aluminum bracket that also serves as a heat sink for the scanning mirror's servo. Adjustment of the scanning angle is performed by rotating the mirror over large angles and measuring the reference beam height at various positions using the reference target. This can be done with the dichroic mirror in place, but this would require that the dichroic be positioned such that no angular  $y$ -component is introduced (and this could be verified by rotating the dichroic cube while in the path of a reference beam known to be parallel to the table, measuring the reflected beam height at different angles). This angle can be later verified by, among several other possible methods, scanning a focused laser line at high power over a planar sample of dyes or quantum dots, and then measuring the angle of the area that is photobleached.

## **A.3        Dichroic Mirror**

The purpose of the dichroic mirror is to reflect the excitation beam into the microscope base side port, while allowing the longer wavelength emitted light to propagate through it and into the spectrometer. Since the dichroic will be stationary during data acquisition, there is no limitation on its position along the  $z$ -axis -- it doesn't need to be set at a focal point of any lens. The dichroic mirror is designed to have maximal reflectance of 488 nm light and with maximal transmission of longer wavelengths when set at a 45-degree angle from the incident beam, giving a 90-degree angle to the excitation beam. It is important to note that the remaining emission path optical elements should not be aligned without the dichroic in place since the dichroic will introduce a slight offset to the  $x$ -position of the beam (see **Figure A.4**).



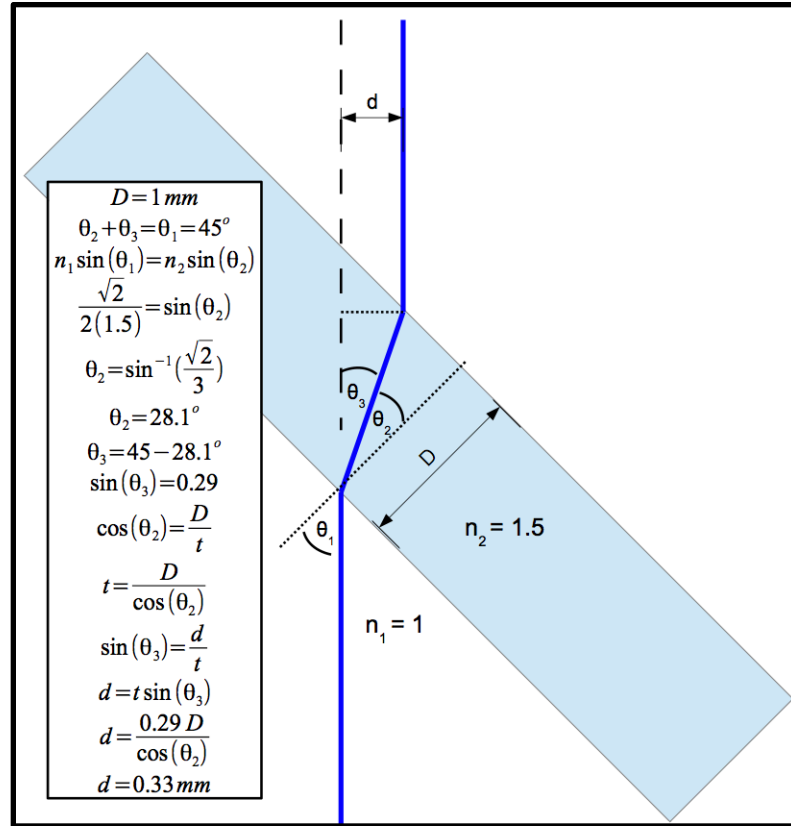


Figure A.4: Emission path offset due to dichroic mirror. The dichroic mirror has a substrate of glass with a thickness of 1 mm. Emission light or alignment beam light (shown here as a blue ray) incident from the bottom of the diagram is refracted at each air-glass interface, resulting in an overall shift of  $d = 0.33 \text{ mm}$ . Sizes and angles are exaggerated for easier viewing. For the calculation,  $t$  is the thickness of glass traversed by the ray traveling through the dichroic.

The dichroic is mounted in a 30 mm cage system cube with a 2-axis kinematic rotation mount. The cube is mounted on a fixed post that is clamped to the table. The  $y$ -position of the dichroic mirror is not very important since the overall diameter of the emission light path is much smaller than the height of the dichroic. The  $x$ - and  $z$ -positions of the dichroic are only important in the context of allowing clearance for physical support and room for adjustment of the scanning mirror  $x$ - and  $z$ -positions. However, the cage cube is used to approximately center lens L3 on the emission path via cage rods, so it is beneficial to center the cube to the reference beam  $x$ -position. The  $x$ -displacement

introduced by the dichroic (**Figure A.4**) is not very important for centering L3 since this lens has a focal length of 175 mm with a 25 mm aperture, and can easily accommodate the small displacement. The dichroic angle in the  $x$ - $z$  plane should be 45 degrees from the reference beam. This can be set using the reference target, measuring the distance to the center of a row of the M6 screw holes in the optics table at two  $z$ -positions, one close to the dichroic and one at the end of the optics table. The reference beam is a 543 nm HeNe laser, so most of this light will pass straight through the dichroic, but some will be reflected at the first air-glass surface, and some will be reflected off of the glass-air back surface of the dichroic – it is essential that the first reflection is used for the alignment. At this point there may be a small angle of the beam relative to the optics table surface ( $y$ -component), and it is extremely important to use the kinematic mount of the dichroic to change this angle to make the beam parallel to the optics table ( $x$ - $z$  plane). If this angle is not parallel it will introduce an angle to the excitation beam at the sample plane, resulting in an asymmetric excitation point spread function.

## **A.4        Excitation Path Cage Systems**

The line generator lens, cylindrical lenses, and lens L1 are all placed within 30 mm cage systems supported by adjustable posts that are clamped to the optics table. These cage systems are each aligned to the reference beam. Once again, it is important to select the beam that is reflected off of the front surface of the dichroic mirror. Once completed, the cage system alignment will then approximately center the SM1 mounted components, but since there will be some error introduced by tiny surface defects, minor flexing of supports, and possibly other minor defects introduced by the mounting hardware or the

optical elements themselves, the more sensitive components will require finer control over the  $x$ - and  $y$ -positioning, but the cage alignment will provide a good starting position. Lenses CYL2 and L1 have large focal lengths and 25 mm apertures, so they do not require  $x$ - $y$  translators, and can be mounted directly to the 30 mm cage systems via SM1 lens tubes. Once the cage systems are aligned, the collimated free space excitation laser beam is aligned to these cages.

**Figure A.5** shows the alignment of the 30 mm cage systems used to mount lenses L1 and CYL2. The optical elements are removed prior to alignment in order to allow the reference beam to propagate unperturbed through the entire excitation path. The cage that holds L1 is aligned first, followed by that of CYL2, and finally the line-generator lens optics cage. A final check can be performed by connecting the cage rods between the major sections, verifying that the threads line up and match easily. The optical elements will be placed (or replaced) after the cage alignment and after the 488 nm excitation beam is aligned to the cages and reference beam.

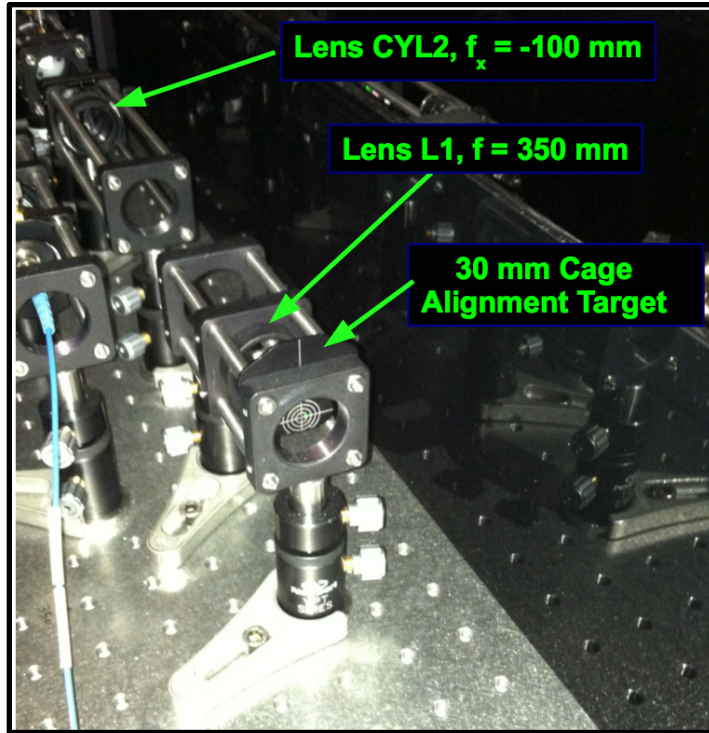


Figure A.5: Excitation path cage system alignment. When properly aligned, the reference beam reflected by the first surface of the dichroic will pass through the center (1 mm) aperture of the alignment target at each end of the cage system. For shorter cages, such as the one that holds lens L1, longer rods are used with an additional post (not shown) in order to maximize the accuracy of the alignment. These extended rods are then replaced one at a time with the shorter ones.

## A.5 Excitation Laser Beam

The 488 nm excitation laser beam is collimated using an air objective that is mounted in a  $z$ -translator within a 30 mm cage system. There is also an  $x$ - $y$  translator that positions the fiber tip relative to the objective. The cage that holds this free space collimation system is set parallel to the optics table using the reference target, and then clamped into position such that it is directed into a beam steering mirror set that will center the beam along the cage systems, making this beam co-linear (and antiparallel) to the reference beam used to position the cages. The beam steering mirrors are mounted in two-axis kinematic

adjusters, set at approximately 45 degrees relative to the excitation beam, and positioned such that the beam is reflected off of the centers of the mirrors. **Figure A.6** shows the layout of the free space excitation laser path, and an alignment target used for centering the beam in the cages. When properly aligned, both the green (543 nm) and blue (488 nm) beams will pass through the center of the alignment target at all positions within the 30 mm cage systems.

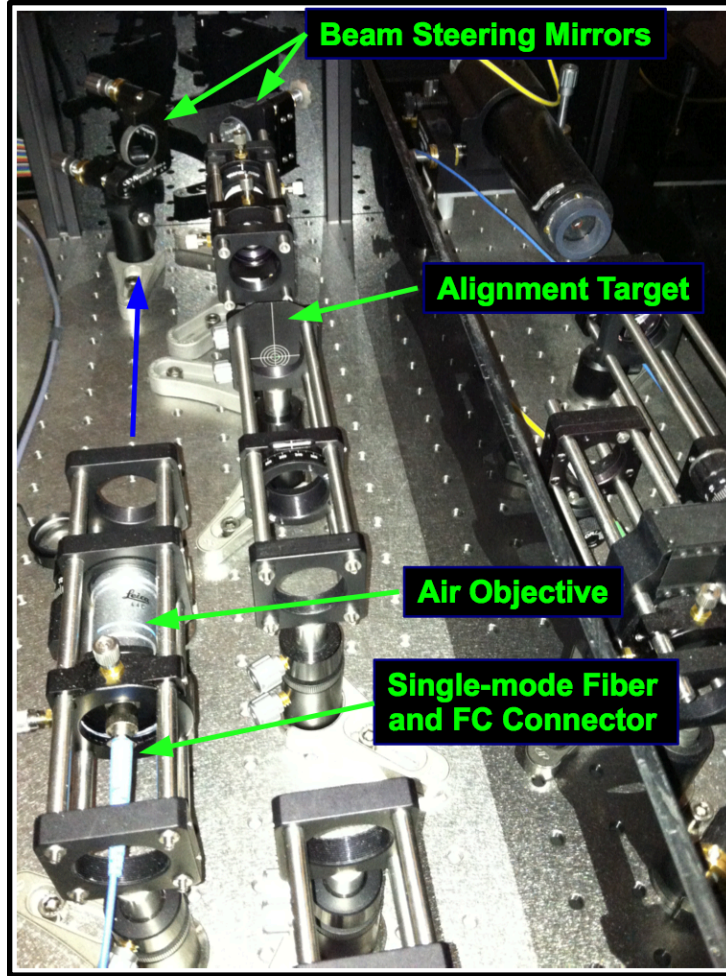


Figure A.6: Excitation laser beam alignment. Laser light from the fiber (lower left) is collimated by the air objective and propagates in the direction of the blue arrow, towards the first beam steering mirror (top left). The beam is reflected again at the second beam steering mirror, passing through the cage systems, towards the alignment target. When aligned, the green reference beam will pass through the center of the target (from the bottom of the figure) while the blue excitation beam will pass through the same target center from the opposite direction.

## A.6 Laser Line Generator Lens

Since the free space excitation laser beam is collimated, the  $z$ -position of the line generator lens is not important, but the having the proper  $y$ -position and angles in the  $x$ - $y$ ,  $x$ - $z$ , and  $y$ - $z$  planes are essential. An  $x$ - $y$  translator stage is used for the  $y$ -position and the

angle in the  $x$ - $y$  plane since the translator also allows a small amount of rotation. The lens itself has a unique shape and so a custom machined mount was created so that it could be placed in a standard SM1 lens tube. This mount can be rotated within the lens tube until it is very close to the angle needed, and then a small rotation adjustment can be made using the translator mount (which can slightly rotate the lens tube). In the current design, due to budgetary and spatial constraints, there are no degrees of freedom available for making adjustments to the angles in the  $x$ - $z$  and  $y$ - $z$  planes, but this did not seem to be a significant problem – a very minor adjustment to the second beam steering mirror (closest to the line generator lens) seems to correct for whatever small angles happen to be introduced, and this doesn't seem to affect the overall beam quality. Another important consideration is that as the lens is translated along the  $y$ -axis, a slight rotation is introduced by the translator mount (which operates in this way by design), and this slight rotation must be corrected by rotating the lens within the translator.

The current design uses a line generator lens that has a 15-degree fan angle, which happened to be the smallest angle available from common vendors at that time. A smaller fan angle would allow more space between the line generator and the first cylindrical lens, which would not only relax spatial constraints on mounting hardware (possibly allowing for multi-axis rotation and translation mounts), but also that the focal length of the cylindrical lens would be larger, which would decrease the sensitivity to tiny defects in the lens surface and curvature, especially with off-axis light. A newer line generator lens was found to be available with a 5-degree fan angle, and was acquired along with the appropriate cylindrical lens, but was not yet implemented at the time of this writing. This modification is expected to improve the quality of the excitation beam point spread

function and provide greater available intensity of the excitation light as it is focused to the line at the focal plane of the microscope objective.

**Figure A.7** shows the alignment of the line generator lens. The line needs to be centered on the target along the entire excitation path in order to match the reference beam, which will ensure the line is centered at the back of the objective. The line generator mount can be rotated slightly such that the line is along the vertical axis of the alignment target, and this should be verified at all positions along the excitation path. The  $y$ -position of the lens controls the intensity distribution along the  $y$ -axis of the line, and since changing the  $y$ -position may introduce a slight rotation, this adjustment should be completed before final rotations are made in the  $x$ - $y$  plane.

Lastly, the line generator lens is designed specifically for a Gaussian beam profile with a  $1/e^2$  diameter of 0.8 mm. Adjusting the  $z$ -position of the laser collimation objective lens relative to the fiber tip will change the beam diameter at the line generator lens, and the relatively large distance between the objective and the line generator lens ensures that any divergence angle introduced because of this will be very small. The targeted result from this is that the intensity distribution along the  $y$ -axis of the line is as uniform as possible (and one could also obtain the fan angle by measuring the line sizes at known spacing along the  $z$ -axis, but the intensity distribution is a far more important property in this application).



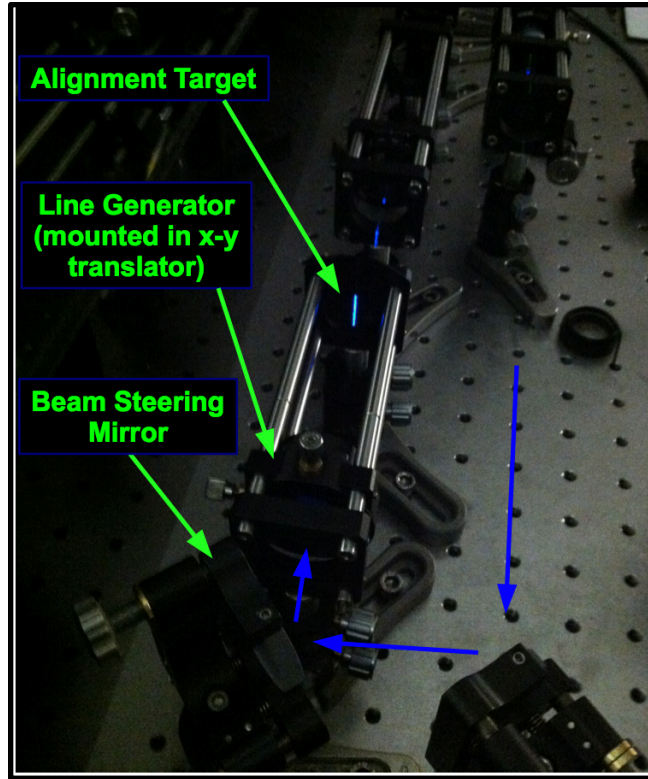


Figure A.7: Laser line generator lens alignment. The blue arrows represent the collimated free space laser beam as it is reflected by the beam steering mirrors, going into the line generator lens. The alignment target is used to verify the  $x$ -position and the angle of the line in the  $x$ - $y$  plane.

## A.7 Cylindrical Lens (CYL1)

The purpose of the first cylindrical lens is to collimate the laser line along the  $y$ -axis, providing a line of uniform intensity that is about 6.7 mm in length. This lens is held in a 30 mm cage system rotation mount. The lens itself has an overall circular aperture ( $d=12.5$  mm), while the lens surface is cylindrical, and it is held within the SM1 lens tube using an adapter. The alignment consists of translating the rotation mount along the  $z$ -axis within the cage system until the laser line is collimated along the  $y$ -axis, as can be measured at various points along the remaining excitation path. Since the excitation light

after the first cylindrical lens is collimated, the placement of this lens along with the line generator lens is independent of the next element (CYL2).

## **A.8 Lenses CYL2 and L1**

The second cylindrical lens (CYL2) is intended to expand the beam in the  $x$ -dimension to fill the back of the objective. Since this is a concave lens ( $f = -100$  mm), it is placed approximately 250 mm along the  $z$ -axis from lens L1, which is itself positioned about 350 mm from the scanning mirror's axis of rotation. Since both of these lenses have very long focal lengths and wide apertures, the  $z$ -position can be set by measuring the distance between elements ( $\pm 1$  cm will have almost no observable impact on the overall beam quality), and the  $x$ - and  $y$ -positions along with the angles in the  $x$ - $z$  and  $y$ - $z$  planes can simply rely on the alignment of the cage systems in which they are mounted.

## **A.9 Overall Excitation Path**

**Figure A.8** shows a white paper strip resting on one of the cage plates in the reference beam alignment cage that is attached to the microscope objective turret. In this case, the laser line is shown before collimation by CYL1, illustrating that the blue excitation beam is centered with the green reference laser, and this should be verified throughout the excitation path. When the laser line is collimated and expanded to fill the back aperture of the objective (and all excitation elements are in place), ideally the beam will form a rectangular shape on the paper strip, centered in the aperture defined by the RMS threaded objective port.

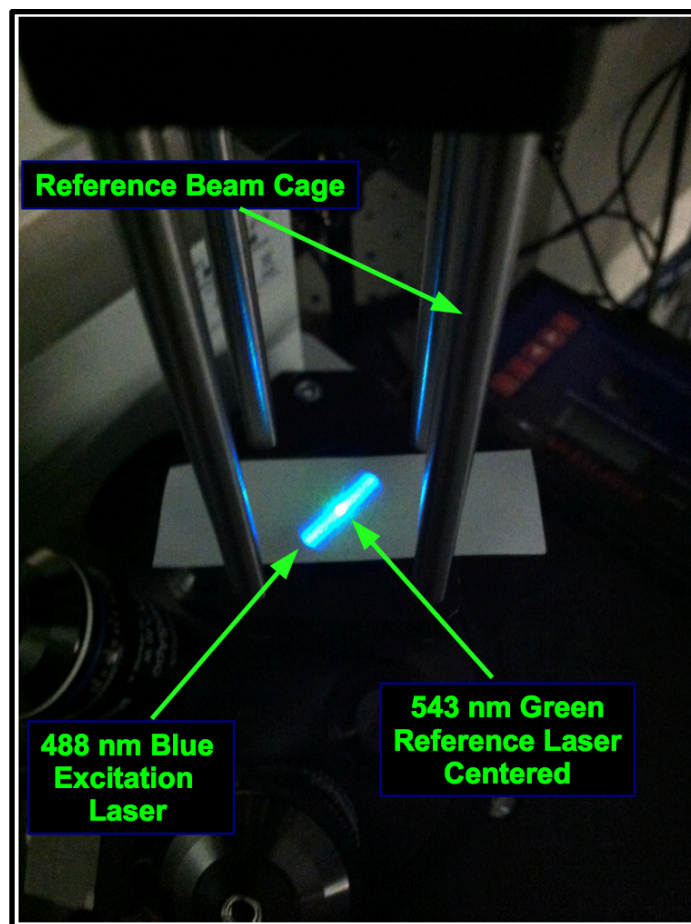


Figure A.8: Overall excitation beam alignment. A paper strip is set on the cage plate closest to the objective port in order to see both the excitation beam (coming up from the base) and reference laser beam (directed down from the top of the cage) in alignment with respect to each other and the objective when it is placed. With the excitation laser line centered in the  $x$ - and  $y$ -dimensions along the entire excitation path, the angle and position should be correct up to the objective port. In this figure, the green laser is somewhat difficult to see against the blue line, but this is much easier when observing it directly.

The excitation path can now be considered aligned well enough at this point such that the reference beam can be used to align the emission path elements. There will be some fine-tuning required for the excitation path elements, but that will require the use of the CCD cameras, and so the emission path will need some basic alignment first.

## A.10 Widefield Emission Path

Emission light collected by the objective will exit the microscope base and will be de-scanned such that the emission light will be centered along that path regardless of the scanning mirror angle, and this should already be the case if the excitation path has been aligned correctly up to this point. This will be verified later during a final check of the alignment. **Figure A.9** shows the emission path elements from the dichroic mirror to the widefield camera.

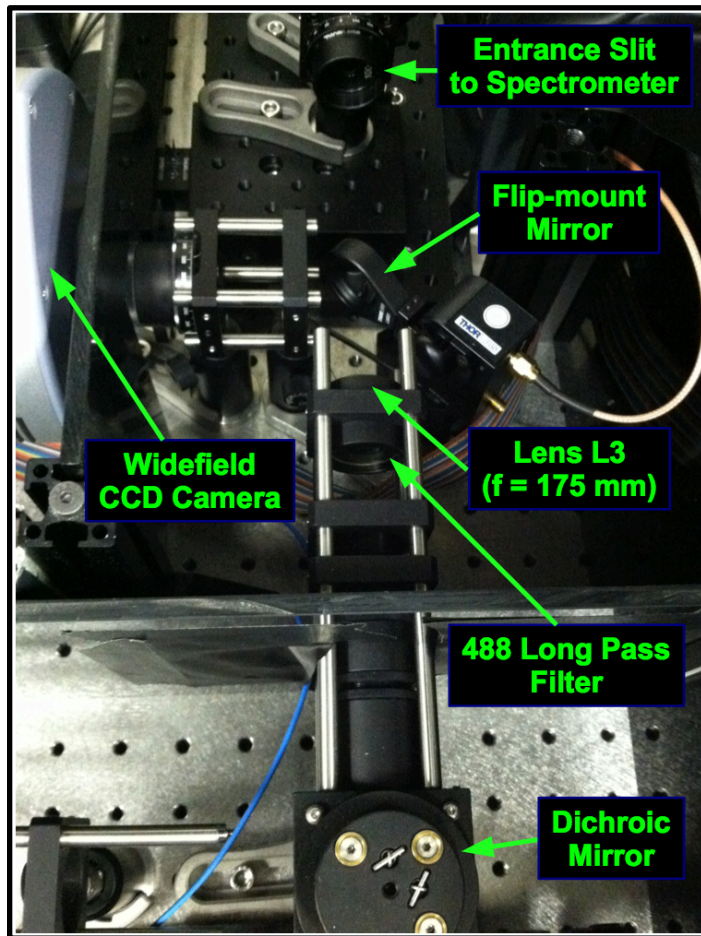


Figure A.9: Widefield emission path. Lens L3 ( $f = 175$  mm, achromatic doublet) is mounted in an SM1 lens tube held in a 30 mm cage system that extends from the cage cube holding the dichroic mirror. The flip-mount mirror is shown in the down position, directing the light into the widefield CCD camera, which is mounted on a 30 mm rotation plate. The entrance slit to the spectrometer is shown near the top of the figure, and is positioned at the focal point of lens L3.

Placements of the 488 long-pass filter, lens L3, and the widefield camera are initially performed by measuring (or in some cases estimating) the distances between elements, and for most cases up to this point, it has been found sufficient for placement along the  $z$ -axis due to the fairly long focal length of lens L3. The  $x$ - and  $y$ -positions of the long-pass filter and lens L3 are already set sufficiently well by the 30 mm cage system. The flip-mount mirror and widefield camera are fairly easily aligned using the green reference beam and an alignment target in the cage system that holds the CCD camera. It has been found that the CCD camera sensor is not perfectly aligned within the housing, in terms of both the  $x$ - and  $y$ -positions and the angle within the  $x$ - $y$  plane – this can be corrected later with a slight translation and/or rotation when a fluorescent sample is centered and in focus under widefield using the eye-pieces (assuming an inherent trust of the microscope base internal alignment).

## **A.11 Fine-tuning the Excitation Path**

With the emission path aligned (to first order) up to the widefield CCD camera, attention can be given to the finer adjustments necessary for the excitation path elements. The first step is to remove the reference beam cage, replacing it with the 60x water objective (and replacing the  $x$ - $y$ - $z$  piezo stage). A planar sample of quantum dots (or fluorescent beads or dyes) is used for verifying the alignment of the excitation beam. The planar sample of quantum dots is prepared by diluting 1  $\mu\text{M}$  quantum dot stock solutions to 20 nM in PBS and then placing  $\sim 300$   $\mu\text{L}$  of this dilution into each well in an 8-well chamber. The solution is then incubated at 4° C for at least 2 hours to ensure an even distribution over

the glass surface. The quantum dot solution was then carefully removed from each well and replaced with 1x PBS. This produces a thin plane of quantum dots adhered to the glass surface, but with relatively very little in solution, such that almost all of the fluorescent light emitted will be from the sample plane, where the emitter density is high enough to clearly display the geometry of the excitation beam at the focal plane.

With a planar sample loaded it is placed in focus at first by using the eyepieces and then by using the widefield CCD camera. If the sample is out of focus on the widefield CCD, minor adjustments are made to the  $z$ -positions, starting with the most sensitive elements in the emission path (lens L2), and moving to the least sensitive elements (L3 and the CCD itself). Care should be taken to ensure that the lenses and CCD are estimated to be within at most a few millimeters of the specified working distances from the relevant surfaces or there is likely something else that will need to be adjusted first. While checking the focus of the widefield, it is also useful to verify the  $x$ - and  $y$ -position by loading a sample (or finding something in the planar sample) that has a unique feature which can be centered in the field of view using the eyepieces and then also in the widefield CCD camera.

## **A.12 Spectrometer Alignment**

The spectrometer alignment, like that of the other components described previously, is done by first measuring the distances between surfaces and centering with a reference beam and then fine-tuning their positions using the camera with a fluorescent sample or calibration source. If previously removed, the collimated reference beam (green HeNe

543 nm laser) must be replaced and aligned to the excitation path cage systems, and removing the  $x$ - $y$ - $z$  piezo stage.

**Figure A.10A** shows the relative positions of the spectrometer components in the  $x$ - $z$  plane. In this case the  $x$ -axis is vertical and the  $z$ -axis is horizontal, and the distances here are determined by the spectrometer design. The entrance slit is placed (within the rotation mount and  $x$ -translator stage) at  $\sim 175$  mm from lens L3 and centered in the  $x$ - $y$  plane using the reference beam. After the rotation mount is fixed in position, the slit is removed from the rotation mount to allow easier alignment of the remaining spectrometer components. The concave mirror is placed first, at a  $z$ -position of 323 mm ( $261 + 62$ ) measured from where the slit would be and is centered in the  $x$ - $y$  plane using the reference beam (the reflected beam should be coaxial to the incident beam). Then the first surface of the spherical prism is placed at 261 mm from where the entrance slit would be and the reference beam is again used to center the spherical prism in the  $x$ - $y$  plane. A reference target (set to the beam height within the spectrometer) is placed after the spherical prism and the prism is then rotated within the mount until the transmitted reference beam is on the  $x$ -axis of the target as demonstrated in **Figure A.10B**.

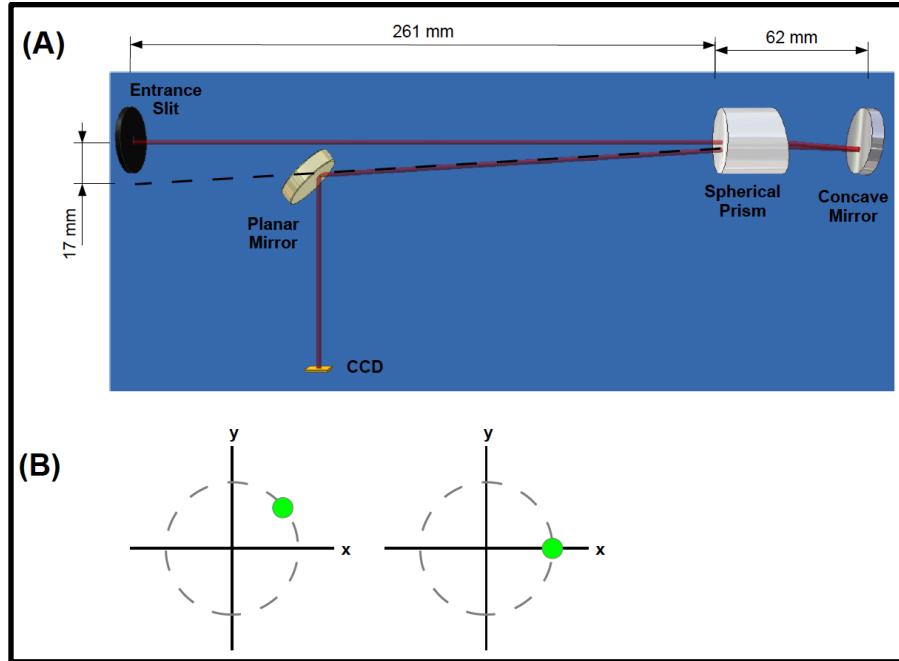


Figure A.10: Spectrometer layout and alignment. The diagram shown in (A) illustrates the positioning of the elements in the  $x$ - $z$  plane ( $x$ -axis is along the vertical direction and the  $z$ -axis is horizontal). The transmitted reference beam projected onto a reference target that is placed between the spherical prism and concave mirror is depicted in (B). The dashed line represents the possible positions of the beam on the target as the spherical prism is rotated in the  $x$ - $y$  plane. The left side shows the beam when the prism is not at the correct angle and the right side is the desired result.

Once the spherical prism has been determined to be at the correct position and rotation, the concave mirror is rotated to create the proper angle of the reflected beam in the  $x$ - $z$  plane (this is done by rotating the post, not the kinematic mount since that can introduce an angle relative to the  $y$ -axis). The reference target is placed such that it is centered at  $x = 17$  mm from where the entrance slit would be, as shown in **Figure A.10A** and the concave mirror is rotated to center the reflected beam on the reference target. As the concave mirror post is rotated, there should be no change in the  $y$ -position of the reflected beam, and if so, one or more of the previously aligned components may need to be adjusted.



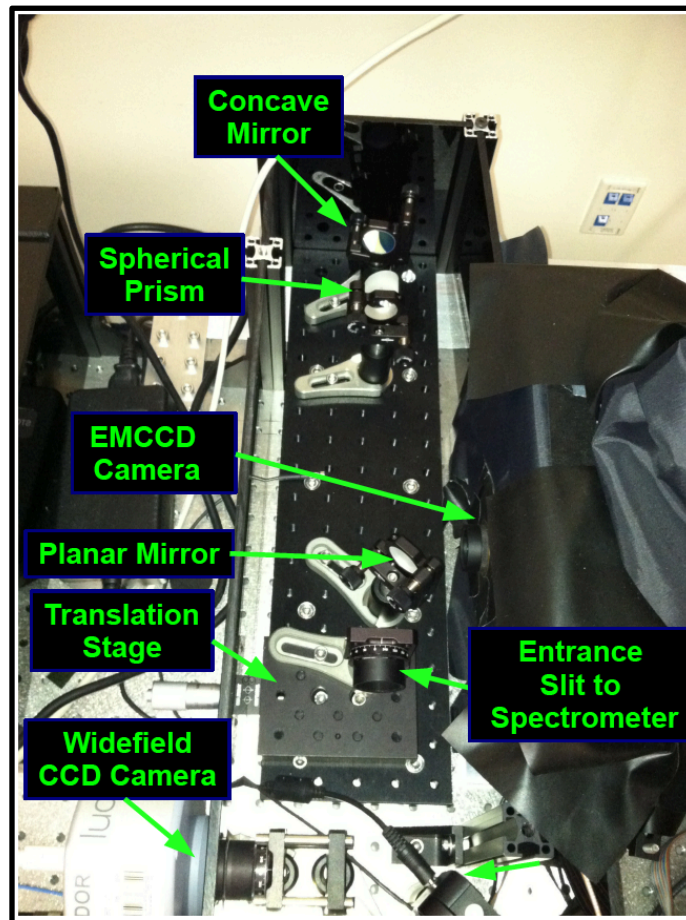


Figure A.11: Spectrometer and EMCCD. The spectrometer components are all mounted to a removable breadboard to facilitate the setup and it allows the entire spectrometer to be removed as a single unit while maintaining the relative positions of the components. The emission light path just clears the mounting hardware for the planar mirror by several mm (more than the required aperture of  $\sim 1$  mm at that position).

**Figure A.11** shows the actual spectrometer hardware (as of this writing). The entrance slit is  $100\text{ }\mu\text{m}$  wide (along the  $x$ -axis), and the overall point spread function of the system is very sensitive to the slit position and angle, so the slit is mounted in a rotation mount that is set on a translation stage that allows micrometer control over the  $x$ -position. This not only makes the centering of the slit easier, it also allows one to intentionally place an

edge of the slit into the emission path such that the slit image is observed on the EMCCD camera. This allows the camera to be placed at the correct position along the  $z$ -axis (where the edge of the slit is in focus).

When the correct angle is made to the concave mirror (by having the reflected reference beam centered at the target at  $x = 17$  mm from the slit, measured in the same  $x$ - $y$  plane as the slit), the planar mirror is then positioned such that the reflected beam from the concave mirror can be selectively reflected into the EMCCD camera, without obstructing the incoming beam. The angle of this planar mirror is such that the beam will be reflected at about 90 degrees into the camera. The overall magnification of the spectrometer is close to 1, so the camera will be positioned where the total distance of the beam path from the first surface of the prism spectrometer to where the EMCCD sensor will be is about 261 mm (the same as the distance from the slit to the first surface of the prism). It is important to keep the camera off (shutter closed) and capped for added protection during initial alignment. The camera is positioned within the  $x$ - $y$  plane using the reference beam and then at the approximate  $z$ -position, using only a measurement at first. This concludes the initial emission path alignment that is preformed using the reference beam and the spectrometer entrance slit can be replaced and the piezo stage can be re-installed.

## **A.13 Fine-Tuning the Emission Path**

This phase of the alignment procedure involves loading a planar sample of quantum dots (QDot 525), exciting the sample with the 488 nm laser line and viewing the emitted light on the EMCCD camera in live focus mode, which will show the  $\lambda$ - $y$  data – not scanning the laser line, but rather keeping the line at a single  $x$ -position in the sample instead. The

emission spectra of the quantum dots will be distributed along the  $x$ -dimension of the camera, and each quantum dot will have a unique emission peak. In addition to this, each quantum dot will blink, and this combination results in a number of features in the field of view that can be brought into focus when the camera is positioned correctly.

The camera height is adjusted such that the line ( $y$ -axis) is centered in the field of view. The camera's  $x$ -position is set such that the quantum dot 525 emission is fully within the pixel array and has at least 2 rows of dark pixels (which will be used for a frame-by-frame baseline adjustment in post processing). The angle of the camera within the  $x$ - $y$  plane can be verified by viewing emissions from the overhead lamp (in the illumination tower on the microscope base), verifying that the spectra are aligned along the  $x$ -axis, and this can be done while the quantum dot sample is still loaded. The  $z$ -position is set correctly when the individual quantum dots are as clearly resolved as possible. The entrance slit can also be translated along the  $x$ -axis such that one of the edges of the slit is slightly obstructing the emission path and this will be in focus at the EMCCD camera if the sensor is at the correct  $z$ -position. Once the EMCCD camera is in position, the slit is translated to an  $x$ -position where the maximum amount of light reaches the camera (the point at which the slit will be centered on the emission path).

## Appendix B

### Materials and Methods

#### B.1 Imaging of QDs non-specifically adhered to glass

The quantum dots (Invitrogen Corporation Qdot® 525, 565, 585, 605, 625, 655, 705, and 800) were each diluted to 50 pM in 1x PBS and then mixed together in equal volumes. 300 uL of this mixture was then added to each well in an 8-well chamber. 10 uL of 2M NaCl (aqueous) was then added to each well and then incubated at 4° C for up to 8 hours to allow the quantum dots to attach to the glass. The solution was then replaced by 1x PBS. 250 frames of data (providing  $x$ ,  $y$ , and  $\lambda$  information) were acquired at 30 frames/sec over an area of 30  $\mu\text{m}^2$  (the intended scan rate for our typical live cell imaging) with an excitation laser line intensity of  $\sim 1000 \text{ W/cm}^2$ . Continuous planar samples were also used for obtaining ensemble emission spectra of each lot of quantum dots as well as laser line alignment and characterization. For this we diluted each type of quantum dot to 20 nM in PBS and placed 300 uL of this dilution into each well in an 8-well chamber. 10 uL of 2M NaCl (aqueous) was added to each well and then incubated at 4° C for 8 hours. The quantum dot solution was then removed from each well and replaced with 1x PBS.

#### B.2 Reagents

Purification [1] of mouse monoclonal anti-DNP IgE and preparation [2] of functionally monovalent QD-IgE was previously reported. Streptavidin conjugated quantum dots were

purchased from Invitrogen either individually (525-Q10141MP, 565-Q10131MP, 585-Q10111MP, 605-Q10101MP, 625-A10196, 655-Q10121MP, 705-Q10161MP, 800-Q10171MP) or in the Qdot® Streptavidin Sampler Kit (Q10151MP). Biotin-X, SSE used for monovalent biotinylation of IgE for linkage to streptavidin QDs was purchased from Invitrogen (B6352). Biotin was purchased from Invitrogen (B1595). CellMask™ orange plasma membrane stain was purchased from Invitrogen (C10045). Multivalent DNP-BSA was purchased from Invitrogen (A23018). DNP<sub>3</sub> (manuscript in preparation Mahajan A, Barua D, Cutler P, Lidke DS, et al.), which is a small trimer of peptides that presents three DNP moieties for crosslinking DNP-specific IgE, was synthesized by AnaSpec (Fremont, CA). Plasmid used for transfection of GFP-actin into RBL-2H3 cells was purchased from Clontech (pAcGFP1-Actin 632453). Biotinylated EGF at a 1:1 ratio was purchased from Invitrogen (E-3477). The EGFR inhibitor PD153035 was purchased from Calbiochem (234491).

### **B.3 Image Acquisition for SPT Experiments on Live Cells**

Samples were maintained at 34-36 °C using an objective heater (Bioptechs, Butler, PA, USA) for imaging. For an acquisition rate of 27 fps, a region of interest (ROI) of 3.7 µm in *x* and 7.4 µm in *y* is acquired. This ROI consists of 32 steps (*x* dimension; ~0.116 µm steps) of the line across the sample by the scanning mirror and 64 pixels (*y* dimension; ~0.116 µm pixel size) along the line.

## B.4 Single Particle Tracking (Preprocessing, Localizations, and Trajectory Building)

Immediately prior to the acquisition of each HSM image, 1000 frames of dark images were acquired for background correction. The mean dark image was subtracted from each frame of the HSM image. The spectrometer was aligned so that several columns of spectral pixels are dark due to a long pass filter.. The mean value of a dark column of pixels was subtracted from the SPT image to correct a baseline offset. The HSM image was then multiplied by a calibrated gain factor [3] to convert arbitrary pixel counts to photons.

The steps in SPT in an HSM image are similar to steps used in traditional SPT algorithms: image segmentation, single particle localization, and trajectory building. Uniform and maximum filtering procedures outlined in previous work by Huang et. al. [4] for two dimensions are expanded to three dimensions  $(x,y,\lambda)$  and used to identify centers for sub-volumes in which to localize single molecules. The empirically determined sub-volume size used for single molecule localization in this work was 25 spectral pixels by 7 spatial pixels by 7 spatial pixels. A 3D Gaussian PSF/spectral model and Poisson noise model (**Appendix E**) were used to model the spatial and spectral features of individual QDs. The variance in the parameters estimated by the localization algorithm converges to the CRB (**Figure E.1, Appendix E**). Multiple 3D Gaussians were used to fit multiple spatially and spectrally overlapping QDs (**Figure E.2, Appendix E**). An artifact of using a line-scanning instrument is that blinking during the scanning of a single QD causes errors in QD localization in the scan direction (**Figure E.3, Appendix E**). Typically, each sub-volume was fit using 1-4 emitter models. Accurate fits were then

selected using an empirically derived filtering scheme. Trajectories are built from filtered localizations using a cost matrix approach to form a linear assignment problem [5] (Appendix E).

## **B.5 Cell Culture**

A431 human epithelial carcinoma cells were cultured and passaged in DMEM (Sigma-Aldrich), with 10% FBS (Invitrogen), penicillin, and streptomycin [6]. RBL-2H3 cells were cultured and passaged using MEM (Gibco® 11095-080) supplemented with penicillin-streptomycin, L-glutamine, and 10% FBS [7,8]. For all experiments using GFP-actin, RBL-2H3 cells were transiently transfected by electroporation with an Amaxa Nucleofactor II using program T-020. Transiently transfected cells were used within 24-48 h of transfection. For all image acquisitions, cells were plated in Lab-Tek 8-well chambers (Thermo Scientific, 177402) approximately 24-48 hours prior to the experiment at  $\sim 2 \times 10^4$  cells per well.

## **B.6 Cell Treatment for SPT of QD-IgE**

Procedures for labeling RBL-2H3 cells with QD-IgE for SPT were adapted from previous work [2]. For mcSPT experiments, cells were incubated in 200  $\mu$ l of Hanks' balanced salt solution (HBSS) with 1 nM of each color of QD-IgE simultaneously for 15 min at 37 °C. For the experiment, cells were incubated in 200  $\mu$ l of HBSS with optimized concentrations of each color of QD-IgE (2 nM of 605, 625, and 655; 4 nM of 565 and 585; 10 nM of 525, 705, and 800) for 15 min at 37 °C. Final volume of HBSS in each well was 200  $\mu$ l. All SPT experiments were performed within 1 hour of labeling. For the mcSPT experiment (**Figure 5**), 100  $\mu$ l of crosslinker (DNP<sub>3</sub>; final concentration of 1 nM)

equilibrated at 37 °C was added to the well ~7 minutes prior to the collection of the acquisition. For the high density mcSPT experiment (**Figure 7**), 100 µl of crosslinker (DNP-BSA; final concentration of 1 µg/ml) equilibrated at 37 °C was added ~20 seconds into the image acquisition.

## **B.7 3D-scanning of Live Cells**

RBL-2H3 cells were incubated in 200 µl of 5 nM QD-IgE (655) in HBSS for 30 minutes at 37 °C followed by 2 washes with HBSS. The cells were incubated with 200 µl of 5 µg/ml CellMask orange for 3 min at 37 °C followed by 3 washes with HBSS. Imaging was performed immediately after labeling. Crosslinker (DNP-BSA; final concentration 10 µg/ml) was added ~60 seconds into the image acquisition. In order to assure rapid mixing of crosslinker and to prevent focal drift, 100 µl of crosslinker stock at 3x final concentration in HBSS preheated to 37 °C was added (contains 200 µl HBSS).

Z-stacks covering an ROI of 14.8 µm in *x*, 14.8 µm in *y*, and 7.0 µm in *z* were acquired at a rate of 7.72 seconds per *z*-stack. Each *z*-slice for this ROI consists of 128 steps (*x* dimension; ~0.116 µm steps) of the line across the sample by the scanning mirror and 128 pixels (*y* dimension; ~0.116 µm pixel size) along the line to make each *z*-slice, and each *z*-stack for this ROI contains 29 *z*-slices with a step size of 0.25 µm. In order to conserve CPU memory for storage and post-processing, the data was binned into 32 spectral bins instead of 128. It is important to note that altering the number of spectral bins does not significantly alter the acquisition time with the current camera configuration. A total of 50 *z*-stacks were acquired giving a total acquisition time of ~6.5 min. *Z*-stacks were processed using 3D deconvolution. The experimentally measured PSF



was used with the built-in Matlab deconvolution algorithm *deconvlucy*. An isosurface rendering was then used to represent the data.

## B.8 Hyperspectral Superresolution

Cells were Swiss 3T3 fixed in 4% paraformaldehyde (PFA) and labeled with Alexa488 secondary antibody on anti-beta tubulin primary and ATTO532 clathrin. OSB = “Shi” recipe with BME (450 uL of Glucose Tris buffer + 50 uL Gluox buffer + 20 uL BME 1.43 M). Glucose Tris buffer = [50 mM Tris, 10 mM NaCl, 10% glucose by weight], pH 8.0. Gluox buffer = 1 mL Tris buffer + 8.8 mg Glucose Oxidase + 3.7 mg Catalase. Tris buffer = [50 mM Tris, 10 mM NaCl], pH 8.0. Laser was at 20% on ND filters 1.1 (open), exposure time 2 ms, ROI 64x64, 1000 frames per data set, 8 data sets per ROI.

## References

1. Liu FT, Bohn JW, Ferry EL, Yamamoto H, Molinaro C a, et al. (1980) Monoclonal dinitrophenyl-specific murine IgE antibody: preparation, isolation, and characterization. *Journal of immunology* (Baltimore, Md : 1950) 124: 2728–2737. Available: <http://www.ncbi.nlm.nih.gov/pubmed/7373045>.
2. Andrews NL, Lidke K a, Pfeiffer JR, Burns AR, Wilson BS, et al. (2008) Actin restricts FcεRI diffusion and facilitates antigen-induced receptor immobilization. *Nature cell biology* 10: 955–963. Available: <http://dx.doi.org/10.1038/ncb1755>.
3. Van Vliet LJ, Sudar D, Young IT (1998) Digital fluorescence imaging using cooled charge-coupled device array cameras. In: Celis JE, editor. *Cell Biology. A laboratory handbook*. Academic Press, Vol. III. pp. 109–120.
4. Huang F, Schwartz SL, Byars JM, Lidke KA (2011) Simultaneous multiple-emitter fitting for single molecule super-resolution imaging. *Biomed Opt Express* 2: 1377–1393.

5. Jaqaman K, Loerke D, Mettlen M, Kuwata H, Grinstein S, et al. (2008) Robust single-particle tracking in live-cell time-lapse sequences. *Nat Meth* 5: 695–702. Available: <http://dx.doi.org/10.1038/nmeth.1237>.
6. Low-Nam ST, Lidke KA, Cutler PJ, Roovers RC, Van Bergen en Henegouwen PMP, et al. (2011) ErbB1 dimerization is promoted by domain co-confinement and stabilized by ligand binding. *Nat Struct Mol Biol* 18: 1244–1249. Available: <http://dx.doi.org/10.1038/nsmb.2135>.
7. Andrews NL, Pfeiffer JR, Martinez a M, Haaland DM, Davis RW, et al. (2009) Small, Mobile FceRI Receptor Aggregates Are Signaling Competent. *Immunity* 31: 469–479. Available: <http://www.pubmedcentral.nih.gov/articlerender.fcgi?artid=2828771&tool=pmcentrez&rendertype=abstract>.
8. Wilson BS, Pfeiffer JR, Oliver JM (2000) Observing FceRI Signaling from the Inside of the Mast Cell Membrane. *J Cell Biol* 149: 1131–1142 ST – Observing FceRI Signaling from the. Available: <http://jcb.rupress.org/cgi/content/abstract/149/5/1131>.

## Appendix C

### Polarization Effects on PSF

In some cases, fluorophores may have a fixed dipole orientation throughout the image acquisition (such as with organic dyes attached to rigid surfaces or objects). In this case, the dipole orientation itself may modify the point spread function at the image plane. This is a basic calculation that can be used in simulation or in fitting acquired data.

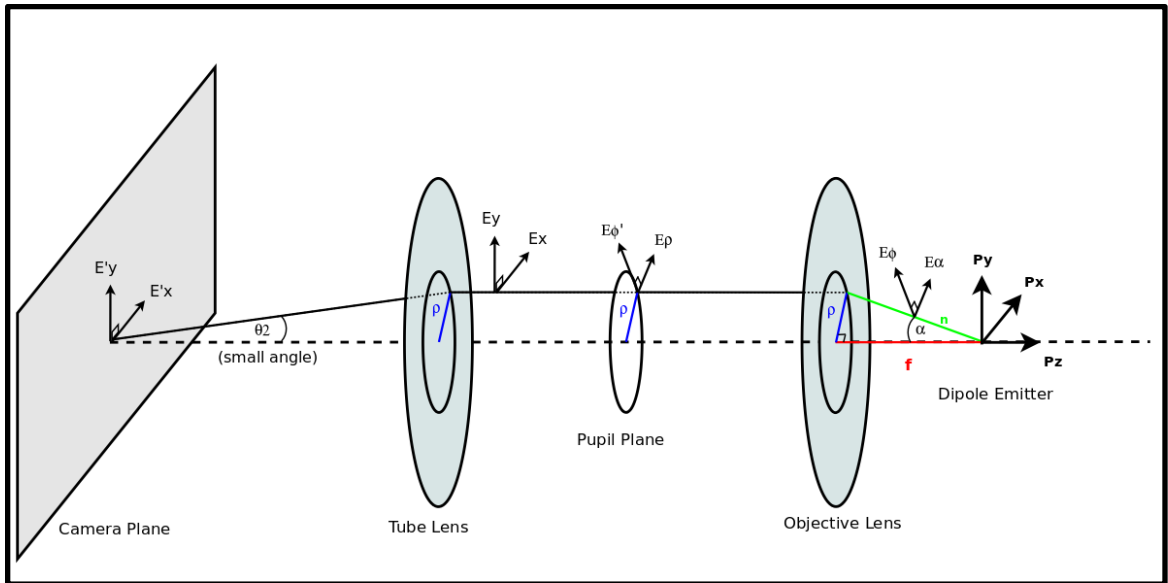


Figure C.1: Polarization effect on the point spread function.

For this derivation we start with a dipole emitter at the farthest point on the right side of the **Figure C.1**. Since we ultimately seek the intensity of this radiation, we start with looking at the way the  $E$  field is transformed along the path from the source to the

detector. From Jackson 3rd edition, p.411, Eq. 9.18 [1], the  $E$  field from a radiating dipole at a point which is a distance  $r$  from the source is:

$$\vec{E} = k^2(\hat{n} \times \hat{p}) \times \hat{n} \frac{e^{ikr}}{r} + [3\hat{n}(\hat{n} \cdot \hat{p}) - \hat{p}]\left(\frac{1}{r^3} - \frac{ik}{r^2}\right)e^{ikr} \quad (1)$$

where  $\hat{n}$  is the unit vector pointing from the source to the field point and  $\hat{p}$  is the unit vector for the polarization of the dipole.

The last term goes to zero as  $r$  becomes large, so this is called the “near-field” term and can be neglected at large distances. Also, the objective lens takes the diverging field and collimates it, transforming the spherical waves into plane waves traveling along the negative  $z$ -axis. In the end we will be interested in the intensity, so we can ignore the exponential term since it will be multiplied by its complex conjugate. Also, if we consider a fixed wavelength then  $k$  will remain constant. These conditions simplify equation (1) to:

$$\vec{E} = (\hat{n} \times \hat{p}) \times \hat{n} \quad (2)$$

In order to simplify things we will break the polarization down into  $x$ ,  $y$ , and  $z$  components and then analyze how each of these components transforms through the system.

Let:

$$\begin{aligned}
\vec{E}_1 &= (\hat{n} \times \hat{x}) \times \hat{n} \\
\vec{E}_2 &= (\hat{n} \times \hat{y}) \times \hat{n} \\
\vec{E}_3 &= (\hat{n} \times \hat{z}) \times \hat{n}
\end{aligned} \tag{3}$$

Throughout the calculation we will need to convert between cylindrical, spherical, and Cartesian coordinates, so the following transformations will be used:

#### **Spherical to Cartesian Coordinates:**

$$\begin{aligned}
\hat{r} &= \hat{x}(\sin \theta \cos \phi) + \hat{y}(\sin \theta \sin \phi) + \hat{z}(\cos \theta) \\
\hat{\theta} &= \hat{x}(\cos \theta \cos \phi) + \hat{y}(\cos \theta \sin \phi) + \hat{z}(-\sin \theta) \\
\hat{\phi} &= \hat{x}(-\sin \phi) + \hat{y}(\cos \phi)
\end{aligned} \tag{4}$$

#### **Cylindrical to Cartesian Coordinates:**

$$\begin{aligned}
\hat{\rho} &= \hat{x}(\cos \phi) + \hat{y}(\sin \phi) \\
\hat{\phi} &= \hat{x}(-\sin \phi) + \hat{y}(\cos \phi) \\
\hat{z} &= \hat{z}
\end{aligned} \tag{5}$$

#### **Cartesian to Cylindrical Coordinates:**

$$\begin{aligned}
\hat{x} &= \hat{\rho}(\cos \phi) + \hat{\phi}(-\sin \phi) \\
\hat{y} &= \hat{\rho}(\sin \phi) + \hat{\phi}(\cos \phi) \\
\hat{z} &= \hat{z}
\end{aligned} \tag{6}$$

The coordinate system will be oriented such that the positive  $z$ -axis will go from left to right; the positive  $y$ -axis will point upwards, and the positive  $x$ -axis will point into the page. The first task will be to convert each polarization component into spherical components. This is done because at the objective lens the spherical  $\phi$  component will be transformed into the cylindrical  $\phi$  component and will remain constant between the

objective lens and the tube lens. Likewise, the  $\alpha$  component, which is just  $(\pi - \theta)$ , will become the  $\rho$  component, and will also remain constant between lenses.

We can write  $\hat{n}$  as (see **Figure C.12**):

$$\hat{n} = \frac{\vec{n}}{|\vec{n}|} = \frac{\rho\hat{\rho} - f\hat{z}}{\sqrt{f^2 + \rho^2}} \quad (7)$$

and  $f$  can be expressed in terms of  $\rho$  and  $\theta$ :

$$\tan \alpha = \frac{\rho}{f}$$

$$f = \frac{\rho}{\tan \alpha} = \frac{\rho \cos \alpha}{\sin \alpha} = \frac{\rho \cos(\pi - \theta)}{\sin(\pi - \theta)} = \frac{-\rho \cos \theta}{\sin \theta} \quad (8)$$

$$\begin{aligned} \hat{n} &= \frac{-f\hat{z} + \rho(\hat{x} \cos \phi + \hat{y} \sin \phi)}{\sqrt{f^2 + \rho^2}} = \frac{\hat{x}(\rho \cos \phi) + \hat{y}(\rho \sin \phi) - f\hat{z}}{\sqrt{f^2 + \rho^2}} \\ &= \frac{\hat{x}(\rho \cos \phi) + \hat{y}(\rho \sin \phi) + \hat{z}(\frac{\rho \cos \theta}{\sin \theta})}{\sqrt{f^2 + \rho^2}} = \frac{\hat{x}(\rho \cos \phi) + \hat{y}(\rho \sin \phi) + \hat{z}(\frac{\rho \cos \theta}{\sin \theta})}{\sqrt{(\frac{\rho^2 \cos^2 \theta}{\sin^2 \theta}) + \rho^2}} \\ &= \frac{\hat{x}(\cos \phi) + \hat{y}(\sin \phi) + \hat{z}(\frac{\cos \theta}{\sin \theta})}{\sqrt{(\frac{\cos^2 \theta}{\sin^2 \theta}) + 1}} = \hat{x}(\cos \phi \sin \theta) + \hat{y}(\sin \phi \sin \theta) + \hat{z}(\cos \theta) \end{aligned} \quad (9)$$

Now that  $\hat{n}$  is in Cartesian coordinates, it can be easily crossed into each polarization component  $(\hat{x}, \hat{y}, \hat{z})$  and used to obtain the  $E$  field components. Starting with  $\vec{E}_1 = (\hat{n} \times \hat{x}) \times \hat{n}$ ,

$$\begin{aligned} \hat{n} \times \hat{x} &= -\hat{z}(\sin \phi \sin \theta) + \hat{y}(\cos \theta) \\ (\hat{n} \times \hat{x}) \times \hat{n} &= -\hat{y}(\sin \phi \cos \phi \sin^2 \theta) + \hat{x}(\sin^2 \phi \sin^2 \theta) - \hat{z}(\cos \theta \cos \phi \sin \theta) + \hat{x}(\cos^2 \theta) \\ \vec{E}_1 &= \hat{x}(\sin^2 \phi \sin^2 \theta + \cos^2 \theta) + \hat{y}(-\sin \phi \cos \phi \sin^2 \theta) + \hat{z}(-\cos \theta \cos \phi \sin \theta) \end{aligned} \quad (10)$$

The  $\hat{\alpha}$  component of  $\vec{E}_1$  is  $E_{1\alpha} = \vec{E}_1 \cdot \hat{\alpha}$ . Since  $\alpha = (\pi - \theta)$ ,  $\cos \alpha = -\cos \theta$ ,  $\sin \alpha = \sin \theta$ , and using equation (4),

$$\begin{aligned}
\hat{\alpha} &= \hat{x}(-\cos \alpha \cos \phi) + \hat{y}(-\cos \alpha \sin \phi) + \hat{z}(-\sin \alpha) \\
&= \hat{x}(\cos \theta \cos \phi) + \hat{y}(\cos \theta \sin \phi) + \hat{z}(-\sin \theta)
\end{aligned} \tag{11}$$

$$\begin{aligned}
E_{1\alpha} &= \vec{E}_1 \cdot \hat{\alpha} \\
&= \cos \theta \cos \phi \sin^2 \theta \sin^2 \phi + \cos \phi \cos^3 \theta - \cos \theta \sin^2 \phi \cos \phi \sin^2 \theta + \sin^2 \theta \cos \phi \cos \theta \\
&= \sin^2 \theta \cos \phi \cos \theta + \cos^3 \theta \cos \phi \\
&= \cos \theta \cos \phi (\sin^2 \theta + \cos^2 \theta) \\
&= \cos \theta \cos \phi
\end{aligned} \tag{12}$$

At the objective lens, and from the objective to the tube lens,  $E_{1\rho}$  is equal to  $E_{1\alpha}$ , so

$$E_{1\rho} = \cos \theta \cos \phi \tag{13}$$

Now for the  $\hat{\phi}$  component of  $\vec{E}_1$ , using equation (4) again:

$$\begin{aligned}
E_{1\phi} &= \vec{E}_1 \cdot \hat{\phi} \\
&= -\sin^2 \theta \sin^3 \phi - \sin \phi \cos^2 \theta - \sin \phi \cos^2 \phi \sin^2 \theta
\end{aligned} \tag{14}$$

Note that similar to the previous case this  $E_{1\phi}$  is equal to  $E_{1\phi'}$  at the objective lens and from the objective to the tube lens. Now  $E_{1\phi'}$  and  $E_{1\rho}$  must be converted back into Cartesian coordinates, which will later be used in the discrete Fourier transform at the tube lens. Starting with the  $x$ -component and using equation (5),

$$\begin{aligned}
E_{1x} &= \vec{E}_1 \cdot \hat{x} \\
&= \vec{E}_1 \cdot (\hat{\rho} \cos \phi - \hat{\phi} \sin \phi) \\
&= \cos \theta \cos^2 \phi + \sin^2 \theta \sin^4 \phi + \sin^2 \phi \cos^2 \theta + \sin^2 \phi \cos^2 \phi \sin^2 \theta \\
&= \cos \theta \cos^2 \phi + \sin^2 \phi (\sin^2 \theta \sin^2 \phi + \cos^2 \theta + \cos^2 \phi \sin^2 \theta) \\
&= \cos \theta \cos^2 \phi + \sin^2 \phi (\sin^2 \theta + \cos^2 \theta) \\
&= \cos \theta \cos^2 \phi + \sin^2 \phi
\end{aligned} \tag{15}$$

Now for the  $y$  component:

$$\begin{aligned}
E_{1y} &= \vec{E}_1 \cdot \hat{y} \\
&= \vec{E}_1 \cdot (\hat{\rho} \sin \phi + \hat{\phi} \cos \phi) \\
&= \cos \theta \cos \phi \sin \phi - \sin^2 \theta \sin^3 \phi \cos \phi - \sin \phi \cos^2 \theta \cos \phi - \sin \phi \cos^3 \phi \sin^2 \theta \\
&= \sin \phi \cos \phi (\cos \theta - \sin^2 \theta \sin^2 \phi - \cos^2 \theta - \cos^2 \phi \sin^2 \theta) \\
&= \sin \phi \cos \phi (\cos \theta - 1)
\end{aligned} \tag{16}$$

Now the same technique can be applied to  $\vec{E}_2$ . We start by recalling from equation (9) that

$$\hat{n} = \hat{x}(\cos \phi \sin \theta) + \hat{y}(\sin \phi \sin \theta) + \hat{z}(\cos \theta) \tag{17}$$

$$\begin{aligned}
\vec{E}_2 &= (\hat{n} \times \hat{y}) \times \hat{n} \\
\hat{n} \times \hat{y} &= \hat{x}(-\cos \theta) + \hat{z}(\cos \phi \sin \theta) \\
(\hat{n} \times \hat{y}) \times \hat{n} &= \hat{z}(-\cos \theta \sin \phi \sin \theta) + \hat{y}(\cos^2 \theta) + \hat{y}(\cos^2 \phi \sin^2 \theta) - \hat{x}(\cos \phi \sin^2 \theta \sin \phi) \\
\vec{E}_2 &= \hat{x}(-\cos \phi \sin^2 \theta \sin \phi) + \hat{y}(\cos^2 \theta + \cos^2 \phi \sin^2 \theta) + \hat{z}(-\cos \theta \sin \phi \sin \theta)
\end{aligned} \tag{18}$$

As before, we can get the  $\hat{\alpha}$  and  $\hat{\phi}$  components by taking the dot product with each unit vector. Recalling equations (5) and (12),

$$\begin{aligned}
\hat{\alpha} &= \hat{x}(\cos \theta \cos \phi) + \hat{y}(\cos \theta \sin \phi) + \hat{z}(-\sin \theta) \\
\hat{\phi} &= \hat{x}(-\sin \phi) + \hat{y}(\cos \phi)
\end{aligned}$$

$$\begin{aligned}
E_{2\alpha} &= \vec{E}_2 \cdot \hat{\alpha} \\
&= -\cos^2 \phi \cos \theta \sin^2 \theta \sin \phi + \cos^3 \theta \sin \phi + \cos^2 \phi \sin^2 \theta \cos \theta \sin \phi + \cos \theta \sin^2 \theta \sin \phi \\
&= \cos \theta \sin \phi (-\cos^2 \phi \sin^2 \theta + \cos^2 \theta + \sin^2 \theta + \cos^2 \phi \sin^2 \theta) \\
&= \cos \theta \sin \phi \\
E_{2\rho} = E_{2\alpha} &= \cos \theta \sin \phi
\end{aligned} \tag{19}$$



$$\begin{aligned}
E_{2\phi} &= \vec{E}_2 \cdot \hat{\phi} \\
&= \cos \phi \sin^2 \theta \sin^2 \phi + \cos^2 \theta \cos \phi + \cos^3 \phi \sin^2 \theta \\
E_{2\phi'} = E_{2\phi} &= \cos \phi \sin^2 \theta \sin^2 \phi + \cos^2 \theta \cos \phi + \cos^3 \phi \sin^2 \theta
\end{aligned} \tag{20}$$

$$\begin{aligned}
E_{2x} &= \vec{E}_2 \cdot \hat{x} \\
&= \vec{E}_2 \cdot (\hat{\rho} \cos \phi - \hat{\phi} \sin \phi) \\
&= \cos \theta \sin \phi \cos \phi - (\cos \phi \sin^2 \theta \sin^3 \phi + \cos^2 \theta \cos \phi \sin \phi + \cos^3 \phi \sin^2 \theta \sin \phi) \\
&= \cos \theta \sin \phi \cos \phi - \sin \phi \cos \phi (\sin^2 \theta \sin^2 \phi + \cos^2 \theta + \cos^2 \phi \sin^2 \theta) \\
&= \cos \theta \sin \phi \cos \phi - \sin \phi \cos \phi (1) \\
&= \sin \phi \cos \phi (\cos \theta - 1)
\end{aligned} \tag{21}$$

$$\begin{aligned}
E_{2y} &= \vec{E}_2 \cdot \hat{y} \\
&= \vec{E}_2 \cdot (\hat{\rho} \sin \phi + \hat{\phi} \cos \phi) \\
&= \cos \theta \sin^2 \phi + \cos^2 \phi \sin^2 \theta \sin^2 \phi + \cos^2 \theta \cos^2 \phi + \cos^4 \phi \sin^2 \theta \\
&= \cos \theta \sin^2 \phi + \cos^2 \phi (\sin^2 \theta \sin^2 \phi + \cos^2 \theta + \cos^2 \phi \sin^2 \theta) \\
&= \cos \theta \sin^2 \phi + \cos^2 \phi
\end{aligned} \tag{22}$$

Once again, the same technique can be applied to  $\vec{E}_3$ . Recalling from equation (9),

$$\hat{n} = \hat{x}(\cos \phi \sin \theta) + \hat{y}(\sin \phi \sin \theta) + \hat{z}(\cos \theta) \tag{23}$$

$$\begin{aligned}
\vec{E}_3 &= (\hat{n} \times \hat{z}) \times \hat{n} \\
(\hat{n} \times \hat{z}) &= -\hat{y}(\cos \phi \sin \theta) + \hat{x}(\sin \phi \sin \theta) \\
(\hat{n} \times \hat{z}) \times \hat{n} &= \hat{z}(\cos^2 \phi \sin^2 \theta) - \hat{x}(\cos \theta \cos \phi \sin \theta) + \hat{z}(\sin^2 \phi \sin^2 \theta) - \hat{y}(\cos \theta \sin \phi \sin \theta) \\
\vec{E}_3 &= \hat{x}(-\cos \theta \cos \phi \sin \theta) + \hat{y}(-\cos \theta \sin \phi \sin \theta) + \hat{z}(\sin^2 \theta)
\end{aligned} \tag{24}$$

The same method is used for the  $\hat{\alpha}$  and  $\hat{\phi}$  components by taking the dot product with each unit vector. Recalling equations (5) and (12),

$$\begin{aligned}
\hat{\alpha} &= \hat{x}(\cos \theta \cos \phi) + \hat{y}(\cos \theta \sin \phi) + \hat{z}(-\sin \theta) \\
\hat{\phi} &= \hat{x}(-\sin \phi) + \hat{y}(\cos \phi)
\end{aligned}$$

$$\begin{aligned}
E_{3\alpha} &= \vec{E}_3 \cdot \hat{\alpha} \\
&= -\cos^2 \theta \cos^2 \phi \sin \theta - \cos^2 \theta \sin^2 \phi \sin \theta - \sin^3 \theta \\
&= -\cos^2 \theta \sin \theta (\cos^2 \phi + \sin^2 \phi) - \sin^3 \theta \\
&= -\cos^2 \theta \sin \theta - \sin^2 \theta (\sin \theta) \\
E_{3\rho} &= -\sin \theta
\end{aligned} \tag{25}$$

$$\begin{aligned}
E_{3\phi} &= \vec{E}_3 \cdot \hat{\phi} \\
&= \cos \theta \cos \phi \sin \theta \sin \phi - \cos \theta \sin \phi \sin \theta \cos \phi \\
E_{3\phi'} &= 0
\end{aligned} \tag{26}$$

$$\begin{aligned}
E_{3x} &= \vec{E}_3 \cdot \hat{x} \\
&= \vec{E}_3 \cdot (\hat{\rho} \cos \phi - \hat{\phi} \sin \phi) \\
&= -\sin \theta \cos \phi
\end{aligned} \tag{27}$$

$$\begin{aligned}
E_{3y} &= \vec{E}_3 \cdot \hat{y} \\
&= \vec{E}_3 \cdot (\hat{\rho} \sin \phi + \hat{\phi} \cos \phi) \\
&= -\sin \theta \sin \phi
\end{aligned} \tag{28}$$

In summary, equations 15, 16, 21, 22, 27, and 28 are the  $x$  and  $y$  components of the  $E$  fields at the tube lens from dipole emitters polarized along the  $x$ -,  $y$ -, and  $z$ -axes.

$$\begin{aligned}
E_{1x} &= \cos \theta \cos^2 \phi + \sin^2 \phi \\
E_{1y} &= \sin \phi \cos \phi (\cos \theta - 1) \\
E_{2x} &= \sin \phi \cos \phi (\cos \theta - 1) \\
E_{2y} &= \cos \theta \sin^2 \phi + \cos^2 \phi \\
E_{3x} &= -\sin \theta \cos \phi \\
E_{3y} &= -\sin \theta \sin \phi
\end{aligned} \tag{29}$$

In order to calculate the intensity ( $|\vec{E}|^2$ ) that is projected onto the camera, we will first express the actual polarization as a normalized linear combination of the three basis polarization vectors and then apply these weights to the  $E_1$ ,  $E_2$ , and  $E_3$  values that were just calculated. The intensity will be the real part of the product of the Fourier transformed  $E$  fields with their complex conjugates.

Starting with a generic polarization vector,

$$P_i = aP_x + bP_y + cP_z \quad (30)$$

and so,

$$\begin{aligned} E_{1x} &= a(\cos \theta \cos^2 \phi + \sin^2 \phi) \\ E_{1y} &= a(\sin \phi \cos \phi (\cos \theta - 1)) \\ E_{2x} &= b(\sin \phi \cos \phi (\cos \theta - 1)) \\ E_{2y} &= b(\cos \theta \sin^2 \phi + \cos^2 \phi) \\ E_{3x} &= c(-\sin \theta \cos \phi) \\ E_{3y} &= c(-\sin \theta \sin \phi) \end{aligned} \quad (31)$$

$$\begin{aligned} I_x &= \text{Re}([\mathcal{F}(E_{1x} + E_{2x} + E_{3x})] \cdot [\mathcal{F}(E_{1x} + E_{2x} + E_{3x})]^*) \\ I_y &= \text{Re}([\mathcal{F}(E_{1y} + E_{2y} + E_{3y})] \cdot [\mathcal{F}(E_{1y} + E_{2y} + E_{3y})]^*) \end{aligned}$$

where  $F(E)$  is the (discrete) Fourier transform of  $E$ . The cross terms of the  $x$  and  $y$  components ( $FE_{ix}FE_{jy}$ ) are very small and may be neglected when  $\theta_2$  is very small (see **Figure C.1**), and so  $I_x$  and  $I_y$  are calculated independently.

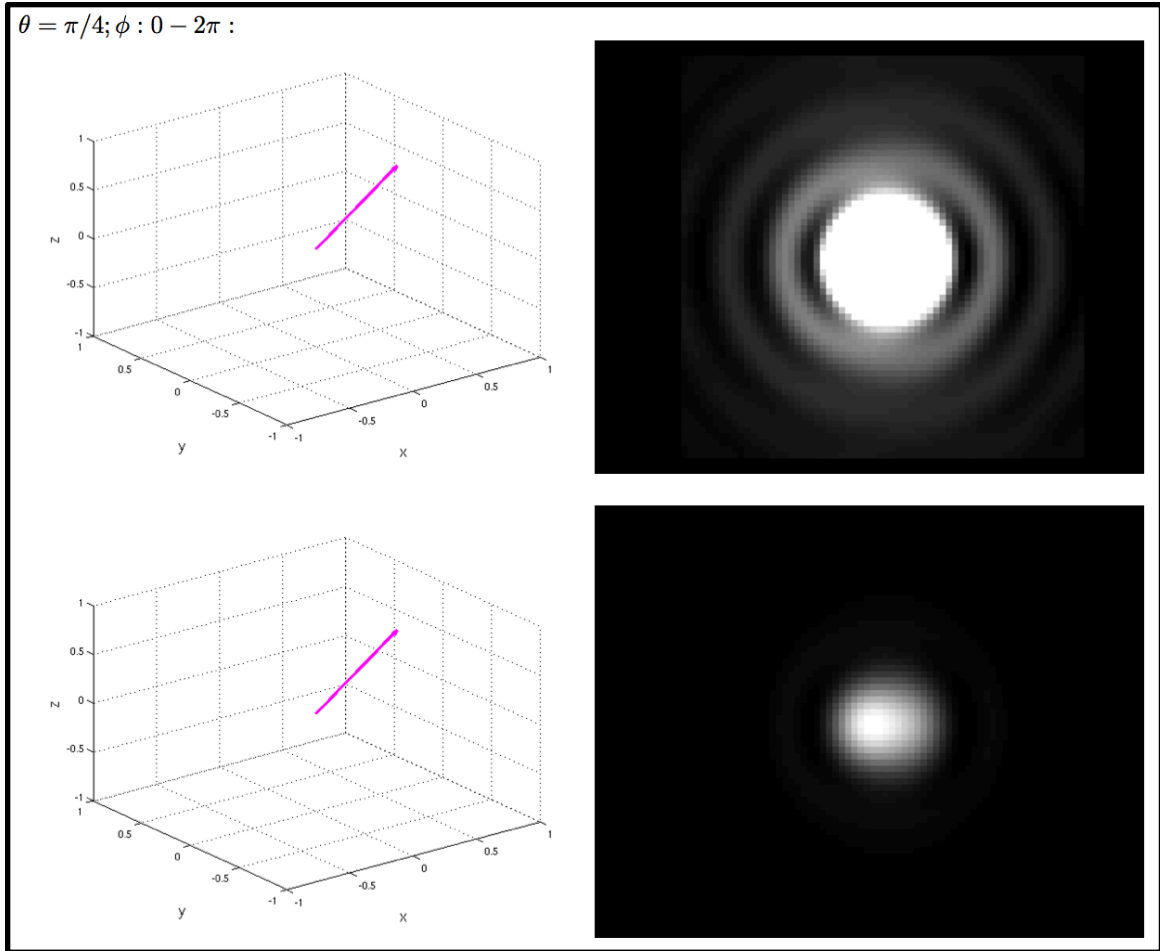


Figure C.2: Simulation showing a dipole emitter at  $\theta = \pi/4$  and  $\phi$  can be any value from zero to  $2\pi$  (shown at zero). The pink arrow indicates the dipole orientation. On the right side, the modified PSF is simulated on a 128x128 pixel camera at the image plane, where the top figure shows a log stretch and the bottom figure shows the normal values.

## References

1. Jackson JD (1999) Classical Electrodynamics. 3rd ed. Wiley.

## Appendix D

### Quantum Dot Emission Spectra

**Figures D.1 through D.8:** Ensemble quantum dot emission spectra and observed intensity. (A) shows spectral features of individual QDs (colored lines; 5 randomly selected spectra) and the ensemble of all individual QDs (black line). (B) is a histogram of fit spectral emission peaks ( $\theta_\lambda$ ) identified by 3D Gaussian fitting ( $x, y, \lambda$ ) for individual QDs. The red tick indicates the expected emission peak for the given QD. (C) is a histogram of the fit standard deviation in the spectral dimension ( $\theta_{\sigma\lambda}$ ) identified by 3D Gaussian fitting for individual QDs. (D) is a histogram of fit photons per frame ( $\theta_{\sigma\lambda}$ ) for individual QDs. These data were acquired at 27 FPS, on a sparse sample of quantum dots adsorbed to a glass coverslip, with an ROI of 32x64 pixels, and laser intensity of  $\sim 5400$  W/cm<sup>2</sup>.

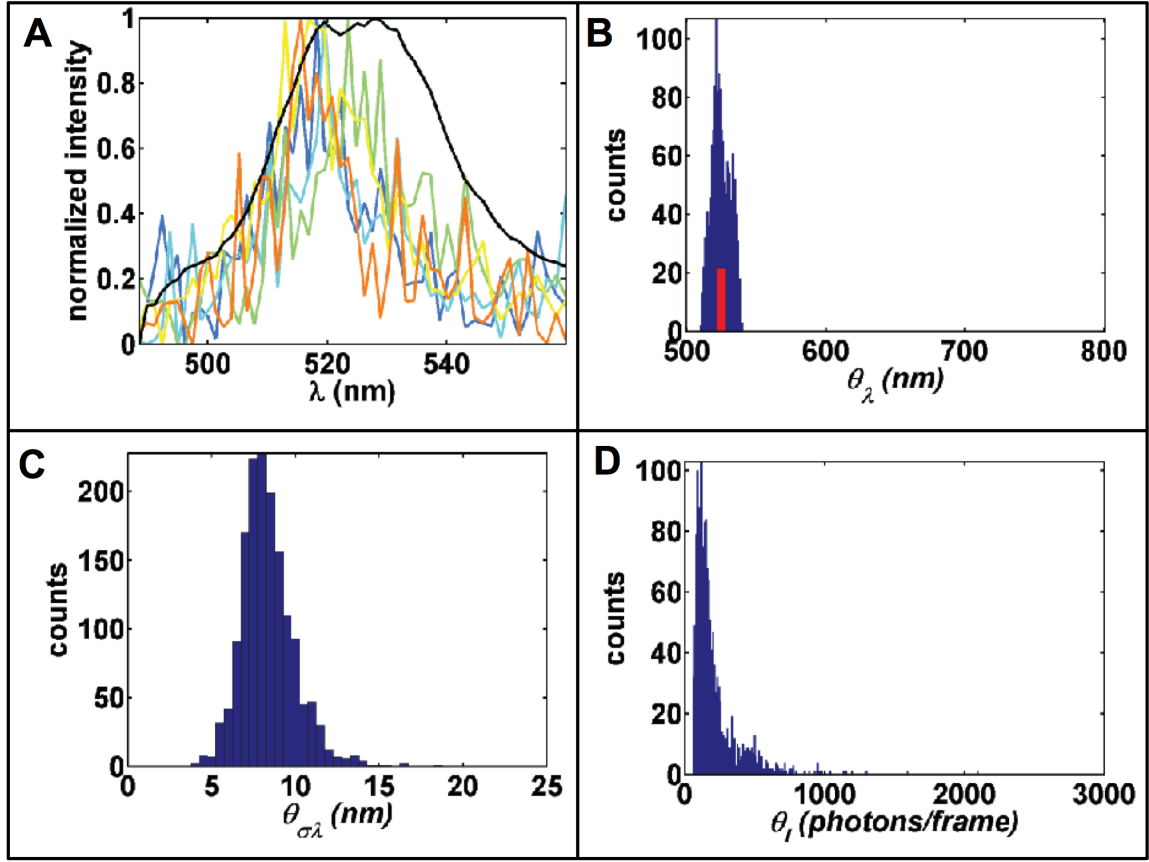


Figure D.1: QD 525 ensemble emission spectra and observed intensity.

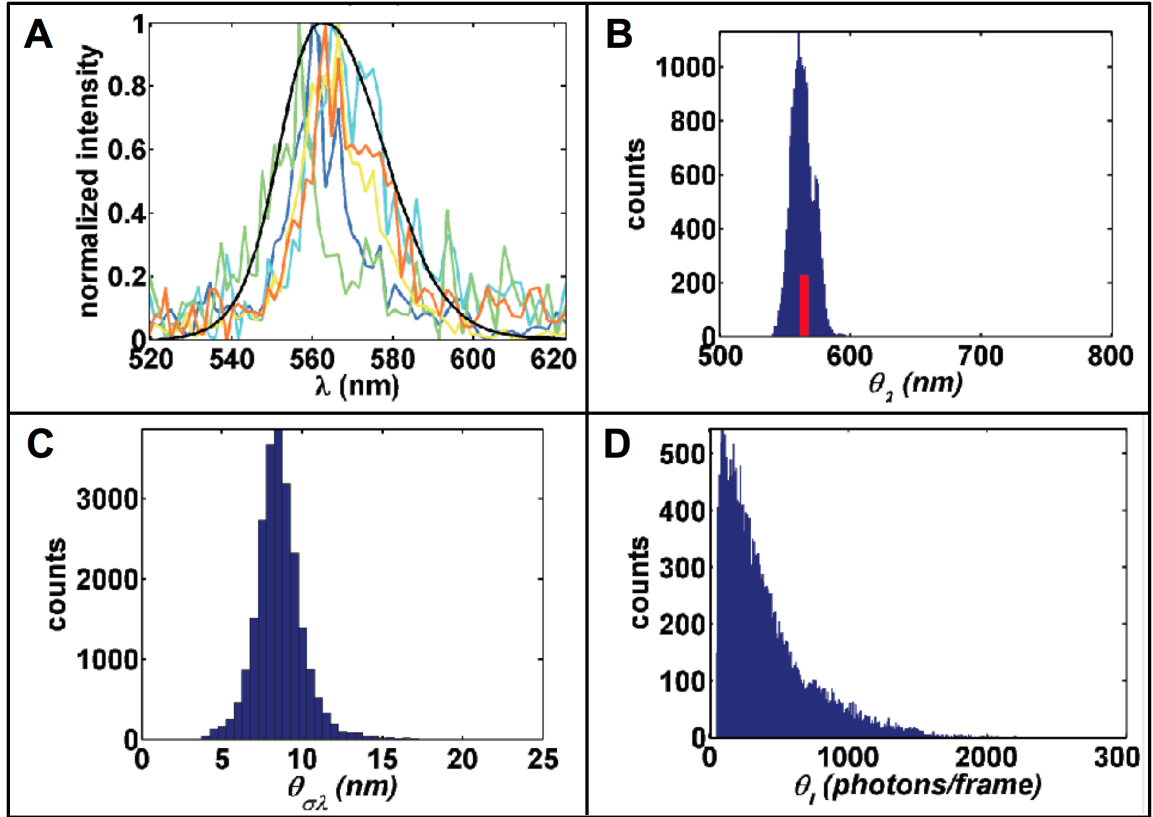


Figure D.2: QD 565 ensemble emission spectra and observed intensity.

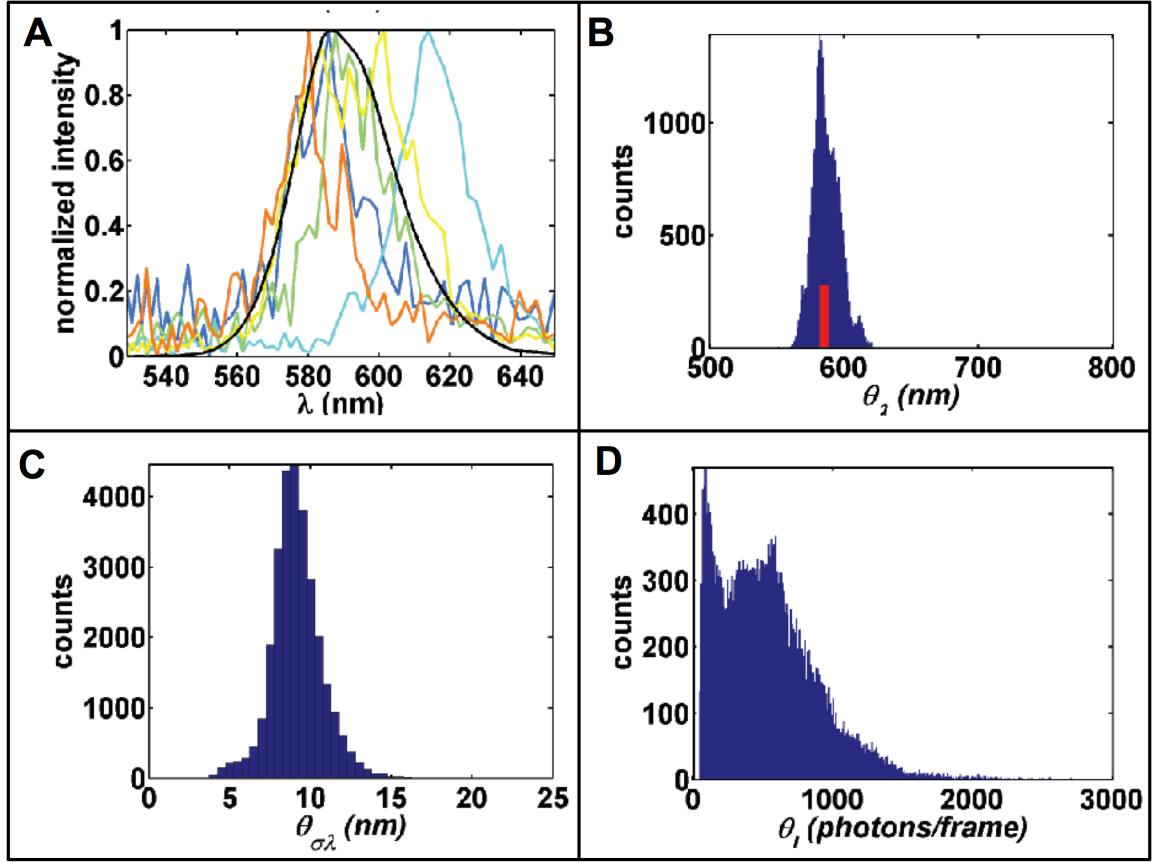


Figure D.3: QD 585 ensemble emission spectra and observed intensity.



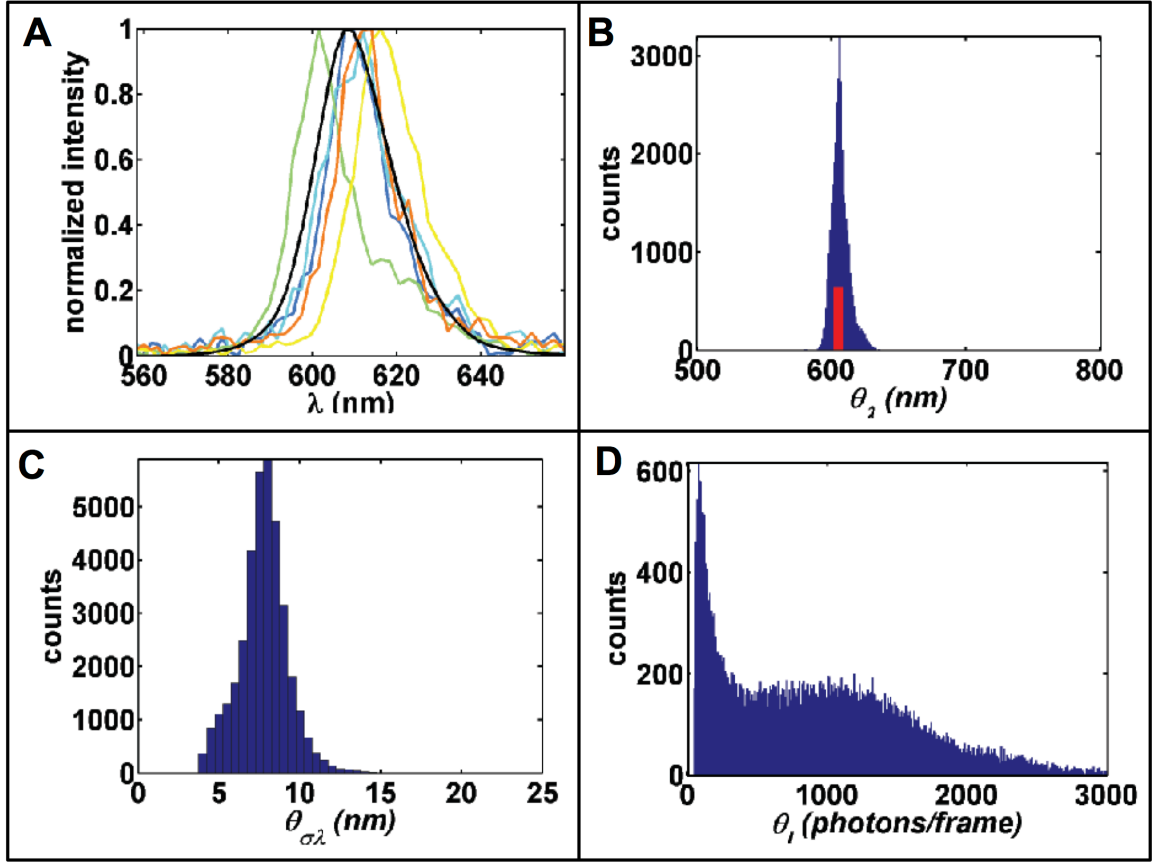


Figure D.4: QD 605 ensemble emission spectra and observed intensity.

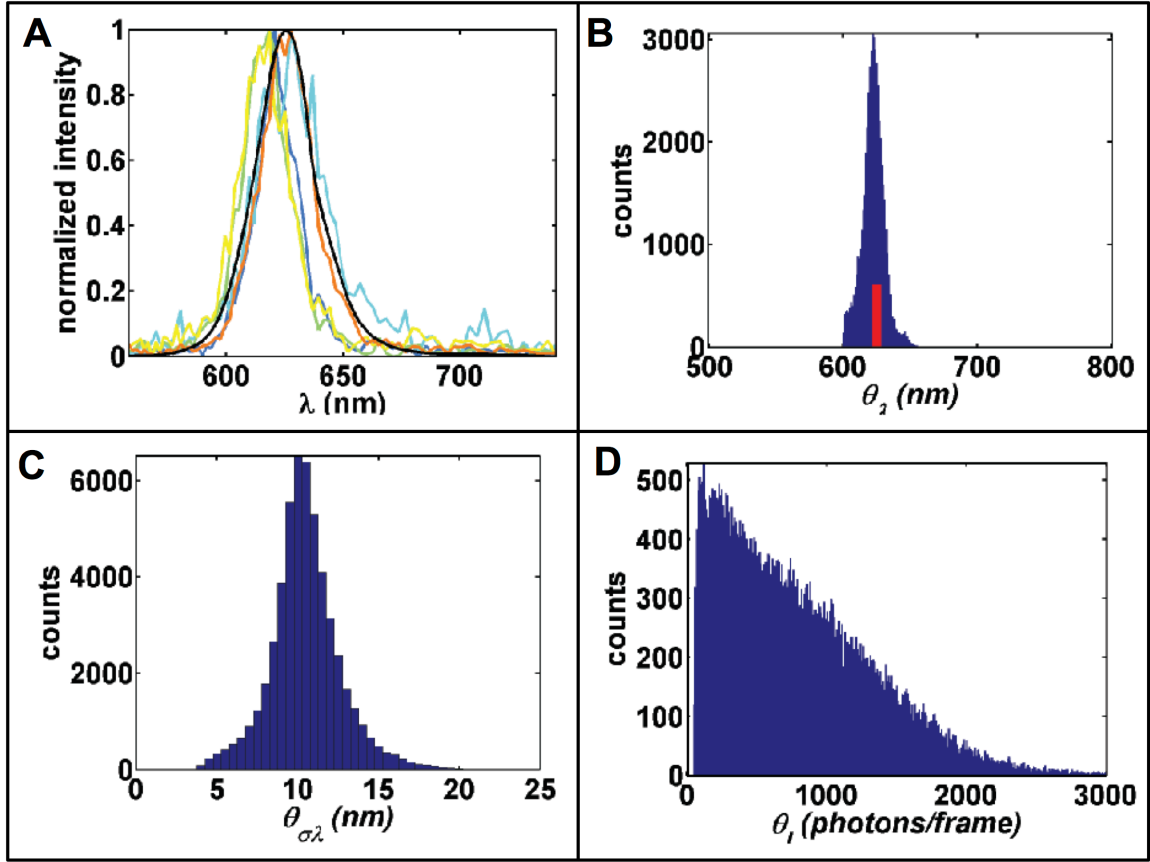


Figure D.5: QD 625 ensemble emission spectra and observed intensity.

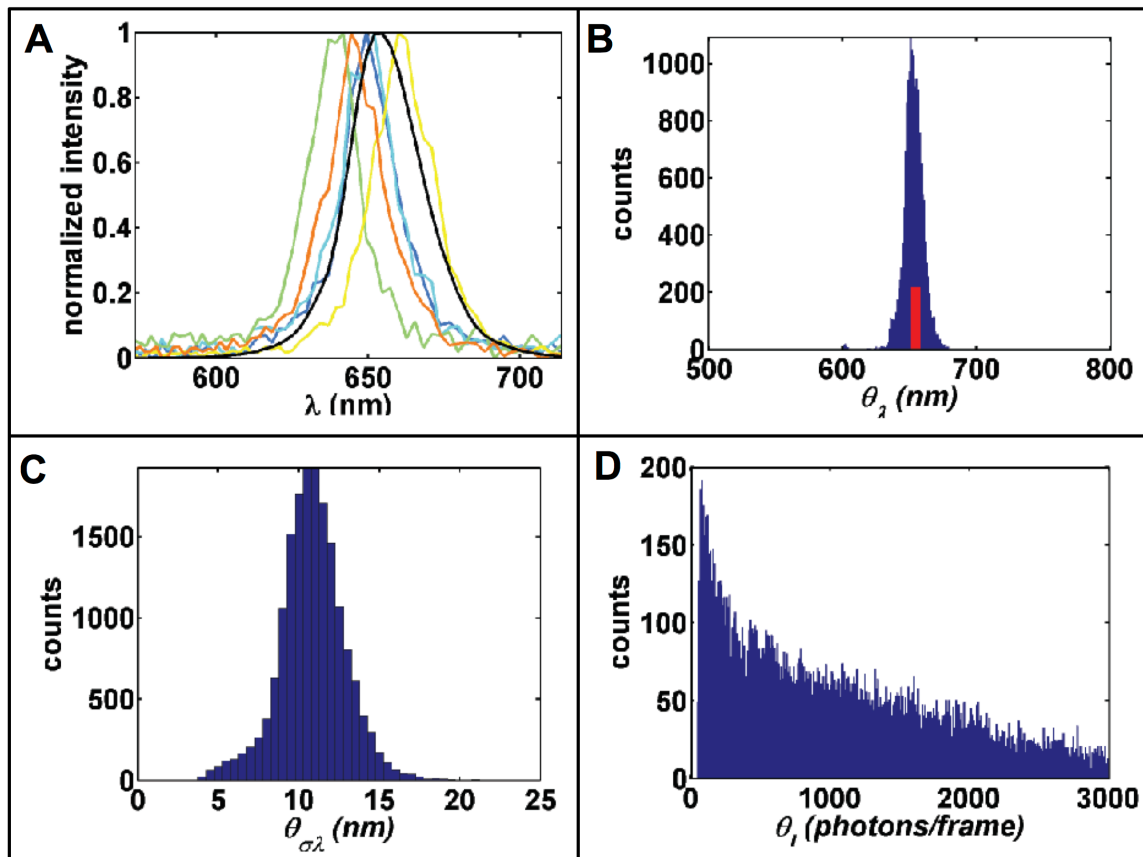


Figure D.6: QD 655 ensemble emission spectra and observed intensity.

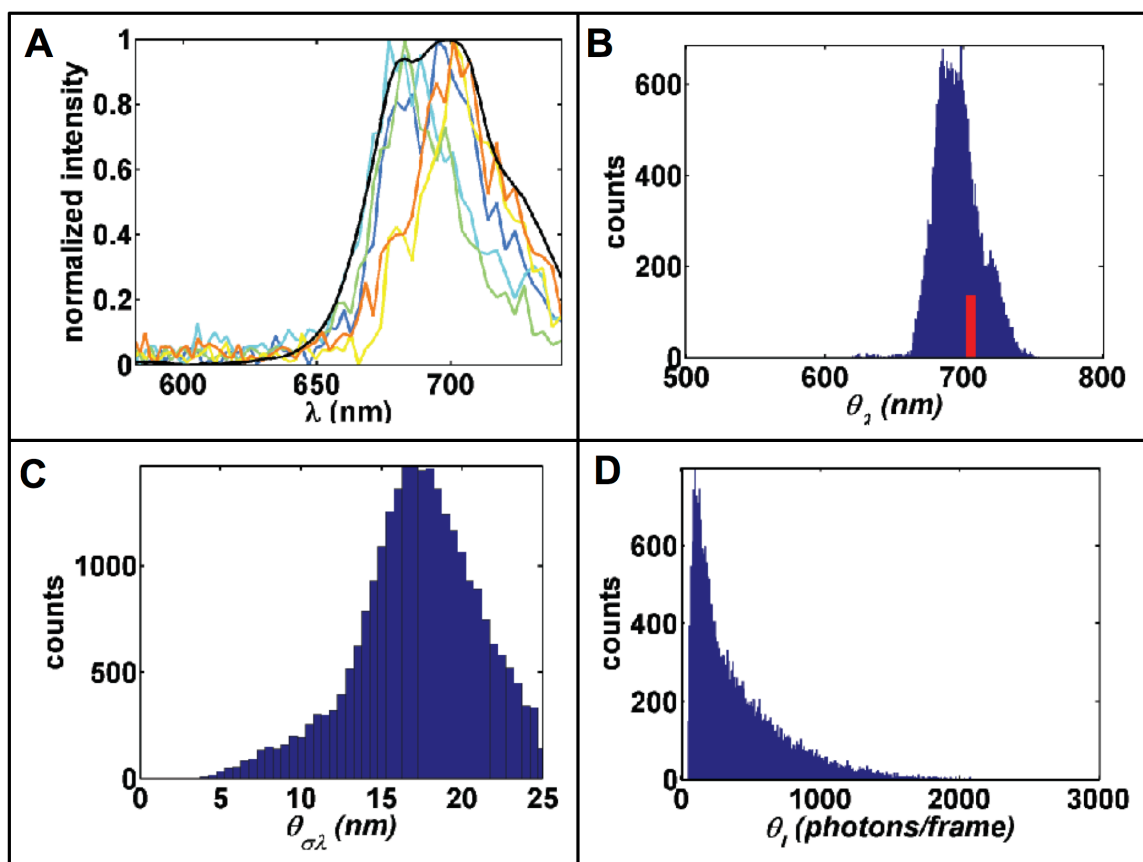


Figure D.7: QD 705 ensemble emission spectra and observed intensity.

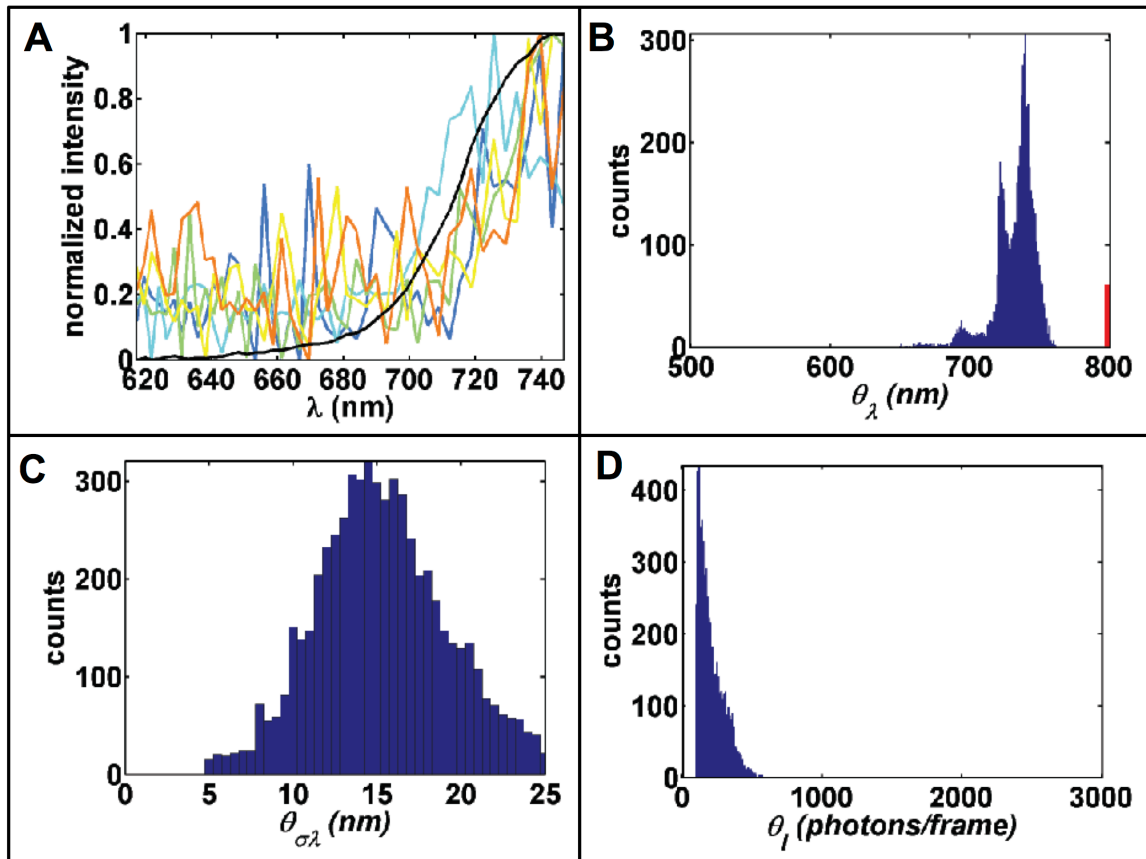


Figure D.8: QD 800 ensemble emission spectra and observed intensity.

# Appendix E

## Emitter Localization and Track Reconstruction

The following analysis methods used for processing the HSM data are originally documented in [1] and were developed at UNM by Patrick Cutler, Keith Lidke, and Fang Huang.

### E.1 3D Gaussian Fitting

The 3D Gaussian model used to estimate the microscope PSF and spectral features of individual QDs is

$$PSF(x, y, \lambda) = \frac{1}{(2\pi)^{3/2} \theta_{\sigma_x} \theta_{\sigma_y} \theta_{\sigma_\lambda}} e^{-\frac{(x-\theta_x)^2}{2\theta_{\sigma_x}^2} - \frac{(y-\theta_y)^2}{2\theta_{\sigma_y}^2} - \frac{(\lambda-\theta_\lambda)^2}{2\theta_{\sigma_\lambda}^2}}.$$

Definitions of all variables are included in **Table E.1**.

Symbol	Description
<i>General Variables</i>	
$\lambda$	Spectral position
$y$	Spatial position along the line
$x$	Spatial position in the scan direction
$\lambda_{width}$	Width of a spectral pixel
$\mu_k$	Counts in pixel $k$ of single QD model
$\mu_{k_{All}}$	Counts in pixel $k$ of $N$ QD model with background
$d_k$	Counts in pixel $k$ of experimental image
$\sigma_\theta$	Theoretical error (standard deviation) for model parameter as approximated by the Cramér Rao Bound
<i>Model Parameters for an individual QD</i>	
$\theta_I$	Photon counts
$\theta_\lambda$	Position of spectral emission peak of QD
$\theta_{\sigma_\lambda}$	Spectral spread (standard deviation) of QD
$\theta_y$	Position of QD along $y$ (line) dimension
$\theta_{\sigma_y}$	Microscope point spread function in $y$ (line) dimension
$\theta_x$	Position of QD along $x$ (scan) dimension
$\theta_{\sigma_x}$	Microscope point spread function in the $x$ (scan) dimension
$\theta_{bg}$	Background offset

Table E.1: Gaussian fitting variables.

Due to the optical setup of the HSM, the intensity for a single QD is distributed over several spatial and spectral pixels. The contribution of a single QD to the detected counts in pixel  $k$  of an HSM image is modeled by

$$\mu_k(x, y, \lambda) = \theta_I \int_{A_k} PSF(u, v, w) du dv dw,$$

where  $A_k$  is the area for a single pixel. Integration of the equation above gives

$$\mu_k(x, y, \lambda) = \theta_I \Delta E_x(x, y, \lambda) \Delta E_y(x, y, \lambda) \Delta E_\lambda(x, y, \lambda),$$

where the contribution of the Gaussian in the spectral dimension is

$$\Delta E_\lambda(x, y, \lambda) = \frac{1}{2} \left[ \operatorname{erf} \left( \frac{\lambda - \theta_\lambda + \lambda_{width}/2}{\sqrt{2}\theta_{\sigma_\lambda}} \right) - \operatorname{erf} \left( \frac{\lambda - \theta_\lambda - \lambda_{width}/2}{\sqrt{2}\theta_{\sigma_\lambda}} \right) \right].$$

The terms  $\Delta E_x(x, y, \lambda)$  and  $\Delta E_y(x, y, \lambda)$  are equivalently defined relative to  $x$  and  $y$  respectively. The 3D Gaussian model for a single QD is depicted in **Figure E.1A**. The model is easily expanded to  $N$  spatially and spectrally overlapping QDs with background

$$\mu_{k_{All}}(x, y, \lambda) = \sum_i^N \mu_{k_i}(x, y, \lambda) + \theta_{bg}.$$

Model parameters for individual QDs are fit to experimental data by maximizing the likelihood function:

$$L(\theta|D) = \prod_k \frac{\mu_{k_{All}}(x, y, \lambda)^{d_k} e^{-\mu_{k_{All}}(x, y, \lambda)}}{d_k!}.$$

Parameter optimization is performed using the Newton-Raphson method which is an extension of previous work [2]. The variance in parameter estimates approaches the theoretical limit set by the Cramér Rao Bound for simulated data (**Figure E.1B**). The accuracy for localizing two highly overlapping emitters simultaneously is demonstrated in **Figure E.1C** and **E.1D**. Relatively accurate localizations (spatial and spectral) for both QDs is achieved with a high degree of spatial overlap and spectral separation distances down to 20 nm.



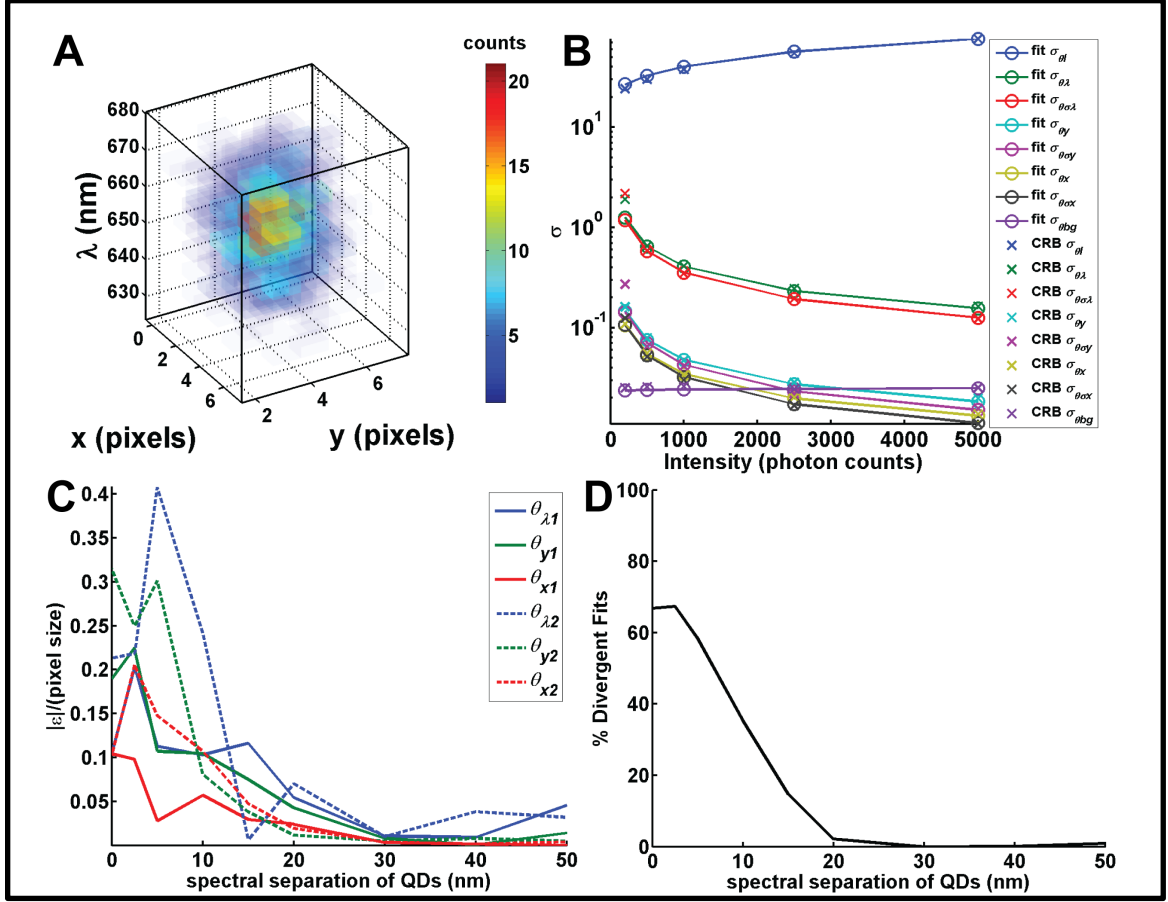


Figure E.1: 3D Gaussian model. (A) 3D pixelated Gaussian model for a single QD with Poisson noise. (B) The standard deviation in parameter estimates from 500 fits of simulated data with Poisson noise (open circles) agree well with the theoretical standard deviation (square root of the Cramér Rao Bound; x). No blinking was included in this simulation. (C) and (D) show results for fitting. Simulations of 2 QDs with a fixed spatial separation (0.5 pixels or ~60 nm) and variable spectral separation (0 to 50 nm) are fit with a 2 QD model. (C) The relative accuracies (absolute error ( $\epsilon$ ) normalized by the pixel size) for positional parameters for QD 1 (solid lines;  $\theta_{x1}$ ,  $\theta_{y1}$ ,  $\theta_{\lambda1}$ ) and QD 2 (dashed lines;  $\theta_{x2}$ ,  $\theta_{y2}$ ,  $\theta_{\lambda2}$ ). (D) The percent of divergent fits (yielded unreasonable parameter estimates).

Similar to previous work, the 3D Gaussian fitting algorithm is implemented in Compute Unified Device Architecture (CUDA) for Graphics Processing Units (GPUs). The algorithmic implementation for fitting single and multi-QD models for an individual sub image is an adaptation of previous work (Figure E.2).

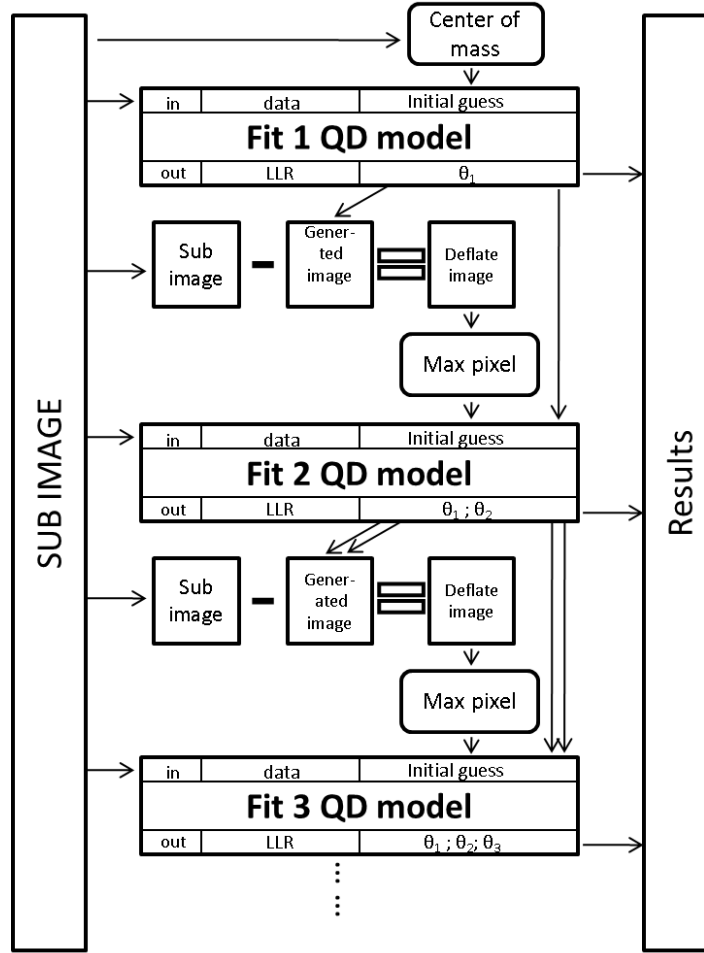


Figure E.2: Multi-QD fitting routine. QD fitting is performed sequentially for 1 to  $N$  QDs. Figure adapted from Huang et al. More details about the fitting steps are included in the text.

1. Single and multi-emitter fitting performed on each sub-volume. Typically, 1-4 emitter fitting
2. Initial estimate(s)
  - a.  $\theta_l$  summation of all pixels divided by number of models (double check code)
  - b. Position  $(\theta_\lambda, \theta_y, \theta_x)$ 
    - i. 1-emitter model: center of mass used for position estimates
    - ii. m-emitter model
      1. Result from select alternating iteration for model m-1 used for deflation
      2. Maximum pixel after deflation used as initial estimate for model m
  - c. Spread  $(\theta_{\sigma_x}, \theta_{\sigma_y}, \theta_{\sigma_z})$

- i. Standard values identified from localizations of 8 color of QDs on glass
    - ii. Typical values are 10 nm ( $\theta_{\sigma_\lambda}$ ), 1.14 pixels ( $\theta_{\sigma_y}$ ), and 0.80 pixels ( $\theta_{\sigma_x}$ )
  - d. Zero used for  $\theta_{bg}$
- 3. Parameter optimization
  - a. Newton-Raphson iterative update method used to optimize model parameters
  - b. Upper limits for single steps used to aid in convergence.
  - c. Alternating iteration scheme
    - i. Large parameter space for simultaneous fitting of multiple parameters leads to divergence from expected results; therefore, a scheme for limiting the number of parameters estimated simultaneously has been devised.
    - ii. Alternate between fixing and fitting specified model parameters. Typical, scheme depicted below:
      1. 50 iterations: optimize  $\theta_\lambda, \theta_y, \theta_x$
      2. 50 iterations: optimize  $\theta_I, \theta_\lambda, \theta_y, \theta_x$
      3. 100 iterations: optimize  $\theta_I, \theta_\lambda, \theta_{\sigma_\lambda}, \theta_y, \theta_x$
      4. 50 iterations: optimize  $\theta_\lambda, \theta_{\sigma_\lambda}, \theta_y, \theta_{\sigma_y}, \theta_x, \theta_{\sigma_x}$

QD blinking while the excitation line is scanning over a single QD causes errors in localization in the scan dimension of the line (**Figure E.3**). The assumption that the mobility of individual receptors is dimension independent means that this artifact has a minimal impact on physical interpretation of the data. This artifact causes difficulties for the 3D Gaussian model in x (scan dimension) and complicates several facets of SPT in HSM images:

- (1) The log likelihood ratio test cannot be used to select the appropriate model;
- (2) The CRB does not accurately approximate the variance in parameter estimates in x (scan dimension).

Thusly, an empirically determined algorithm is used to identify ‘appropriate’ fits (see below).

### Steps for Filtering QD Localizations

1. Eliminate fits with unreasonable fit parameters
2. Eliminate multi-emitter fits in which localizations are too close to one another.
  - An error scaling term ( $a$ ) defined by the user is used to identify closeness of position parameter values. The error scaling term is defined independently for spatial and spectral dimensions.
  - Fits in which position parameters for QD<sub>*i*</sub> ( $\theta_{\lambda_i}$ ,  $\theta_{y_i}$  or,  $\theta_{x_i}$ ) and for QD<sub>*j*</sub> ( $\theta_{\lambda_j}$ ,  $\theta_{y_j}$  or,  $\theta_{x_j}$ ) are closer together than their combined errors multiplied by the error scaling term  $a_\lambda \sqrt{\sigma_{\theta_{\lambda_i}}^2 + \sigma_{\theta_{\lambda_j}}^2}$ ,  $a_y \sqrt{\sigma_{\theta_{y_i}}^2 + \sigma_{\theta_{y_j}}^2}$ , and  $a_x \sqrt{\sigma_{\theta_{x_i}}^2 + \sigma_{\theta_{x_j}}^2}$  respectively
3. Compare all models (1 to m-emitters) for a single sub-volume in which all  $\theta$  and  $\sigma_\theta$  values pass filtering steps 1-2. Use log likelihood ratio to compare models with user-defined p-value for the chi squared distribution with the degrees of freedom equal to the difference in the number model parameters [3].
4. Identify repetitive localizations and select localization with lowest relative error
  - Repetitive localizations are identified by the same procedure as that used in step 2.
  - Relative error is defined as  $\left(\frac{a_\lambda * \sigma_{\theta_\lambda}}{\lambda_{width}}\right)^2 + \left(\frac{a_y * \sigma_{\theta_y}}{y_{width}}\right)^2 + \left(\frac{a_x * \sigma_{\theta_x}}{x_{width}}\right)^2$

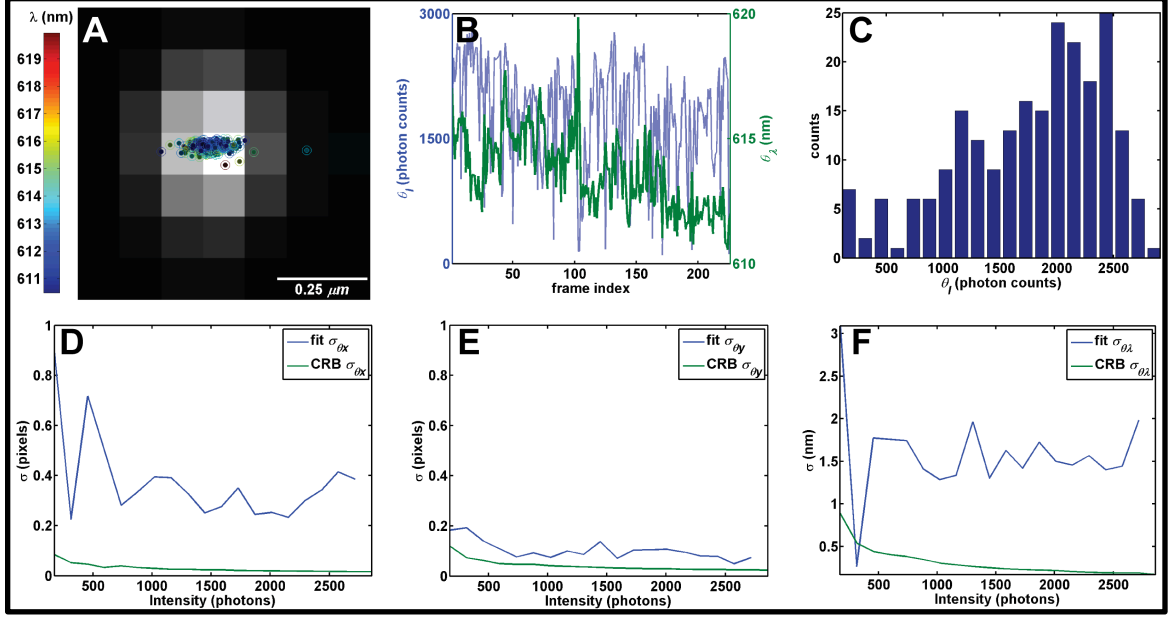


Figure E.3: (A) Localizations for a single QD605 overlaid on the sum projection of raw data. Coloration of localizations corresponds to the localized emission peak (color bar). The estimated intensity (left axis; blue) and spectral emission peak (right axis; green) are shown over time ( $\sim 3.8$  fps) in (B). Note the blue shifting of the QD is observed in (A) and (B). Localizations were binned by intensity in (C) and the standard deviation of the localization parameters were compared to the square root of the CRB in (D), (E), and (F). The standard deviation in the line dimension (E) corresponds well to the theoretical lower bound. The standard deviation in the scanning dimension (D) and the spectral dimension (F) do not correspond well with theory. This is attributed to QD blinking during the line scan and QD blue shifting respectively.

## E.2 Track Reconstruction

Cost matrices are used to build trajectories in two steps: frame-to-frame and gap closing.

Physical models are used to derive the costs for linking localizations, starting a new trajectory (birth), and ending a trajectory (death). The cost for connecting observations 1 and 2 is

$$l_{m,n} = -\log \left( P(x_2, y_2, t_2 | x_1, y_1, t_1) P(\lambda_2 | \lambda_1) \right).$$

Under the assumption of Brownian motion, the probability of making observation 2  $(x_2, y_2, t_2)$  given observation 1  $(x_1, y_1, t_1)$  is

$$P(x_2, y_2, t_2 | x_1, y_1, t_1) = e^{\frac{-(\theta_{x_1} - \theta_{x_2})^2 - (\theta_{y_1} - \theta_{y_2})^2}{4D\Delta t + 2\sigma_1^2 + 2\sigma_2^2}},$$

where

$$\sigma_1^2 = \sigma_{\theta_{x_1}}^2 + \sigma_{\theta_{y_1}}^2$$

is the spatial localization error for observation 1 and  $\sigma_2^2$  is similarly defined for observation 2. Similarly, due to the spectral emission peak, the probability of making observation 2 ( $\lambda_2$ ) given observation 1 ( $\lambda_1$ ) is

$$P(\lambda_2 | \lambda_1) = \text{erf} \left( \frac{|\theta_{\lambda_1} - \theta_{\lambda_2}|}{\sqrt{2(\sigma_{\theta_{\lambda_1}}^2 + \sigma_{\theta_{\lambda_2}}^2 + \sigma_{\lambda_{\text{jump}}}^2)}} \right),$$

where  $\sigma_{\lambda_{\text{jump}}}^2$  accounts for the variance in the observed spectral emission peak due to spectral jumping or bluing of individual QDs. The cost for a previously unobserved QD blinking on (birth) or a currently tracked QD blinking off (death) is determined by particle density and estimated blinking rates. Building a cost matrix from physical models is discussed in more detail in a manuscript in preparation by Relich P, Cutler PJ, Huang F, Lidke KA.

The cost matrix built from costs of linking, birth, and death is treated as a linear assignment problem to link localizations into trajectories. The spectral information of localized QDs greatly improves the accuracy of trajectories and permits SPT at higher labeling densities (**Figure E.4**).

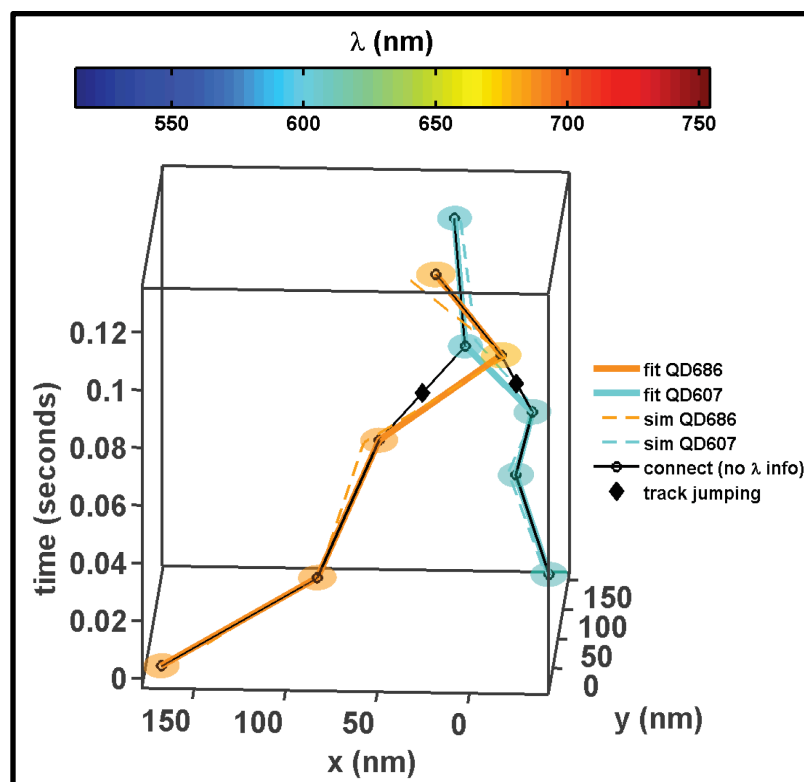


Figure E.4: Spectral information improves trajectory connections. Hyperspectral image data (100 frames) with diffusing QDs were simulated (QD simulation parameters attained from the characterization of QDs) and localized (Appendix E). Trajectories were subsequently built either using (solid colored lines) or ignoring spectral information (solid black lines). Localizations are shown in ellipsoids (size of the ellipsoid corresponds to 3x the estimated localization accuracy), and solid colored lines correspond to the connected trajectories. Dashed colored lines represent the ‘true’ simulated trajectories. The black line with circles identifies trajectories built from connecting localizations without spectral information. Black diamonds represent positions where tracks jump from one true underlying track to another.

## References

1. Malik MD, Cutler PJ, Liu S, Byars JM, Lidke DS, et al. (2013) Multi-color Quantum Dot Tracking using a High-Speed Hyperspectral Line-Scanning Microscope. Manuscript in review.
2. Smith CS, Joseph N, Rieger B, Lidke K a (2010) Fast, single-molecule localization that achieves theoretically minimum uncertainty. Nature methods 7: 373–375. Available: <http://www.pubmedcentral.nih.gov/articlerender.fcgi?artid=2862147&tool=pmcentrez&rendertype=abstract>.
3. Härdle WK, Simar L (2012) Applied Multivariate Statistical Analysis. 2nd ed. Springer.